Bose-Einstein Correlations in 14.6 A·GeV/c Si + Au → $2K^+$ + X Central Collisions

by

Vincent Cianciolo

B.S. University of Michigan, Ann Arbor (1988)

Submitted to the Department of Physics
in partial fulfillment of the requirements for the degree of

Doctor of Philosophy

at the

MASSACHUSETTS INSTITUTE OF TECHNOLOGY

May 1994

Author .....
Department of Physics
May 9, 1994

Certified by .....
George S. F. Stephans
Principal Research Scientist, Laboratory for Nuclear Science
Thesis Supervisor

Certified by .....
Wit Busza
Professor, Department of Physics
Thesis Co-supervisor

Accepted by .....
George Koster
Chairman, Physics Graduate Committee

Bose-Einstein Correlations in 14.6A·GeV/c Si + Au → 2K⁺ + X Central Collisions

by

Vincent Cianciolo

Submitted to the Department of Physics
on May 10, 1994, in partial fulfillment of the
requirements for the degree of
Doctor of Philosophy

Abstract

This thesis presents a comparison of the Bose-Einstein correlations of $\approx 50,000$ K^+K^+ pairs and $\approx 110,000$ $\pi^+\pi^+$ pairs created in $14.6\,A \cdot GeV/c$ $^{28}Si + {}^{197}Au$ central collisions. Bose-Einstein correlations of K^+K^+ and $\pi^+\pi^+$ pairs are complementary probes of the space-time size and the dynamics of the baryon-rich matter created in central heavy ion collisions at the AGS. This is the first Bose-Einstein correlation analysis of K^+K^+ pairs created in heavy ion collisions.

This measurement was taken by the E802 collaboration, as a part of BNL AGS experiment E859. Data were collected with a magnetic spectrometer enhanced by a second level trigger with 40μsec online particle identification capability. Spectrometer angles were chosen to optimize acceptance overlap for the two species. Centrality was determined by a hardware trigger on the total charged particle multiplicity.

Several different 1-, 2- and 3-dimensional analyses have been performed for both species. The K^+ source parameters are observed to be at least 50% smaller than the π^+ source parameters in every source parameterization tested. The duration of K^+ emission may be extremely small. The K^+ source parameters are consistent with the size of the ^{28}Si projectile. The π^+ source parameters are consistent with other measurements using the same apparatus. Both the π^+ and K^+ sources appear oblate with the major axis (perpendicular to the beam) $\approx 25\%$ larger than the minor axis (parallel to the beam). Cuts were made on the average pair momentum ($\langle p^{pair} \rangle$). With increasing $\langle p^{pair} \rangle$, there is an observed trend towards decreasing source-size parameters, and decreasing chaoticity parameter. Cuts were also made on the single-particle rapidity for the π^+'s. Results from this cut unambiguously show dynamical correlations. Many systematic errors on the extracted source parameters were examined. Systematic uncertainty on the various parameters is estimated to be 5–10%, comparable to the statistical uncertainty.

The data have been compared to the RQMD model. Bose-Einstein correlations are incorporated into the model *post hoc*, using a semi-classical formalism developed by Pratt. RQMD correlation functions are consistent with the data. An examination of the space-time distribution of the RQMD source reveals the sensitivity of the technique to the collision dynamics.

Thesis Supervisor: George S. F. Stephans
Title: Principal Research Scientist, Laboratory for Nuclear Science

Thesis Co-supervisor: Wit Busza
Title: Professor, Department of Physics

I prefer the errors of enthusiasm to the indifference of wisdom.

— Anatole France

Contents

CONTENTS

List of Tables

List of Figures

LIST OF FIGURES

LIST OF FIGURES

Chapter 1

Introduction

The goal of the research described in this thesis was to probe the hot, baryon-rich matter created in relativistic heavy ion collisions. The technique employed was the Bose-Einstein correlations of positive kaons (K^+'s).

This *Introduction* chapter presents an overview of the theoretical motivations for the study of relativistic heavy ion collisions, and briefly discusses the state of the field. The motivations for the specific measurement made in this thesis are outlined, and the former and current measurements of K^+K^+ Bose-Einstein correlations are reviewed. Finally, the basics of Bose-Einstein correlation measurements are reviewed and their contribution to our understanding of heavy ion collisions is discussed. Chapter 2, *Experimental Apparatus*, describes the battery of detectors that were needed to collect the data used in this analysis. Chapter 3, *Collaboration Software*, outlines all of the standard analysis programs used to convert raw information (e.g., ADC and TDC channels) into interesting information (i.e., identified particles). Chapter 4, *Correlation Analysis*, details all of the steps needed to extract a Bose-Einstein correlation measurement from identified particles. Chapter 5, *Results*, summarizes all of the results of the Bose-Einstein correlation analysis of the spectrometer data. Chapter 6, *Bose-Einstein Correlations in Models*, lists the different types of phenomenological models that are used to try to understand complicated heavy ion collisions. The *post hoc* imposition of Bose-Einstein correlations on one particular model, RQMD, are discussed. Results are compared to data. Chapter 7, *Conclusions*, will summarize the lessons learned in this analysis. Various appendices examine aspects of the analysis too detailed to include in the general discussion.

1.1 QCD and the Elusive QGP Phase Transition

It must be acknowledged that, without hope of observing the Quark Gluon Plasma (QGP), relativistic heavy ion collision research would probably not be the burgeoning field it is today. More than 500 physicists world-wide have joined this quest in the eight years since relativistic heavy ion beams were first accelerated at the BNL AGS and the CERN SPS. But, it is this author's strongly held opinion, that if the QGP is the only discovery made in the course of relativistic heavy ion research, it will be a *very* sterile quest.

Using the metaphor of the quest, we need to take our eyes off the horizon, and stop and smell the roses. After all, we are creating, in the laboratory, matter at temperatures and densities that may not have existed since microseconds after the Big Bang. Making our immediate goal the careful characterization of this matter will have important, beneficial, psychological consequences. In addition, since nature has always been surprising, we will probably make all sorts of discoveries that we did not expect.

In the field theory of the strong force, Quantum ChromoDynamics (QCD), different values of the strong charge are known as "color." Quarks carry color, anti-quarks carry anti-color, and gluons carry both. Despite many experimental searches, a free quark has never been found. Rather, all known objects are color-singlet combinations of a quark–anti-quark pair (mesons) or three (anti-)quarks ((anti-)baryons). This phenomenon is known as "color confinement." Inside a QGP, the QCD binding potential is Debye screened, and the color-singlet restriction is removed.

The existence of the phase transition to a QGP can be motivated on very general grounds. At some temperature, the energy will be larger than the quark-quark binding energy. At some density, the color-bound objects will overlap, and the multitude of color charges will screen the long-range binding potential. If one could compress a nucleus to several times the density of an individual nucleon, then the individual nucleons would overlap. Under these conditions, it seems intuitive that the picture of nucleons as three isolated quarks would break down. Jaffe has argued that it does not really matter if the hadrons overlap, the quark-quark bonds must be broken [Jaf]. He suggests that the figure of merit for a critical density is more accurately phrased in terms of the density for which the Fermi energy is great enough to drive the reaction $p + p \rightarrow p + \Delta$. The minimum momentum of the two incoming protons in this reaction is $p_{min} = 545\,\mathrm{MeV/c}$. This gives us a critical density $\rho_c = 8.95\rho_0$, where $\rho_0 = 0.17\,\mathrm{fm}^{-3}$, is the density of normal nuclear matter.

Perturbative QCD has been a very successful theory. But, at small energy transfers (or large

distances), the strong coupling constant becomes so large that perturbation theory becomes impossible. The only currently available alternative is lattice QCD. Interest in the QGP stems from the prediction by lattice QCD that a QGP is formed at a critical temperature of 200 MeV and a critical density of 5-10 ρ_0 [Mül85, and references therein]. In much the same way that the solution to a textbook problem often becomes clear when the answer is known, verification of the predicted transition (and any other discoveries made along the way) may provide important guidance in the construction of a calculable theory of the strong force.

Heavy ion collisions are thought to be the most promising means of producing the QGP. They are expected to produce extreme conditions of temperature and density over relatively long times and in relatively large volumes. Under these conditions, it is hoped that thermalization will occur, and that we will be able to see macroscopic evidence of the phase transition. The conditions predicted to be necessary to create the QGP are indicated on the schematic nuclear matter phase diagram, shown in figure 1-1. At the AGS, we believe we are creating nuclear matter in the lower right corner of this figure.

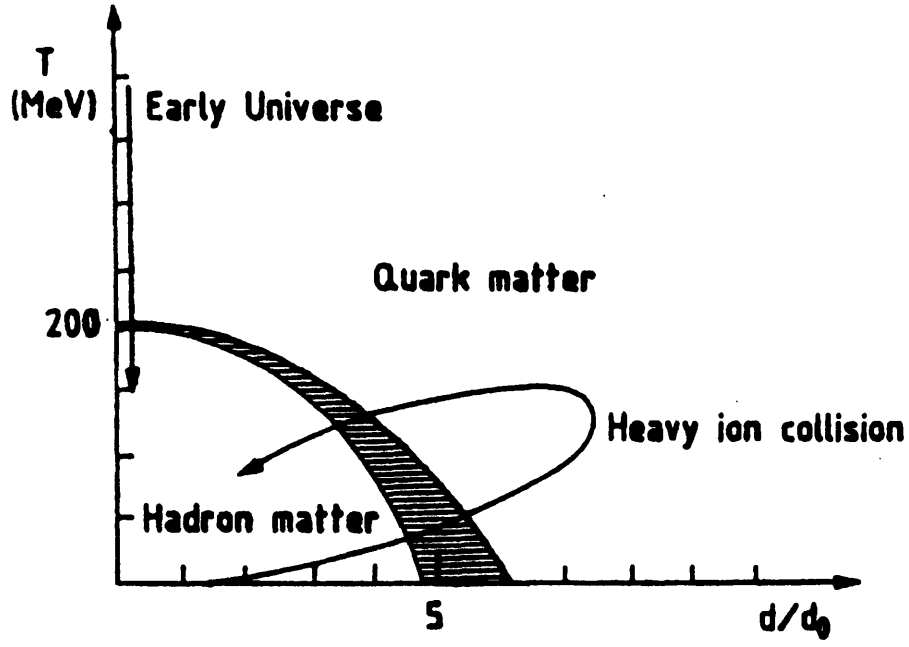

Figure 1-1: Schematic nuclear matter phase diagram [Jac89]. The density, d, is given in units of normal nuclear matter density, d_0.

When the results of relativistic heavy ion collisions came under theoretical scrutiny, naive hopes for easy observation of the QGP were dashed. It was discovered that many of the proposed

signatures for QGP production were also signatures for hot, dense nuclear matter without QGP formation. As a result, even though many of the signatures have been observed, there is no conclusive evidence for QGP formation.

Suppression of the J/Ψ (and other $q\bar{q}$ resonances) is one proposed signature of QGP formation. The physical picture is that color screening inside the plasma will reduce the $c\bar{c}$ attractive potential, making it more likely that these quarks will combine with light quarks to form D mesons. In hot hadronic matter, the observed number of J/Ψ's is reduced by absorption.

Enhanced strangeness production has been proposed as a signature of QGP formation. In a plasma, it takes 300 MeV (twice the strange quark mass) to create $s\bar{s}$ pairs. In a hadronic gas, where we are forced to produce color singlets, it takes 1000 MeV (twice the kaon mass) to produce an $s\bar{s}$ pair. If, as expected, the QGP is accompanied by chiral restoration, the strange quark mass is reduced to 150 MeV, and strangeness production is further enhanced. However, cascade codes, with no QGP formation, are nearly able to reproduce the observed enhancement [Mor94].

If a QGP is created, the transition into a colored state vastly increases the number of degrees of freedom (37/3) [Mül85]. Before the QGP can hadronize into color singlet states, it must expand so that hadronization does not decrease the entropy density. This expansion may be observable in Bose-Einstein correlations, which are sensitive to the space-time extent of the produced particles [Ber89, Pra86, Pra92].

I will not keep the reader in suspense - we have seen no evidence for QGP production. But, we have made a world-class measurement, and learned a lot about the richness and limits of Bose-Einstein measurements of relativistic heavy ion collisions.

1.2 Motivations for this Measurement

I would characterize the original motivation of the E802 collaboration (and of the author) for making the K^+ correlation measurement as a healthy mix of adventure and ambition. There was a palpable sense of exploring uncharted territory. The few previous kaon correlation measurements, details of which are given in section 1.3, were severely limited by the paucity of kaons. At the same time, dreams of the QGP and a Nobel Prize have certainly drifted through the minds of every physicist studying relativistic heavy ion collisions. Kaon correlations were seen as a potentially important probe of the QGP if it was created. The enhanced strangeness production observed by E802 [A+90a] was a predicted signature of the QGP [RM82, Raf84] and it was hoped that a high-statistics K^+ correlation measurement could expose any exotic

production mechanism. It was also hoped that the relatively small K^+-baryon cross-section, see figure 1-2, would allow a K^+ correlation measurement to probe an earlier and hotter source region than that probed by the more common $\pi\pi$ correlation measurements. Also mentioned as motivations in the experimental proposal [RLZ88] were the facts that kaons and pions have different resonance contributions, and suffer from different amounts of Coulomb distortion. These differences were hoped to be useful in a systematic understanding of correlation measurements of different species.

Experimental capabilities and theoretical desires for a given measurement often advance together. The measurement of K^+ correlations nicely illustrates this hypothesis. The first suggestions to make such a measurement [GP90, GM89] were published nearly simultaneously with the E859 experimental proposal [RLZ88], of which the K^+ correlation measurement was an important part. More ideas for the using kaon correlations soon followed [Gyu92, Pra92, Prab].

As discussed above, formation of the QGP is predicted to result in very long emission durations. The authors of [GP90] show that the large transverse radius, observed in NA35 pion correlation measurements [Hum88], could be explained equally well by calculations using a resonance gas model, and hydrodynamical calculations assuming QGP formation. This was described as an "accidental numerical coincidence." It was the result of long-lived resonances contributing to pion formation and mimicing the extended source predicted for QGP formation. In the models tested in [GP90], this problem was avoided in K^+ interferometry by virtue of the different resonance contributions to K^+ production.

The different resonances thought to contribute to pion production are listed, along with their decay proper time, in table 1.1. The $K^*(892)$ is the only resonance thought to contribute to $K^\pm$ production. It should be noted that the actual resonance contributions are not known for heavy ion collisions at AGS energies. Unfortunately, none of these resonances could be directly measured by E859. Only the $K^*(892)$ has a major decay mode without any neutral particles. Unfortunately, the small solid-angle (25 msr) of the Henry Higgins spectrometer made it impossible for us to measure this critical resonance.[1] A detailed acceptance calculation has not performed, but the essential problem is illustrated in figure 1-3, which shows the opening angle distribution for the $K^*(892)$ as a function of momentum. The maximum opening angle of the Henry Higgins spectrometer is indicated by the solid line.

If the QGP is formed in a heavy ion collision, it should co-exist in a mixed phase with the hadronic gas [F+86]. It has been suggested that while in this mixed phase, the QGP should

[1]Evidence for the $K^*(892)$ was not seen in a sample of 261,831 π^-K^+ events collected simultaneously with the K^+K^+ data set used in this analysis

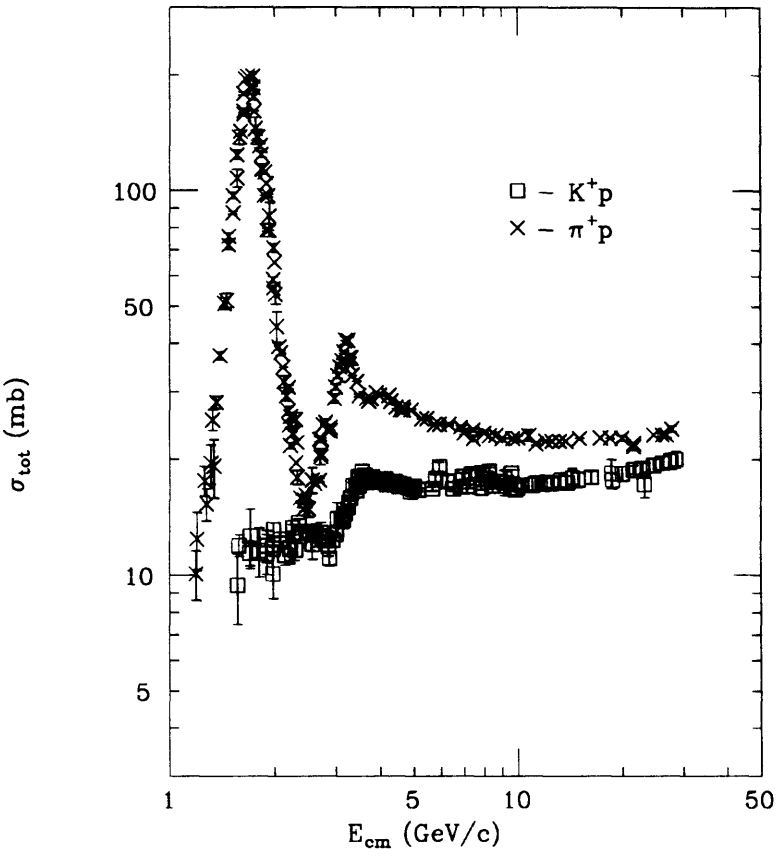

Figure 1-2: σ_{tot} for K^+p and π^+p, as a function of E_{cm} of the collision. From [Gro90, data points obtained through the PDG online facility].

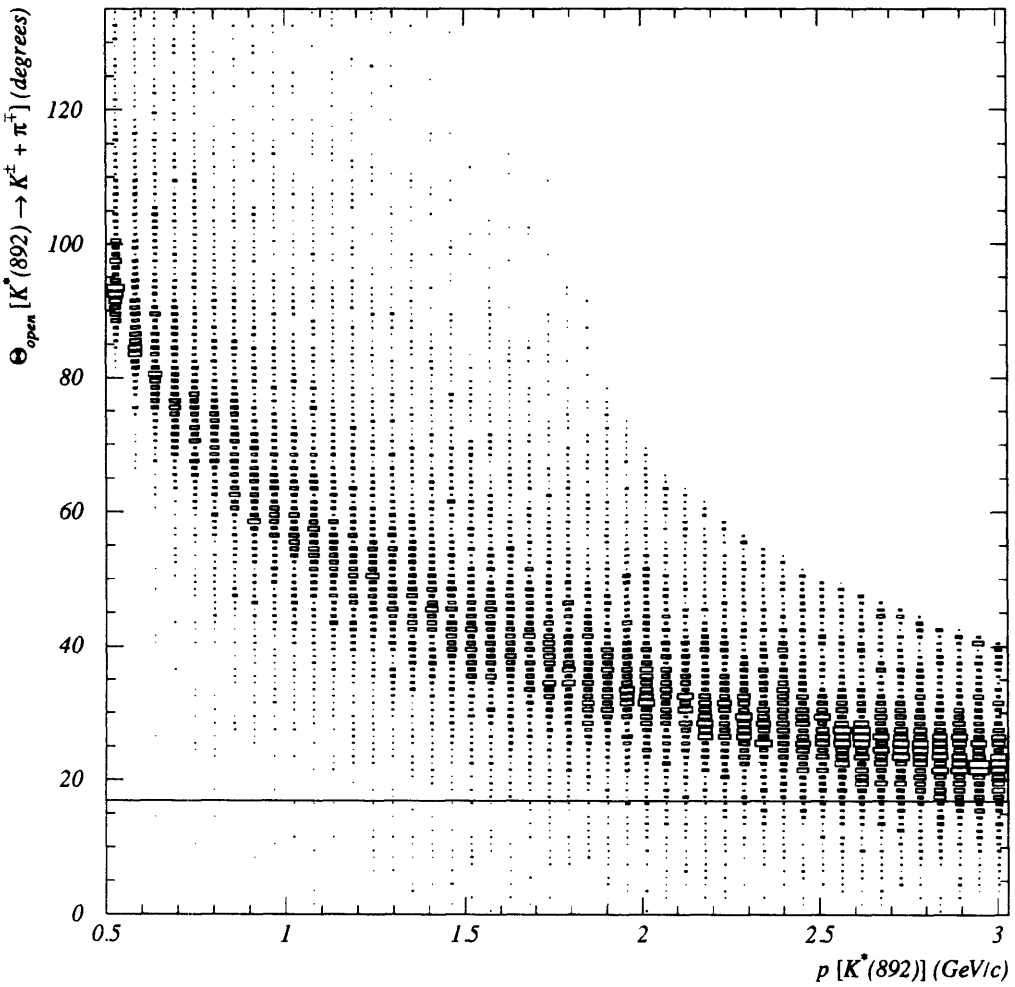

Figure 1-3: This figure shows the opening angle of $K^*(892) \rightarrow \pi^{\pm} + K^{\mp}$ as a function of the $K^*(892)$ momentum. The maximum opening angle of the Henry Higgins spectrometer is indicated by the solid line. This figure represents 50,000 $K^*(892)$ with a flat momentum distribution. Courtesy of T. Sung.

Resonance	Daughter Products in Contributing Decay Mode	Branching Ratio into Contributing Decay Mode	$c\tau$ (fm)	COM Decay Momentum (MeV/c)
$\omega(783)$	$\pi^+\pi^-\pi^0$	88.8%	23.4	327
$\eta(549)$	$\pi^+\pi^-\pi^0$	23.6%	1.64×10^5	175
$\eta'(958)$	$\pi^+\pi^-\eta(549)$	44.2%	947	231
$K^*(892)$	$K^\pm\pi^\mp$	$\sim 100\%$	3.96	288

Table 1.1: List of long-lived resonances contributing to pion production.

exist as droplets [V+91]. Competing surface and shape energies result in a predicted radius distribution for the droplets, with $\langle r \rangle \approx 1\,\text{fm}$. Bose-Einstein correlations have been suggested as a signature for such droplet formation, since two identical particles emitted from a single droplet would result in a small radius component in the correlation function [Pra92]. K^+ correlations were singled out as especially promising, because of their small meson-baryon cross-section and lack of long-lived resonances. In a more recent article [Prab], the case for K^+ correlations viewing the droplets has been weakened. In this new analysis, kaon production is assumed to be equally divided between the QGP droplets and the hadron gas (as opposed to entirely from the QGP droplets) and the emission-time distribution is not a δ-function.[2]

1.3 Other Kaon Correlation Measurements

Only three previous kaon Bose-Einstein correlation measurements have been made [C+78, Å+85, Mor90]. Extracted source parameters from each of these measurements indicated that the kaon source was smaller than the pion source. But, small kaon production cross-sections limited the significance of each of these measurements. [Å+85, Mor90] were forced to combine different projectile/target combinations, and both positive and negative identical kaon pairs.

CERN experiment NA44 [B+93a] is currently collecting data. This experiment has obtained excellent statistics for K^+K^+ pairs in $200\text{A} \cdot \text{GeV/c}\ ^{32}\text{S} + ^{208}\text{Pb}$ collisions. Smaller data samples have been collected for K^+K^+ pairs in $450\,\text{GeV/c}\ \text{p} + ^{208}\text{Pb}$ collisions and K^-K^- pairs in $200\,\text{A} \cdot \text{GeV/c}\ ^{32}\text{S} + ^{208}\text{Pb}$ collisions. Preliminary kaon source parameters are found to be

[2]Pratt has interpreted this result in a very favorable light:

> ... since the distortion of identical particle Bose-Einstein correlations is small... it allows us to safely extract source sizes from correlation functions without considering the effects of density inhomogeneities.

smaller than pion source parameters [Hum94].

1.3.1 Cooper *et al.*

Kaon Bose-Einstein correlations were first measured by Cooper, *et al.*, who compared $K^0_sK^0_s$ and $K^0_sK^{\pm}$ phase space distributions in $p\bar{p}$ annihilations at 0.76 GeV/c [C+78]. The first indication of Bose-Einstein correlations in kaons was found in the asymmetry parameter,

$$B_T \equiv \frac{N\left(\phi > \frac{\pi}{2}\right) - N\left(\phi < \frac{\pi}{2}\right)}{N\left(\phi > \frac{\pi}{2}\right) + N\left(\phi < \frac{\pi}{2}\right)}, \tag{1.1}$$

which was found to be greater for indentical kaons than for non-identical kaons. Here ϕ is defined to be the angle between the transverse momentum of the two particles. A phase-space analysis using known resonances was found to adequately describe the non-identical kaon data, and the large relative momentum portion of the identical kaon data. This same analysis failed to explain the low relative momentum identical kaon data. Fits to the Kopylov and Cocconi correlation functions, see equation 1.26 and equation 1.27, were performed. The source radius obtained for kaons was found to be smaller than source radii obtained for pions at the same energy [A+77], see table 1.2. The data quality is illustrated in figure 1-4, taken from [C+78]. This figure shows the phase-space calculation results, with and without Bose-Einstein correlations, for low relative momentum slices.

Reaction	p_{lab} (GeV/c)	R (fm)	$c\tau$ (fm)	Reference
$p\bar{p} \rightarrow 2K^0_s\pi^+\pi^-$	0.76	0.9 ± 0.2	2.3 ± 0.7	[C+78]
$p\bar{p} \rightarrow 2\pi^+2\pi^-\pi^0$	0-0.70	1.8 ± 0.1	1.4 ± 0.2	[A+77]

Table 1.2: Comparison of kaon and pion source parameters in $p\bar{p}$ collisions. From [C+78].

1.3.2 Åkesson *et al.*

Åkesson *et al.* used the Axial Field Spectrometer to measure the Bose-Einstein correlation of kaons, combining K^+K^+ and K^-K^- pairs from $\alpha\alpha$ collisions at $\sqrt{s} = 126$ GeV, pp collisions at $\sqrt{s} = 63$ GeV, and $p\bar{p}$ collisions at $\sqrt{s} = 53$ GeV [Å+85]. Data were fit to the Kopylov correlation function, modified because data was insufficient to simultaneously determine all three fit

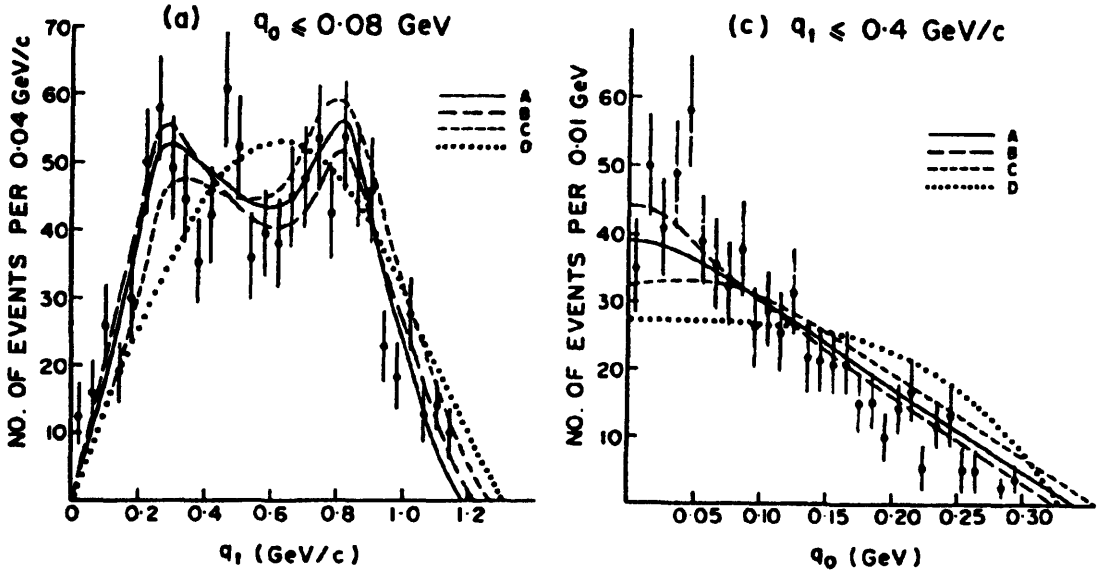

Figure 1-4: This figure, taken from [C+78], shows the first Bose-Einstein correlation measurement of kaons for $p\bar{p} \rightarrow 2K^0_s\pi^+\pi^-$. The panels show low relative momentum slices for the two variables in the chosen correlation functional forms, see equation 1.26 and 1.27. Note that the q_t in the figure refers to the variable q_{Tpair} in this analysis. The A curves show the final phase-space calculation with resonances and the Kopylov form for the correlation function. The B curves show the same calculation using the Cocconi form of the correlation function. The C curves show the calculation without any corrrelation function and the D curves do not include any resonances.

parameters:[3]

$$C_2\left(q_{Tpair}\right) \equiv 1+\lambda'\left[2J_1\left(q_{Tpair}r\right)/\left(q_{Tpair}r\right)\right], \tag{1.2a}$$

$$\lambda' \equiv \frac{\lambda}{\left[1+\left(q_{Lpair}c\tau\right)^2\right]}. \tag{1.2b}$$

Data in the relative momentum slice, $q_{Lpair} \leq 0.30\,\mathrm{GeV/c}$, are shown in figure 1-5, along with the fitted correlation function of the form given in equation 1.2. The fit parameters for pions and kaons, plotted as a function of the total charged multiplicity, $\langle n_{ch}\rangle$, are shown in figure 1-6. The kaon source radii are seen to be smaller than the pion radii at comparable values of $\langle n_{ch}\rangle$.

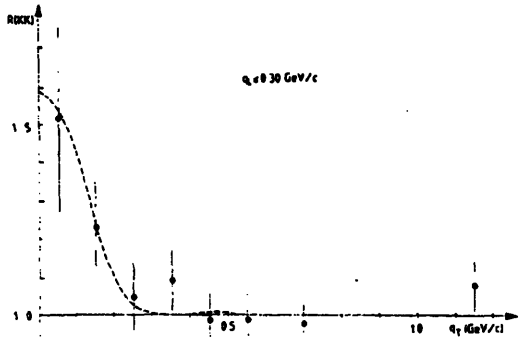

Figure 1-5: This figure, taken from [Å+85], shows the first Bose-Einstein correlation measurement of charged kaons in $pp, p\bar{p}, \alpha\alpha \rightarrow K^+K^+$ (or K^-K^-) $+ X$ collisions. Data are plotted along with the correlation function fit to equation 1.2. Note that the q_l and q_t in this figure are equivalent to q_{Lpair} and q_{Tpair} respectively.

1.3.3 E802 Kaon Correlations

The last previous kaon Bose-Einstein correlations measurement was made by experiment E802 [Mor90]. The measured correlation function, $C_2(Q_{inv})$, shown in figure 1-7, consisted of 1500 K^+K^+ pairs obtained by combining data from $^{28}Si + {}^{27}Al$ and $^{28}Si + {}^{197}Au$ collisions at the 5° and 14° spectrometer settings. No source parameters were quoted, but the radius was clearly smaller than that measured by E802 for the pion source. This was a strong incentive for E859, since it proved that a solid measurement could be obtained with an improved trigger.

[3]Note that for $\beta = 1$, $q_0 = q_{Lpair}$.

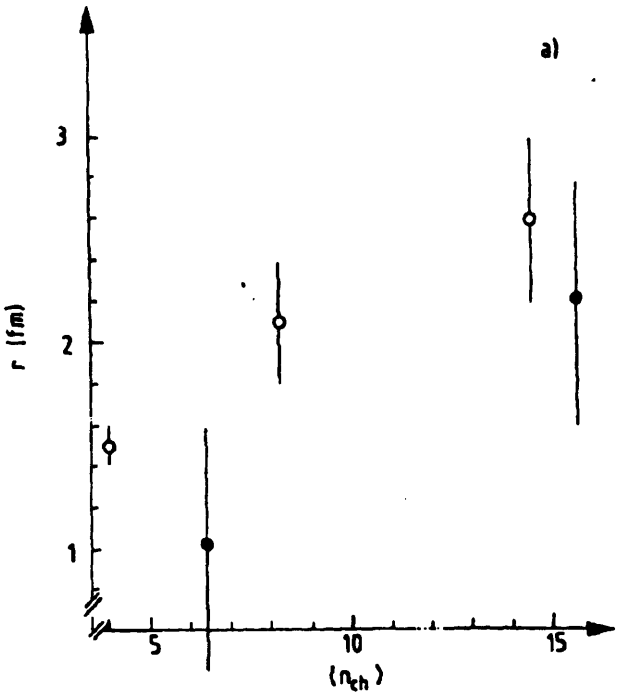

Figure 1-6: $\langle n_{ch} \rangle$ dependence of kaon (solid symbols) and pion (open symbols) source radii from [Å+85]. The kaon radii are seen to be marginally smaller than the pion radii at corresponding values of $\langle n_{ch} \rangle$.

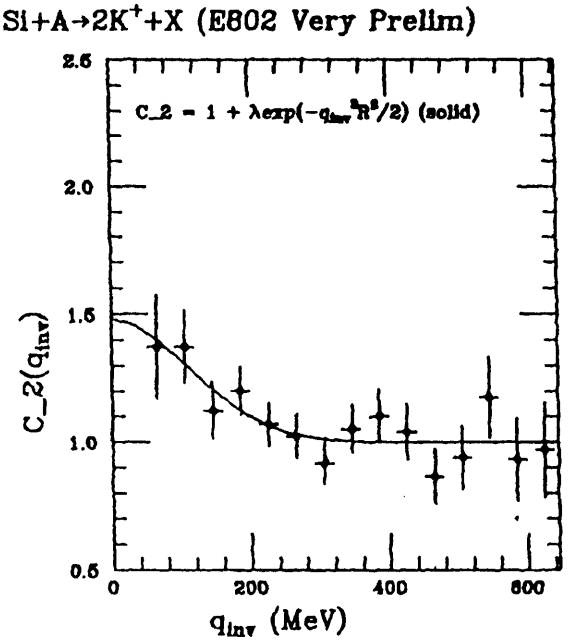

Figure 1-7: E802 K^+K^+ correlation function. From [Mor90].

1.3.4 NA44 Kaon Correlations

CERN experiment NA44 is a second-generation heavy ion experiment, specialized for measuring Bose-Einstein correlations [B+93a]. It is a focussing spectrometer, using several dipole and quadrupole magnets to maximize the acceptance for pairs with small relative momentum. NA44 is the only experiment currently capable of making a high statistics measurement of the K^- source.

Two scenarios have been suggested to result in a K^- source that is larger than the K^+ source. For QGP formation at finite baryon densities, where the chemical potential of kaons, K^+ and K^0, $\mu_K = \mu_q - \mu_s > 0$, strange quarks are concentrated (distilled) in the plasma phase. Such quarks do not hadronize into anti-kaons, K^- and $\bar{K}^0$, until late in the collision process [G+87].[4] This would result in very different source distributions for kaons and anti-kaons as measured by Bose-Einstein correlations [GM89, Gyu92]. Such a difference could also result from the different meson-baryon cross-sections for kaons and anti-kaons.

A three-dimensional analysis of the K^+ source has been performed using the $q_L q_{Tside} q_{Tout}$ parameterization [Hum94], see equation 1.32. Low relative momentum slices of the various projections [5] are shown in figure 1-8. The kaon source parameters are found to be smaller than the pion source parameters extracted by the same experiment, see table 1.3. Preliminary results have been compared to RQMD predictions and will be summarized in chapter 6. A preliminary analysis has also been performed for the K^- source. The source parameters for K^-'s were found to be similar to those for K^+'s [Hum94].

	$\pi^-\pi^-$	$\pi^+\pi^+$	K^-K^-	K^+K^+
R_L	4.4 ± 0.4	4.9 ± 0.3	3.6 ± 0.6	2.8 ± 0.3
R_{Tside}	3.7 ± 0.5	4.4 ± 0.2	NA	2.4 ± 0.3
R_{Tout}	3.6 ± 0.2	4.1 ± 0.1	3.2 ± 0.4	2.7 ± 0.2

Table 1.3: Comparison of NA44 source radii, R_L, R_{Tside}, and R_{Tout}, obtained in $^{32}S + ^{208}Pb$ collisions [Hum94].

[4] They may not be released at all, if strange quark matter is indeed stable. So-called strangelets are an area of intense interest [G+94, and references therein].

[5] Note that the fits are performed for these slices, not over the entire phase space. This is a result of the focussing spectrometer which limits the NA44 measurement to one transverse component at a time.

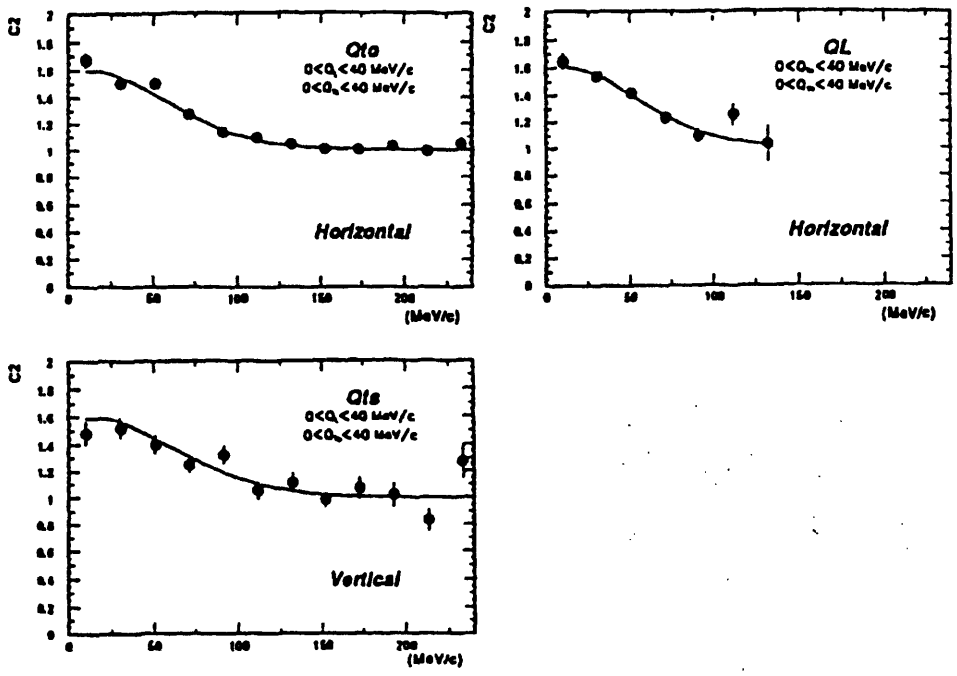

Figure 1-8: This figure shows low relative momentum slices of the NA44 correlation function, $C_2(q_L, q_{Tside}, q_{Tout})$, for $^{32}S + ^{208}Pb \rightarrow 2K^+ + X$[Hum94]. Solid lines are fits to equation 1.32.

1.4 Identical Particle Interferometry Basics

A simple derivation of the correlation function serves to illustrate many important features of intensity interferometry. Figure 1-9 shows a schematic source of identical[6] particles, two of which are detected at $\mathbf{r}_1$ and $\mathbf{r}_2$, with momenta $\mathbf{p}_1$ and $\mathbf{p}_2$. The particles originate at x and y and

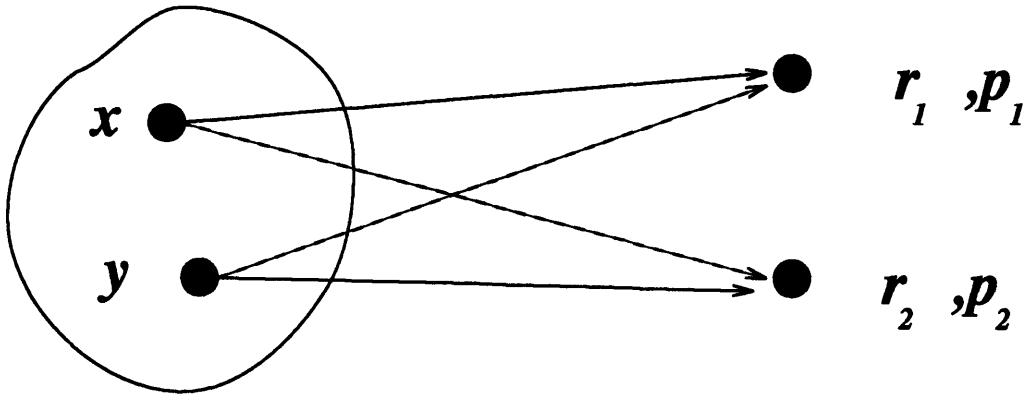

Figure 1-9: Schematic of the particle source used to derive intensity interferometry. See text for details.

their paths are indistinguishable.[7] We have to sum the amplitudes of the two indistinguishable processes. If we assume the particles to be Bosons, then the sum needs to be symmetrized.

Plane Waves

If we assume that the Bosons' wavefunctions are plane waves, then we can write the symmetrized amplitude as:

$$A_{12} = \frac{1}{\sqrt{2}}(\exp(i\mathbf{p}_1 \cdot (\mathbf{r}_1 - \mathbf{x}))\exp(i\mathbf{p}_2 \cdot (\mathbf{r}_2 - \mathbf{y})) + \exp(i\mathbf{p}_1 \cdot (\mathbf{r}_1 - \mathbf{y}))\exp(i\mathbf{p}_2 \cdot (\mathbf{r}_2 - \mathbf{x}))). \quad (1.3)$$

But, the wavefunctions for charged particles are Coulomb waves, and there will be some contribution from the strong interaction. The Coulomb distortion of phase space is usually corrected for with the standard Gamow factor:

$$G(\eta) = \frac{2\pi\eta}{\exp(2\pi\eta) - 1}, \quad (1.4a)$$

[6]Bowler [Bow92] derives the unexpected result that intensity interferometry signals are, in principle, observable from particle/anti-particle pairs. For this to occur, the pair needs to be emitted from the same space-time point, so the effect is likely to be small.

[7]Indistinguishability is simply an experimental reality. Detectors located 1 m from two sources 100 fm apart would need a momentum resolution, $\delta p/p = 10^{-13}$ to distinguish the sources of the individual sources. Thanks to Mark Baker for making this point clear.

$$\eta = \frac{\alpha m}{Q}. \tag{1.4b}$$

Here α is the fine-structure constant, and m is the mass of the particle of interest. This Gamow factor assumes a point source, and so overestimates the true correction due to the screening in a finite-sized source. This overestimate is discussed in section 4.3.5 and is found to be small. Systematic studies indicate that any reasonable error in the Coulomb correction will have little effect on the results.

The strong interaction is short-range, and the large size of the sources created in heavy ion collisions greatly reduces its effect on correlation measurements [Bow88].

No Dynamical Correlations

The next step in the derivation is to obtain the probability for emission of two particles at momenta $\mathbf{p}_1, \mathbf{p}_2$. We integrate the complex square of the amplitude over an emission function, $g(\mathbf{p}, \mathbf{r})$. The assumption of no dynamical correlations is equivalent to the assumption that the emission function factorizes: $g(\mathbf{p}, \mathbf{r}) = f(\mathbf{p})\,\rho(\mathbf{r})$. With this assumption, the integral becomes a simple Fourier transform:

$$\frac{\mathcal{P}_2(\mathbf{p}_1, \mathbf{p}_2)}{\mathcal{P}_1(\mathbf{p}_1)\mathcal{P}_1(\mathbf{p}_2)} = \int d^4\mathbf{x}\, d^4\mathbf{y}\, |A_{12}|^2\, g(\mathbf{x})g(\mathbf{y}), \tag{1.5a}$$

$$= 1 + |\tilde{\rho}(\mathbf{p}_1 - \mathbf{p}_2)|^2 \tag{1.5b}$$

The basic result of this assumption is that intensity interferometry of Bosons (hereafter referred to as Bose-Einstein correlations) leads to an enhancement in the probability for observing two identical particles at low relative momentum. The range of this enhancement in relative momentum will be $\mathbf{q} \sim \hbar/\mathbf{r}$. The enhancement in a certain relative momentum projection will be sensitive to the source size in the conjugate spatial variable. However, this geometrical interpretation comes at a price: if the factorization assumption is valid, then Bose-Einstein correlations can tell us nothing about the phase space evolution of the source. Regardless of the validity of the factorization assumption, we can make the following statement:

> Bose-Einstein correlations measure the separation of those particles that are accepted by the measuring apparatus, at a small enough relative momentum to be subject to Bose-Einstein enhancement.

No Coherence

An assumption at the core of this derivation is that the emitting source is not coherent. If

the source is coherent, then we cannot, even in principle, distinguish two separate emission points. Under these conditions, $|A_{12}|^2 = 1$, and the correlation function is flat.[8]

An observed deviation of the correlation function intercept from its predicted value of one has resulted in an almost universal adoption of the "chaoticity" parameter λ [D+82]. With this parameter, the correlation function becomes:

$$C_2 = 1 + \lambda\,|\tilde{\rho}(\mathbf{p}_1 - \mathbf{p}_2)|^2 \tag{1.6}$$

λ can arise from other processes besides coherence, and very likely the observed values of $\lambda < 1$ arise from long-lived resonance production. The relative momentum extent of the Bose-Einstein enhancement for particles emitted from such resonances is too small to be resolved by current detectors.

Insensitivity to Parameterization

The insensitivity of the Fourier transform to details of shape was first pointed out in [G+60]. Zajc has emphasized this point, and makes it clear that it is a result of the fact that separation distributions generated from very different position distributions all "look" Gaussian. Figure 1-10 demonstrates this point with data. The π^+ 1D correlation function data is plotted along with correlation functions from a spherical shell, a solid sphere, and a spherical Gaussian. The radius parameter of the Gaussian parameterization was fit to the data. The size parameters of the different parameterizations are selected to give similar values of the *rms* separation.

Applications of Bose-Einstein Correlations

Intensity interferometry was pioneered by Hanbury-Brown and Twiss (HBT) who used the technique to measure the size of stellar radio sources [HB74, and references therein]. The first application of the technique to particle physics was made by Goldhaber, Goldhaber, Lee, and Pais (GGLP) who used the technique to explain the observed difference between opening angle distributions of like and unlike sign pion pairs created in $\mathrm{p\bar{p}}$ collisions [G+60].[9] Some very interesting atomic physics experiments are currently being performed that use identical particle interferometry to elucidate interesting quantum mechanical effects [G+93] and to test the validity of special relativity [C+93a]. Time considerations do not allow detailed descriptions of these experiments here, but interested readers are encouraged to read these very approachable articles.

[8]Note that this does not mean that the interference pattern, which is due to amplitude interferometry, is flat!
[9]HBT, GGLP, intensity interferometry, and Bose-Einstein correlations are used interchangably in the literature.

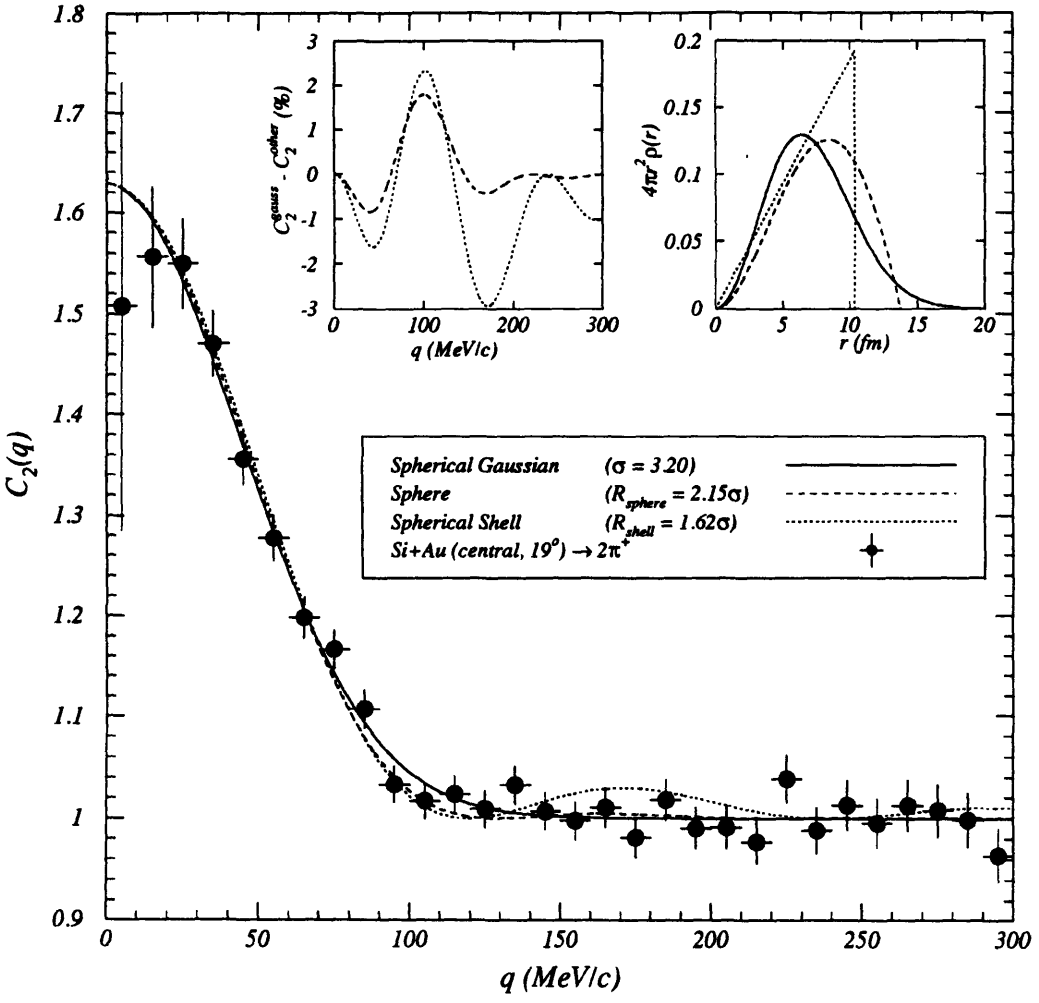

Figure 1-10: Comparison of the measured $\pi^+\pi^+$ correlation function to the predictions of spherical Gaussian, spherical shell and hard sphere parameterizations. The upper left panel shows the fractional difference between the parameterizations, seen to be everywhere less than 5%. The upper right panel vividly illustrates the reason for this insensitivity of the Bose-Einstein correlation technique: the separation distributions for these parameterizations, and in fact any distribution with a comparable *rms* value, are very similar.

Interest in using this technique to examine heavy ion collisions was motivated by the geometrical information thought to be obtainable. As emphasized throughout this thesis, this naive view is no longer held. We now have a better understanding of the sensitivity of Bose-Einstein correlations to collision dynamics. This sensitivity makes Bose-Einstein correlations a more powerful probe than previously realized. At the same time, any simple geometrical interpretations are compromised. Reviews of Bose-Einstein correlations in nuclear and particle physics can be found in [BGJ90, Lor89, Sol94].

The first formulation of intensity interferometry in terms of a correlation function was given by Kopylov [KP74]. The following, rigorous, formulation of the correlation function in terms of the inclusive single-particle and two-particle cross-sections was given by Gyulassy [GKW79]:

$$C_2(\mathbf{p}_1,\mathbf{p}_2) \equiv \frac{\langle n\rangle^2}{\langle n(n-1)\rangle^2}\frac{\sigma\frac{d^6\sigma}{d^3\mathbf{p}_1 d^3\mathbf{p}_2}}{\frac{d^3\sigma}{d^3\mathbf{p}_1}\frac{d^3\sigma}{d^3\mathbf{p}_1}}. \tag{1.7}$$

The factors in the first fraction are the average first and second binomial moments of the multiplicity distribution, introduced to enforce $C_2 = 1$ for an uncorrelated source, regardless of the multiplicity distribution. This correlation function can be written in a more intuitive manner in terms of properly normalized probability distributions:

$$C_2(\mathbf{p}_1,\mathbf{p}_2) = \frac{\mathcal{P}_2(\mathbf{p}_1,\mathbf{p}_2)}{\mathcal{P}_1(\mathbf{p}_1)\mathcal{P}_1(\mathbf{p}_2)}. \tag{1.8}$$

Unfortunately, this formulation is not experimentally feasible. Current state of the art correlation analyses can only analyze three dimensions of this six dimensional quantity.

In the discussion on page 29, we obtained a form for the correlation function in terms of the relative momentum, $\mathbf{q} \equiv \mathbf{p}_2 - \mathbf{p}_1$. Guided by this, we operationally define the correlation function as:

$$C_2(\mathbf{q}) \equiv \frac{\textit{Actual}(\mathbf{q})}{\textit{Background}(\mathbf{q})}. \tag{1.9}$$

Here, the *Actual* distribution is simply the measured relative momentum distribution in whichever parameterization is being examined. The ideal *Background* distribution contains all effects that enter into the *Actual* distribution except the Bose-Einstein symmetrization, i.e., Coulomb repulsion, event class (centrality), kinematic correlations, etc. The standard technique used to generate *Background* distributions in relativistic heavy ion collisions is known as *event-mixing*. This was the technique chosen for this analysis.

There are several reasons to be cautious with an event-mixed *Background*. First, energy and momentum are not explicitly conserved. This should not be a concern for a relativistic

heavy ion collision since no single particle represents a large fraction of the system's total energy. If an experiment is analyzing correlation functions as a function of reaction-plane (the azimuthal orientation of the target and projectile) then event-mixing must be performed with the coordinates defined relative to the measured reaction plane. As first noted by Zajc [Zaj82, Z+84], the errors associated with an event-mixed *Background* are not Poisson. This is was found to be a negligible problem with the data sets used in this analysis, as discussed in section 4.3.1. Zajc was also the first to note [Zaj82, Z+84], that the event-mixed background retains some degree of the correlation. This occurs because the event-mixing procedure integrates over the observed, correlation function-distorted, two-particle momentum distribution. This effect was found to be small (2–5%) for the data sets used in this analysis. More detailed discussion can be found in appendix B.

The event-mixing algorithm has two advantages. First, the centrality distribution is made explicitly the same in the numerator and denominator. Second, complicated questions of single-particle acceptance drop out. To see this, one simply needs to realize that with the event-mixing technique, the spectrometer efficiency and acceptance can be factorized into single-particle and two-particle components [Mor90]:

$$\mathcal{P}_2{}^{obs}(\mathrm{p}_1,\mathrm{p}_2) = \mathcal{P}_2(\mathrm{p}_1,\mathrm{p}_2)\xi_1(\mathrm{p}_1)\xi_1(\mathrm{p}_2)\xi_2(\mathrm{p}_1,\mathrm{p}_2), \tag{1.10a}$$

$$\mathcal{P}_1{}^{obs}(\mathrm{p}_1) = \mathcal{P}_1(\mathrm{p}_1)\xi_1(\mathrm{p}_1), \tag{1.10b}$$

$$\mathcal{P}_1{}^{obs}(\mathrm{p}_2) = \mathcal{P}_1(\mathrm{p}_2)\xi_1(\mathrm{p}_2). \tag{1.10c}$$

When we take the division according to equation 1.10, we see that the ξ_1 terms cancel. The remaining two-particle acceptance (TPAC) effects, ξ_2, must be accounted for. Examination of the effects of the TPAC on this analysis can be found in section 4.2.5, and appendix A.

1.5 Relative Momentum Variables

In this section I will define all of the relative momentum projections used in this analysis for source parameterization. Throughout this discussion 4-vectors will be indicated with boldface type (e.g., Q), 3-vectors will have an arrow superscript (e.g., $\vec{q}$), and scalers will be plain text (e.g., q). Table 1.4 summarizes each relative momentum variable used in this analysis, the source parameter which it measures, and gives a rough physical interpretation. The different projections are illustrated in figure 1-11. Note that throughout this analysis, the beam axis is defined to be the z-axis.

1.5 Relative Momentum Variables

In this section I will define all of the relative momentum projections used in this analysis for source parameterization. Throughout this discussion 4-vectors will be indicated with boldface type (e.g., Q), 3-vectors will have an arrow superscript (e.g., $\vec{q}$), and scalers will be plain text (e.g., q). Table 1.4 summarizes each relative momentum variable used in this analysis, the source parameter which it measures, and gives a rough physical interpretation. The different projections are illustrated in figure 1-11. Note that throughout this analysis, the beam axis is defined to be the z-axis.

Relative Momentum Variable		Conjugate Source Parameter: Physical Interpretation	
Q	$\equiv \sqrt{(\vec{p}_1 - \vec{p}_2)^2 - (E_1 - E_2)^2}$	R_Q	: σ of a spherical Gaussian measured in the pair rest frame.
q_{dana}	$\equiv \sqrt{q_0^2 + q^2}$	R_{dana}	: σ of a spherical Gaussian measured in the chosen, fixed frame. Explicitly assumes $R = \tau$.
q	$\equiv \lvert\vec{p}_1 - \vec{p}_2\rvert$	R	: σ of a spherical Gaussian measured in the chosen, fixed frame. $R_{rms} = \sqrt{3}R$.
q_0	$\equiv \lvert E_1 - E_2\rvert$	τ	: *rms* duration of boson emission.
q_L	$\equiv \lvert p_{z1} - p_{z2}\rvert$	R_L	: *rms* size parallel to the beam axis.
q_T	$\equiv \vec{q} \times \hat{z}$	R_T	: σ of a twi-dimensional Gaussian perpendicular to the beam axis.
q_{Tout}	$\equiv \vec{q} \cdot \hat{z}$	R_{Tout}	: σ of a two-dimensional Gaussian perpendicular to the beam axis and parallel to $\hat{\beta}_{\pi\pi}$. Contribution from source lifetime.
q_{Tside}	$\equiv \lvert\vec{q_T} \times \hat{\beta}_{\pi\pi}\rvert$	R_{Tside}	: σ of a two-dimensional Gaussian perpendicular to the beam axis *and* $\hat{\beta}_{\pi\pi}$. No contribution from source lifetime.
q_{Lpair}	$\equiv \vec{q} \cdot \hat{\beta}_{\pi\pi}$	R_{Lpair}	: *rms* size parallel to $\hat{\beta}_{\pi\pi}$. Full contribution from source lifetime.
q_{Tpair}	$\equiv \vec{q} \times \hat{\beta}_{\pi\pi}$	R_{Tpair}	: σ of a spherical Gaussian perpendicular to $\hat{\beta}_{\pi\pi}$. No contribution from source lifetime.

Table 1.4: Definition of relative momentum variables and rough physical interpretations.

The first variables of interest are the 3-vector and scaler components of the relative momentum:

$$\vec{q} \equiv \vec{p}_1 - \vec{p}_2 \tag{1.11}$$

and,

$$q_0 \equiv |E_1 - E_2| . \tag{1.12}$$

1.5. RELATIVE MOMENTUM VARIABLES

These can be combined into the four-vector, Lorentz invariant relative momentum:

$$\mathbf{q} \equiv (q_0, \vec{q}). \tag{1.13}$$

We will also need to combine these quantities into the form:[10]

$$q_{dana} \equiv \sqrt{q^2 + q_0^2}. \tag{1.14}$$

The magnitudes of the vector quantities are given by:

$$\begin{aligned} q &\equiv |\vec{q}| && \text{(1.15a)} \\ &= \sqrt{\vec{q} \cdot \vec{q}}, \text{ and,} && \text{(1.15b)} \end{aligned}$$

$$\begin{aligned} Q &\equiv |\mathbf{q}| && \text{(1.16a)} \\ &= \sqrt{-\mathbf{q} \cdot \mathbf{q}} && \text{(1.16b)} \\ &= \sqrt{q^2 - q_0^2} && \text{(1.16c)} \end{aligned}$$

We are also interested in different projections of the relative momentum. The longitudinal projection (along the beam axis) is given by:

$$q_L \equiv \vec{q} \cdot \hat{z}. \tag{1.17}$$

The transverse projection perpendicular to the beam axis) is given by:

$$\begin{aligned} \vec{q}_T &\equiv \vec{q} \times \hat{z} && \text{(1.18a)} \\ q_T &= |q_T| && \text{(1.18b)} \end{aligned}$$

Note that this component is unaffected by Lorentz boosts along the beam axis. We can further decompose $\vec{q}_T$ into components parallel and perpendicular to the pair momentum:

$$q_{Tout} \equiv \frac{\vec{q}_T \cdot \vec{p}^{pair}}{|\vec{p}^{pair}|}, \text{ and,} \tag{1.19}$$

[10]This quantity was suggested by Dana Beavis and the name stuck.

$$q_{Tside} \equiv \frac{\left|\vec{q}_T \times \vec{p}^{pair}\right|}{\left|\vec{p}^{pair}\right|}. \tag{1.20}$$

Note that q_{Tside} is perpendicular to both the beam axis (presumably a close approximation to the source axis) and the pair axis. Its conjugate source parameter, R_{Tside}, thus gives the source size without any Lorentz difficulties. The price that we pay for this feature is that q_{Tside} averages over the different angles that $\vec{p}^{pair}$ makes with the source. For a non-spherical source, this means that R_{Tside} averages over different source components.

For Lorentz studies, we also want to decompose the relative momentum vector parallel and perpendicular to $\vec{p}^{pair}$:

$$q_{Lpair} \equiv \frac{\vec{q} \cdot \vec{p}^{pair}}{\left|\vec{p}^{pair}\right|}, \text{ and,} \tag{1.21}$$

$$q_{Tpair} \equiv \frac{\left|\vec{q} \times \vec{p}^{pair}\right|}{\left|\vec{p}^{pair}\right|}. \tag{1.22}$$

1.6 Source Parameterizations

In this section I will describe all of the source parameterizations along with motivations, cautionary notes and the resulting correlation functions. All of the source parameterizations used in this analysis are Gaussians but a few non-Gaussian distributions are mentioned for completeness. We use Gaussian parameterizations for several mundane reasons:

- As discussed on page 38, HBT measurements are primarily sensitive to the *rms* relative separation. With current statistics we are insensitive to the subtle correlation function features that arise from non-Gaussian distributions.

- A Gaussian distribution has a finite *rms* separation. This is the true quantity of interest, and it is vital to comparisons between different parameterizations.

Note that a Gaussian source distribution *does not* give rise to a Gaussian correlation function since $C_2(Q) \sim |\tilde{\rho}(Q)|^2$.[11] Also note that all source parameterizations include the "coherence parameter", λ, discussed on page 38. Throughout this section, $\hbar = c = 1$.

[11] Controversy surrounds the decision to choose between a Gaussian source parameterization and a Gaussian correlation function. The two camps are thankfully divided by the expanse of the Atlantic Ocean. A nice defense of the American position can be found in [Zaj93].

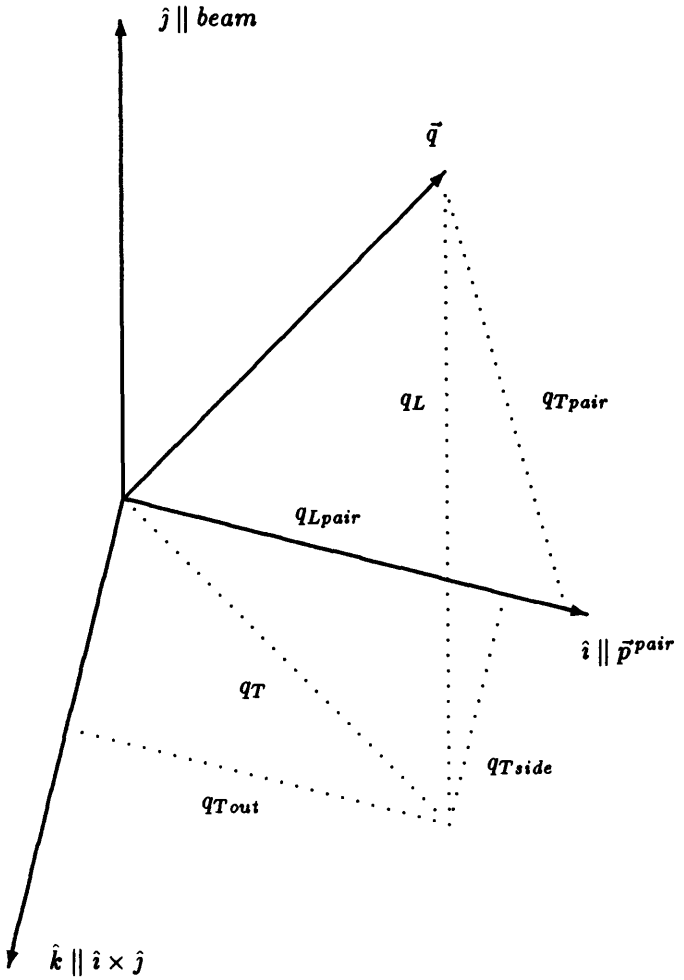

Figure 1-11: Illustration of relative momentum projections.

The first source distribution proposed [G+60], was a Gaussian in the 4-vector separation, r:

$$\rho(r) \sim \exp\left(-\frac{r^2}{2R^2}\right) \tag{1.23a}$$

$$C_2(Q) = 1 + \lambda \exp\left(-Q^2 R_Q^2\right). \tag{1.23b}$$

I will refer to this as the Q parameterization. The Q parameterization is appealing because of the minimal statistical requirements for extracting fit parameters from a one-dimensional correlation function. It also serves as an excellent introduction to the subtle and often non-intuitive Lorentz properties of extracted HBT fit parameters.

The first thing to remember in thinking about these properties is the fact that the quantity that we are interested in measuring is *the source size in the source rest frame*. This means that there are *two* relevant boost parameters:

1. The boost of the source,$\vec{\beta}_s$, relative to some fixed reference frame in which we will measure the relative momentum of each pair.

2. The boost of the source, -$\vec{\beta}_{\pi\pi}$, relative to each pair.

One must also keep in mind the fact that the emission duration of the source, and the size of the source parallel to $\vec{\beta}_{\pi\pi}$, are intimately connected by the basic relationship, $x = vt$. This means that the emission duration will always have a component of the source size, and the source size will always have a component of the emission duration. This connection can also be expressed in a very useful relationship between the vector and scaler components of the relative momentum:

$$q_0 = \vec{q} \cdot \vec{\beta}_{\pi\pi} \tag{1.24a}$$

$$= q\beta_{\pi\pi} \cos(\alpha).^{12} \tag{1.24b}$$

An important consequence of equation 1.24 is that $q_0 \leq q$, eliminating half of the phase space plane. This severely limits the number of q_0 bins at the small values of q where the correlation function is greater than one. This makes τ a very difficult parameter for the fitting procedure to determine.

[12]Note that $\beta_{\pi\pi}$ and $\cos(\alpha)$ are different for every pair.

1.6. SOURCE PARAMETERIZATIONS

Using equation 1.24 let us rewrite the Lorentz invariant correlation function given in equation 1.23:

$$C_2(Q) = 1 + \lambda \exp\left(-\left[q^2 - q_0^2\right] R_Q^2\right), \tag{1.25a}$$

$$= 1 + \lambda \exp\left(-q^2 R_Q^2 \left[1 - \beta_{\pi\pi}^2 \cos^2(\alpha)\right]\right), \tag{1.25b}$$

$$\equiv 1 + \lambda \exp\left(-q^2 R_Q^2 / \gamma_{\pi\pi}^2\right), \tag{1.25c}$$

where we have defined $\gamma_{\pi\pi}^2 = \left[1 - \beta_{\pi\pi}^2 \cos^2(\alpha)\right]^{-1}$. Equation 1.25 is the correlation function of a spherically Gaussian source source with $\tau = 0$ and $R = R_Q/\gamma_{\pi\pi}$. But this means that R_Q measures a *Lorentz extended* source. This non-intuitive result is due to the HBT prescription for measuring distances — simultaneous in the frame of the moving object. In general, an HBT source parameter, evaluated in a frame different than the frame of the source, will be larger than its proper value. This is derived from basic relativity principles in appendix C.

As if a Lorentz extended source was not bad enough, equation 1.25 also shows that the Lorentz conversion factor is $(1 - \beta_{\pi\pi}^2 \cos^2(\alpha))$, which is different for every pair. In order to avoid averaging over an ensemble of reference frames, one can turn to multidimensional source parameterizations in which the relative momenta are calculated in a fixed reference frame. Objections to these forms have been raised on the grounds that since they are not Lorentz-invariant, they cannot be correct. Zajc [Zaj93] points out that this approach is valid as long as the correct source reference frame is chosen as the frame in which to evaluate the relative momenta.

The first of these forms was suggested by Kopylov [KP74], and so I will refer to it as the *Kopylov* parameterization. In this parameterization, the source is modeled as a disk of radius, R, with an exponential emission time distribution. The correlation function becomes:

$$C_2\left(q_{Tpair}, q_0\right) = 1 + \lambda \frac{\left(2J_1\left(q_{Tpair}R\right) \,/\, q_{Tpair}R\right)^2}{1 + q_0^2\tau^2}, \tag{1.26}$$

where J_1 is the order 1 Bessel function. Cocconi derived a similar correlation function for a Gaussian source distribution[Coc74]:

$$C_2\left(q_{Tpair}, q_0\right) = 1 + \lambda \frac{\exp\left(-\left(q_{Tpair}R/2\right)\right)^2}{1 + q_0^2\tau^2}, \tag{1.27}$$

The next form parameterizes the source as a Gaussian in space and time:

$$\rho(r,t) \sim \exp\left(-\frac{r^2}{2R^2}-\frac{t^2}{2\tau^2}\right), \tag{1.28a}$$

$$C_2(q,q_0) = 1+\lambda\exp\left(-q^2R^2-q_0^2\tau^2\right). \tag{1.28b}$$

This is known as the q_0q parameterization.

In high energy heavy ion collisions one might expect a prolate source, extended along the beam axis. To avoid averaging over such a non-spherical source, equation 1.28 can be decomposed into the $q_Lq_Tq_0$ parameterization:

$$\rho(r_L,r_T,t) \sim \exp\left(-\frac{r_L^2}{2R_L^2}-\frac{r_T^2}{2R_T^2}-\frac{t^2}{2\tau^2}\right), \tag{1.29a}$$

$$C_2(q_L,q_T,q_0) = 1+\lambda\exp\left(-q_L^2R_L^2-q_T^2R_T^2-q_0^2\tau^2\right). \tag{1.29b}$$

Limited statistics and pathologies in the τ parameter (to be discussed below) often prompt experimental groups to fix $\tau = 0$. This results in the q_Lq_T parameterization:

$$\rho(r_L,r_T) \sim \exp\left(-\frac{r_L^2}{2R_L^2}-\frac{r_T^2}{2R_T^2}\right), \tag{1.30a}$$

$$C_2(q_L,q_T) = 1+\lambda\exp\left(-q_L^2R_L^2-q_T^2R_T^2\right). \tag{1.30b}$$

With this parameterization any non-zero source lifetime will be folded into the source size along the direction of $\vec{p}^{\,pair}$. The distribution of $\vec{p}^{\,pair}\cdot\vec{q}_T$ is plotted in figure 1-12, showing that in the E859 spectrometer, $\vec{p}^{\,pair}$ is primarily parallel to $\vec{q}_T$.

We have used a modified version of the $q_Lq_Tq_0$ parameterization where we have chosen $\vec{p}^{\,pair}$ (instead of the beam axis) as our symmetry axis:

$$\rho\left(r_{Lpair},r_{Tpair},t\right) \sim \exp\left(-\frac{r_{Lpair}^2}{2R_{Lpair}^2}-\frac{r_{Tpair}^2}{2R_{Tpair}^2}-\frac{t^2}{2\tau^2}\right), \tag{1.31a}$$

$$C_2\left(q_{Lpair},q_{Tpair},q_0\right) = 1+\lambda\exp\left(-q_{Lpair}^2R_{Lpair}^2-q_{Tpair}^2R_{Tpair}^2-q_0^2\tau^2\right). \tag{1.31b}$$

This will be called the $q_{Lpair}q_{Tpair}q_0$ parameterization. The value of τ obtained from this parameterization is free from any spatial source size contamination since R_{Lpair} explictly extracts the spatial component parallel to $\vec{p}^{\,pair}$. This parameterization is very similar to the so-called modified Goldhaber form given in [Mor90]. The only difference is that in the above equation, R_{Lpair} and τ were treated as separate parameters. But, $q_0 = \beta_{\pi\pi}q_{Lpair}$ and the

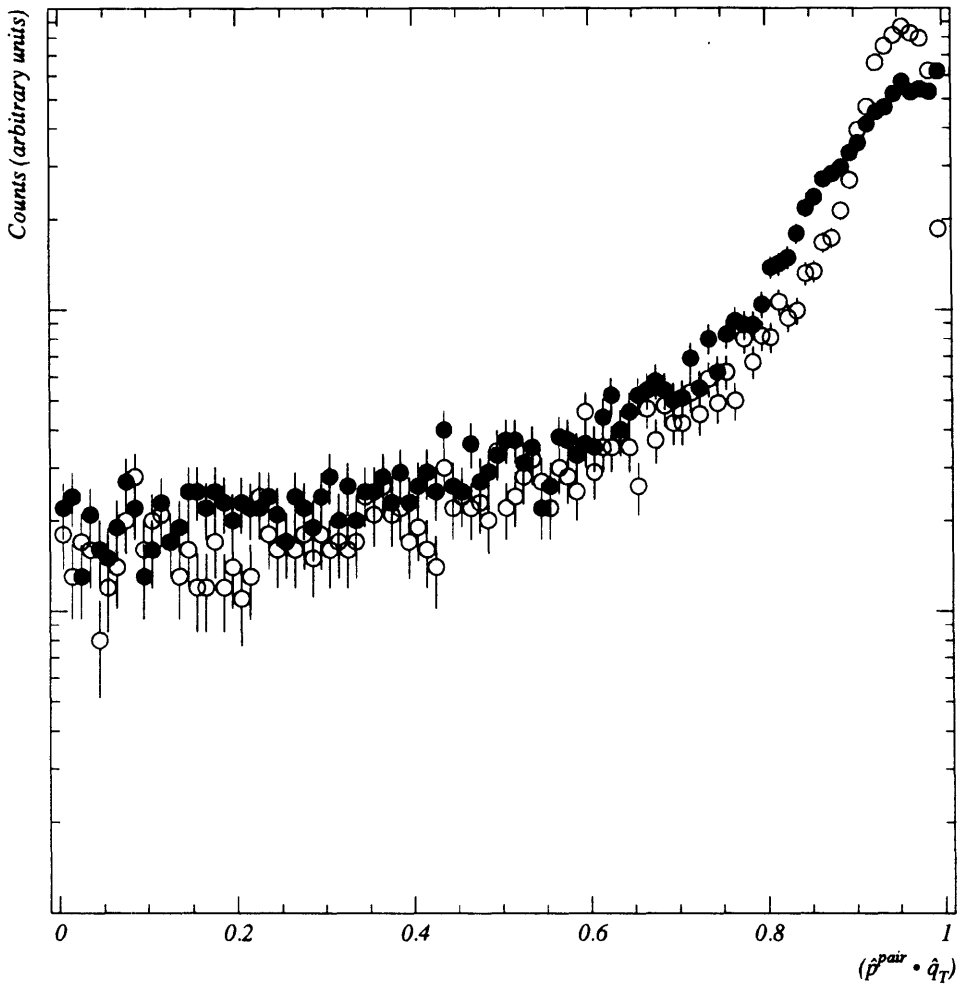

Figure 1-12: $\hat{p}^{pair} \cdot \hat{q}_T$ for π^+'s (open symbols) and K^+'s (filled symbols).

correlation is worsened by the small range of $\beta_{\pi\pi}$ measured in our spectrometer.

Bertsch has suggested another three-dimensional parameterization in a different attempt to accurately extract a source lifetime [Ber89]. The $q_L q_{Tside} q_{Tout}$ parameterization is:

$$\rho(r_L, r_{Tside}, r_{Tout}) \sim \exp\left(-\frac{r_L^2}{2R_L^2} - \frac{r_{Tside}^2}{2R_{Tside}^2} - \frac{r_{Tout}^2}{2R_{Tout}^2}\right), \tag{1.32a}$$

$$C_2(q_L, q_{Tside}, q_{Tout}) = 1 + \lambda \exp\left(-q_L^2 R_L^2 - q_{Tside}^2 R_{Tside}^2 - q_{Tout}^2 R_{Tout}^2\right). \tag{1.32b}$$

It has been suggested that a large value of $R_{Tout} - R_{Tside}$ could be a signature for the QGP [Ber89].

Finally, Yano and Koonin [YK78] suggested a Lorentz invariant source parameterization which parameterizes the source as a space-time Gaussian, and determines the values of the parameters in the source rest frame:

$$C_2(\mathbf{q}, \mathbf{u}_s) = 1 + \lambda \exp(-(\mathbf{q}\cdot\mathbf{u}_s)^2(R_{vec}^2 + \tau^2) + (\mathbf{q}\cdot\mathbf{q})R_{vec}^2). \tag{1.33}$$

This form then also allows one to determine the source velocity, $\mathbf{u}_s$.

Chapter 2

Experimental Apparatus

2.1 E859 - An Overview

The Brookhaven National Laboratory (BNL) Alternating Gradient Synchrotron (AGS) opened a new chapter in its storied history when it first accelerated heavy ion beams (OK, so maybe ^{16}O is not really "heavy") in 1986. E802, the predecessor to E859, was a groundbreaking experiment — one of the first generation of experiments to study the high baryon density environment created in heavy ion collisions at AGS energies. It was very successful [A+87a, A+90a, A+91c, A+91b, A+91a, A+92a, A+92b] in meeting its many goals [HN85], but the answers it found raised a lot of new questions. Some of these questions required more precise measurements of previously measured quantities. Others required extending previous measurements to wider ranges in phase space and centrality. Still others demanded entirely new measurements.

In 1988, the E802 collaboration proposed to answer many of these questions with improvements to the E802 apparatus [RLZ88]. These improvements included an array of phoswich scintillator telescopes in the fragmentation region and a second level trigger with on-line particle identification capability. Upgrades to some of the drift chambers were necessary to handle the increased beam intensity required for full exploitation of the new trigger.

The following list, taken from [Ste94], summarizes the physics issues addressed by E859. All of the goals stated in the E859 proposal [RLZ88] were achieved. In addition, more ambitious goals were set as different physics topics became interesting and the true power of increased

beam rates was realized.

- K^+, K^-, and $\bar{p}$ → Good statistics over a large rapidity range for a variety of targets and centralities [Rot94, Sun94, Zac94, Mor94, Sak92].
- Λ → Spectra, inverse $m_\perp$ slope, and dn/dy near mid-rapidity [Sun94].
- $\bar{\Lambda}$ → Spectrometer-integrated ratio to Λ [Rot94, Sun94].
- ϕ → First measurement in heavy ion collisions at the AGS. Spectra, inverse $m_\perp$ slope, and dn/dy near mid-rapidity [Wan94].
- $\pi^\pm$ → Improved statistics at the smallest values of $p_\perp$ in the acceptance ($\approx$ 200 MeV/c).
- High $p_\perp$ → Measurements of several particle species for peripheral collisions.
- Low y → Measurements of spectra and yield of target-rapidity p, d, t [S^+93a].
- K^+K^+ → First good statistics measurement for *any* system ([Vos94], this analysis).
- $\pi^\pm\pi^\pm$ → Source parameters measured over a broad range of centrality and number of participants [Sol94].
- pp → Proton source sizes measured for central collisions for several targets [Vut92].
- Non-identical particle correlations → These measurements provide additional information about the source parameters due to the Coulomb and strong interactions[Vos94].

The E859 experimental apparatus is shown in figure 2-1. Beam definition detectors serve to define and count valid beam particles and provide the experimental start time. There are three event characterization detectors. The Target Multiplicity Array measures the total charged particle multiplicity in a collision. The Zero Degree Calorimeter measures an event's forward-going kinetic energy. A lead-glass calorimeter measures the total neutral energy produced in the collision. A 25 msr rotating magnetic spectrometer tracks and identifies particles over a limited range of acceptance. The analyzing magnet, four drift chambers and two multiwire proportional chambers provide momentum determination. A plastic scintillator time-of-flight wall and a segmented gas Čerenkov detector provide particle identification for kaons below 2.9 GeV/c and pions and protons below 5 GeV/c. A 1 msr gas Čerenkov complex provides very high momentum particle identification.

Although the E859 magnetic spectrometer covers only 25 msr, it can rotate through a polar angle range of 5–44° with respect to the beam axis. This greatly increases its total coverage, as shown in figure 2-2.

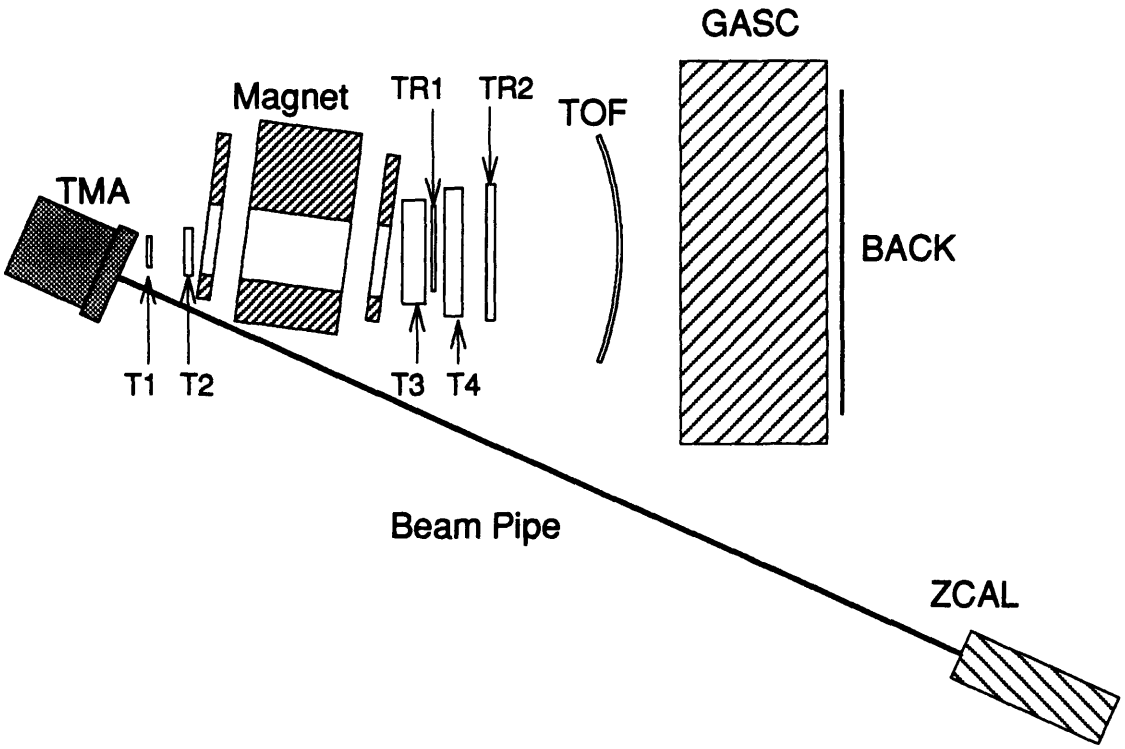

Figure 2-1: Schematic of the E859 experimental apparatus. Courtesy of D. Morrison.

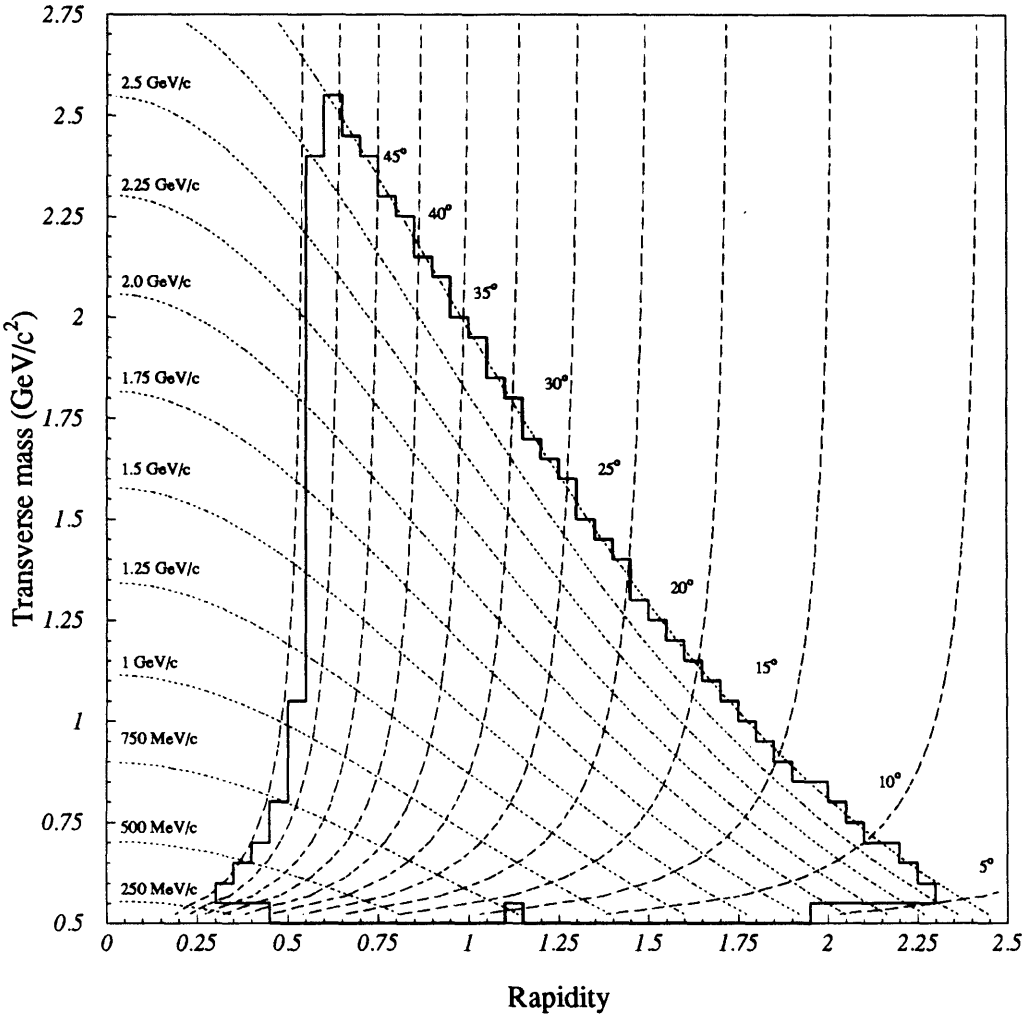

Figure 2-2: Available E859 spectrometer coverage. Dotted lines indicate momentum cutoffs, dashed lines indicate angular cutoffs. Courtesy of D. Morrison.

In the following sections, I will describe the creation of heavy ion beams at the AGS and all E859 detector subsystems used in this analysis. Detectors not used in this analysis are presented in appendix E for completeness, and to provide the reader with references that contain the gory details.

2.2 Heavy Ion Acceleration at the AGS

We could not achieve any of our experimental goals without a good heavy ion beam. So, a brief tour of the life of a ^{28}Si ion is appropriate. This section is a summary of more detailed accounts that can be found in [T+88] and [Col92].

The AGS heavy ion beam begins inside the veteran Tandem Van de Graaff accelerator facility. Injection into a synchrotron is complicated by the requirement of a high-current, pulsed source. The source that was developed to meet this need is shown in figure 2-3. Positive cesium

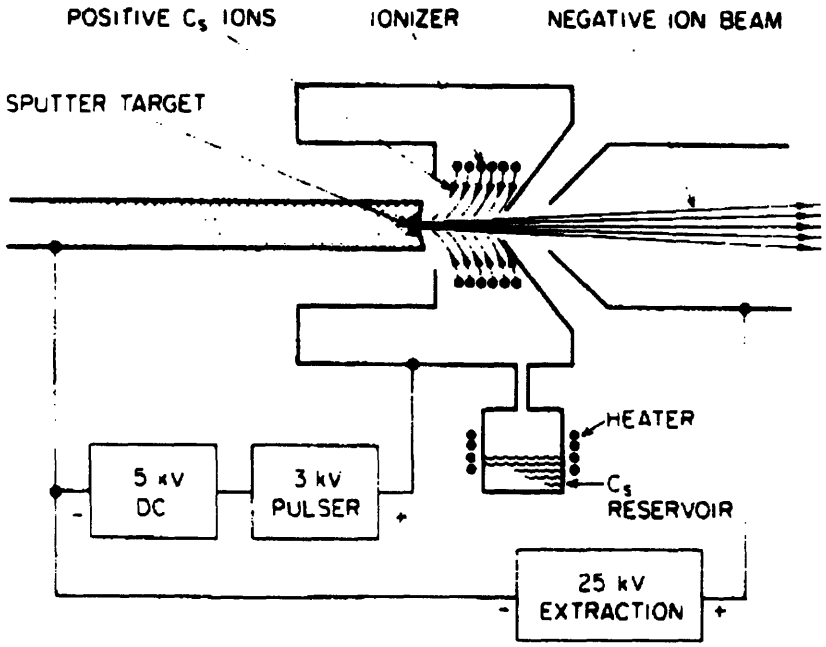

Figure 2-3: Schematic of the AGS high current heavy ion sputter source. From [T+88].

ions are accelerated through a 3-5 kV potential difference and focussed onto a target. Target atoms obtain a negative charge by stripping an additional electron off the highly electronegative cesium ions. They are subsequently accelerated though an extraction voltage of $\approx$25 kV.

Since the vacuum in the AGS ring is only $\approx 10^{-7}$ Torr, it is necessary to inject fully stripped

ions. Otherwise, remaining electrons would be stripped by residual gases during acceleration. Ions whose charge-to-mass ratio had changed would be quickly deflected into the AGS walls. Stripping heavy ions is a catch-22. Their low charge-to-mass ratio makes partially stripped heavy ions difficult to accelerate. But, since the probability of stripping an electron from an ion is very small until the ion velocity is comparable to the orbital velocity of that electron, it is difficult to fully strip slow heavy ions. In the Tandem Van de Graaff acceleration process, ^{28}Si ions go through three stages of alternating acceleration and stripping, see figure 2-4. Upon

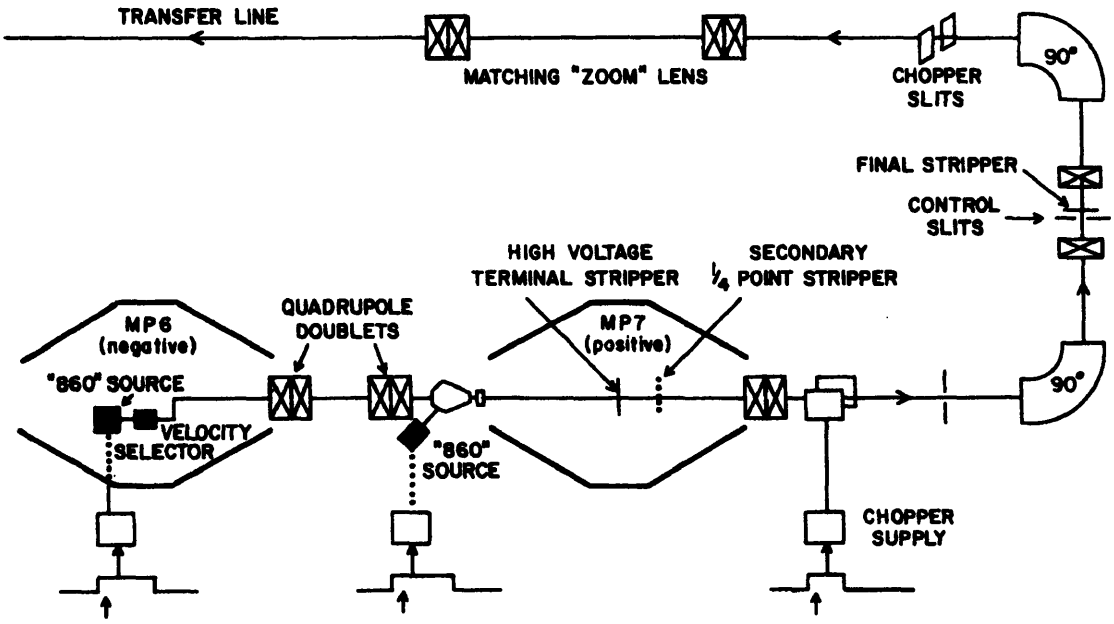

Figure 2-4: Schematic of the pre-AGS acceleration system. Note that both MP6 and MP7 are used in the three-stage configuration necessary for ^{28}Si acceleration. From [T+88].

leaving the Tandem Van de Graaff complex, the ^{28}Si ions are fully stripped, with an energy of $\approx 6.6\,\mathrm{A}\cdot\mathrm{MeV}$. They then pass through a series of velocity filters and into the 680 m heavy ion transfer line (HITL). For ^{28}Si ions, this entire process is only about 2.5% efficient.

In order to accelerate ions heavier than ^{28}Si, it was necessary to construct a "Booster" ring to act as an injector to the AGS. For heavy ion acceleration the most important feature of the booster is its excellent ($\approx 5 \times 10^{-11}$ Torr) vacuum system. This allows acceleration of non-fully stripped ions which increases the efficiency of ^{28}Si extraction by a factor of seven and enables the acceleration of nuclei as large as ^{197}Au [A+92c]. The booster also eliminates the need for the third stage of stripping/acceleration, providing a spare Tandem Van de Graaff. At some

point in the not too distant future, the AGS will become the injector for the Relativistic Heavy Ion Collider (RHIC) being constructed at BNL, see figure 2-5. There the search for the QGP will continue in ^{197}Au + ^{197}Au collisions at $\sqrt{s} = 200\,\mathrm{A}\cdot\mathrm{GeV}$.

Because of the low efficiency of the extraction process and the low energy of the resulting ions, two modifications of the AGS were necessary for heavy ion operation. The first modification was a new injection system that allowed "multi-turn stacking" of the *positive* injected ions (during proton operation the AGS accumulates H^- ions, stripping them at the end). Multi-turn stacking is a process in which several pulses of heavy ions are sequentially injected into the AGS and allowed to circulate without acceleration. A special "bumper" magnet spreads the pulses around the ring. After the ring is filled, twelve pulses, the heavy ions are accelerated from $6.6\,\mathrm{A}\cdot\mathrm{MeV}$ to the proton injection energy of $200\,\mathrm{A}\cdot\mathrm{MeV}$. This requires the second modification, a new, low-frequency RF system. Acceleration to full energy takes 1.1 sec. After this, the RF system is turned off and the magnets are held nearly constant for the ≈ 1 sec beam "spill" into the experimental areas. Electronic signals indicating the position in the spill cycle were provided to the experiment and were used as timing gates by the data acqusition system, see section 2.13.

The maximum beam intensity achieved by the AGS was $\approx 10^9$ ^{28}Si/spill. The maximum beam intensity allowed in the E859 experimental area was 5×10^6 ^{28}Si/spill. This beam intensity was an optimization balancing the desire for higher beam intensities to aid in the search for rare events, against the bureaucratic hassle and experimental inaccesibility associated with the safety procedures and precautions that go along with higher beam intensities. In truth, this intensity was beyond the abilities of most of the E859 detector systems to handle, and the maximum sustained beam intensity was $\approx 2 \times 10^6$ ^{28}Si/spill. The intensity in the E859 area was changed by defocussing the beam, passing it through collimators, and refocussing it downstream. The beam intensity and spatial profile were monitored with segmented wire ionization chambers (SWICs) whose visual readout was monitored by the experiment.

2.3 Coordinate Systems

To orient the reader, I will first define the E859 *beam* and *spectrometer* coordinate systems. The beam axis is defined to be the z-axis of the beam coordinate system. θ is defined to be the polar angle with respect to this axis. The y-axis is vertical, pointing up. To maintain a right-handed coordinate system, the x-axis is then defined to be horizontal, pointing away from the beam. ϕ is defined to be the azimuthal angle measured clockwise from the x-axis.

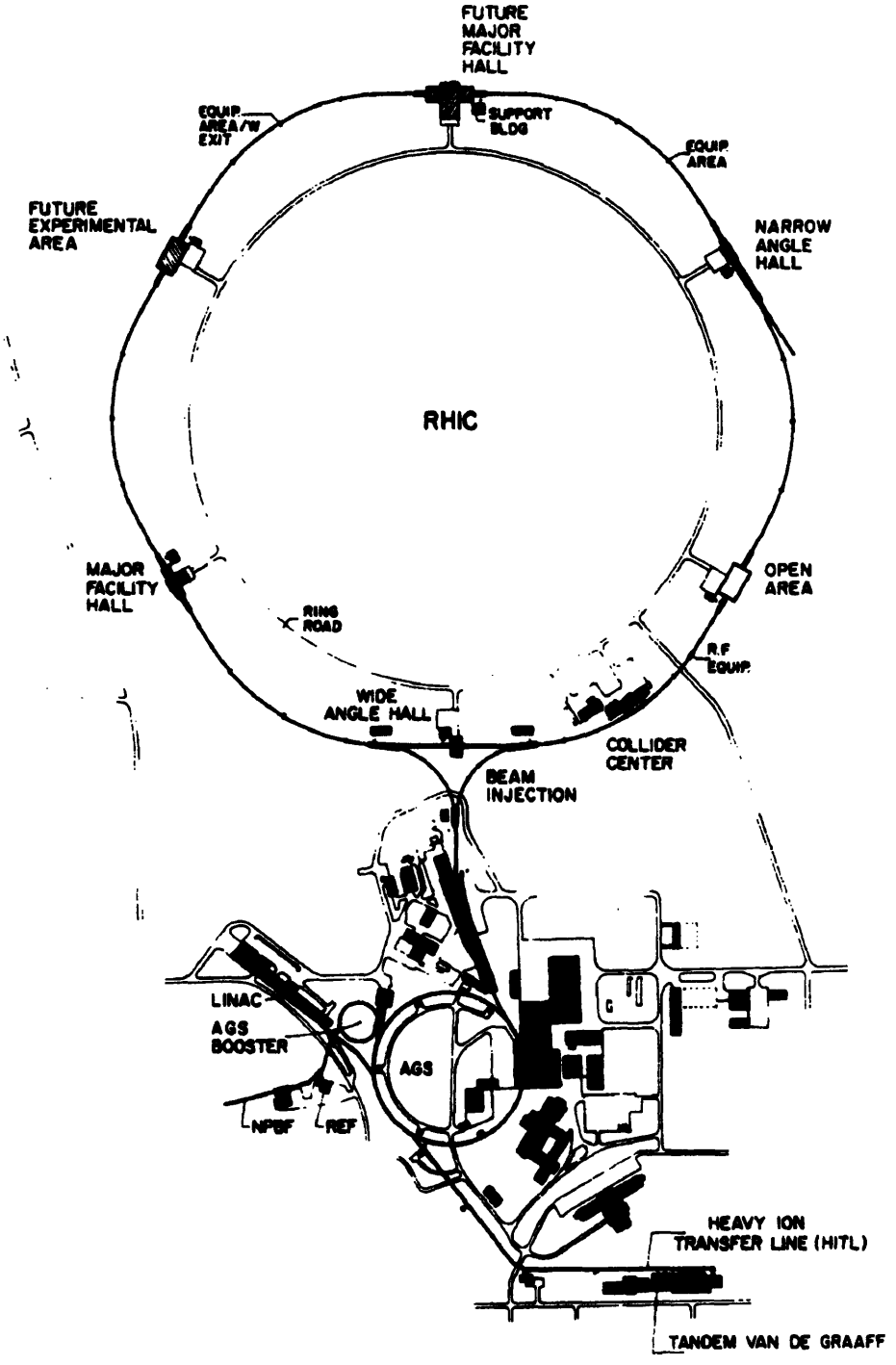

Figure 2-5: Aerial view of the BNL heavy ion acceleration facility including RHIC. From [T+88].

Elements of all detectors are numbered in increasing order of the x- and/or y-axes, except for the time-of-flight wall which is the exception that proves the rule.

The z-axis of the spectrometer coordinate system is defined to be the axis perpendicular to all the spectrometer detectors.[1] The y-axis is defined to be vertical and pointing up. The drift chamber wire angles, are measured *from the vertical* in this system.

2.4 Target Assembly

To paraphrase an old saying, it takes two to collide. Once we have a beam, we need a target. The E859 targets are foils of material fabricated by an evaporation technique. They are placed in 22 mm diameter aluminum frames and completely occlude the $4 \times 2\,\mathrm{mm}^2$ beam spot. The targets are arrayed along a drive chain which rotates to place the selected target in front of the beam. Target selections are made by remote control and verified by video camera. The entire target assembly is in an aluminum vacuum chamber maintained at $\approx 10^{-4}$ Torr. To minimize the effects of the vacuum chamber, its walls were made very thin (2 mm $\sim$ 1.7% ^{28}Si interaction length). The downstream portion, known as "the snout," was machined as a hemisphere, with the target at its center, so that all particles emanating from the target would pass through the same amount of material. A small opening in the snout connects to the beam pipe assembly to allow non-interacting beam particles to exit without passing through the chamber walls.

2.5 Beam Counters

The beam counters define valid beam particles, count them, and set the experimental start time. A schematic of the five plastic scintillator detectors that comprise the beam counters is shown in figure 2-6. I will describe the counters, and their functions, proceeding from upstream to downstream. See section 2.14 for details on how *BEAM* and interaction(*INT*) triggers were formed.

Six meters upstream of the target are the Up, Down, East and West (UDEW) detectors. These are four large scintillator paddles arranged in two planes. The planes are oriented so that one (UD) provides vertical beam collimation and the other (EW) provides horizontal beam collimation.

Two meters upstream of the target is BTOT, which has dimensions of $7.6 \times 5 \times 0.1\,\mathrm{cm}^3$. Both

[1]Note that by some perversity, this is 7.4° greater than the nominal *spectrometer angle setting*, which is defined to be parallel to the beamside vertical face of the spectrometer magnet, Henry Higgins.

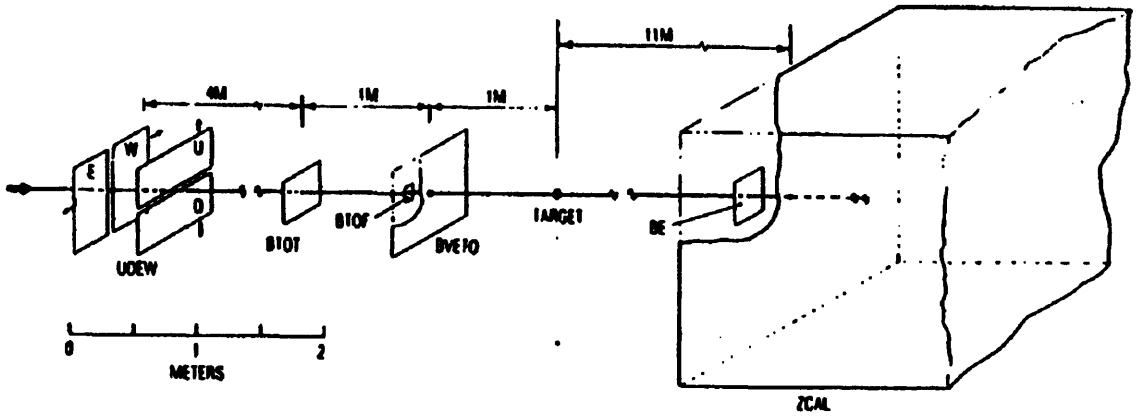

Figure 2-6: Schematic of the E859 beam counter detectors.

horizontal ends are read out by Hamamatsu phototubes. The thickness is a balance between the desire for excellent charge determination (thick scintillator) and the desire for minimum non-target material in the beam (thin scintillator). Discriminators on the phototube outputs select beam particles with the correct charge state (14^+ for ^{28}Si).

One meter upstream of the target is the BTOF counter, which is rotated by 45° around an axis perpendicular to the beam. This allows two vacuum coupled phototubes to view the light from the scintillator faces, see figure 2-7. This eliminates the jitter associated with the

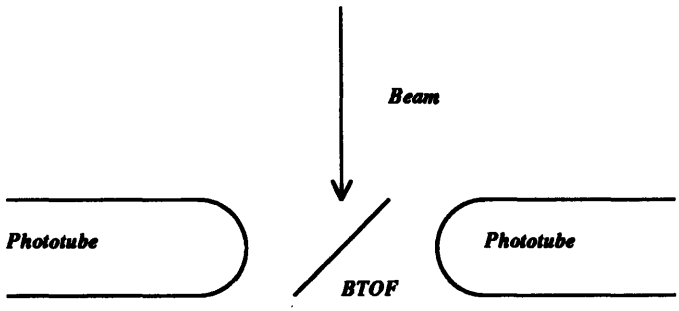

Figure 2-7: Schematic of BTOF orientation and readout.

propagation of light through scintillator, in order to provide an experimental start time with the best possible resolution.

One important change to the BTOF counter for E859 resulted from the fact that radiation damage from high beam intensities caused unacceptable light output reduction within forty-eight hours. Reducing the threshhold on the BTOF discriminator was a temporary solution that maintained the integrity of the beam counting that was critical to cross-section determinations.

But, as the light output decreases the timing resolution gets poorer, going from ≈ 55 psec to ≈ 70 psec [Keh]. To solve this problem, a 40 cm piece of scintillator was mounted in a mechanism that remotely lowered the scintillator into the beam, one 1 cm segment at a time.

Immediately following BTOF is the BVETO counter (commonly referred to as HOLE). This detector has a 1 cm diameter hole through which a valid beam must pass, thus eliminating particles that interacted in the upstream counters.

For E859, the BTOT, BTOF and HOLE detectors were all mounted in individual steel vacuum chambers, see figure 2-8. These chambers were an improvement over the old setup

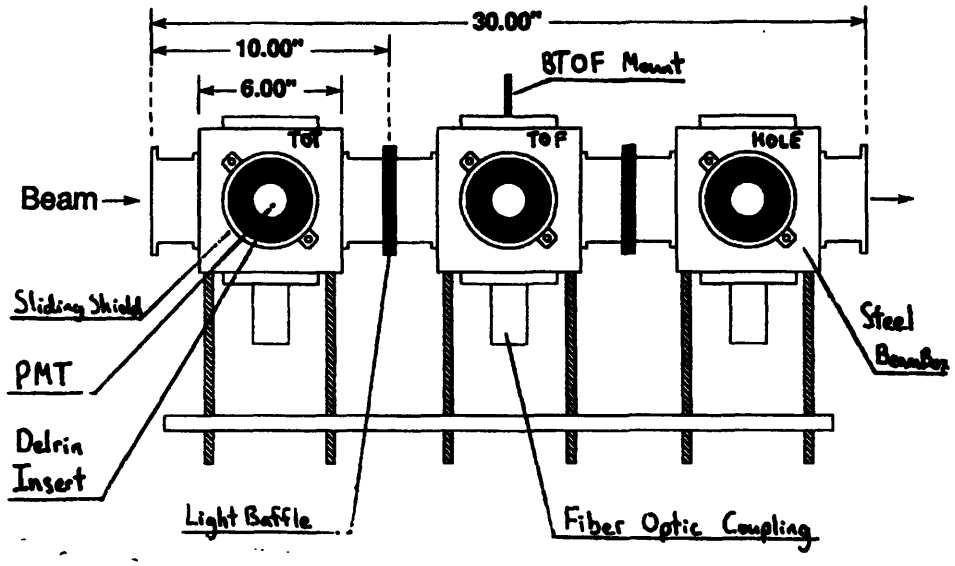

Figure 2-8: Schematic of the E859 beam counter holders. Courtesy of W.L. Kehoe.

because the photomultiplier tubes were no longer under vacuum, making them much easier to service.

Eleven meters downstream of the target, just prior to the ZCAL, is the "bullseye" (BE). This detector is $7.6 \times 10.2 \times 0.16\,\text{cm}^3$. Its purpose is to make a post-target charge measurement of the projectile which is used to determine if a target interaction has occurred.

2.6 Target Multiplicity Array (TMA)

The TMA is the event characterization detector used for all analysis in this thesis. This section is a summary of a more complete description of the TMA that can be found in [Abb90].

The TMA surrounds the target and is designed to measure the multiplicity of all charged particles emitted in the reaction — a good measure of centrality. The TMA consists of streamer tubes operated in proportional mode. Particles with kinetic energies above 25 MeV can penetrate the material surrounding the TMA active area and still deposit enough energy to pass the hardware threshold.

The TMA is divided into two parts. The *wall* covers a polar range of $6° \leq \theta \leq 40°$, and the full 2π azimuthal range except for a rectangular notch on the Henry Higgins side of the array to reduce background in the spectrometer. The *barrel* is a cylinder coaxial with the beam line that covers a polar range $30° \leq \theta \leq 143°$ and an azimuthal range of $15° \leq |\phi| \leq 165°$. Two panels about $\phi = 0°$ were removed to reduce background in the spectrometer[2]. Two panels about $\phi = 180°$ are removed to reduce background in the phoswich array. The total segmentation during E859 was 2988 pads. There were on average ≈ 200 dead or hot pads which were corrected for in the analysis [Rem], see section 3.3. Figure 2-9 shows the response of the TMA in a central $^{28}Si + ^{197}Au$ event.

2.7 F0

F0 is a 21-element plastic scintillator "picket-fence" hodoscope placed in front of T1 and arranged in two adjacent planes perpendicular to the spectrometer axis. The slats are $0.6 \times 1.2 \times 12.8\,cm^3$. Slats in the two different planes were staggered by roughly the slat width.

F0 was a part of the *SPEC* trigger definition, see section 2.14.3. F0 was also to be used for timing if any problems arose in the beam counters as a result of the increased beam intensities. In fact the beam counters performed admirably, see section 2.5, and F0 was never used in this capacity. An attempt was made to utilize the y-information from F0 in the track reconstruction algorithm, but this was abandoned because the y-resolution was not good enough to be useful. In fact, for this analysis, the main significance of F0 is its thickness, $t \approx 0.03 X_0$. Not including the target, this is about 2/3 of the integrated material radiation length in front of the spectrometer. No detailed description of F0 exists.

2.8 Tracking Chambers (T1-4)

[Sau77] is regarded as the "wire chamber Bible" and the title is well deserved. It is an excellent collection of the wisdom and folklore surrounding these complicated devices and

[2] In principle these panels could be replaced at some angle settings, but they never were.

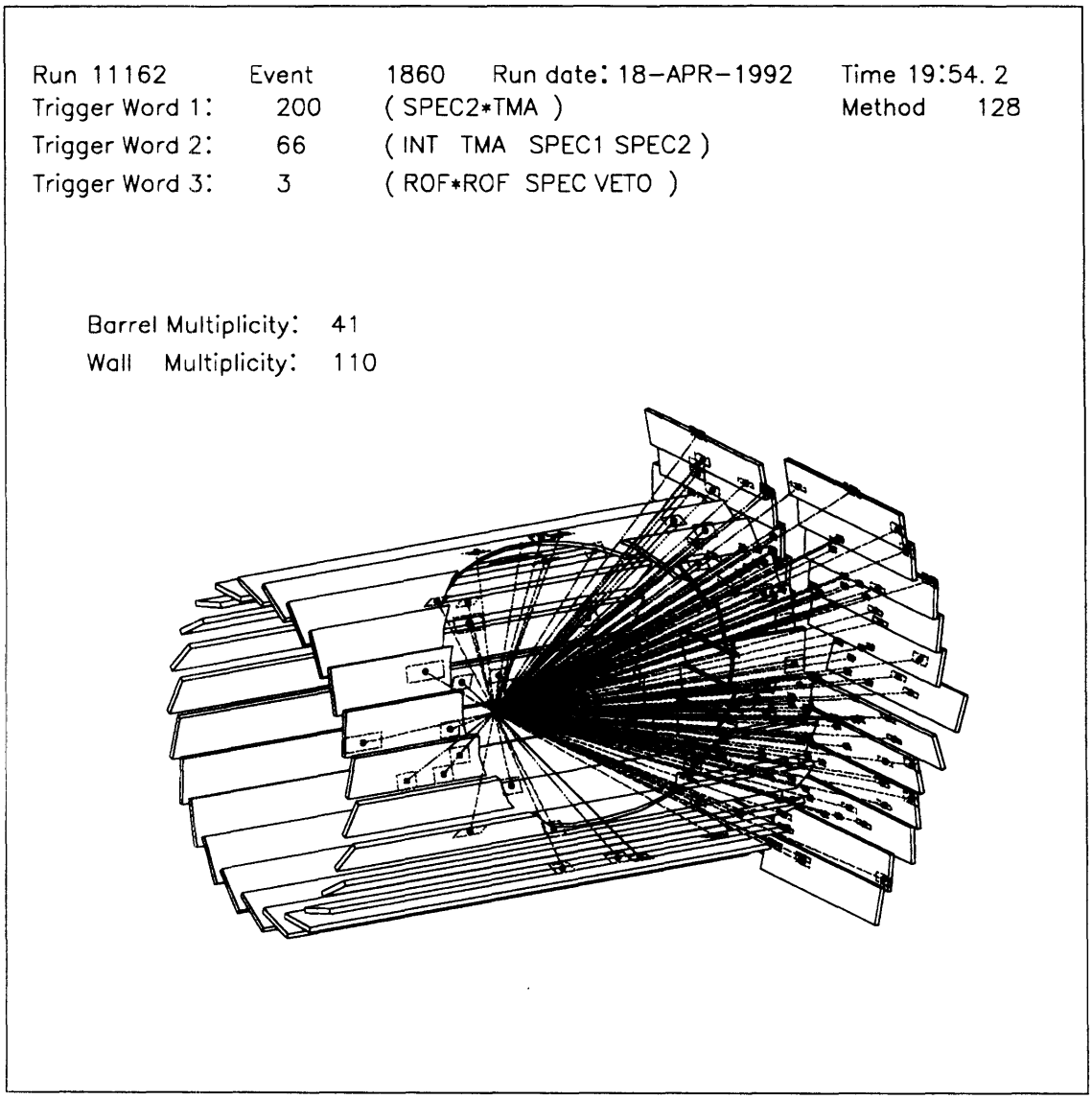

Figure 2-9: Schematic of the TMA during a central $^{28}Si + ^{197}Au$ event. Lines simply connect the target position to the struck pads.

should be the starting point of anyone wishing a grounding in wire chamber techniques. I refer to [Col92] as the "E802 drift chamber Bible," and its title is also well deserved. Anyone wanting to know the gory details of the E802 drift chambers should start there. A brief geneology of the drift chamber can be found in appendix F.

In this section, I will review the general properties of E859 drift chambers, see table 2.1. Special emphasis will be given to those aspects of the chambers that have changed for E859 operation and those aspects which have a direct bearing on this analysis.

2.8.1 Design Considerations

One shortcoming of drift chambers, and indeed many other detectors, is that their active elements are only two-dimensional. This is known as projective geometery, and means that our information is limited to those two dimensions. For instance, a charged particle could pass anywhere along the length of a drift cell and still give the same signal. At this point the astute but naive reader is thinking "Aha! use two MWPC's with wires pointing in two orthogonal directions." But, with two planes, N tracks will produce N^2 possible intersections and this is no good if there is more than one track. In principle, a third plane of wires will uniquely identifiy the true intersections. This is because there is a vanishingly small probability that a line connecting the two interactions will be parallel to the wires in the third plane. In the real world there are many effects which make it desirable to have planes in four or more directions. Different directions are known as views. In E859, the view name refers to the direction of information that is obtained, the direction perpendicular to the wires.

Drift chambers have a further disadvantage known as the left-right ambiguity. This ambiguity arises from the fact that we do not know on which side of the wire the track passed. The result is that we have two lines of possible track positions, effectively doubling the hit density on the chambers. Figure 2-10 shows how this compounds the problems of projective geometry. The ambiguity can be removed by staggering the sense wire positions of one plane relative to neighboring planes in that view. Figure 2-11 shows the two different staggering schemes used in the E859 drift chambers. Only hits from the correct sides of the wires will line up.

2.8.2 Design Decisions

T1 was constructed at BNL using a traditional wire-winding technique. The wires were soldered to traces and epoxied into place. The chamber was formed from ten individual planes made from stock printed circuit-board G-10, which were assembled gas-tight. The ten planes

2.8. *TRACKING CHAMBERS (T1-4)*

Chamber	Width (cm)	Height (cm)	Depth (cm)	# Views	# Planes	Plane Separation (mm)
T1	26.4	13.6	3.0	5	10	3.2
T2	40.8	21.1	17.6	4	12	7
T3	113.7	52.1	27.3	4	13	7
T4	143.5	58.7	21.6	4	10	7

Chamber	View	Plane #	Angle	Wires/ Plane	Drift Length (mm)	Stagger (mm)
T1	x	1, 2	0	32, 32	4	0, 4
	v	3, 4	-45	32, 32	4	0, 4
	y	5, 6	-90	16, 16	4	0, 4
	u	7, 8	45	32, 32	4	0, 4
	w	9, 10	-27	32, 32	4	0, 4
T2	x	1, 2, 3	0	28, 27, 27	14	0, 7, 7
	y	4, 5, 6	-90	13, 13, 14	14	0, 0, 7
	u	7, 8, 9	-30	28, 28, 28	14	0, 7, 7
	v	10, 11, 12	30	28, 28, 28	14	0, 0, 7
T3	u	1, 2	30	36, 36	16.1	0, 0
	x	3, 4, 5	0	36, 36, 36	15.3	0, 0.7, 0
	y	6, 7, 8	-90	16, 16, 16	15.3	0, 0.7, 0
	v	9, 10	-30	36, 36	16.1	0, 0
	x	11, 12, 13	0	36, 36, 36	15.3	0, 0.7, 0
T4	u	1, 2	30	44, 44	16.5	0, 0
	x	3, 4, 5	0	40, 40, 40	17.5	0, 0.7, 0
	y	6, 7, 8	-90	16, 16, 16	17.2	0, 0.7, 0
	v	9, 10	-30	44, 44	16.5	0, 0

Table 2.1: List of E859 drift chamber properties.

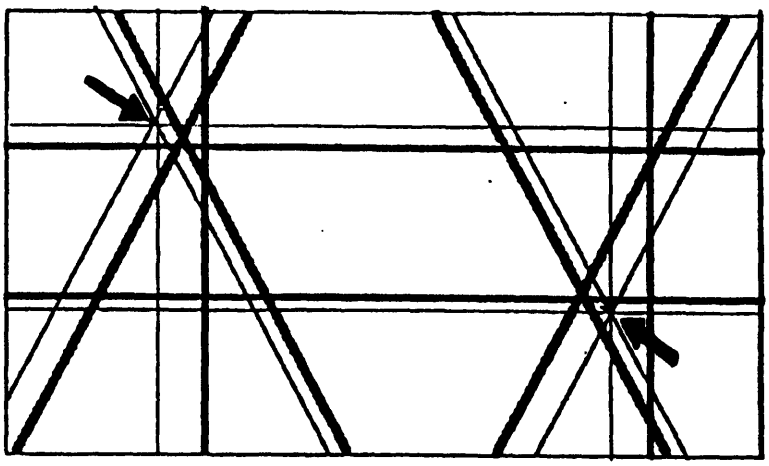

Figure 2-10: This figure illustrates the confusion that can arise when projective geometry is combined with the left right ambiguity. At actual vertices, those indicated by arrows, all of the views cross. Thicker lines indicate extra hits that result from the left-right ambiguity. From [Col92].

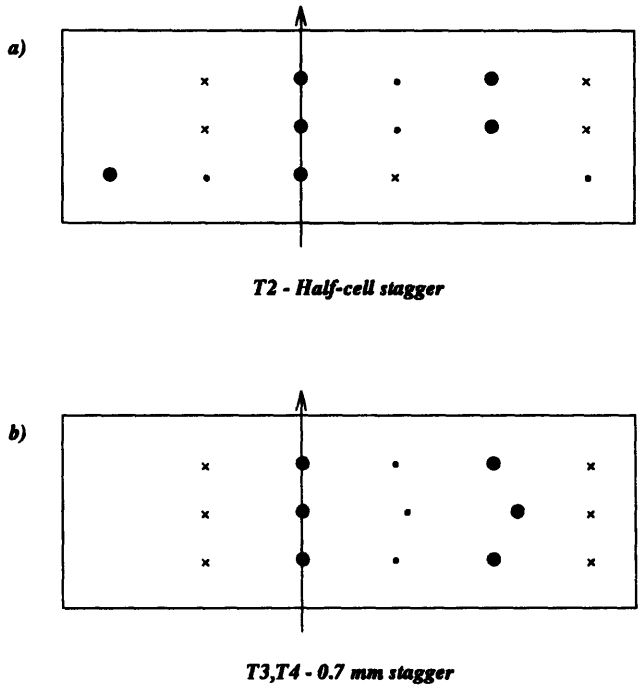

Figure 2-11: Illustation of wire "staggering" to resolve the left-right ambiguity. The drift cell and wire sizes are not to scale. The field wires are marked by x's and the sense wires are marked with small circles. Potential hit positions are marked with large circles and the actual tracks are indicated by arrows. Adapted from [Col92].

were divided into five different views with two planes each. Complementary planes (e.g., x, x') were staggered by half of a drift cell. The gas mixture was 50% argon plus 50% isobutane, which has a saturated electron drift velocity of 50 μm/nsec.

T1 was made very thin, with a plane separation of only 3.2 mm. The hope was that it could be used as a space-point detector. Unfortunately, the efficiency was rather low, ≈85% [Rot94]. In addition, the field configuration was such that the inefficiency was much more pronounced away from the wire. This combines with the half-cell stagger in a pathological manner - the more likely it is that a track fires a wire in one plane of a view, the less likely it is to fire the wire in the complementary view. As a result of these inefficiencies, T1 was never usable as a spacepoint detector.

T2, T3 and T4 were constructed at MIT using a crimping technique developed at SLAC. This technique has proven to be very robust - in seven years of operation, not a single wire has broken. In the following discussion I will review the construction highlights of the MIT chambers. It may help to consult figure 2-12. Holes are drilled into a G-10 frame with 50μm

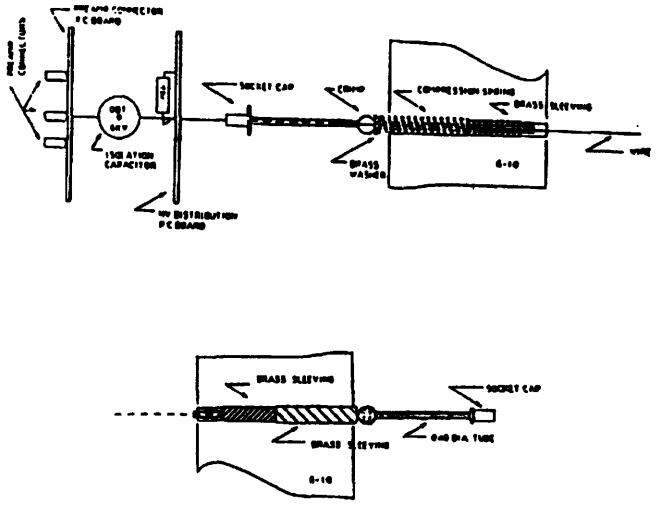

Figure 2-12: Illustration of the crimping technique used to construct the MIT drift chambers.

precision, although not necessarily that accurately as we will see below in the saga of the T2 wire-by-wire angle correction. The wires are crimped into tubes that rest in the G-10 holes. Tension, originally set by gripping a forceps (roughly 30 g) to one end of the wire before crimping, is maintained by a spring that sits between the tube and the G-10 at one end. Each chamber has a different number of planes at different views, see table 2.1. Complementary views in T2

are staggered by half of a drift cell. The gas mixture was 50% argon plus 50% ethane bubbled through an ethanol bath at 0°C. This gas mixture has a saturated electron drift velocity of 50 μm/nsec. All of the MIT chambers have a plane separation of 7 mm, the minimum allowed by the crimping device, making them impractical as space point detectors.

T2, T3 and T4 were all developed at MIT, near a big-city radio station, where it was serendipitously discovered that their wires make very good antennas. For this reason, great care was taken to shield the active areas. The preamplifier circuit was built at MIT, and takes a further precaution against such pickup. A sense wire and a neighboring field wire are fed into the two inputs of a differential amplifier. The assumption is that any pickup on the two wires will be nearly identical and will therefore cancel. Protecting against pickup from the radio station paid off — when the chambers were installed on the electronically noisy AGS floor they were very quiet. The preamplifier output signals were driven over 20 ft of shielded, twisted-pair cable to a discriminator circuit that was also designed at MIT. This circuit has an RC circuit element at its input that differentiates the preamplifier signal. This eliminates the long signal tail resulting from ionized gas molecules and limits the signal width to $\approx$40 nsec. Figure 2-13 shows the pulse width distribution for a wire in T2. From the electron drift velocity of 50 μm/nsec, we

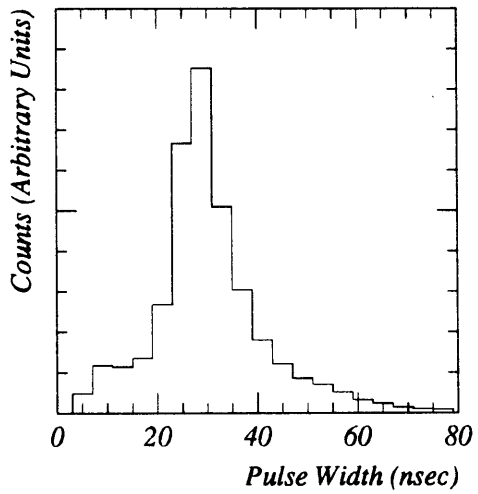

Figure 2-13: Typical pulse-width distribution for the E859 drift chambers. A 40 nsec width corresponds to 2.0 mm pulse separation capability.

can see that this corresponds to a 2 mm distance. This means that the chambers are capable of resolving two tracks that pass as close as 2 mm, a feature critical to the correlation analysis. Section 4.2.5 discusses the corrections necessary to account for the reduced efficiency of the drift chambers at these smallest separations. Figure 2-14 shows circuit diagrams for both the preamplifier and the discriminator.

2.8.3 Improvements for E859

The first big improvement to the tracking chambers for E859 was a completely new T2. Improvements include 50% greater segmentation, one additional plane in both the U and V modules and a more stable field configuration. Its size was also reduced, primarily in the y-direction, to match the solid angle defined by T1. The X and Y modules were combined into one G-10 block, as were the U and V modules.

A machining error in the T2UV G-10 frame resulted in wire angles that varied across each plane. The problem is illustrated in figure 2-15 which shows two plots of the active area of one T2U plane. Both figures 2-15a and 2-15b show the actual positions of each wire as solid lines. In figure 2-15a, the dashed lines show the calculated wire positions assuming that the wire is at the design angle (-30° in our funny coordinate system, see section 2.3) with one end in the correct position. One can see, that on the side of the chamber where the wire positions have not been fixed, they are about half of a wire space off. This is a result of a machining error - a row of field and sense wires, and a row of cathode wires (half of a sense cell) are missing from each end of the chamber. Although it is clear from figure 2-15a that this error results in wires at different angles than intended, the less tractable problem is that the wires in the corners are at different angles than the wires in the rest of the chamber.

This should be obvious with a little thought. Wires in the middle of the chamber, with both ends in the horizontal pieces of G-10, have a constant shift, δx, and a constant height, y. So, their angular shift,

$$\delta\theta = \tan^{-1}\left(\frac{x}{y}\right) - \tan^{-1}\left(\frac{x}{y}\left(1+\frac{\delta x}{x}\right)\right) \tag{2.1}$$

is constant. Wires in the corners have the same shift, δx, but they are shorter. So, $\delta x/x$ and $\delta\theta$ are larger. Wires in the upper right corner have a shift in δy, but the argument is the same. This is illustrated more clearly in figure 2-15b, where the dashed lines show the calculated wire positions assuming that the wires are at the angle of the middle wires (fit to be -28.830°) with one end in the correct position.

This shift does not completely explain residuals observed when reconstructed tracks are

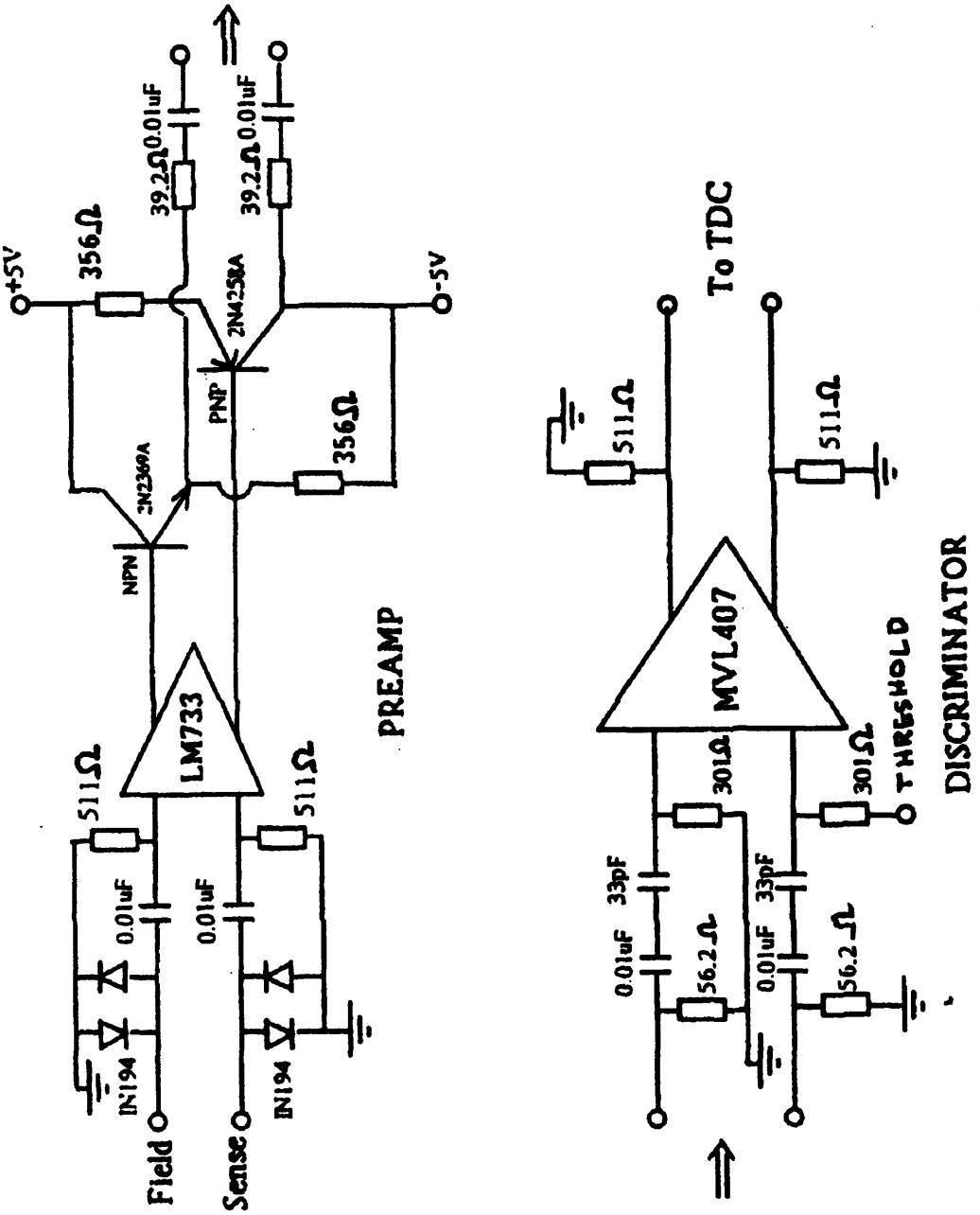

Figure 2-14: Circuit diagrams of the MIT drift chamber electronics. See text for details.

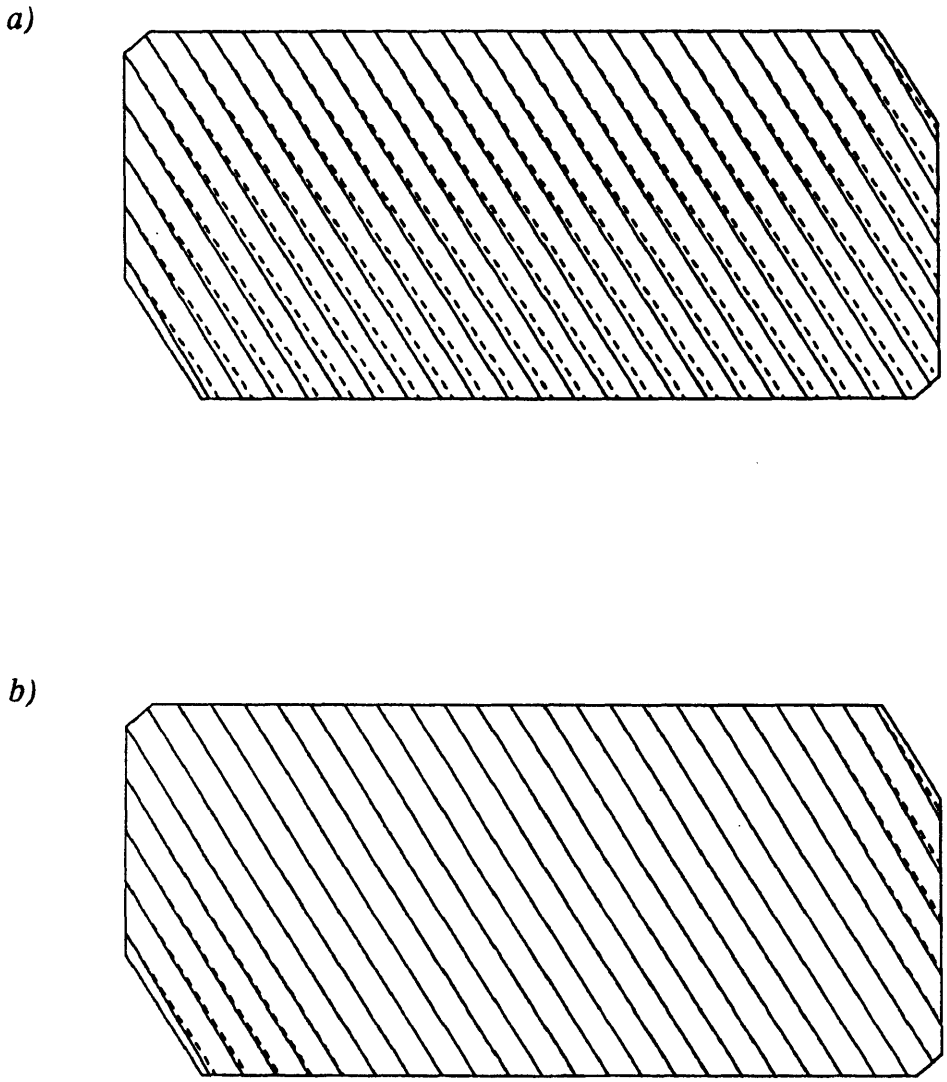

Figure 2-15: Illustration of the machining error complicating the geometry description of the T2 drift chamber. See text for details.

used to predict the wire positions [Ste], so an angular correction to each wire is calculated as a part of the general geometry determination procedure, see section 3.5.1.

The second improvement to the tracking chambers for E859 was the addition of three planes of x-information, known as T3.5, to the downstream end of T3. One of these planes was strung with high-resistive wires so that the y-position of a track could be determined from the difference in the current recorded at opposite ends of the chamber. Although the new x-information was very valuable for track reconstruction, see section 3.7, the resolution on the y-position was very bad, and the information was never used. The cause of this failure was never confirmed, but the working hypothesis implicates the FASTBUS ADC used during the experiment. The specifications on this ADC indicate that it is much more sensitive to overshoot than the CAMAC ADC that was successfully used during testing.

2.9 Henry Higgins

The heart of E859 was its dipole analyzing magnet, Henry Higgins, which was recycled from a previous experiment[3]. Henry Higgins has an ordinary steel yoke with a $0.84 \times 0.42 \times 2.4\,\mathrm{m}^3$ gap. There are two main coils and two sets of correction coils. There are field clamps to minimize the fringe fields. All data analyzed in this thesis were taken with a 0.4 T field corresponding to a $p_\perp$-kick of 0.177 GeV/c.

Henry Higgins is canted 7.4°, clockwise as viewed from above, with respect to the axis perpendicular to all spectrometer detectors.[4] The field is vertical so that the particles bend in the horizontal plane. The AGS polarity convention was adopted, which for our spectrometer means that A-polarity fields bend positive particles away from the beam. Therefore A-polarity fields point down and are assigned negative values. The opposite polarity is labeled B.

2.10 Trigger Chambers (TR1, TR2)

Two multiwire proportional chambers were added to the spectrometer in E859 for use in the second level trigger. The additional information they provided also greatly improved track reconstruction capabilities, see section 3.7. TR1 is $48\frac{3}{8} \times 31\frac{3}{8} \times 3\frac{1}{8}\,\mathrm{in}^3$ and is located between T3 and T4, $\approx 442\,\mathrm{cm}$ from the target. Ideally TR1 would have been located between T3 and

[3]The origin of the magnet name remains shrouded in mystery.

[4]It was placed at this angle before this author joined the experiment and before writing this thesis he had received nothing but muttered curses in response to inquiries about why this was done. The motivation was to get a little more acceptance for the lowest angle particles.

Henry Higgins, because in its current position it reduces the acceptance for particles bending towards the beam. This does not have any ramifications on this analysis but it does eliminate acceptance overlap between angle settings that were used in previous cross-section analyses to estimate systematic errors. TR2 is $72\frac{1}{8} \times 47\frac{1}{8} \times 4\,\text{in}^3$ and is located between T4 and TOF, $\approx$509 cm from the target.

Except for positioning and size, the chambers are identical. Both chambers were recycled after many years of use as drift chambers in the BNL Multiparticle Spectrometer (MPS). Details of their original construction can be found in [Etk79, EK80]. In E859, the chambers were reconfigured as single-plane wire chambers (no time information was recorded) giving information on particle positions in the spectrometer bend plane. The frames are constructed with a polyester-fiberglass composite and mounted on an aluminum plate. The wire separation is 1/4″ and the depth of the active area is 1/4″. Anode wires are 0.001″ diameter gold-plated tungsten, cathode and field wires are 0.003″ diameter stainless steel. The gas mixture was 70% argon plus 30% isobutane bubbled through dimethoxymethane. Operating voltages for the chambers were $\approx$2.5 kV for the anode and cathode wires and $\approx$2.2 kV for the field wires. A 9.5 V threshold, divided down by ten on the chamber, was applied. Chamber readout was performed using the LeCroy Proportional Counter Operating System (PCOS) described in section 2.14.4.

The efficiency was observed to be in excess of 99%, see [Sun94]. Cross-talk of 5-10% was caused by tracks crossing more than one cell, and by noise on the rather old preamplifier/discriminator cards.

2.11 Time-of Flight Wall (TOFW)

The TOFW is a 160-element plastic scintillator "picket-fence" hodoscope arranged in an arc ($R \approx 2.4$ m) roughly 6.6 m from the target. Each slat is $1.6 \times 1.6 \times 78\,\text{cm}^3$ except for every sixteenth slat which is twice as wide.[5] This makes for rather bizarre distributions of $dn/dslat$, the deciphering of which is one of the rites of passage for any new heavy ion group member. The distance from the target was a compromise balancing the need for excellent timing resolution with the need to collect kaons before they decay ($c\tau = 370.9$ cm). In its current position, roughly 58% of 1 GeV/c kaons survive to the TOF wall. The TOFW slats had distribution of σ_{TOF} that was peaked at 100 psec with a tail extending to $\approx$ 120 psec, see section 3.6.3 for details. A conservative position was taken for particle identification (PID), with $\sigma_{TOF} = 120$ psec fixed

[5]The presence of double-wide slats was due to difficulties in the geometrical arrangement of the phototubes. Extra space was needed, so the sixteenth slats were widened to maintain hermiticity of the TOF wall.

for each slat, see section 3.8 for details. With this timing resolution, the pion and kaon 3σ tails do not begin to overlap until $p \approx 1.8\,\mathrm{GeV/c}$.

In order to provide both timing and energy loss information, the analog signal is passively split and sent into both a TDC and an ADC. The ADC information is used to make charge cuts in the particle identification code, see section 3.8. This information is also vital because a particle's recorded time can have a pulse-height dependence of as much as 20 psec. If not accounted for, this would result in a severe worsening (10-20%) of the ideal resolution. This effect is known as a slewing effect or a time-walk effect [S+86].

Details of our entire TOF calibration procedure, including the correction for the slewing effect, can be found in section 3.6.

2.12 Gas Čerenkov (GASČ) and BACK Counter

The segmented GASČ is located immediately behind the TOFW, $\approx 8.2\,\mathrm{m}$ from the target. It consists of 40 cells inside an cylindrical aluminum tank. The tank is filled with 4 atm (absolute) of Freon-12, corresponding to an index of refraction, $n = 1.0045$. There are two different sized cells, $23 \times 28 \times 72\,\mathrm{cm}^3$ and $23 \times 28 \times 101\,\mathrm{cm}^3$. The cells are constructed with aluminized-mylar and have an elliptical mirror at the downstream end to focus the Čerenkov light onto a phototube. The index of refraction of the Freon-12 is monitored with a Fabry-Perot interferometer. The photomultiplier gain is monitored with an LED system.

The GASČ was constructed to separate pions from kaons (and electrons) when the momentum is too high for the TOF information to be sufficient. The momentum threshold to fire the GASČ, given by

$$p_{\check{c}} = \frac{m}{\sqrt{n^2 - 1}}, \tag{2.2}$$

is mass dependent. The GASČ can decide between two different mass hypotheses, m_1 and m_2, if a particle's momentum lies between $p_{\check{c}}(m_1)$ and $p_{\check{c}}(m_2)$. Table 2.2 lists $p_{\check{c}}$ for different particles in the GASČ.

Between its Freon-12 and its aluminum housing, the GASČ represents ≈10% of an interaction length. Some PID decisions require that a track *not* fire the GASČ, but for this decision to be valid, one must make sure that the track traversed the entire GASČ. This is why the BACK counter was built. It uses the same technology as the TMA, see section 2.6, but it is arranged as a flat wall behind the GASČ. It consists of 1536 $10 \times 12\,\mathrm{cm}^2$ pads.

A more detailed description of the construction of both the GASČ and the BACK can be found

Particle	$p_{\check{c}}$ (GeV/c)
e	0.0054
μ	1.12
π	1.47
K	5.20
p	9.88

Table 2.2: GASČ momentum thresholds for different mass particles.

in [Kur92]. See section 3.8 for a detailed account of how these two detectors are incorporated into the PID decision.

2.13 Data Acquisition System and Trigger Supervisor

The brain of E859 consists of the Data Acqusition System (DAQ) and the Trigger Supervisor (TS). More detailed writeups can be found in [W+87, L+87, WIL87]. The DAQ and the TS, while distinct, are very intertwined. I will therefore combine them into one discussion. Together they are responsible for many tasks:

- Making a trigger decision based on multiple trigger inputs and second-level vetoes.
- Providing all experimental control logic. This includes *BUSY* and *FAST CLEAR* signals, start signals and gates for TDC's, ADC's, etc., and interrupt signals for crate readout controllers.
- Reading out all CAMAC and FASTBUS data.
- Assembling the data into event data structures.
- Translating the data from geographical addresses (e.g., crate, slot and channel) into logical addresses (e.g., chamber, plane and wire).
- Porting data to storage media.

The DAQ and the TS are implemented with three crates of VME modules and a VAX 11/785 host computer (BNL802). The maximum sustained throughput was 165 kByte/s. A schematic of the DAQ, the TS and their communication links is shown in figure 2-16.

The single most important part of the DAQ is the 68010 microprocessor-based VME module known as "the Chairman." This module manages the activities of all fellow residents of the

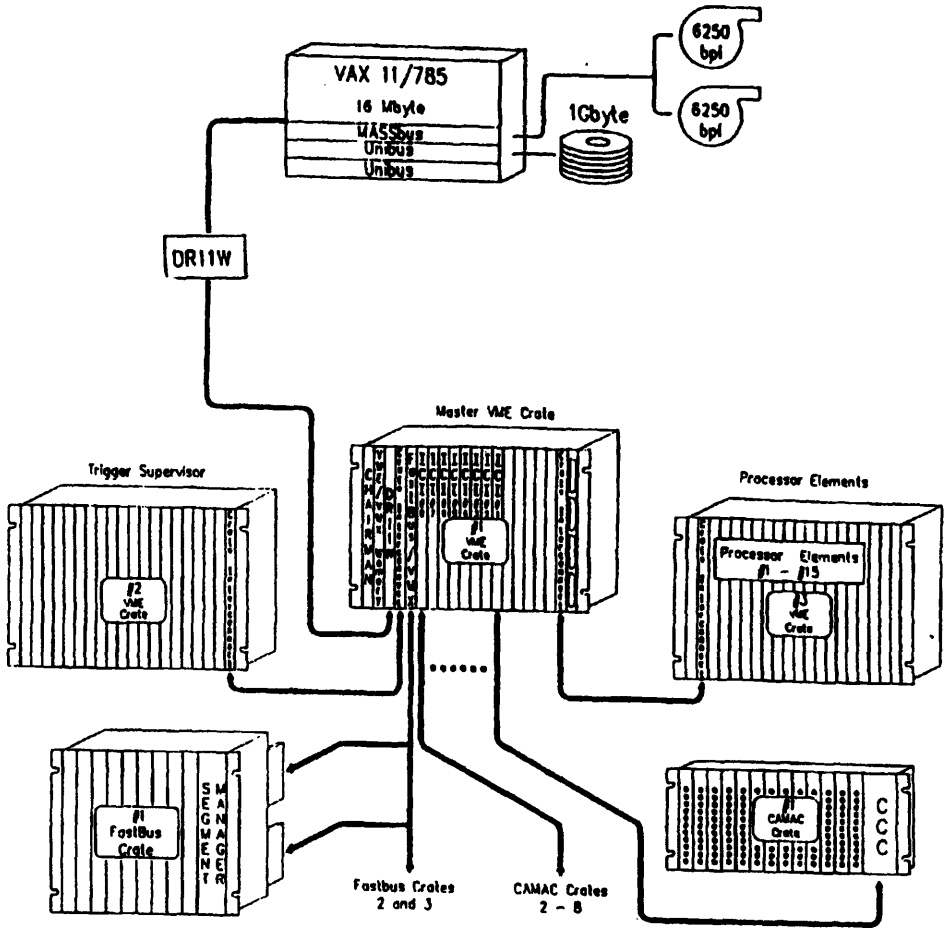

Figure 2-16: Schematic of the E859 data acquisition system. See text for details.

DAQ "Master Crate." These modules in turn control readout, translation and formatting of all of the experiment's data and allow communication among the different DAQ VME crates and between the DAQ and BNL802.

Eight 68000 microprocessor-based Intelligent CAMAC Interfaces (ICI) reside in the Master Crate [SL87a]. These modules are commonly referred to as "XYCOM's" after the microprocessor manufacturer. The XYCOM's allowed parallel read out and translation of all the experiment's CAMAC data with each XYCOM processing one CAMAC crate of data.

A FASTBUS/VMX interface was another member of the exclusive Master Crate club [SL87b]. This module allowed communication between the DAQ and several FASTBUS crates controlled by LeCroy 1821 Segment Managers. The Segment Managers were responsible for readout of all the experiment's FASTBUS data. Translation was performed in the processor elements described below.

The first of two VME crate interconnect modules in the Master Crate allowed communication with the DAQ's second VME crate. This crate consisted of 15 68020 processor elements. These processor elements were responsible for translating FASTBUS data and formatting the events using the YBOS software package developed at CDF [Qua89]. This package provides memory management and data structures, known as "banks." Each event is comprised of a YBOS bank for each detector plus two YBOS banks that identify the event according to number, type, etc. (LRID), and contain the trigger summary for the event (EVCL).

The second VME crate interconnect module in the Master Crate allows communication with the Trigger Supervisor (TS). The TS is designed to allow the user to control and monitor the trigger conditions for the entire experiment. During normal running the TS is run in a "coupled" mode in which each detector shares a common trigger, a common *BUSY* signal and common gates. An uncoupled mode is supported for detector testing purposes. If the TS decides that an event should not be kept, *FAST CLEAR* signals are issued and *BUSY* signals are held for 6 μsec. If the TS decides to keep an event, interrupt signals are sent to the DAQ which begins event processing.

The TS can take up to eight trigger inputs from each of a maximum of sixteen partitions. Each trigger input could be scaled down by as much as 2^{24}. Typically, less than five of these inputs were ever simultaneously used. See figure 2-17 for a schematic of the TS inputs.

The TS was designed in anticipation of the development of second level triggers implemented as vetoes. A partition's positive first level trigger decisions can be revoked if a veto signal arrives within a hardware-settable pause interval. For most of E859 running this pause interval was set to 40μsec. Another TS feature was known as "veto-override." This is the ability to configure

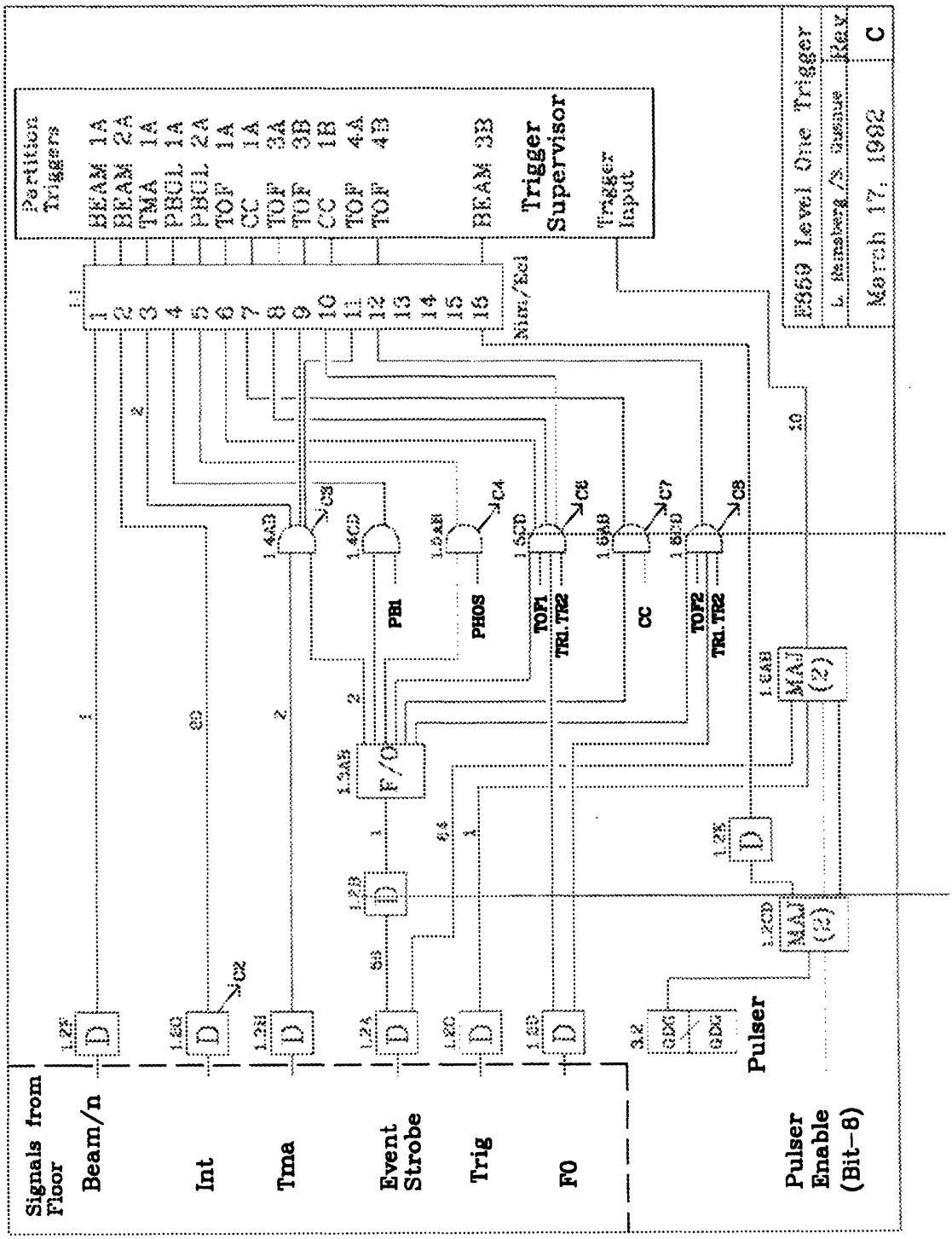

Figure 2-17: Electronic diagram of the first level trigger inputs to the E859 trigger supervisor.

any of a partition's eight individual triggers to ignore the second level veto. This feature was exploited by taking data, known as "veto-out runs," where the second level veto was recorded, but its decision was ignored by the TS. These runs were used as diagnostic tests to study any second level trigger bias, see section 3.1.9.[6]

The last module in the Master Crate is a DR11-W link that allows communication between the DAQ and BNL802. BNL802 served as a human interface to the DAQ and the TS. BNL802 allowed the user to configure the trigger conditions, monitor the performance and start and stop runs. It was also an interface to two 6250 bpi 9-track tape drives (used for permanent data storage) and a disk-resident event-pool (used for online analysis and monitoring). In order to synchronize the configuration and initialization of the second level trigger with the beginning of a run, BNL802 was made to communicate with BNL859, the VAX 3400 computer that controlled the second level trigger. See section 3.1.5 for details of how this was done.

2.14 Triggering

A trigger is simply an indication, from some piece of equipment, that an event is interesting and should be kept for further analysis. In E859 we have used a number of different triggers based on beam definition, event characterization and particle identification. The following list contains the functional definitions of all the triggers used for this analysis.

- *BEAM* → Selects beam particles with the correct charge and trajectory.
- *INT* → Selects valid beam particles that undergo an interaction as determined by the amount of forward-going charge.
- *TMA* → Selects violent collisions by counting the number of charged particles.
- *SPEC* → Selects events that have a track candidate in the spectrometer.
- *LVL2* → Selects events that have a programmable number of PID track candidates in the spectrometer.

Triggers are often segregated into different "levels" according to rather arbitrary time definitions. First level triggers are the fastest, usually $t < 1\mu$sec. They generally consist of fast hardware decisions such as the presence or absence of a discriminator level (e.g., "Was this scintillator hit?"). Second level triggers are slower, with $t < 1$ msec. Second level trigger decisions are usually made using harware lookup tables. Third level triggers can take much longer,

[6] A trigger that throws out interesting events, in a non-random fashion, is called biased.

and usually involve some sort of online software analysis, e.g., fast reconstruction, etc. Each level of triggering must reduce the the rate of events that need to be analyzed by the more time-consuming succeeding levels.

2.14.1 *BEAM* and *INT* Triggers

All trigger decisions start with a valid beam particle. The various detectors that make up the beam definition system are described above in section 2.5. The logic diagram for the various beam counter triggers and scalers is shown in figure 2-18. The *BEAM* trigger selects beam particles with the correct charge and geometry. Its definition in terms of the various beam counter detectors is given by:

$$BEAM = \overline{UDEW} \wedge \overline{HOLE} \wedge \overline{PRE} \wedge \overline{BTOT_U} \wedge \overline{BTOF_U} \wedge BTOT_H \wedge BTOF_H, \qquad (2.3)$$

where the overbar indicates complementary logic.

$\overline{UDEW}$ and $\overline{HOLE}$ enforce geometry constraints. $\overline{PRE}$ is a signal that rejects events that arrive within a settable *follow time* of the previous event. Events that are followed too closely by another event are accepted, but marked with a *FOLLOW* bit that can be used to reject such an event in offline analysis. In E859 the follow time was only 100 nsec. This is significantly less than it was for E802 since the beam rates were much higher. In order to provide further protection, two new bits of event-time separation information were recorded by E859. For each event with the *INT* bit set, *INTPRE* and *INTFOL* were set if there was an interaction in a 10 μsec window before or after the given event. If two particles arrive within $\delta\tau \approx 10$ nsec, the rise times associated with the beam trigger electronic modules make the second particle invisible to both *PRE* and *FOLLOW* logic. These events need to be eliminated with cuts on the charge deposited in the beam counter scintillators. $BTOT_U$ and BTOF_U are the signals of their respective counter filtered by a discriminator with an ultra-high threshold set to reject any particles above the standard charge state. This helps to filter events in which two beam particles arrive inside of the *PRE* blind spot. $BTOT_H$ and $BTOF_H$ are the signals of their respective counter filtered by a discriminator with a high threshold set to reject any particles below the standard charge state.

The definition of *INT* is very straightforward:

$$INT = BEAM \wedge \overline{BE}. \qquad (2.4)$$

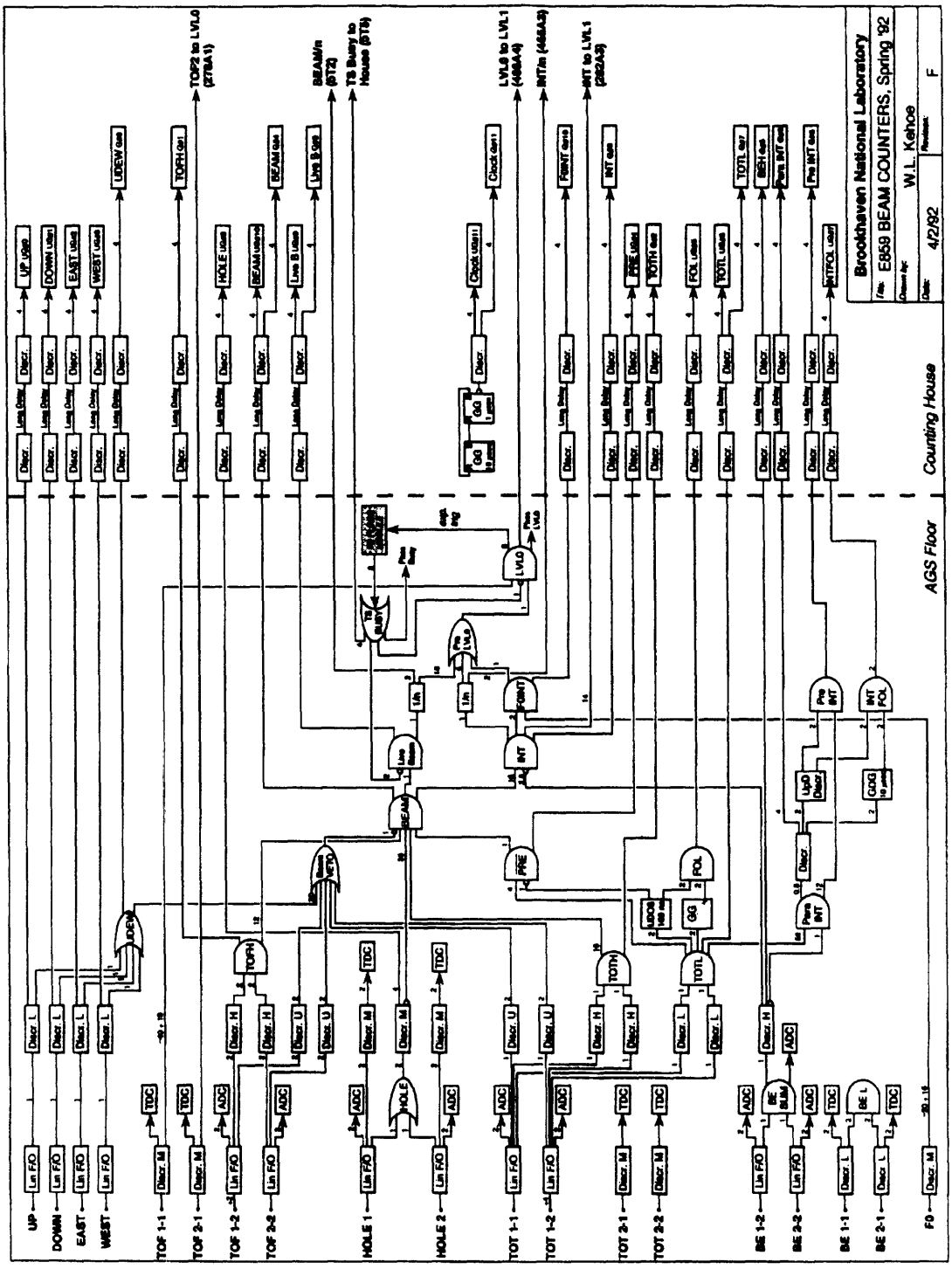

Figure 2-18: Beam counter trigger logic diagram.

The bullseye detector, decribed in section 2.5, will fire if the amount of charge deposited indicates that the beam particle remained intact.

Typically *BEAM* and *INT* triggers were scaled down by some factor, N, so that they made up $\approx$5–10% of the accepted trigger mix.

2.14.2 TMA Trigger

A sum of the discriminated TMA pad outputs is formed and the output is used as a first level centrality trigger.[7] The discriminator threshold determines the centrality level below which events were rejected[8]. The procedure for setting the TMA threshold was admittedly primitive. First, an *INT* scaledown was calculated as:

$$\frac{1}{N} = centrality \cdot \frac{\sigma_{int}^{target}}{\sigma_{int}^{target} - \sigma_{int}^{targetout}}, \tag{2.5}$$

where *centrality* is the fraction of the interaction cross section that you wish to trigger on and σ_{int}^{target} and $\sigma_{int}^{target\ out}$ are the interaction cross sections with the target in and out respectively. Next, the discriminator threshold is adjusted until the *TMA* and *INT*/*N* scalers, integrated over $\approx$ 10 spills, are equal. A strict cut can be made offline, and some intricate mechanisms for determining the number of struck TMA pads corresponding to a particular centrality have been developed in the cross-section analyses [Mor94]. The analysis presented in this thesis is relatively insensitive to the exact cut, see section 4.2.6.

2.14.3 *SPEC* Trigger

A *SPEC* trigger gives a very fast indication of the presence of a track candidate in the spectrometer. The trigger definition is given by:

$$SPEC = F0 \wedge TR1 \wedge TR2 \wedge TOF. \tag{2.6}$$

The addition of *TR1* and *TR2* made the E859 version of the *SPEC* trigger much more restrictive than the E802 version. Even so, it was nothing compared to the power and grandeur of the E859 *LVL2* trigger. A *SPEC2* trigger, which required two TOF hits, was also available. This

[7] We unthinkingly call the TMA sum a *centrality* trigger. This is a measure of our confidence that multiplicity and centrality are well correrlated variables. This confidence has been earned by the high degree of correlation between TMA, ZCAL, and PBGL, each of which measure a different variable expected be correlated with centrality. See appendix E for details on ZCAL and PBGL.

[8] This trigger could be trivially complemented to run in peripheral mode where events above some TMA threshold were rejected. This feature was used to measure π^+ correlations in peripheral collisions. [Sol94]

trigger was not used in this analysis since $\bar{p}$ triggers were taken in conjunction with the $2K^+$ triggers.

2.14.4 Second Level Trigger (*LVL2*)

If Henry Higgins is the heart of E859 and the DAQ is its brain, then surely the *LVL2* trigger is its soul, its very reason for existence. As you might imagine, I had a hand in the development of the trigger and I admit to being somewhat emotionally attached. All discussion of the software necessary to control, configure and debug the *LVL2* trigger is postponed to section 3.1

Motivation

As stated in section 2.1, the goals of E859 all required the enhanced collection of rare events.

> "Why not turn the beam intensity up? You said in section 2.2 that the AGS beam intensity was 500 times greater that used by E859."

Good question. In fact, most E859 detector systems saturate at an interaction rate of 2×10^4 interactions/spill (obtained with a beam intensity of 2×10^6 ^{28}Si/spill and a 1% interaction length target). The problem is that this rate is more than an order of magnitude beyond our DAQ processing capability. Since E802 did not have a *LVL2* trigger, it could only utilize a beam rate of $\approx 5 \times 10^4$ ^{28}Si/spill. Most interactions contain nothing of interest that has not already been studied in detail by E802. Some, but not enough of the uninteresting events can be eliminated by the first level triggers discussed above. So, a decision was made to develop a second level trigger and utilize the veto-input feature of the TS, see section 2.13. The *LVL2* trigger was supposed to filter out as many of the remaining uninteresting events as possible.

The filtering capability of the trigger is expressed in terms of a quantity known as the *rejection factor*. The definition of the rejection factor is very simple:

$$R \equiv \frac{LVL1}{LVL2}. \tag{2.7}$$

But, one has to be careful about the definitions of *LVL1* and *LVL2*:

- *LVL1* → Since *LVL1* triggers can be configured to ignore the *LVL2* veto decision, only count those *LVL1* triggers that can actually be vetoed.

- *LVL2* → Similarly, only count those *LVL2* triggers which have started as a vetoable *LVL1* trigger.

Rejection factors will be discussed in more detail later in this section.

The following requirements for the *LVL2* trigger were decided upon:

- The trigger needed to be able to perform online track reconstruction and PID in order to selectively filter on rare particles such as $K^{\pm}$ and $\bar{p}$.
- There is no external clock in a fixed-target environment, so the trigger needed to be data-driven. Data-driven simply means that the presence of data begins the processing cycle, each stage of which generates control signals that drive the processing to completion.
- The trigger configuration (e.g., the number or type of particle demanded) needed to be easily programmable.
- The trigger decision needed to be made very fast ($< 100\,\mu$sec) so as not to contribute to the experimental dead time. This motivated a hardware lookup table approach.
- The trigger needed to achieve rejection factors of roughly $R = 10$. More than this was desirable for the rarest events (e.g., $2\,K^+$ and $\bar{p}$) and less than this was acceptable for more abundant events (e.g., $1\,K^+$ at the most forward angles). See table 2.3 for a list of the actual rejection factors achieved.

Rejection Factors

A brief discussion of rejection factors is necessary to gain an understanding of what a trigger can and cannot do. Throughout this discussion the deadtime contribution of the *LVL2* trigger, which is small, will be ignored.

We first write an expression for the ratio of the number of good events written to tape per spill under two different beam intensity and/or trigger conditions:

$$\frac{G_1}{G_2} \equiv \frac{fR_2E_2}{fR_1E_1} \tag{2.8a}$$

$$= \frac{R_2E_2}{R_1E_1}, \tag{2.8b}$$

where:

$$f \equiv \text{fraction of interesting events in an untriggered sample.} \tag{2.9a}$$

$$R_1, R_2 \equiv \text{rejection factors.} \tag{2.9b}$$

$$E_1, E_2 \equiv \text{events written to tape per spill.} \tag{2.9c}$$

This formulation assumes that the trigger does not throw out any event of interest. This assumption had better be good.

To understand the implications that this has on the trigger, consider the following extreme cases:

- *Beam Limited* - This refers to situations in which the beam intensity is maximized, because of radiation concerns, saturation of detectors, etc., but the event collection rate is below the DAQ maximum. In this case, the product RE is a constant because every event that is rejected is just one less event written to tape. Under these conditions a trigger will not help very much. If rejection factors are increased beyond this point, the interesting data will be more strongly concentrated on the data tapes, but it will take proportionately longer to fill a data tape.
- *Tape Limited* - This refers to situations in which the DAQ is completely saturated, or can be saturated by increasing the beam intensity. In this case the event rate is constant and the collection rate for interesting events will increase by the rejection factor.

Table 2.3 shows the rejection factors that the *LVL2* trigger achieved under different experimental conditions. In many cases, E859 was brought to the beam limit goal. Some attempted trigger conditions left the experiment so beam-limited that complementary data could be productively taken in parallel (e.g., K^+, K^-, and $\bar{p}$).

I would now like to re-express equation 2.8 in terms of the experimental live time because this is a number that can be quickly determined from the experimental scalers. We first write an expression for the fractional live time in terms of the number of events written to tape:

$$L \equiv 1 - \frac{T_t E}{T_s}, \tag{2.10}$$

where:

$$T_t \equiv \text{time to write an event to tape.} \tag{2.11a}$$

$$E \equiv \text{events written to tape per spill.} \tag{2.11b}$$

$$T_s \equiv \text{spill time.} \tag{2.11c}$$

This assumes two things:

Trigger	System	Angle	Field	RF
$K^+/K^-/\bar{p}$	Si+Al	14	4A	6.7
			4B	5.1
		24	4A	9.8
			4B	10.3
		34	4A	13.9
			4B	15.5
		44	4A	21.7
			4B	24.0
$K^+/K^-/\bar{p}$	Si+Au	14	4A	4.8
			4B	3.6
		24	4A	8.1
			4B	7.2
		34	4A	13.5
			4B	13.3
		44	4A	20.5
			4B	19.6
$K^+/K^-/\bar{p}$	Au+Au	24	2A	2.4
			2B	2.6
		34	2A	4.1
			2B	4.5
		44	2A	7.5
			2B	9.2
$K^-/\bar{p}$	Si+Al	5	4B	2.7
		14	4A	20.7
			4B	10.0
		24	4A	31.0
			4B	23.6
$K^-/\bar{p}$	Si+Au	5	4B	2.5
		14	4A	13.8
			4B	7.7
		24	4A	25.0
			4B	19.1
$\bar{p}$	Si+Al	14	4B	19.0
		24	4B	48.0
$\bar{p}$	Si+Au	14	4B	11.0
		24	4B	29.0
K^+	Si+Al	5	4A	2.4
K^+	Si+Au	5	4A	2.0
$2K^{\pm}/\bar{p}$	Si+Au (central)	14	4A	15.3[a]
$2\pi^+$	Si+Au (central)	19	4A	10.6[b]
$2\pi^-$	Si+Au (peripheral)	14	4B	8.4
$2\pi^-/\Lambda$	Si+Au (central)	14	4B	3.4
$2\pi^+$	Au+Au (central)	21	4B	2.8

[a]Trigger conditions for the $2K^+$ data set in this analysis.
[b]Trigger conditions for the $2\pi^+$ data set in this analysis

Table 2.3: *LVL2* rejection factors under different experimental conditions. Data sets are minimum bias unless otherwise noted.

1. All experimental dead time results from writing events to tape. This is a good assumption, and without it the above expression is complicated by additional terms to account for the dead time arising from *LVL1* trigger decisions.

2. The time to write an event to a tape does not depend on the trigger type. This assumption is good to $\approx 30\%$ if we compare triggered and untriggered events. It is much better than this if we are comparing two different *LVL2* triggering conditions. Without this assumption, the above expression would have to be written as a sum over event types of different sizes.

If we substitute equation 2.10 into equation 2.8, we obtain:

$$\frac{G_1}{G_2} = \frac{R_2(1-L_2)}{R_1(1-L_1)}. \tag{2.12}$$

Note that singularities are avoided because $L = 1$ corresponds to the situation where *no* events are being written to tape. It may seem counterintuitive that the number of good events written to tape per spill decreases with live time. But, remember that the live time is inversely proportional to the number of events written to tape.

Design Decisions

The *LVL2* design requirements outlined at the beginning of this section resulted in the decision to implement the trigger logic, almost exclusively, with commercially available CAMAC modules from the LeCroy ECLine family. This decision had many advantages:

- The modules were designed, debugged, supported, and replacable.

- The modules were not application-specific. This made them flexible enough to reconfigure as the trigger design evolved. For instance, the late addition of a lookup table with information on a particle's charge allowed a 2K/$\bar{\text{p}}$ trigger condition not originally anticipated. This greatly enhanced our $\bar{\text{p}}$ yields [Rot94]. This same modification made a Λ trigger possible [Sun94].

- CAMAC resident modules are easily programmable.

- Data are processed on the LeCroy-standard ECLbus, a front-panel 16-bit bus using differential ECL levels. At 10 MHz the ECLbus is 10 times faster than the CAMAC backplane. Since the bus connections are twisted-pair cables, the configuration is customizable.

- The modules are designed to be operated in a data-driven mode. Every one is equipped with Output and Output Ready (OR) signals. The timing relationship between these two signals is exactly that required for the Input and Input Enable (IE) gates of following modules. See figure 2-19 for an example timing diagram.

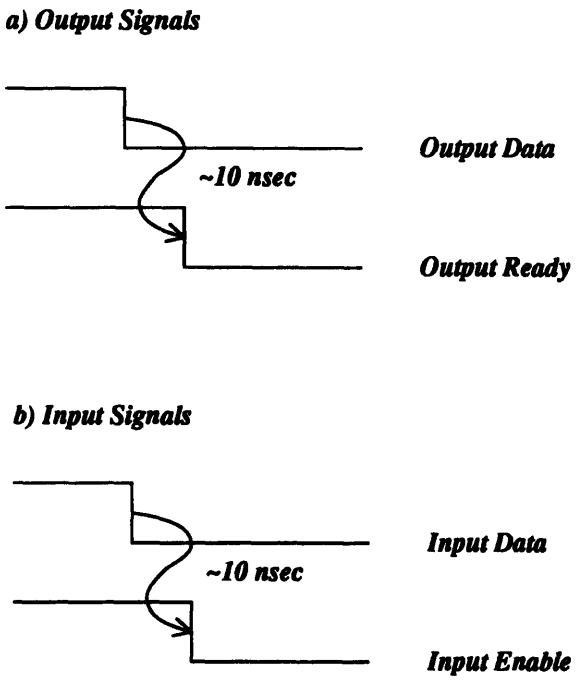

Figure 2-19: Timing diagram of LeCroy ECLine input and output signals. Note that the relationship is the same, which allows the output from one module to be used as the input to following modules, precisely the condition required for data-driven processing.

The Basic Idea

Figure 2-20 is a flow chart showing the trigger logic basics. The *LVL2* trigger decision is based on information from TR1, TR2 and TOF. With the receipt of a valid *LVL1* trigger, the *LVL2* digitization continues to completion in $\approx 5\,\mu$sec. At this point, data are loaded into the *LVL2* trigger processor elements which loop over all combinations of hit TR1 wires and hit TOFW slats. For every TR1-TOF combination, a lookup table (MLU_TR2P) is interrogated to predict a corresponding TR2 hit from straightline geometry. Only tracks that could have originated from the target are allowed. In parallel, other lookup tables are interrogated to determine the momentum (MLU_MOM) and velocity (MLU_DPATH, MLU_TOFCOR) of the particle candidate. For tracks confirmed on TR2, the momentum and velocity are presented

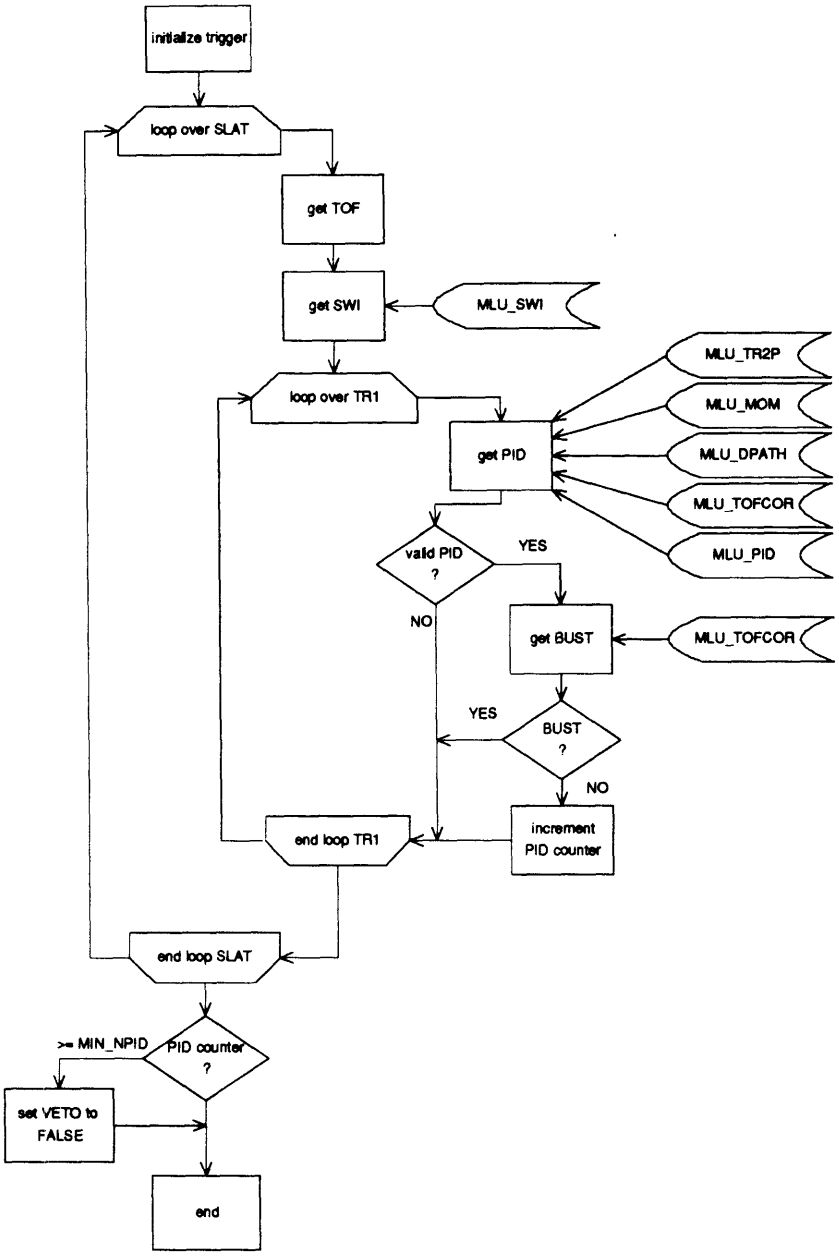

Figure 2-20: *LVL2* trigger flow chart. See text for details.

to a lookup table (MLU_PID) that contains PID cuts in any projection of these two variables. In practice, the cuts were always momentum and mass windows. The trigger contains further logic that allows it to count to two. A BUST condition can be enforced, in which a single TOF slat is allowed to contribute a maximum of one track (MLU_TOFCHK). If processing finishes within the TS pause interval (40 μsec) and the event fails to satisfy the desired physics condition the *LVL2* veto signal is issued and the event is rejected. If there are so many combinations ($\geq\approx 100$) that the trigger processing does not finish within 40 μsec, then the event is kept for further analysis. Such events are called "timeouts."

Ideally, the start of data digitization would be signaled by the presence of a vetoable *LVL1* trigger. Unfortunately, the TS takes 250 nsec to make a decision. This delay would have required the installation of many spools of delay cables to enforce the correct overlap between signals and their required gates. To avoid this, data digitization is started with the EVENT STROBE signal gated on computer busy. EVENT STROBE is split; one branch clears all countinghouse trigger modules, the other branch is used as the gate for TR1, TR2 and TOFW signals. A delayed version of the same event's EVENT STROBE is used to clear the TR1, TR2 and TOFW readout devices. The delay value is set to be $\delta \approx 270$ nsec if the TS decides that an event passes no *LVL1* criteria, and $\delta \approx 40$ μsec if the event does satisfy some *LVL1* trigger. More details can be found in [CL91].

The Trigger Modules

In the following sections I will outline the function of each module used in the *LVL2* trigger. I will start with those modules used to read out TR1 and TR2. Next, I will discuss the modules needed to digitize the TOFW information. Finally, I will discuss those modules that are used by the trigger to process this data.

Loading TR1 and TR2 (PCOS III) TR1 and TR2 information is processed with modules belonging to the LeCroy Proportional Counter Operating System (PCOS III). PCOS begins with chamber-mounted preamplifier/discriminator cards that are read out by CAMAC resident Delay-and-Latch modules. These modules are controlled by a dedicated CAMAC crate controller which provides zero-suppressed bit patterns of hit wires across the ECL bus. Computer control of the crate controller is achieved with a MicroVAX 3400 workstation and another LeCroy CAMAC module, the Databus Interface. For a more detailed discussion of the E859 PCOS III implementation, see [CL91].

16-channel Preamplifier/Discriminator Card (LeCroy Model #2735) A computer-controllable threshold of up to 7.7 V was available. To reduce cross-talk, this was bypassed by a 9.5 V external threshold. Applied thresholds were divided by a factor of ten on the chambers.

32-Channel Delay and Latch (LeCroy Model #2731a) These modules reside in a dedicated CAMAC crate, slaved to a specialized crate controller described below. Each module receives data from two 2735 cards across twisted-pair cables.

Internal wire-wrap headers are available to obtain ungated (prompt) signals for each input channel. These were connected as grand-*OR*'s to TTL open collector outputs. Outputs from each module were daisy-chained so that the resulting signal indicated the presence of one or more hits in each chamber. These signals were used to create a *SPEC* trigger more restrictive than that used by E802, see section 2.14.3.

Data present in the 2731a modules in coincidence with an EVENT STROBE signal are latched (stored) in order to be read in by the trigger processing elements. The 2731a's have a very nice feature, called 'Ripplethru Delay', which eliminates the need for delay cables to insure correct coincidence between the chamber data and the EVENT STROBE. This feature is a computer-controllable in-module delay, $\delta \leq 782.5$ nsec. This time was not long enough to incorporate the TS *LVL1* decision, so the trigger digitization needed to be started with EVENT STROBE. Steering bits allow data from different 2731a modules in a single crate to be read in by distinct trigger processor elements.

Digital Readout Controller (LeCroy Model #2738) One of these modules resides in the E859 PCOS crate where it manages the 2731a modules. This module presents the trigger chamber data to the trigger processing elements, zero-suppressed and in ascending numerical order, via the ECLbus. Data Ready (DR) is a control signal provided to indicate the presence of valid data in a matter compatible with this next stage of the trigger. A BUSY signal, whose trailing edge indicates that the last hit has been processed, is also provided. Figure 2-21 shows a timing diagram of the 2738 control signals.

Databus Interface (LeCroy Model #4299) This module provides computer access to the PCOS modules. It allows the user to set the 'Ripplethru Delay' and the 2735 thresholds. It also allows the user to load and read test wire patterns. This feature was expanded into a series of diagnostic programs detailed in section 3.1.7.

Loading TOFW The inverted NIM outputs from the TOF discriminators in the counting-house are delayed and input to BNL-designed NIM/ECL converters. These converters are

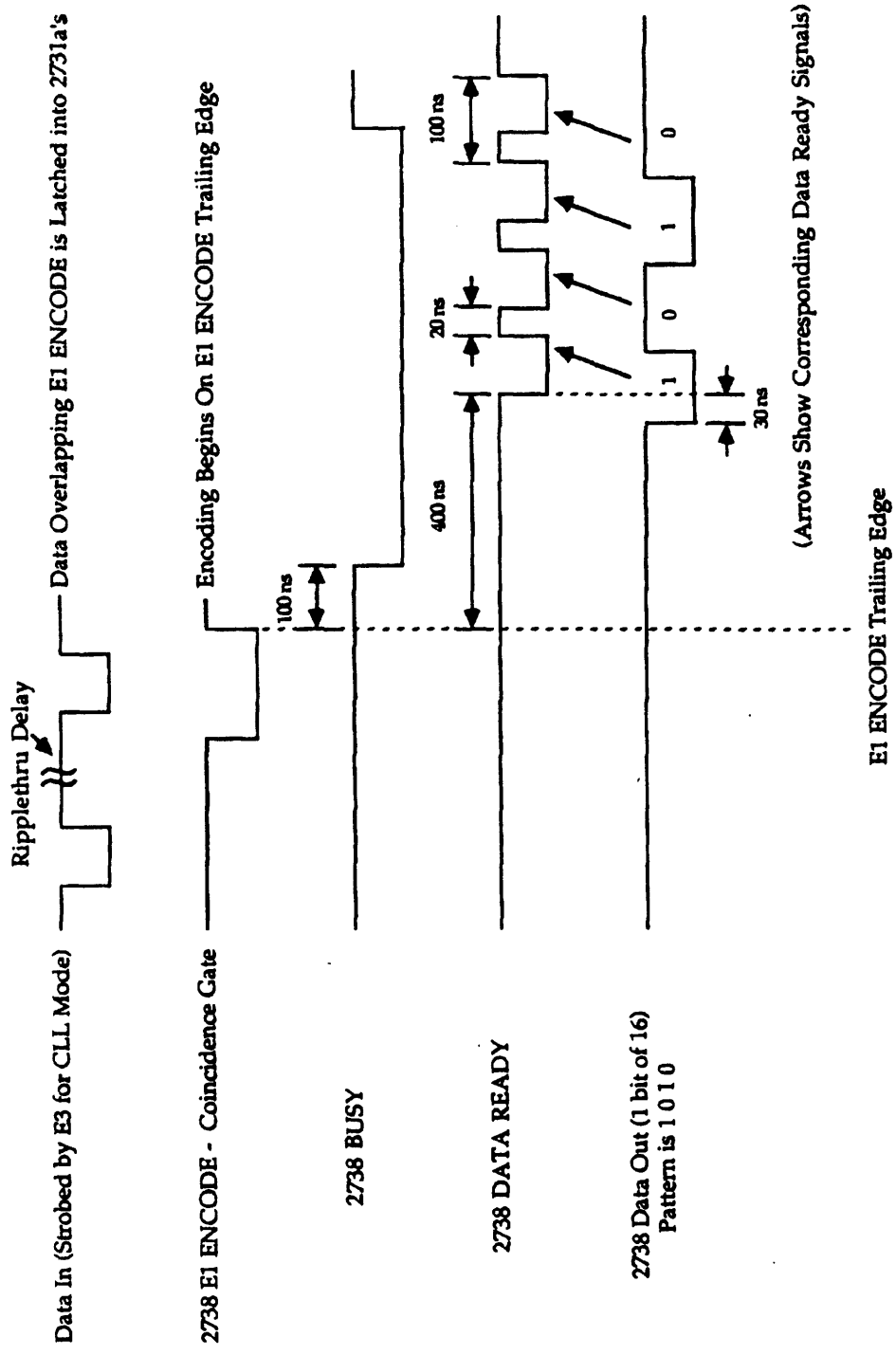

Figure 2-21: Timing diagram of the 2738 control signals. From [CL91].

single-slot CAMAC modules that accept 16 channels of NIM input through rear-panel connectors and present their ECL equivalents on a 34-pin front-panel connector. These signals are input to a LeCroy 16-channel Time-to-FERA Converter (TFC) module. The output of these modules were designed to be input to the LeCroy 16-channel Fast Encoding Readout ADC (FERA). Together the TFC and FERA make a fast ($\approx 5\,\mu$sec) 16-channel TDC, and are known as a FERET.

16-channel TFC - (LeCroy Model #4303) The TFC module is designed to create a constant amplitude pulse with a time duration equal to the difference between the input START and STOP signals. With a front-panel potentiometer the amplitude of the TFC output can be adjusted such that the product of the amplitude and longest acceptable gate exactly saturate FERA dynamic range. The timing resolution of the TFC/FERA system is limited to ≈ 50 psec/channel. The FERA 10-bit dynamic range would thus naively translate into a 50 nsec maximum TOF. Unfortunately, any signal within 40 nsec of the START gate has a less-than-linear response. So $\beta \approx 1$ particles were timed such they arrived at the TFC modules 40 nsec after the START. The charge output of a TFC given a 40 nsec gate is equal to the charge that would be produced by a 20 nsec gate if the response was completely linear with the slope in the linear region. Thus, this non-linearity reduced the maximum TOF to 30 nsec. Figure 2-22 shows this graphically. The 30 nsec gate width has implications for the *LVL2* trigger's ability to process slow protons which can have TOF ≈ 80 nsec in our spectrometer [Rot94].

16-channel FERA - (LeCroy Model #4300B) Two FERA options were available that balanced dynamic range against digitization time. The option with 10-bit dynamic range and 4.8 μs digitization time was chosen. The TFC output charge is fed into a FERA which produces a digital value proportional to the time interval between the START and STOP signals, subject to the non-linearities discussed above. Like PCOS, the FERAs present zero-suppressed data, in numerically ascending order, via the ECLbus. The computer-controllable pedestal subtraction feature is very important to the particle identification ability of the trigger. This allows us to calibrate the absolute T_0 for each channel to within 50 psec, see section 3.1.4.

FERA System Driver - (LeCroy Model #4301) This module collects and distributes all common command and data signals for up to 22 model 4300B FERA's. It also contains a digital-to-analog converter for FERA calibration.

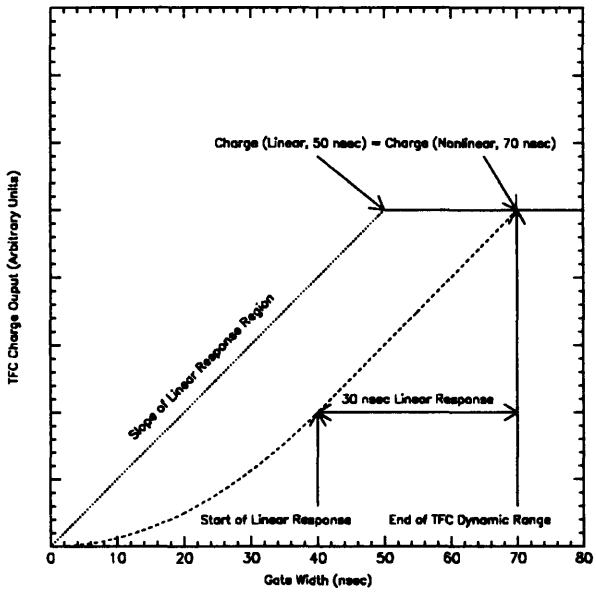

Figure 2-22: LeCroy Model #4303 TFC response and dynamic range.

Trigger Processing Elements As described above, information loaded into the trigger processing elements from TR1, TR2 and TOF is used to determine whether or not an event passes the physics cuts of interest. This section details the data and control signals of the necessary modules.

Arithmetic Logic Unit (ALU - LeCroy Model #2378) The ALU has several different computer-selectable options. It can perform simple arithmetical and logical operations on two 16-bit input words producing 32-bit output words. There are also "accumulator modes" which operate on one input word and the result of previous operations. The *LVL2* trigger uses one ALU to add the times from each slat's two phototubes, TOFU and TOFD. This model number is correct despite the fact that it is the same as the PCOS Digital Readout Controller described above.

Data Array (DA - LeCroy Model #2376 a) The DA is a 1024 × 1-bit random access memory. The *LVL2* trigger uses one DA to store the values of TR2 hit wires. The input word consists of a 10-bit "search address" and a 3-bit "search width" (SWI). If a TR2 wire is found within the search width of the search address, the DA produces one output bit indicating good status.

Data Stacks (DS - LeCroy Model #2375) The DS is a 256 word sequential memory for 16-bit data. There are several control signals that are crucial for the trigger looping scheme discussed below.

There is a Write Pointer (WP) which points to the next available address, and a Read Pointer (RP) which points to the next *unread* word. A write cycle is started when the DS receives a Write Enable (WE) signal. At this time the word present at the front panel input is written into the memory location given by WP, and WP is incremented. A read cycle is started when the DS receives a Read Enable (RE) signal. At this time the word at the memory location given by RP is presented to the front panel, RP is incremented and a Read Ready (RR) signal is issued. The first write cycle also generates a read cycle and the resulting RR signal is the start of the trigger loop.

These two pointers are independent, which allows readout to begin before data has been completely loaded. It can also put the trigger into a condition where data readout has caught up to data loading, i.e., RP = WP. Under this condition the DS behavior is determined by the value of the All Data In (ADI) signal. If this signal is true, indicating the WP will not advance further for this event, then attempting to read at or beyond the current WP generates a Read OverFlow signal (ROF). This signal indicates that all data in the stack have been processed. If ADI is false and RP = WP, then action is delayed until one of these two conditions changes. If data is written into the stack thus advancing WP, then readout continues normally. If ADI becomes true, then a ROF signal is generated as detailed above. As discussed on page 99, a misunderstanding of ADI operation caused an error in trigger operation during the beginning of its first PID run.

Data Register (DR - LeCroy Model #2371) The DR is a 1 word 16-bit memory. The *LVL2* trigger uses two DR's. One is used in the TOFW readout synchronization loop to store the Virtual Station Number (VSN) of the current TOFW panel. The other is used in the "cluster-buster" logic to store the TOF slat number of the previous valid track.

Flip-Flop (FF - BNL custom design) This is an in-house module designed to provide a CAMAC flip-flop in ECL logic. The *LVL2* trigger uses three of these modules. One in the logic that the trigger uses to count to two. And, two (in the trigger configurations where the one-particle and two-particle triggers have been separated) to latch trigger decisions until TS interrogation at 40 μsec.

Memory Lookup Unit (MLU - LeCroy Model #2372) The Memory Lookup Unit is a computer-programmable 16-bit $\times$ 4096 word random access memory. The MLU input word requests

the memory value at that same address to be presented as output. The 2732 allows the user to trade input address space for output address space. In other words, the 16×4096 memory can be thought of as 4096 16-bit words, or 8192 8-bit words, or 16,384 4-bit words, etc. The mode in which an MLU operates is computer-controllable and known as the dimensionality, D. The number of output bits is given by 2^D.

Acronym	Meaning	
WP	Write Pointer	Data Stack
WE	Write Enable	Data Stack
RP	Read Pointer	Data Stack
RE	Read Enable	Data Stack
RR	Read Ready	Data Stack
ROF	Read Overflow	Data Stack
ADI	All Data In	Data Stack
STAT	Status Bit	Data Array
SBR	STatus Bit Ready	Data Array

Table 2.4: *LVL2* trigger signal acronyms. See text for details.

LVL2 Operation

Figure 2-23 is the complete *LVL2* electronics diagram showing how the seven crates of CAMAC modules described above were connected into the single-purpose computer we know as the *LVL2* trigger. It is difficult to get much more than the appropriate sense of awe from this diagram. A ×8 magnification color version exists for explanation purposes, but cannot be included in a thesis. Figure 2-24 is a block diagram showing the geographical locations of the different *LVL2* functions. There is an exact correspondence between figure 2-23 and figure 2-24 which can be seen if the figures are overlayed. In the rest of this section I will describe the operation of each of these functions in some detail.

Trigger Chamber Readout Data from the trigger chambers is processed by the PCOS III dedicated controller described above. Steering bits direct TR1 information into a Data Stack and the TR2 information into a Data Array. This happens much faster than the TOFW readout, digitization and sychronization. It leaves the TR1 Data Stack (DS_TR1) ready to go, its ADI is true, RP = 1 and WP = # TR1 hits.

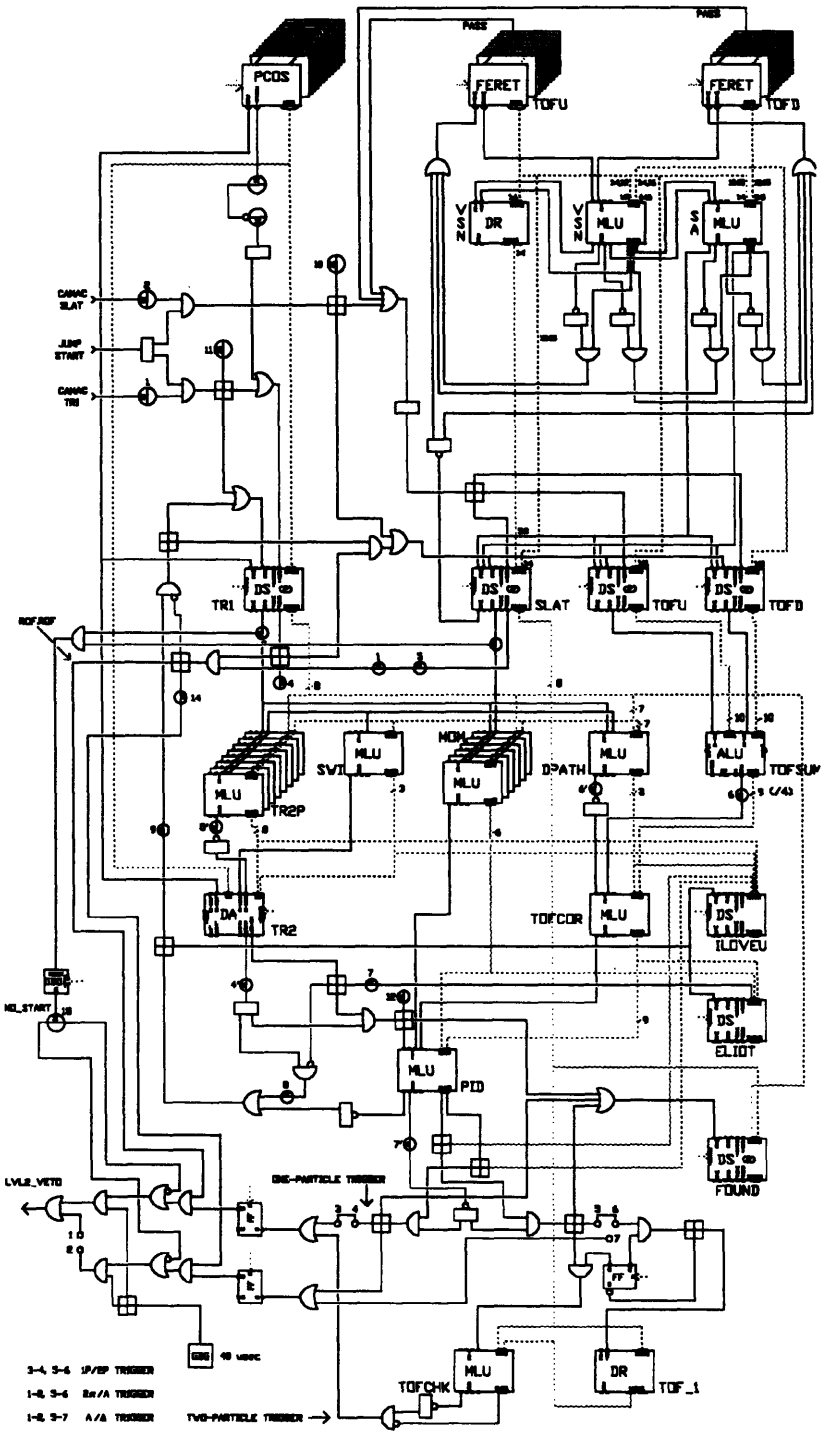

Figure 2-23: *LVL2* electronics diagram, see text for details. Courtesy of L.P. Remsberg.

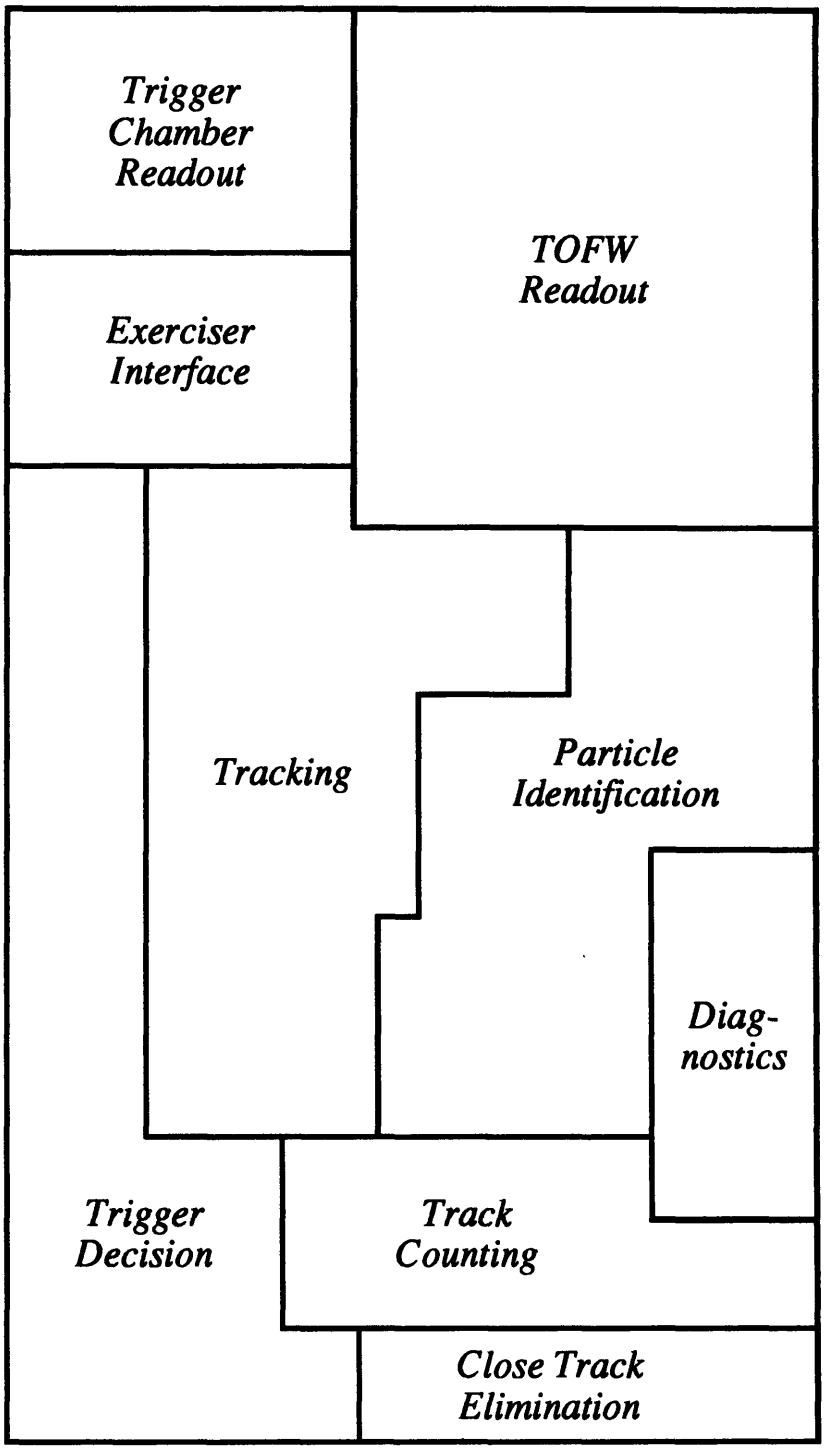

Figure 2-24: Geographical block diagram of the *LVL2* trigger electronics. Adapted from [Zajb].

TOFW Readout TOFW digitization takes $\approx 5\,\mu$sec. The TOFW is divided into ten panels with sixteen slats in each panel. Each slat is read out by two phototubes (UP and DOWN). If one of the phototubes fails to fire there will be an unmatched entry in the TOFW readout. Since we want to sum the times from the two phototubes to get the particle's time-of-flight this entry must be eliminated. To do this, synchronization logic using two MLU's (MLU_VSN and MLU_SA) and a DR (DR_VSN) has been implemented.

The UP phototubes from each panel are read out a by single FERA. The same is true for the DOWN tubes. UP and DOWN FERA's are each controlled by separate #4301 System Drivers. Each FERA unit is programmed with a Virtual Station Number (VSN - the TOFW panel number). Each FERA channel has a different Sub-Address (SA - the slat number in the panel). Thus, VSN and SA uniquely determine the slat number. MLU_VSN and MLU_SA compare the current slat numbers presented by the UP and DOWN System Drivers. If the number is the same, the slat number and the times corresponding to each phototube are loaded into three separate Data Stacks (DS_SLAT, DS_TOFU and DS_TOFD). If the slat numbers do not match, the MLU's will issue signals to increment the System Driver corresponding to the side with the extra hit. This is possible because the TOFW slats are stored in numerically ascending order. A more detailed writeup of this synchronization logic can be found in [LeC87].

The PASS signal from the last FERA indicates that all TOFW data has been read out. The logical OR of the PASS signals from the two controllers is used as the ADI input to all three TOF Data Stacks. As discussed above, ADI indicates that all data has been read into a Data Stack.

Our misunderstanding of ADI led to a trigger error for the first portion of the February 1991 run. At that point, only the DS_SLAT ADI was being used; for DS_TOFU and DS_TOFD, *ADI* was disconnected and left in its default (TRUE) state. Occasionally the tracking loop would catch up with the TOF sychronization loop (we will discuss the tracking loop in the next section). If this happened, the read cycle would be inhibited in DS_SLAT since its ADI would be correctly FALSE. But, in DS_TOFU and DS_TOFD, ADI was TRUE. So, their read pointers would be reset to zero and readout would begin with the times corresponding to the first slat. If there were more slats to process after this condition, their information would be correctly loaded into all three Data Stacks. The slat number would also be correctly loaded into the next stages of the trigger processing. But, until the next event, the slat and timing information for all slats would be mismatched. This led to a rather serious trigger bias and all PID triggered data taken before this problem was fixed were ignored.

A similar, but harmless, error went unfixed until the September 1993 run. Once again the

problem arose because the tracking loop could catch up with the TOF synchronization. Now all ADI signals were properly set and if all currently loaded slat information had been read (RP = WP), read cycles were suspended. This meant that the TOF ROF signal, which stops the loop, was also suspended. This made it possible for the trigger to execute an extra loop. This was a minor problem whose only ramification was a small worsening in the rejection factors for two-particle triggers (e.g., an event with one pion looped over twice would count as a two pion event). It did not introduce any trigger bias. The solution to this problem was to postpone the start of the trigger processing until all of the slat information was read out of the synchronization loop. This was achieved by adding the ADI signal into the RE input for the three TOF Data Stacks.

This solution was a byproduct of our attempts to fix the last known remaining trigger problem. This problem is more serious because it may introduce a trigger bias, but it affects only a very small portion ($\approx 1/2\%$) of the events. I will personally give a gold star to the person who figures out what is causing this problem. The symptom of the problem is that a slat, along with its TOFU and TOFD times, will be loaded into the TOF Data Stacks twice and the following slat and times will be skipped over. The result of this problem may be only an effective TOFW inefficiency which would not represent any bias. But, since the origin of the problem is unknown, it is difficult to be sure that there is no bias.

Tracking and PID The trigger is essentially a hardware implementation of a nested do-loop. It is much easier to combine the discussions of tracking and PID since both sections of the trigger are processed in parallel and use many of the same control signals.

DS_TR1 and DA_TR2 are loaded several microseconds before the slat Data Stacks. DS_TR1 therefore has ADI set to TRUE. The first write cycle initiates the first read cycle, placing the eight-bit TR1 wire number on the DS_TR1 front panel and setting DS_TR1 RR to TRUE. The trigger is poised, eagerly awaiting the first slat write cycle. At that time the first read cycle is also performed, the eight-bit TOFW slat number is presented on the DS_SLAT front panel and DS_SLAT RR is set to TRUE. This starts the trigger loop since the logical AND of these two RR signals form the Input Enable (IE) signal for several MLU's:

MLU_TR2P - The input TR1 and TOF positions define a straight line, and MLU_TR2P returns the number of the TR2 wire that lies on that line. TR1-TOF combinations that form a track outside of the spectrometer return a non-physical TR2 wire number. The eight-bit DS_TR1 and DS_SLAT outputs are combined into one sixteen-bit input address. This requires the MLU's to operate in dimensionality, $D = 0$, rendering them capable of returning only one

bit of output. Since we need eight bits to identify a wire number MLU_TR2P is made up of eight separate MLU's that each predict one bit of the wire number.

MLU_MOM - Assuming that a track originates at the target and undergoes no y-displacement, its momentum is defined by its TR1 wire and TOFW slat. There are five output bits for the magnitude of the momentum giving a momentum resolution of $dp = 3\% \times p_{max}$. A sixth output bit gives the track's sign. These MLU's also operate at $D = 0$, so six MLU's are required for the six bits of information.

MLU_SWI - This MLU gives us the capability of having a slat-dependent search width (SWI) around the predicted value of TR2. This is needed because the TOFW has slats of two different widths. Since only the TOFW slat number (8-bits) is needed as input, MLU_SWI was operated at $D = 4$, allowing all three bits to be returned by one unit (along with 13 unused bits).

MLU_DPATH - With the same assumptions used in MLU_MOM (known track origin and no y-displacement) a track's TR1 wire and TOFW slat will uniquely determine its pathlength in the spectrometer. This MLU returns the difference between the calculated pathlength and the minimum pathlength (L $\approx$ 660 cm). With three output bits, the pathlength difference can be determined to only 12.5%. But, the maximum pathlength difference is only $\approx$ 10% of the total pathlength, so $\delta L/L \leq 1.25\%$. The pathlength for adjacent wires and slats is so similar that the least significant bit of the TR1 wire number and TOFW slat number were removed from the MLU_DPATH input. With only fourteen input bits, MLU_DPATH could be operated at $D = 2$ which produces four output bits, of three were used.

MLU_TR2P and MLU_SWI strobe their outputs into DA_TR2 to look for a TR2 wire within the search width of the predicted TR2 wire. The output of DA_TR2 includes a STAT signal (set to TRUE if the wire is found) and Status Bit Ready (SBR), (set to TRUE when STAT is valid). If STAT is FALSE, then processing for that track is finished. If STAT is TRUE, then MLU_PID needs to be checked.

The track's velocity is being calculated in parallel with the above MLU operations and the TR2 verification. The first step is to calculate the track's TOF with ALU_TOFSUM according to TOF = (TOFU + TOFD)/4. We divide by four (instead of two) because the extra accuracy of the last bit is unnecessary. The (integer!) division is accomplished simply by leaving the two lowest significance output bits unconnected. The output of MLU_DPATH and ALU_TOFSUM serve as input to MLU_TOFCOR which, despite its name, calculates the track's velocity. This

table must be programmed with a timing offset that will allow it to correctly translate FERA channels to a physical flight time, see section 3.1.3. We use nine bits of the MLU_TOFCOR output.

The output of MLU_TOFCOR and MLU_MOM are the input for MLU_PID which is interrogated for every valid track. This MLU is operated at $D = 1$, providing two bits of output. These two bits can usually be interpreted as "one-particle" and "two-particle" bits. To set up a one-particle trigger, define the desired valid PID region in momentum and mass. Set the MLU_PID value at the corresponding address to one. All particles in the defined window will produce an MLU_PID output of one which latches the *LVL2* veto FALSE. To set up a two-particle trigger, define the desired valid PID region in momentum and mass. Set the MLU_PID value at the corresponding address to two. All particles in the defined window will produce an MLU_PID output of two. This signal enters the counting logic which will latch the *LVL2* veto false if it counts two valid tracks. Note that the trigger can be configured to accept one-particle triggers, two-particle triggers, and logical combinations of one and two particle triggers. If we are willing to make a few hardware modifications, we can even demand two different single particles (in a logical AND or OR).

The *LOOP-KICK* signal is formed as the logical OR of $\overline{\text{STAT}} \wedge \text{SBR}$ (from DA_TR2, TRUE for invalid tracks) and the Output-Ready signal from MLU_PID (only TRUE for valid tracks). This signal pushes the trigger processing to completion. It does this by initiating read cycles on DS_TR1 and DS_SLAT (by firing their RE inputs) after each combination finishes its processing. Note that TR1 is the inner loop. This is enforced in hardware by the presence of the DS_TR1 ROF signal as a logical AND in the DS_SLAT RE input signal. This blocks the RE input until DS_TR1 has completed reading out its data. When DS_TR1 has completed readout, its ROF comes true and its RP is reset. When LOOP-KICK comes the next time, DS_TR1 readout begins again with the first TR1 wire and DS_SLAT is incremented to the next TOFW slat. When DS_SLAT is finished processing its ROF signal is forced true. The logical AND of the two stack's ROF signals (ROF $\wedge$ ROF)[9] stops *LOOP-KICK*, indicating the completion of trigger processing.

Counting and Busting Counting and Busting only occur for two-particle triggers. The counting logic simply adds to two, while the BUST logic makes sure that the two particles come from different slats. This reduces the amount of background accepted by the trigger. This does not introduce any bias since slats that are hit twice will have erroneous timing information

[9]You are pronouncing this right if you sound like a dog.

and will not be used in offline analysis.

The heart of the counting logic is a simple Flip-Flop. The Flip-Flop is initialized with Q = FALSE and $\bar{Q}$ (necessarily) = TRUE. The MLU_PID two-particle trigger output bit is logically AND'ed with both Q and $\bar{Q}$. The AND of the first particle to satisfy the two-particle trigger condition with $\bar{Q}$ will be TRUE. This signal strobes the Flip-Flop so that Q is now TRUE and $\bar{Q}$ is (again, necessarily) FALSE. This signal also strobes the track's TOFW slat into a Data Register for use in the BUST circuitry. The AND of any other particles that satisfy the two-particle trigger condition with Q will be TRUE. This signal strobes the Input Enable of MLU_TOFCHK with a sixteen-bit input address made up of the current track's TOFW slat number and the TOFW slat number stored in the DR for the first PIDed track. If the TOFW slat numbers are not identical, the trigger has been satisfied.

Diagnostics There are three diagnostic Data Stacks that store information useful for debugging the trigger. DS_FOUND stores the wire and slat numbers of TR1-TOF combinations that formed valid tracks. These combinations are strobed in a second time if they satisfy the PID cuts. DS_ILOVEU[10] and DS_ELIOT[10]are strobed by LOOP-KICK, and thus store information from *every* combination. Table 2.5 shows the bit representation of the stored information.

Data Stack	Bits	Information
DS_ILOVEU	0-8	MLU_TOFCOR Output Word
	9-14	MLU_MOM Output Word
	15	DA_TR2 STAT
DS_ELIOT	0-7	MLU_TR2P Output Word
	8-10	MLU_SWI Output Word
	11-13	MLU_DPATH Output Word
	14-15	MLU_PID Output Word

Table 2.5: Information stored in the *LVL2* diagnostic Data Stacks.

[10]These are sound gags, say the names out loud.

Chapter 3

Collaboration Software

A tremendous amount of software needs to be written in order to make an experiment the size of E859 work. In this section I will briefly describe the aspects of this software which are vital to *any* analysis of data from the E859 spectrometer. Many of the software tools used by E859 were developed at CERN and by the CDF collaboration at Fermilab. The experiment uses both YBOS [Qua89] and ZEBRA [ZEB92] data structures. All collaboration standard code is written using a program shell known as ANALYSIS CONTROL [SQ87]. This shell provides a convenient way to combine code for several different detectors into one executable. Many important items are stored in several databases based on the VAX relational database (RDB) utility [RDB87].

The original software design for the experiment called for three analysis *passes*. All detector calibrations were to be performed as a part of PASS1. More complicated analyses, primarily track reconstruction, were to be performed as a part of PASS2. PASS3 was to consist of particle identification. In truth, these tasks have become scrambled over the years. Many of the calibration procedures need to be performed in two stages interrupted by human intervention, thus PASS0 was born. PASS1 and PASS2 were subsequently combined into PASS12.[1] PID and TOFW recalibration are both performed in PASS3.

As a result of this tangle, I find it easier to present this section as a series of program chains, each addressing a specific problem. I will first discuss the software necessary to test and implement the *LVL2* trigger. Next, I will describe the procedures needed to calibrate all critical detector systems. Next, I will describe the algorithms used to reconstruct tracks and

[1]New students may not yet appreciate how amused elder graduate students were when the author naively asked what functions were performed in "pass-twelve."

perform particle identification. Finally, I will detail the software that creates the framework for all experimental Monte Carlo calculations.

3.1 *LVL2* Software

Operation and testing of the *LVL2* trigger required a large and varied amount of software. A MicroVAX 3400, known as BNL859, served as the host computer. Communication with the *LVL2* CAMAC modules was achieved with a Q-Bus interface daisy-chained between five KineticSystems 2922 CAMAC crate controllers.

The remainder of this section describes the software written to perform the following tasks:

- *Storage of* LVL2 *configurations in a run-keyed database* - This database is extensively used for offline trigger bias studies.

- *Lookup table generation* - This program chain translates the desired physics goals (e.g., $2K^+$, $\vec{B}$= 4A) into the memory values of the nine different MLUs.

- *TOFW calibration* - This program chain calculated the FERA pedestal values which, when combined with a global offset, would return the proper flight time.

- *Communication of BNL859 with the E859 data acquisition computer (BNL802)* - These routines coordinated the start of a run with initialization of the trigger and storage of the trigger configuration in the *LVL2* database.

- *Trigger control* - This includes routines to load the lookup tables into the MLU units and routines to set the operational state of all trigger modules.

- *Trigger "exercising"* - These are programs which initiate the looping action of the trigger with known inputs. The trigger output can then be compared to expected values. These routines also allow oscilloscope diagnosis of any trigger hardware problem.

- *Online Monitoring* - This program allows immediate diagnosis of a variety of known *LVL2* failure modes.

- *Trigger Emulation* - This program will reproduce trigger response in software given TR1/2 and TOFW input and a *LVL2* configuration.

3.1.1 INTER

Before discussing each of these different software tasks the INTER program needs to be introduced. This program was written by many people, and more details can be found in [Mor94, Mor91]. This program is based on the same KUIP interface as PAW. Many of the functions described below are available as simple INTER commands. These commands may take user-input parameters and have full documentation online thanks to KUIP's menu-driven help capability.

3.1.2 *LVL2* Database

The *LVL2* database was designed, and access routines written by Dave Morrison. It is based on the ZEBRA memory manager [ZEB92] augmented with generalized database manipulation routines written by Brian Cole. The database stores a configuration keyed by the run number. A configuration consists of the MLU contents, the FERA pedestals and the hardware map which translates each CAMAC module into a crate and slot number. All interaction with the database is achieved through the INTER program. For a more detailed writeup, see [Mor91].

3.1.3 Lookup Table Generation

The nine different *LVL2* lookup tables can be divided into two broad categories. MLU_TR2P, MLU_MOM, MLU_DPATH, MLU_TOFCOR[2] and MLU_PID depend on the magnet setting (field and polarity); MLU_VSN, MLU_SA, MLU_SWI, MLU_TOFCHK do not.

Generation of tables that depend on the magnetic setting is a rather complicated process. In the first stage a Monte Carlo simulation is performed. In this simulation, particles are tested for acceptance in the spectrometer. All physics processes (energy loss, multiple scattering, etc.) are ignored. The TR1/2 wires, TOFW slats, momentum and pathlength of all particles in the acceptance are written to unformatted files known as *data files*.

In the next step the data files are read and average values of TR2 wire number, pathlength and momentum are calculated for each TR1-TOFW combination. The momentum and pathlength are then binned. For the pathlength, L, we can calculate the bin size, ΔL:

$$\Delta L = \frac{L - L_{min}}{(L_{max} - L_{min})/N_L}, \tag{3.1}$$

where L_{min} and L_{max} are user-inputs, and $N_L = 8$ since there are three MLU_DPATH output

[2]MLU_TOFCOR depends on the magnet setting only indirectly through its MLU_DPATH input.

bits. This process is slightly more complicated for momentum because of the optional presence of an overflow bin. Momentum is binned according to:

$$\Delta p = \begin{cases} \frac{p-p_{min}}{(p_{pidmax}-p_{min})/N_p} & p_{min} < p < p_{pidmax} = p_{max} \\ \frac{p-p_{min}}{(p_{pidmax}-p_{min})/(N_p-1)} & p_{min} < p < p_{pidmax} < p_{max} \\ 32 & p_{min} < p_{pidmax} < p < p_{max} \text{ (the overflow bin)} \end{cases} \tag{3.2}$$

p_{min}, p_{max} and p_{pidmax} are user-inputs, and $N_p = 32$ since there are five MLU_MOM output bits (the sixth output bit indicates the charge of the combination and is ignored in this discussion). The value of p_{pidmax} controls the size of the overflow bin.

The binned values of β are generated by looping over the binned pathlength and the possible TOFSUM values. The user must enter the global timing offset whose value gives physical flight times.

The *analog* mass corresponding to each momentum and β bin is looped over to make the PID physics table. PID cuts are imposed at the next stage, when the data is put into bit patterns that can be used as MLU input. PID cuts are made at the INTER command line. Current possibilities include momentum cuts, mass cuts and β cuts. There is also an option available to call a user-written routine which will make any cuts desired. In practice, only momentum and mass cuts were used.

The final step in lookup table generation is parsing the physics tables into bit patterns suitable as MLU input. Although a menial task, this was not always trivial. Recall that the MLUs have a programmable dimensionality which determines how its 4096 × 16-bit memory is divided between input address space and the number of output bits. Most of our MLUs operate in dimensionality, $D = 0$ which takes a 16-bit input address and presents 1-bit of output. Unfortunately, the MLUs need to be programmed in dimensionality, $D = 4$, with 16-bit memory values.

The easiest way that I find to discuss the programming of an MLU is to turn the problem around and discuss which portion of the MLU memory a given input word will address. For this discussion it will help to refer to figure 3-1. Consider the general case with arbitrary D. The lower 12 bits of the input address are called the RAM address ($RAM \in [0, 4095]$). The upper 4 bits are called the *nibble*[3] ($nibble \in [0, 2^{4-D} - 1]$). The number of bits in the output word (the region of the MLU memory being addressed) is given by $S = 2^D$. *RAM* determines

[3]Short for "half-byte", I am not making this up.

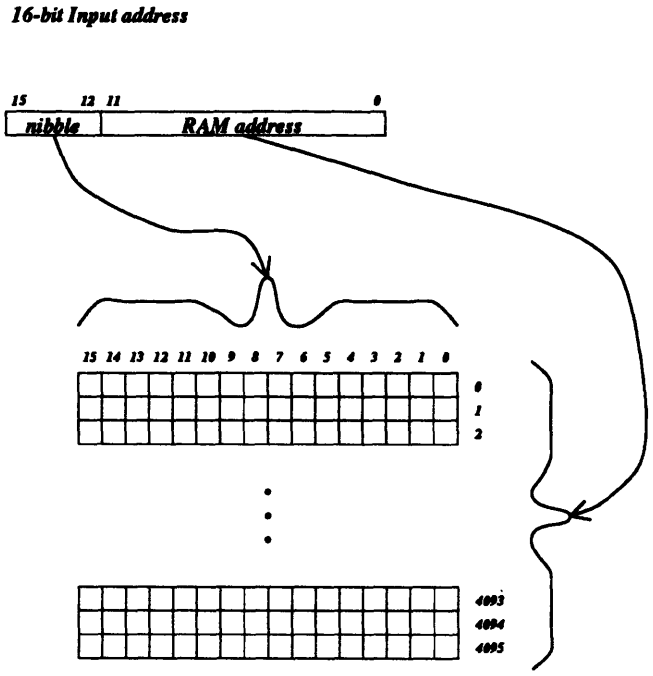

Figure 3-1: Illustration of MLU interrogation. The lower 12 bits of the input address determine the column being interrogated. The upper 4 bits (nibble) and the MLU dimensionality determine the row being interrogated. See text for details.

which of the MLU's 4096 16-bit words is being addressed, *nibble* points to the first bit of output word that is being addressed, $B = S \times$ *nibble*. Thus, for $D = 0$, the output word is always 1 bit long, and the position of this bit is given by the *nibble*. Similarly, for $D = 4$, the output word is 16 bits and the first bit is always 0.

This process needs to be reversed when calculating the memory value with which to program the MLU memory. So, for $D = 0$, sixteen different input addresses are combined to form one MLU address value. For MLU_TR2P and MLU_MOM several MLUs each contain one bit of the output and things get even more complicated.

3.1.4 *LVL2* TOFW Calibration

In calibrating the LVL2 TOFW timing, there were only two variables we could adjust; a global timing offset, T_0^{global} and the FERA pedestal values for each TOFW slat. T_0^{global} needed to be properly accounted for in MLU_TOFCOR so that its values could be properly mapped into physical flight times. The FERA pedestal values are effectively an offset for each slat, and are automatically subtracted before the FERA values were loaded into the data stacks, see page 99.

The method for calibrating these constants was developed by Hiro Sakurai and Ole Vossnack. The FERA pedestal values were initially set to be 128, the exact center of their dynamic range. Several runs were taken with both magnet polarities so that there would be negative tracks illuminating both sides of the TOFW. Negative particles were assumed to be π^-'s (< 5% contamination) from which a value for T_0^{global} could be obtained. With T_0^{global} fixed, initial FERA pedestal values could be obtained. The process was then iterated by using these calibrated FERA pedestals to identify π^+'s which doubled the statistical accuracy of the FERA pedestal values.

During the course of the run the timing calibrations were checked with the online monitor, see section 3.1.8. Calibrations could be maintained within the 50 psec FERET channel width for every slat.

3.1.5 BNL802 and BNL859 Communication

Communication between E859's two computers is achieved through a set of four command files run on BNL802 that use the VMS *remote task* feature. Each command file performs one of the following tasks [Mora]:

1. Initialize the MLU contents.

2. Wait for indication that item #1 has finished.

3. Record *LVL2* trigger configuration in the *LVL2* database.

4. Verify the MLU contents and put all modules into run mode.

3.1.6 Trigger Control

It is important to be able to easily control the state of the trigger, where the state of the trigger is defined by:

- Which of the two mutually exclusive modes the *LVL2* CAMAC modules are in. The first, in which computer communication along the CAMAC dataway is possible, is used to configure the trigger and for debugging. The second, in which intermodule communication across the ECLbus is possible, is used to collect data.
- The MLU dimensionalities.
- The MLU memory values.
- The FERA pedestal values.

Subroutines, callable as INTER commands, exist to control each of these items.

3.1.7 Trigger Exercisers

The *LVL2* trigger was designed to be data-driven. However, it needed to be tested without wasting expensive beam. For this purpose, several programs were written which load the trigger with fake data and use a computer-generated *JUMP-START* signal to begin the trigger processing. These programs start the trigger at different points in its processing and are used in a binary-search manner to diagnose hardware malfunctions.[4]

The exercisers could be run in two modes. In the first mode, some output of the trigger processing could be compared to expected values. This was usually the first thing tested. If there were inconsistencies, the exercisers could be run in an infinite loop mode in which *JUMP-START* is continuously strobed. This mode allows us to trace the trigger logic signals with an oscilloscope.

All of the different exercisers are written up in great detail in [Sol91], but I will mention each of the important ones:

[4]For example, the cabling to the flip-flop at the heart of the trigger might get pulled out by errant signal cables attached to an oscilloscope needed by an overeager graduate student.

- *camac_loop_test* - This is the most primitive of all of the exercisers. Fake data is loaded directly into DS_TR1, DS_TOF, and DA_TR2 and the trigger loop is initiated. The DS_FOUND output is checked to make sure the correct tracks are found. This program does not load sensible timing values, so the PID portion of the trigger cannot be checked.

- *pcos_loop_test* - This exerciser goes one step beyond *camac_loop_test* by loading the trigger chamber information directly into the PCOS 2731a latch modules before initiating trigger processing. After this stage it is identical to *camac_loop_test*.

- *mondo_loop_test* - This exerciser loads TOFW information into the FERAs and so tests the entire TOFW loading and synchronization portions of the trigger logic. Unfortunately it is not possible to load a test bit pattern into the FERAs. Instead, we have to disconnect the FERA input cables from the TOFW discriminators and strobe them directly. This precludes loading physical times into DS_TOFU and DS_TOFD and so this loop also fails to check the PID portion of the loop.

- *pid_loop_test* - As its name suggests, this exerciser was designed to test the PID portion of the loop. The user is prompted for the minimum number of one-particle PID tracks, two-particle PID tracks, non-PID tracks and non-track combinations with which s/he would like to load the trigger. The program loads the current *LVL2* configuration into memory and *randomly* selects hit and timing information that will give the starting conditions requested by the user.[5] After the trigger completes its loop, the trigger emulator program is run, see section 3.1.9. Diagnostic output from every MLU for every combination is compared to the same output from a software version of the trigger.

3.1.8 *LVL2* Monitor

A comprehensive online monitor program was vital to trigger maintenance throughout the run. A VMS remote task was used to automatically write a small fraction of a run's events to a disk using the DAQ's event pool feature. Once this file was closed, this same remote task submitted a command file to run the *LVL2* monitor program.

This program filled many diagnostic histograms, usually histograms that highlighted some problem discovered during the developmental stage. Once the trigger was working, most of

[5]The randomization turned out to be important when it helped us find some combinations that were susceptible to subtle timing problems. These timing problems resulted from the fact that the tracking loop finishes in a different amount of time depending on whether a track is found or not.

these histograms were not needed. They are still all filled, but almost none of them are examined for every run. The histograms that are examined every run include:

- TR1/2 and TOFW distributions which show any dead elements.
- A series of different timing histograms which are used to maintain excellent TOF calibrations.

3.1.9 Trigger Emulation

The trigger emulator program was written to perform a software version of all the trigger's functions given TR1/2 and TOFW input as well as a trigger configuration. This program first accesses the *LVL2* database and reads the requested MLU tables into memory. It then performs the nested loop over TR1 wires and TOFW slats. Checks are made on valid tracks and valid PID. There is logic to count to two, keeping track of the requested busting scheme. The trigger decision is then returned along with diagnostic output showing the values of every MLU for every combination.

The output of this program can be used to make sure the trigger is working, see section 3.1.7. This information can also be used with veto-out runs to perform bias studies and rejection factor studies.

3.2 Beam Counter Calibration

Like the TOFW, BTOT and BTOF have both ADC and TDC information.

There are no calibrations that need to be applied to the TDC information. All valid beam particles must pass the beam species charge cut and so have a well defined energy deposition in the beam counter scintillators. For this reason, there is no need for a slewing correction. Since the BTOF signal defines the experimental start time, any drift in the TDC clock value will result in a global offset, T_0^{global}, see section 3.6.3.

To calibrate the ADC values, a Gaussian is fit to the $\Delta E = \sqrt{ADC_1 \cdot ADC_2}$ distribution in a window around the peak and the fit parameters are stored in the calibration database. This is an improvement over the old method in which $\langle \Delta E \rangle$ and $\langle \Delta E^2 \rangle$ were calculated in a similar window around the peak. The old method was more sensitive to the two-particle peak that became prominent with the high beam intensities of E859. For each run the ADC's on a given scintillator are gain-matched and an overall gain is calculated such that $\langle \Delta E \rangle = Z_{beam}$. The relationship $\Delta E = C Z_{beam}^{1.56}$ was determined empirically [Bea] and is used to extract the

effective charge. Offline cuts are made on the value of this charge to eliminate events with two beam particles in the BTOF ADC time window, see section 4.2.1.

3.3 TMA Calibration

For a much more detailed writeup of the TMA calibration procedure, please see [Abb90].

The first job of the TMA calibration procedure is to remove three different types of problematic TMA elements from consideration in further analysis:

1. *Dead Pads* - These are pads that register a small number of hits compared to their neighboring pads. Dead pads were always due to faulty readout circuit boards.
2. *Hot Pads* - These are pads that register a large number of hits compared to their neighboring pads. Hot pads were also always due to faulty readout circuit boards.
3. *Defective Panels* - These are panels for which every pad is registering an anomalously large number of hits on many events. Defective panels resulted from grounding problems in the TMA module itself.

In order to identify such problems, the TMA PASS0 module fills two histograms for every panel:

1. counts vs pad.
2. events vs n_{pad}/event.

These histograms are individually examined and the problematic elements are stored in the E859 calibration database.

The next job of the TMA calibration procedure is to calculate the number of charged tracks that actually hit the functioning TMA pads. This is not as simple as counting the number of struck pads because a single particle can fire multiple pads, and a single pad can be struck by multiple particles. Since there is no energy loss information recorded for the TMA, there is no way to decide between the different scenarios. The following accounting scheme was chosen based on information obtained from Monte Carlo simulations and developmental studies:

1. Group all adjacent pads into clusters where the size, N, is given by the number of pads in the cluster.
2. Assign a multiplicity to each cluster according to $M = \mathrm{INT}((N+1)/2)$.

Finally, for intermittency analyses, the locations of the hits need to be randomly distributed over the area of their clusters.

3.4 Henry Higgins Calibration

The magnetic field was mapped in an $x-z$ grid on the y-midplane. A Taylor expansion technique was used to extrapolate the field to all locations inside the magnetic field region. Current fluctuations in the magnet coils were observed to be less than 0.2%. Integrated field errors arising from the extrapolation procedure are estimated to less than 1.5% everywhere and less than 0.6% away from the edges of the field gap. See [Vut88] for details on this entire procedure. For this analysis, the field map was only used to generate Monte Carlo data, see section 3.9. The reconstruction code used an effective-edge approximation for the integrated field and a thin-lens vertical focussing approximation to account for fringe fields, see section 3.7.3.

3.5 Drift Chamber Calibration

There are two critical tasks in the drift chamber calibrations. First, we need to locate the wires to a distance $d < 50\mu$m. Second, we need to find the drift-time to drift-distance relationship.

3.5.1 Georgeometry

Ideally, wire locations would not be a property of the data, rather they would be measured. In fact initial wire locations are determined by surveying the vector between a fixed reference point and a point on a chamber mount. The chamber blueprints are then used to find the vector between the measured point and the wires. This method has been plagued with difficulties arising from surveying errors and chamber machining errors. Even if these difficulties were solved, one set of surveyed geometry constants would not be sufficient due to slight distortions of the spectrometer platform upon rotation.

For these reasons a set of programs were written by George Stephans that use reconstructed tracks to fine-tune the wire locations.[6] Detailed writeups can be found in [Ste90, Ste91]. All of these programs require data to be taken with Henry Higgins turned off.[7] The programs are run in a definite sequence, starting with gross chamber changes and ending with modifications of individual wire locations:

- The first step is to find the xyz-location of the chamber centers. A vector is fit to all of the

[6] Obviously the original wire locations must be good enough to reconstruct tracks.
[7] Having tracks point in straight lines makes things *much* simpler.

x-hits used by a reconstructed track and vectors to T1T2 and T3T4 x-hits independently. A profile histogram is made of the difference between the T1T2X vector and the full vector as a function of the track's x-slope. A straight line is fit through this distribution. The offset of this line gives the error in the relative x-separation of the chambers. The same procedure is used to find the error in the relative y-separation of the chambers. The uncertainty-weighted slopes of these two lines determines the error in the z-separation of the chamber.[8] It is impossible to determine from this data which of the chambers is in error, so each chamber is adjusted by half of the positioning error. This procedure is repeated for T3T4.

- The next step is to find positioning and angular offsets for individual planes. One profile histogram is generated for each plane. This histogram contains track residuals as a function of the distance along the wire from the midpoint of the wire, summed over every wire on the plane. A straight line is fit to this distribution. The slope of this line determines the average angle of this wire plane, and the intercept determines the positioning offset of this plane.

- The third step is to adjust the z-locations of individual planes. One profile histogram is generated for each plane. This histogram contains track residuals as a function of the angle relative to the mean track angle of the given wire, summed over every wire on the plane. A straight line is fit to this distribution. The intercept should be zero because of the previous step. The slope gives the z-offset. Note that in front of the magnet the wire spacing and the plane separation are completely ambiguous. For this reason, T1 and T2 have their wire spacing adjusted instead of their plane separation.

- The final step is to fit the angular and positional offsets of every wire. A profile histogram is generated for every wire. This histogram contains track residuals as a function of the distance along the wire from the midpoint of the wire. A straight line is fit to this distribution. As in the second step, the slope of this line determines the angle of this wire, and the intercept determines its positioning offset.

3.5.2 Timing

The drift-time to drift-distance relationship is obtained for every drift chamber plane. Tracks are reconstructed and the hits used on every plane are recorded. The tracks are

[8] In practice, the x-slope dominates the z-position determination since the larger x lever arm allows it to be determined better than the y slope.

projected to each plane and the lead distance, L_{lead}, is recorded. The formula for the lead-time, T_{lead}, of a hit is given by:

$$T_{TDC} = T_{lead} + T_{transit}, \tag{3.3}$$

where T_{TDC} is the time recorded by the driftchamber TDC and $T_{transit}$ can be obtained from:

$$\frac{T_{TOFW}}{L_{TOFW}} = \frac{T_{transit}}{L_{transit}} \tag{3.4a}$$

$$\Rightarrow \frac{T_{TOFW}}{Z_{TOFW}} \approx \frac{T_{transit}}{Z_{transit}}. \tag{3.4b}$$

Once a track is reconstructed we know T_{TOFW}, and therefore $T_{transit}$. A profile histogram of T_{lead} vs L_{lead} is generated and fit with a third-order polynomial. This procedure was developed by Dave Morrison.

Before tracks are reconstructed, we only know the sum, $T_{lead} + T_{transit}$. When storing T_{lead} for drift chamber hits, we have chosen to assume that the particles causing the hits are traveling at $\beta = 1$, and thus minimizing the value of T_{lead}. AUSCON begins track reconstruction with a TOFW hit, and thus each hit that it tries to collect into a track can be adjusted according to the value of $T_{transit}$ calculated from equation 3.3. This transit-time correction can be as large as 2 mm for slow protons in T4. The correction is not made until the TOFW is calibrated since poor calibrations can make it wildly wrong.

3.6 TOFW Calibrations

The main purpose of the TOFW is to provide particle identification. The TOFW has both ADCs and TDCs that need to be calibrated in order to make the data usable for PID. The TDCs provide the primary PID information, the TOF. The ADCs provide energy loss information that is used to determine a particle's charge. Even more critically, this energy loss information is used to determine the slewing correction to the measured TOF. Section 3.6.1 outlines the procedure that was used to determine the data sets used to calibrate the TOFW. Section 3.6.2 details the calibration of the TOFW ADCs. Section 3.6.3 briefly presents the new timing calibration procedure adopted by E859.

3.6.1 Calibration Sets

Changes to the TOFW calibrations can be divided into two categories:

1. Global timing shifts which effect the entire TOFW uniformly.

2. Local timing shifts which effect individual slats.

Global timing shifts can be accounted for by a single timing parameter, T_0^{shift}. This parameter can be determined from the data in a small fraction of a run. Because of this, T_0^{shift} is calculated for every run immediately before PASS3. Each slat needs three parameters to account for local timing shifts:

- T_0^{slat} is used to account for an overall shift in each slat's mean time-of-flight.
- C_{slew} corrects for the pulse-height timing dependence discussed in section 3.6.4.
- C_{clock} is needed because the TDC's have slightly different time-to-charge conversion factors.

Calibration sets consist of $5 - 10$ runs that are combined in order to obtain enough statistics to accurately determine all 480 of these local timing parameters.

Care needs to be taken to optimize the runs that are grouped together into a calibration data set. Not every run needs to have the local timing parameters calibrated. More importantly, the runs need to be carefully chosen so that they do not overlap any condition known to result in a global timing shift. The calibration procedure would be forced to absorb such a shift into the local timing parameters it calculates. Because of this, calibration sets were chosen such that they did not overlap the following conditions:

- Changes in the spectrometer angles.
- Changes in TOFW pedestal values.
- Changes to BTOF scintillator or discriminator threshold.
- Long elapsed *times* between calibration sets. This includes long periods of stable running and long AGS downtimes.

In addition to this, if it was not possible to include runs from both magnet polarities, then as soon as the magnet polarity changed, the TOFW was recalibrated.

PASS3 monitor output was used to judge the accuracy of the calibrations. One calibration set was found to overlap a timing shift of 50 psec on one TOF panel. The runs comprising that calibration data set were changed such that they no longer overlapped the shift. The local timing parameters were recalculated and PASS3 was rerun.

Ron Soltz was responsible for the calibration set selection. For more information on the selection criteria and on the contents of the calibration sets, the reader is directed to [Sol93].

3.6.2 ADC Calibration

A particle crossing a TOFW slat deposits energy which excites photon emission in the scintillator material. Half of the energy propagates towards the phototube at the top of the slat and the other half propagates toward the bottom of the slat. The energy is exponentially attenuated as it propagates along the slat. Therefore, the ADC values can be represented as:

$$ADC_{up} = gain_{up}\left(\frac{\Delta E}{2}\right)\exp\left(-\left(\frac{L/2-y}{L_{att}}\right)\right), \tag{3.5a}$$

$$ADC_{down} = gain_{down}\left(\frac{\Delta E}{2}\right)\exp\left(-\left(\frac{L/2+y}{L_{att}}\right)\right). \tag{3.5b}$$

This leads to the following equation for ΔE in terms of the two ADC values:

$$\Delta E = \frac{2\exp\left(\frac{L}{L_{att}}\right)}{\sqrt{gain_{up}gain_{down}}}\sqrt{ADC_{up}\cdot ADC_{down}} \tag{3.6a}$$

$$\equiv gain\cdot\sqrt{ADC_{up}\cdot ADC_{down}} \tag{3.6b}$$

Minimum ionizing particles deposit $E_{min} \approx 3.2\,\text{MeV}$ in a TOFW slat and show a clear peak in this distribution. The ADC calibration consists of adjusting *gain* such that the minimum ionizing peak of the ΔE distribution is $E_{min} = 100$. The units of calibrated energy loss are known as "Yasuo Units," named after the first master of the TOFW.

3.6.3 Timing Calibration (PIDTCAL)

The equation for a particle's time-of-flight, in terms of known quantities and constants that need to be determined, is given by:

$$T_{obs} = T_0^{shift} + T_{slew}\cdot\left(\sqrt{\frac{1}{E_i}} - \sqrt{\frac{1}{E_{min}}}\right) + T_{clock}\cdot\left(TDC + T_0^{slat}\right) \tag{3.7}$$

The collaboration has long realized that TOFW timing calibration and track reconstruction are necessarily iterative procedures. Tracks need to be reconstructed before the TOFW timing can be calibrated. Even with very rough calibrations, $\beta \approx 1$ particles can be identified. These particles are assumed to be pions and calibration constants are obtained. Once the TOFW is calibrated, the momentum resolution and efficiency of reconstruction algorithms are greatly improved since transit-time corrections can then be made and the TOFW y-position can then be used.

The fact that TOFW timing calibration and PID are similarly iterative procedures was fully

appreciated only recently. The initial TOFW calibration procedure, using only $\beta \approx 1$ particles, can determine T_0^{slat} and T_0^{shift} fairly well since there is fairly little contamination by non-pions. But, all of the $\beta \approx 1$ pions arrive within a fairly narrow (≈ 2 nsec) time window, making it difficult to determine T_{clock}. In fact, in the initial procedure, T_{clock} was fixed at the specification value of 50 psec/channel.[9] T_{slew} is also not well determined in the initial calibration because the $\beta \approx 1$ pions are minimum ionizing particles and therefore do not cover a wide energy loss range. Once initial TOFW timing constants are obtained however, PID can be performed. This makes it possible to use all particle species in a second calibration iteration.

In E802 there never was a collaboration standard PID analysis pass (PASS3), and any TOFW calibration refinement was left to individuals. E859 decided to perform a PASS3. But, before that was done, it was decided to develop a new TOFW calibration procedure that would use PID information to address the shortcomings mentioned above. Ole Vossnack was largely responsible for insisting that the recalibration be performed and for developing this new procedure, PIDTCAL. For a more detailed discussion of this procedure, the reader is directed to [Vos94].

The first step in PIDTCAL is the selection of particles that will be used from the calibration. In the selected option, PID is obtained with the collaboration standard PID algorithm, PICD, see section 3.8. All particles in unambiguous TOF regions were used.

In the initial TOF calibration procedure, T_0^{shift} and T_0^{slat} are determined by fitting Gaussians to the $T_{obs} - T_{exp}$ distributions for every slat. T_{slew} was obtained in a separate procedure in which a straight line was fit to the $T_{obs} - T_{exp}$ vs $\sqrt{\Delta E}$ distributions for every slat. There were occasions when the fitting procedure for these constants failed to converge properly; and T_{clock} was not fit at all. To avoid these problems, PIDTCAL uses a linear regression analysis to uniquely determine the correct values for all of these constants.

3.6.4 The Slewing Correction

In this section I will present a brief discussion of the slewing correction since a pulse-height dependent time-of-flight was very confusing to me at first. To get a feeling for how this works, see figure 3-2 which shows a simplified picture of the discriminator inputs for tracks with large and small energy deposit. This plot has two implicit assumptions:

1. The pulse width of the signals is independent of the energy deposited.

[9] T_{clock} can be measured, but never was.

2. The signals are linear. This assumption is not important, it just simplifies the derivation below.

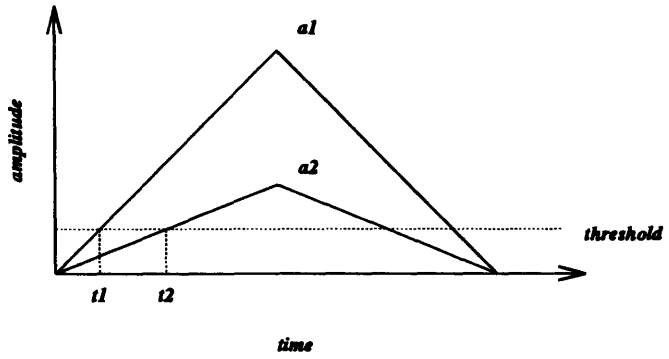

Figure 3-2: Illustration of the TOF slewing effect. See text for details.

We are interested in the particle's start time, but we measure the time at the threshold. Invoking congruent triangles, one can see that that the timing error[10] for the i^{th} particle is given by:

$$t_i = \frac{C}{a_i}, \tag{3.8a}$$

$$= \frac{C}{\sqrt{ADC_i}}, \tag{3.8b}$$

where $C = a_{thresh} t_{peak}$ is a constant for all particles and ADC is the gain-corrected ADC value. The total timing error is the sum of the errors from the up and down phototubes. So, we find:

$$\delta t \equiv \delta t_{up} + \delta t_{down}, \tag{3.9a}$$

$$= C\left(\frac{1}{\sqrt{ADC_{up}}} + \frac{1}{\sqrt{ADC_{down}}}\right). \tag{3.9b}$$

In practice, the slewing correction was fit to the form:

$$\delta t = C' \frac{1}{\sqrt{\Delta E}}. \tag{3.10}$$

This form can be derived from equation 3.5 and equation 3.9 under the assumptions that:

$$gain_{up} = gain_{down}, \tag{3.11a}$$

[10]Notice that the average error can be absorbed into T_0^{slat}.

$$\frac{y}{L_{att}} \ll 1. \tag{3.11b}$$

3.7 AUSCON

3.7.1 Reconstruction Basics

Once the drift chamber and TOF information has been calibrated, the task of track reconstruction can begin. When describing the workings of the experiment to non-physicists I am fond of making an analogy between track reconstruction and a "connect the dots" puzzle. There are however many effects that make track reconstruction quite a bit more difficult than the child's game shown in figure 3-3.

As a trivial point, there is nothing to indicate which hits belong to which track, i.e., the "dots" are not numbered. Also, you have probably never seen a "connect-the-dots" where there were two or more images so that you had to decide which dots went with which image. But, there is often more than one valid track in an event. Sometimes hits are missing due to:

- Efficiency < 100% ($\approx$ 85% for T1, $\approx$ 98% for T2-T4).
- Finite pulse width ($\approx$40 nsec) which merges any hits closer than 2 mm.

There are also extra hits that arise from several sources:

- Electronic cross-talk.
- Tracks that cross cell boundaries within a plane.
- Hits from particles in front of the magnet whose momentum is too low for them to make it through Henry Higgins.
- Non-target interactions, e.g., scatter from the beam pipe, PBGL, etc.
- The left-right ambiguity, discussed in section 2.8.1, that automatically doubles the number of hit positions that need to be considered.

There are also effects of experimental resolution and uncertainty in the actual wire positions.

The confusion that results from all of these complications is illustrated in figure 3-4 and figure 3-5. The top panel of figure 3-4 (3-5) shows a plan (gravity) view of a typical ^{28}Si +^{197}Au event. The bottom panels of these two figures show magnified views of the chambers before

Figure 3-3: A typical example of a "connect-the-dots" puzzle, a simplified analogy for track reconstruction.

and after the magnet. It is not completely clear which hits belong with which track. Especially difficult is deciding which hits in front of the magnet match up with which hits behind the magnet.

As if this were not enough, drift chamber information is necessarily projective. As discussed in section 2.8.1, this means that a track reconstruction program does not even have dots[11] to connect. Rather, it has *lines of possible dots*, at different angles, that it must try to combine into a spacepoint. This means that even if we manage to successfully reconstruct all of the tracks in the plan (x-tracks) and gravity (y-tracks) views, we still need to decide which x-tracks combine with which y-tracks. Figure 3-6 shows beam's eye views of the hits in the four drift chambers, illustrating the difficulty of this task.

3.7.2 Data Structures

Before discussing the actual reconstruction strategy used, a word about data organization is in order. Each detector type stores different pieces of information in a unique YBOS bank [Qua89]. Each of these banks requires a different subroutine to unpack its contents into local variables. Track reconstruction programs are not the only consumers of this data, so it should not be surprising that much of the data stored is irrelevant to track reconstruction programs. The proliferation of calls to different YBOS unpacking routines, and the large number of extraneous variables greatly complicated past track reconstruction programs. In order to avoid this, Dave Morrison implemented a scheme, using the CERN memory management package, ZEBRA [ZEB92], to preprocess this information into detector-independent data structures. Only the required information is stored:

- *STATUS* - Indicates validity of a hit. This has different meanings for different detectors.
- *INDEX* - The pointer into the original YBOS bank.
- *MATE* - The index of matching hit for chambers with left/right ambiguity.
- *DETECTOR* - The pointer to the hit's detector.
- *WIRE* - The hit's wire (or segment).
- *LOCATION 1* - The primary distance to the hit. For chambers this is the distance from the center of the chamber to the hit along the direction perpendicular to the wire. For TOF, this is the x-position.

[11] "Spacepoints" to use a longer word

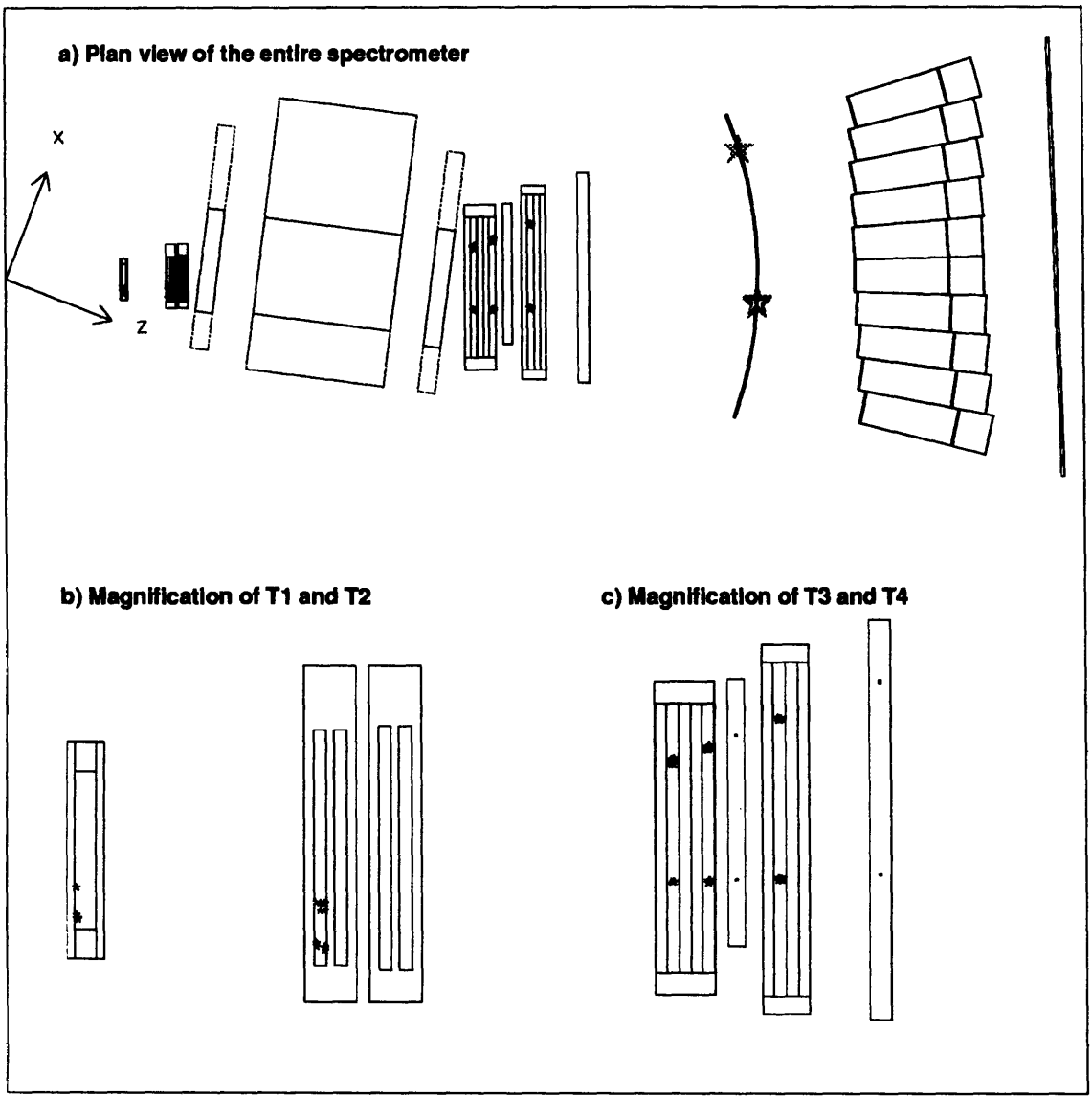

Figure 3-4: Plan view of the Henry Higgins spectrometer in a typical $^{28}Si + ^{197}Au$ event. The bottom panels show magnifications of the drift chambers and wire chambers.

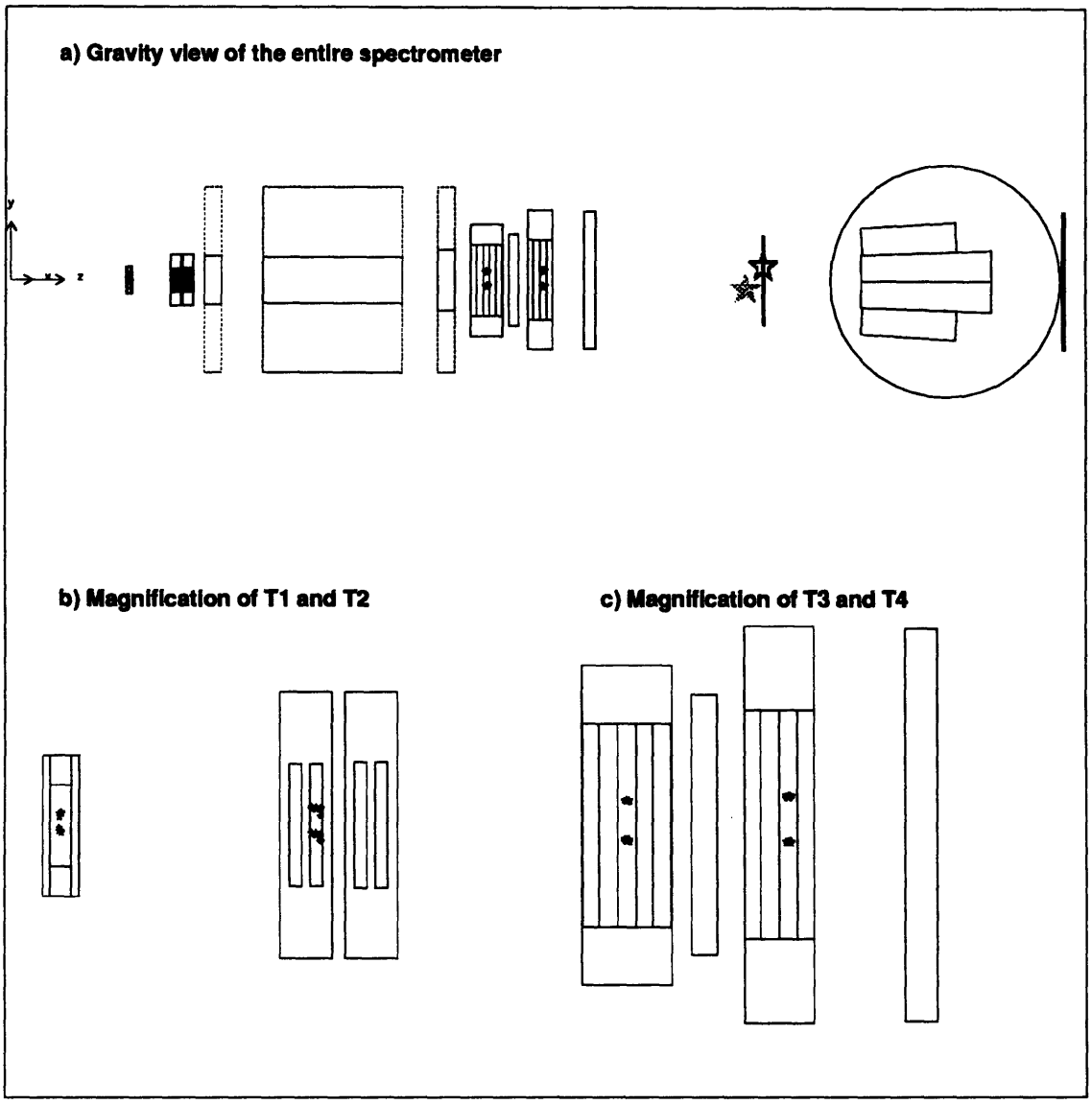

Figure 3-5: Gravity view of the Henry Higgins spectrometer in a typical $^{28}Si + ^{197}Au$ event. The bottom panels show magnifications of the drift chambers and wire chambers.

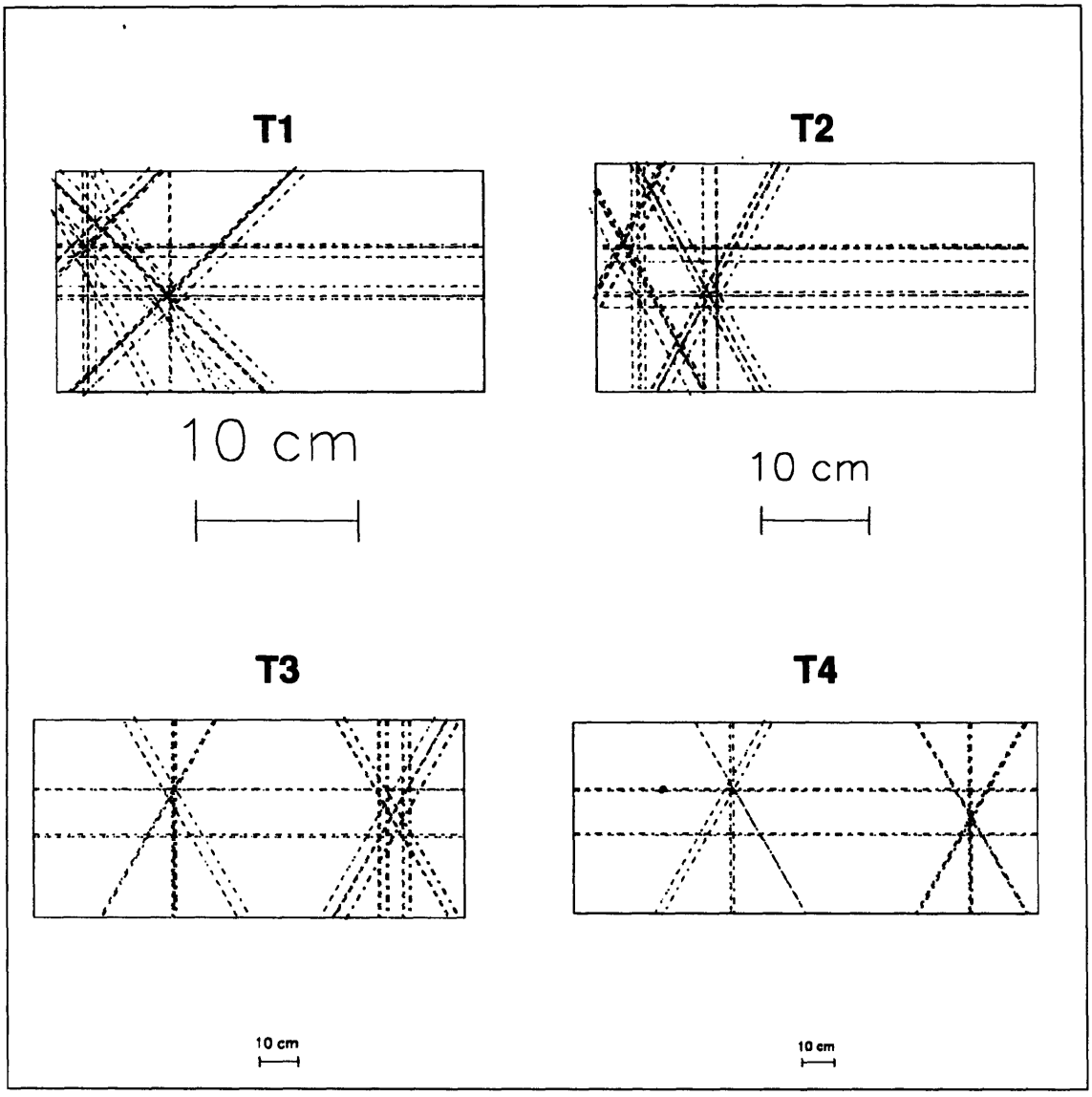

Figure 3-6: Beam's eye views of the four drift chambers in a typical $^{28}Si + ^{197}Au$ event.

- *LOCATION 2* - The secondary distance to the hit. For chambers, this is zero. For TOF, this is the y-position.
- *LOCATION 3* - This is the tertiary distance to the hit. For all detectors, this is the z-position in the spectrometer coordinate system.
- *TIME* - A time associated with the hit. For chambers, this is the lead time. For TOF it is the time of flight.

In addition to these streamlined hit data structures, there are also data structures which store the following information on intermediate track decisions:

- *HEADER* - An array of nine track quality diagnostics.
- *DETECTORS* - A list of detectors that contain hits from the given track.
- *LOCATIONS 1 and 3* - The primary and tertiary locations of a hit.
- *HITS per DETECTOR* - The number of hits from the given track in the given chamber.

All communication between reconstruction subroutines is carried out using these data structures.

3.7.3 The AUSCON Algorithm

The collaboration has tried several reconstruction algorithms in the past. The two that have been accepted by the collaboration for publication purposes are known as RECONSTRUCT (developed by Martin Sarabura [Sar89] and Huan Huang [Hua90]) and TRCK3 (primarily developed by Shige Hayashi and Hiro Sakurai [Sak92]). All of these algorithms suffered from the following problems to varying degrees.

- Greatly reduced efficiency at high multiplicities. This is a big problem for E859 since the rare events of interest often have a large associated multiplicity in the spectrometer.
- Fake track (ghost) production at high multiplicities. Some algorithms were tuned for high efficiency. Instead of losing tracks in E859's high multiplicity environment, these algorithms would generate more than one track out of one track's hits. Most of these ghosts could be eliminated, but these efforts were made after the fact instead of as an integral part of the algorithm. It is vitally important to eliminate ghost tracks in any correlation analysis since they produce a spike at small relative momentum - the same signal as a very large source. At least one heavy ion collaboration has discovered this effect [Morb, Rol].

- Confusion resulting from tracks passing close to a sense wire. Because of the left-right ambiguity, passing close to a wire results in a very high local hit density that magnifies the problems mentioned above.
- Inefficient search algorithms inherent in the microscopic-vector approach used by these codes made them very CPU intensive. This type of approach collects hits in a given view in each chamber and tries to form vectors from these hits. An attempt is then made to match these vectors between chambers. The combinatoric penalty for this sort of algorithm increases as N^2, and N can get very big since it counts hits on every plane and each hit counts twice due to the left-right ambiguity. AUSCON takes a macroscopic approach to reconstruction by first attempting to reconstruct "roads," collections of all hits that may eventually be part of a single track. Only those hits in a given road are looped over in an attempt to find tracks.

The E859 collaboration reconstruction algorithm is known as AUSCON[12]. It was developed by Peter Rothschild, and was largely successful in its attempt to get around all of these problems. Figure 3-7 and figure 3-8 show a schematic of the AUSCON algorithm. Values used for cuts were obtained by balancing the need for efficiency against the need to avoid ghost tracks and were optimized with visual reconstruction. For a complete list of the cut values, see [Rot94].

Monte Carlo studies have shown that the reconstruction has a momentum dependent efficiency, rapidly reaching an asymptotic value of $\approx 95\%$, see [Mor94]. There is also a multiplicity dependence of the order of 5%. These inefficiencies are unimportant to correlation analyses except to the extent that they translate into two-particle inefficiencies. Two-particle inefficiencies can arise because of instrumental limitations on the ability to resolve close hits. They can also arise because of algorithmic difficulties associated with the high hit multiplicities inherent in close tracks. The extent of these inefficiencies and their significance to the data analysis are discussed in section 4.2.5.

T3T4 Reconstruction

Past experience suggests that the simplest place to start reconstruction is in the chambers behind the magnet. Forming straight-line track segments in these chambers (T3T4 vectors) is relatively straight-forward. Compare the environments behind and in front of the magnet:

- T1T2

[12]The program was named after an obscure country in the southern hemisphere.

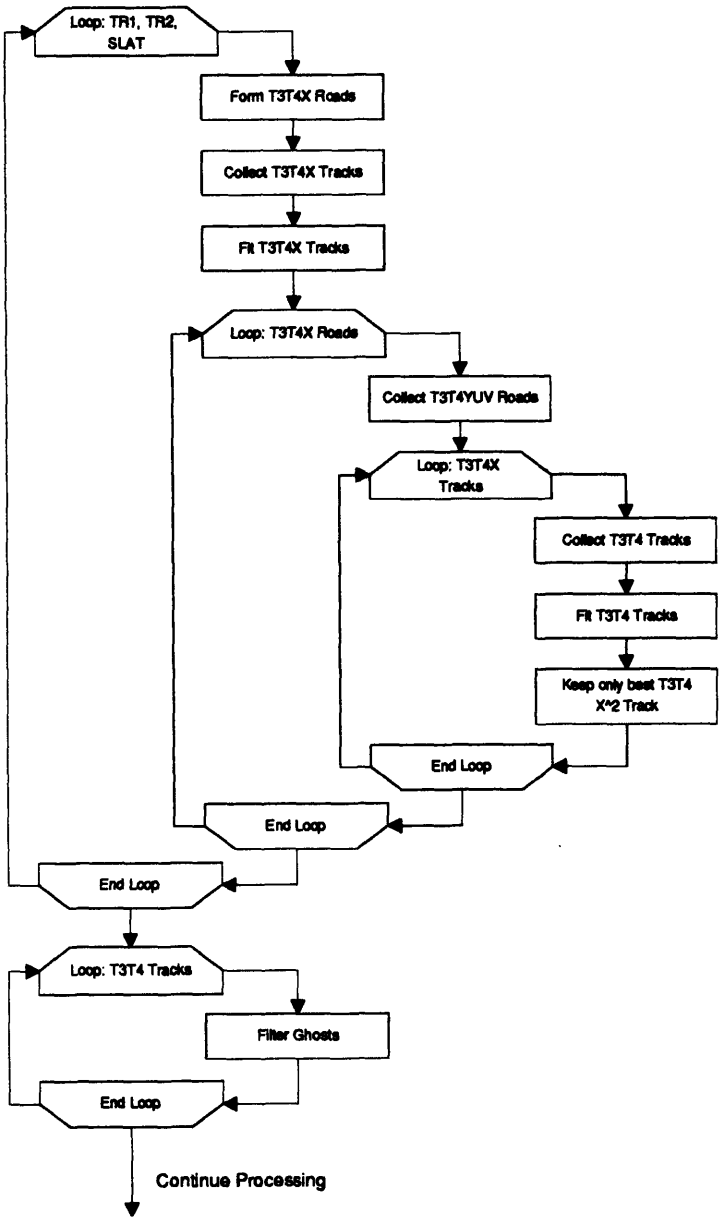

Figure 3-7: First half of the AUSCON algorithmic flow chart, courtesy of M. Cianciolo. See text for more details.

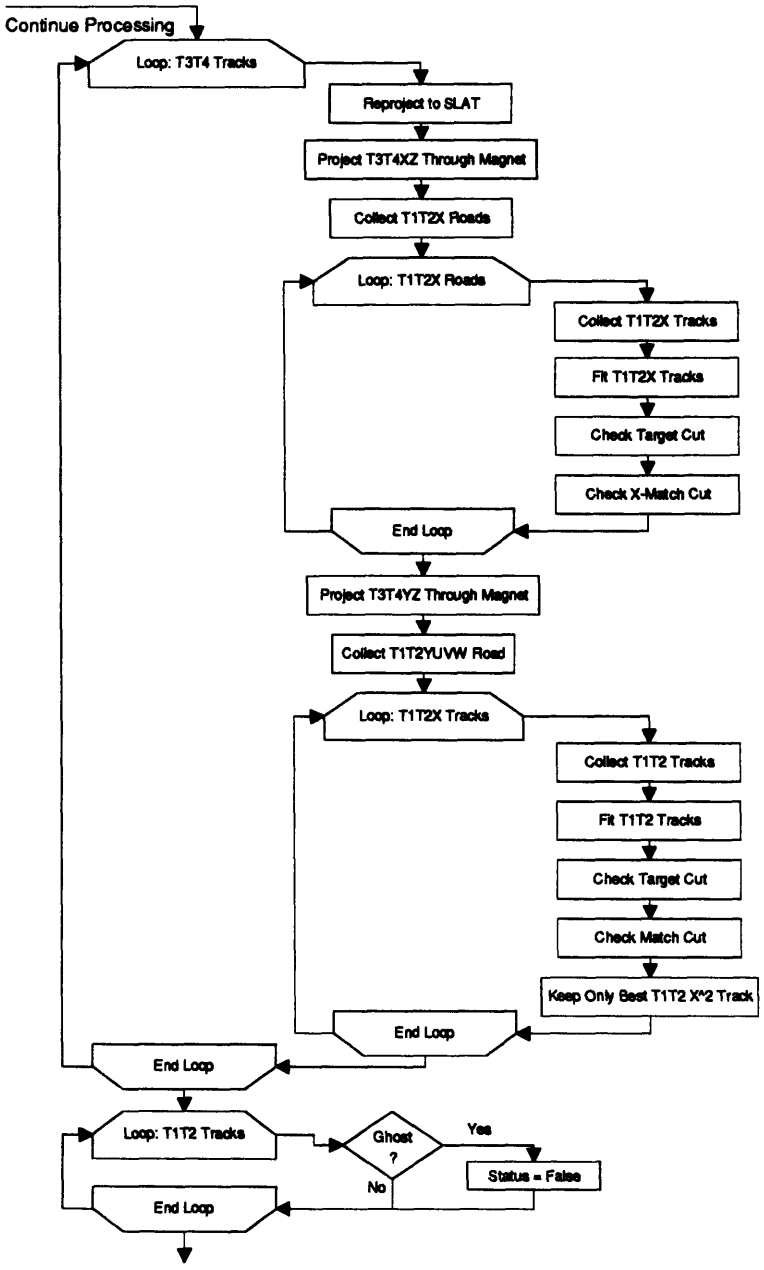

Figure 3-8: Second half of the AUSCON algorithmic flow chart, courtesy of M. Cianciolo. See text for more details.

1. Inefficient T1.
2. Very high track density.
3. 22 drift chamber planes.

- T3T4

1. No inefficient chambers.
2. Lower track density due to magnet sweeping.
3. 23 drift chamber planes plus 2 wire chamber planes plus XY point on TOFW.

AUSCON begins by attempting to find T3T4X roads. Loops over TR1 and TOFW hits are performed. T3T4X roads are collections all of the hits in the X views that lie within a search width of the line connecting the TR1 and TOFW hits. Similar loops are performed over *unused* TR2 hits and TOFW hits to avoid any inefficiency problems on TR1. Since TOF information is associated with drift chamber hits at all times, they can be corrected for transit time as discussed in section 3.5.2. AUSCON allows the user to turn off the transit time correction because if the TOFW is not (or poorly) calibrated, this correction can actually have drastically negative effects on the reconstruction effciency.

At this point AUSCON tries to create T3T4X tracks from the hits in each T3T4X road. Loops over hits on the drift chamber planes with the largest lever arm (first plane on T3 and last plane on T4) are performed. Hits within a much smaller search width (appropriate to the superior drift chamber resolution) are collected into a T3T4X track. To avoid any drift chamber inefficiency, the same loops are performed over unused hits in the second plane in T3 and the second-to-last plane in T4. A two-dimensional vector is fitted through all T3T4X tracks that have enough total hits and enough hits in each module.

AUSCON loops over all TOFW hits that have associated T3T4X tracks. Assuming that the track comes from the target, its y-position behind the magnet can be predicted using the y-position of the TOFW hit and the pathlength of the track to the TOFW hit. All hits in Y views, within a search width of this predicted position, are collected into a T3T4Y road. A loop over Y hits with the biggest lever arm is performed (once again, the same loop will be performed over unused hits on planes with the next-largest lever arm). First, hits on intervening Y planes within a much smaller search width are collected. Next, since to predict positions in U and V views both X and Y information is needed, a loop over T3T4X tracks associated with each T3T4Y road is performed. All U and V hits within a search width of the predicted position are collected. Then U,V,X and Y hits are combined to form T3T4 tracks. A three-dimensional vector

is fit through all T3T4 tracks with enough total hits and enough hits in each module. Each track is projected to the TOF wall and it is demanded that the TOF slat used is the closest to the track.

Finally, the reconstructed T3T4 tracks pass through two filters in order to remove ghost tracks:

- For each T3T4X track, only the T3T4 track with the lowest χ^2 value is kept.
- If T3T4 tracks share too many hits or too many views, the one with the lowest χ^2 is kept.

Track Projection through the Magnet

Because of the harsher environment in front of the magnet, it is very difficult to reconstruct an independent T1T2 track in the same manner as the T3T4 reconstruction procedure described above. As a result, most algorithms, including AUSCON, have proceeded in the following manner:

1. Construct a set of T3T4 vectors.
2. Project these vectors through the magnetic volume assuming a track origin at the target.
3. Attempt to verify each track hypothesis with T1 and T2 hits collected from a volume surrounding the track projection.

AUSCON assumes that the magnetic field is a uniform effective-edge, with length L, centered at z_0. In this approximation, the magnetic field can be represented as:

$$\vec{B}^{edge}(z) = \begin{cases} B_y^{edge} & ; \quad z_0 - L/2 < z < z_0 + L/2 \\ 0 & ; \quad \text{elsewhere} \end{cases} \tag{3.12}$$

Once a particle has been reconstructed, the calculation of its momentum in the bend-plane, p_{xz}, can be obtained from Lorentz's force law for a charged particle in a uniform magnetic field:

$$p_{xz} = \frac{eB}{c} R \tag{3.13}$$

The effective edge approximation makes this calculation very simple. Referring to figure 3-9, we see that a particle in a magnetic field of the assumed form travels along a path s which is a portion of a circle of radius r. We can solve for r by noticing that

$$\alpha = \theta_1 + \theta_2. \tag{3.14}$$

From this we can write the equation for r:

$$r = \frac{D/2}{\sin(\alpha/2)} \tag{3.15a}$$

$$= \frac{D}{2\sin((\theta_1+\theta_2)/2)}, \tag{3.15b}$$

and the equation for p_{xz}:

$$p_{xz} = \frac{eB}{c}\frac{D}{2\sin((\theta_1+\theta_2)/2)}. \tag{3.16}$$

As a matter of historical note, one can derive a formula for the momentum for a charged particle in a more general effective-edge in which we do not demand uniformity of the magnetic field:

$$\vec{B}^{edge}(z) = (0, B_y^{edge}(x,z), 0). \tag{3.17}$$

In this approximation, a particle does not travel in a circle with radius r. Instead, its path is everywhere locally a circle with radius $r(x,z)$. Using this fact, it is shown in [Zaj82] that the momentum of a particle traveling in such a magnetic field is given by:

$$p_{xz} = \frac{eB}{c}\frac{L}{\sin(\theta_1)+\sin(\theta_2)}. \tag{3.18}$$

Note that care must be taken in evaluating the signs of angles θ_1 and θ_2.

For an embarassingly long amount of time we were unable to reconcile these different formulas. It is mostly a geometry problem to prove that these expressions are indeed equivalent for the simplified magnetic field assumed for E859. Referring to figure 3-9, we can see that the relationship between L and D is given by.

$$L = D\cos(\beta). \tag{3.19}$$

Next we note that two radii and their connecting chord form an isoceles triangle. From this one can see the equality of the two angles indicated by γ, which leads to an expression for the angle β,

$$\beta = (\theta_1 - \theta_2)/2. \tag{3.20}$$

Using equation 3.19 and inverting, we reduce the proof to:

$$2\sin((\theta_1+\theta_2)/2)\cos((\theta_1-\theta_2)/2) \stackrel{?}{=} \sin(\theta_1)+\sin(\theta_2) \tag{3.21}$$

This equality can be shown by expanding the terms on the left-hand side of the equation and using the half-angle formula.

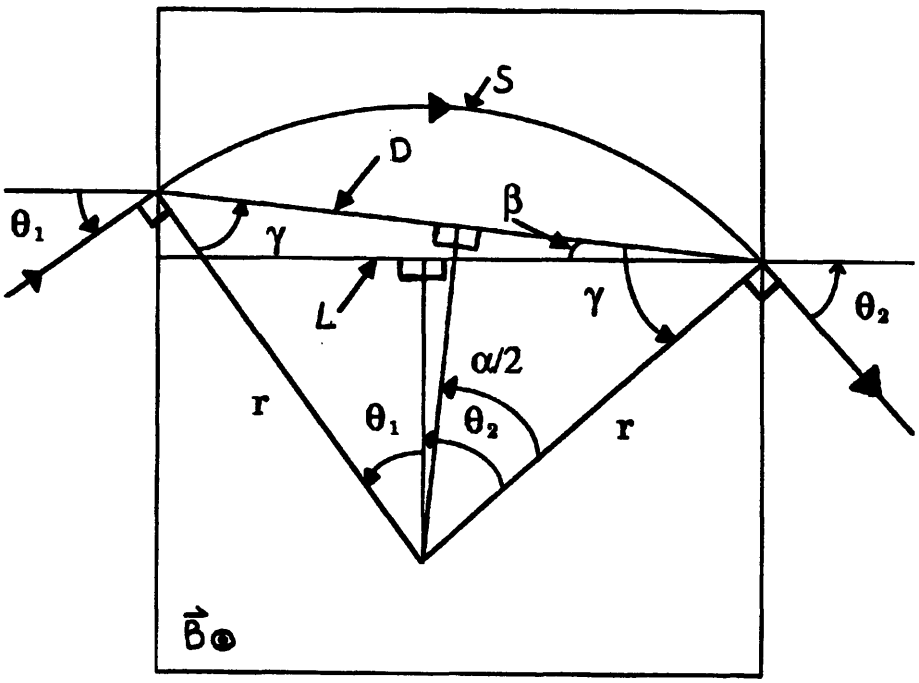

Figure 3-9: Geometry of the effective edge approximation.

To calculate the total momentum,

$$p = \sqrt{p_{xz}^2 + p^2 y}, \tag{3.22}$$

we write:

$$\frac{p_y}{p} = \frac{dy}{ds} \tag{3.23a}$$

$$= \frac{dy/dz}{ds/dz} \tag{3.23b}$$

$$= \frac{dy/dz}{\sqrt{(dx/dz)^2 + (dy/dz)^2 + 1}}. \tag{3.23c}$$

Note that in our spectrometer, $(p_y/p)_{max} \leq 0.06$. Now we write:

$$p = \sqrt{p_{xz}^2 + p_y^2} \tag{3.24a}$$

$$= p_{xz}\sqrt{1 + p_y^2/p_{xz}^2} \tag{3.24b}$$

$$= p_{xz}\sqrt{1+\frac{(p_y/p)^2}{1-(p_y/p)^2}} \tag{3.24c}$$

$$= p_{xz}\sqrt{1+\frac{(dy/ds)^2}{1-(dy/ds)^2}}. \tag{3.24d}$$

Note that the maximum momentum correction is $\delta p \leq 0.2\,p\%$. I point out the magnitude of the correction, because there was a slight error in the actual correction used:

$$p_{AUS} \equiv p_{xz}\sqrt{1+(dy/ds)^2}. \tag{3.25}$$

If we expand equation 3.24, we can write it as:

$$p = p_{xz}\sqrt{1+(dy/ds)^2+(dy/ds)^4+\mathcal{O}(dy/ds)^6}. \tag{3.26}$$

The error in leaving out the denominator in equation 3.25 comes in at $\mathcal{O}(dy/ds)^4$. The maximum value of this error is $\delta p/p \leq 0.0007\%$.

The projection of T3T4X tracks through the magnet makes a spline approximation to the circular path of the track in the magnetic field. That approximation is a solution to the following problem [Zaja]:

- Assume that the track in front of the magnet originates at the target and has an unknown slope, $x = mz$.
- Assume that the track behind the magnet is a straight line with a known slope and intercept, $x = m'z + d$.
- Assume that the path of the track in the magnetic field satisfies a second-order polynomial, $x = a + bz + cz^2$.
- Demand that the functions and their derivatives match at the appropriate magnet face, z_1 or z_2.

This gives four equations and four unknowns, so we can solve for the slope of the track in front of the magnet:

$$m = m' + \frac{d}{(z_1+z_2)/2}. \tag{3.27}$$

If one solves for the z-position of the intercept of the trajectories in front of and behind the magnet, it turns out that the trajectories always meet at the magnet's midplane.

3.7. *AUSCON*

The y-projection of T3T4 tracks through the magnet is complicated by two effects. The algorithm used is discussed in detail in [Hua88], but I will review the basic principles here. The first effect is known as "vertical focussing." This effect results from the fringe fields at the z-edges of the magnet which gives rise to non-zero values of B_z, see figure 3-10.

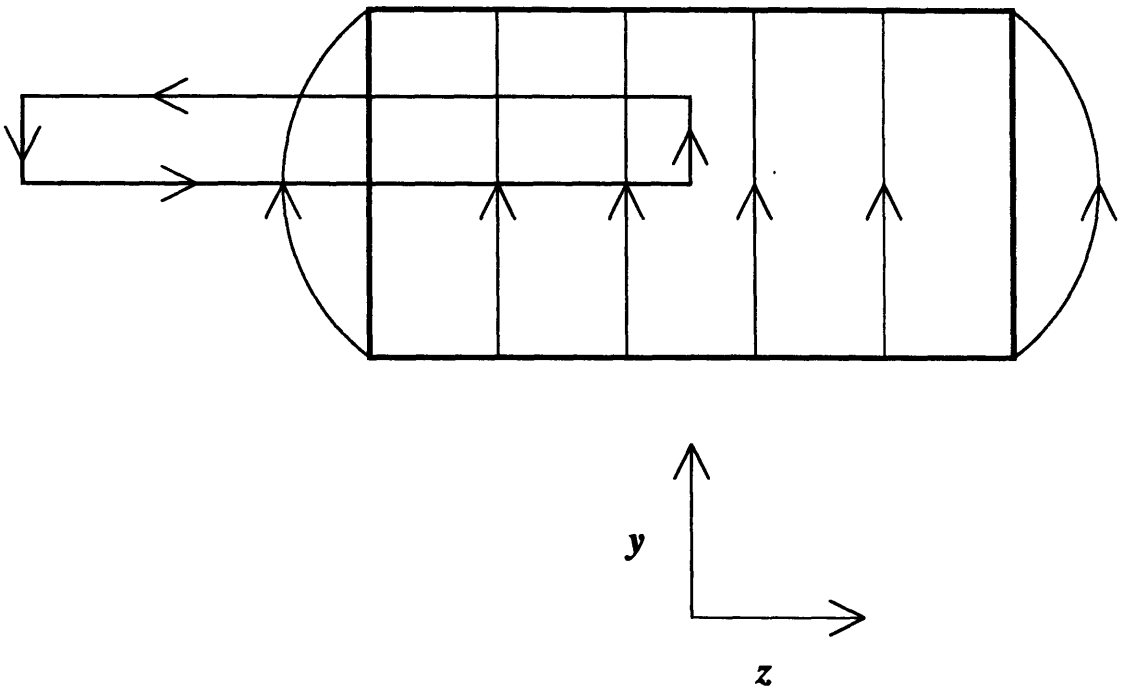

Figure 3-10: Shematic of Henry Higgins' fringe fields. These give rise to a vertical force on charged particles known as "vertical focussing." Also shown is a current loop used in the vertical focussing derivation found in the text.

The author recently discovered, much to his surprise, that vertical focussing could also have a defocussing effect. To show this, I will follow the derivation found in [Hua88], being very careful with minus signs. From Lorentz's law we have:

$$\vec{F} = \frac{q\vec{v} \times \vec{B}}{c}. \tag{3.28}$$

Since we are only concerned about fringe fields in the z-direction, we can write:

$$F_y = \pm \left| \frac{q v_x B_z}{c} \right|. \tag{3.29}$$

This equation is written in this fashion to show that F_y can take on either sign. For the rest of this derivation I will drop the absolute value signs, but retain the $\pm$ signs for emphasis. We

can rewrite equation 3.29 as:

$$m\,dv_y = \pm\frac{qB_z}{c}v_x\,dt \tag{3.30a}$$

$$\frac{p\,dv_y}{v} = \pm\frac{qB_z v_x}{cv}\,ds. \tag{3.30b}$$

We define a right-handed coordinate system with the z-axis *perpendicular to the magnet face*, the y-axis vertical and pointing up, and the x-axis horizontal. The angles α and β are defined such that α is the polar angle with respect to the y-axis and β is the polar angle measured from the z-axis. Using these definitions, we can rewrite equation 3.30 as:

$$p\cos(\alpha)\,d\alpha = \pm\frac{qB_z\cos(\alpha)\sin(\beta)\,ds}{c} \tag{3.31}$$

We integrate these two expressions over the fringe field region assuming that the fringe field is narrow so that β does not change in the fringe field region. This is known as the "thin-lens approximation:"

$$p\Delta\alpha = \pm\frac{q\sin(\beta)}{c}\int B_z ds \tag{3.32a}$$

$$\approx \pm\frac{q\tan(\beta)}{c}\int B_z dz \tag{3.32b}$$

By using Ampere's law on the circuit shown in figure 3-10 and assuming $B_z(y=0)=0$ and $B_y(y) = \textit{constant}$, we get:

$$\int B_z dz = B_y y. \tag{3.33}$$

Which finally leads to:

$$\Delta\alpha = \pm\frac{y}{\left(\frac{pc}{qB_y}\right)\frac{1}{\tan(\beta)}} \tag{3.34a}$$

$$= \pm\frac{y}{\frac{r}{\tan(\beta)}}. \tag{3.34b}$$

Equation 3.34 is identical to that of the familiar thin lens from optics, with a focal length of:

$$f = \pm\frac{r}{\tan(\beta)}. \tag{3.35}$$

A negative sign corresponds to a converging lens and a positive sign corresponds to a diverging lens. Signs enter into equation 3.35 both explicitly and implicitly (in the charge of the particle

and the sign of θ). In general though, the signs work out such that the effect focusses tracks, bending them towards the midplane. Parameters for two thin lenses (one at each of the magnet aperatures) were determined from Monte Carlo simulation. See [Hua88] for complete details.

Because of time considerations, Monte Carlo data are often generated with a homogeneous, effective-edge magnetic field. AUSCON allows the user to turn off vertical focussing corrections since they would be wrong in this case and can in fact seriously impair reconstruction efficiency.

The second y-projection effect is generally known as the "pseudo-vertical focussing" effect. The pseudo-vertical focussing effect would result even if there were no fringe fields. This is because while dy/ds is constant in the magnetic field, ds/dz, and thus dy/dz are increasing. This defocusses tracks, diverging them away from the midplane regardless of sign or angle.

T1T2 Reconstruction

AUSCON begins T1T2 reconstruction with the XZ projection of each T3T4 track to the target position. Hits within a search width of the projection are collected to form T1T2X roads. T1T2X tracks are obtained and fit in the same manner as T3T4X tracks, described earlier in this section. The T1T2X tracks must also satisfy two additional criteria:

- The projected x-location of the T1T2X track at the target z-location must be within a search width of the target x-location.
- The difference between dx/dz of the T1T2X track and the value of this quantity predicted by its associated T3T4 track must be less than some maximum allowed value.

T1T2Y roads are collected from hits within a search width of the Y projection of each T3T4 track. T1T2Y roads and associated T1T2X tracks are used to obtain T1T2 tracks in a manner identical to that used for T3T4 tracks. A three dimensional vector is then fitted through all T1T2 tracks with enough total hits and enough hits in each module. T1T2 tracks were filtered according to the following criteria:

- The projected xy-location of the T1T2 track at the target z-location must be within a search width of the fitted beam xy-location.
- The difference between dx/dz of the T1T2 track and the value of this quantity predicted by its associated T3T4 track must be less than some maximum allowed value.
- The difference between dy/dz of the T1T2 track and the value of this quantity predicted by its associated T3T4 track must be less than the maximum allowed value.

- The "squared-match deviation" of the T1T2 track and its associated T3T4 track must be less than some maximum allowed value. This quantity is obtained by adding, in quadrature, the distance between the T1T2 track and the T3T4 track projected to $z = 0\,\text{cm}$ and projected to $z = 500\,\text{cm}$. This quantity was found to be significantly larger for low momentum tracks due to the increased importance of multiple scattering. As a result, the size of this cut increases as the momentum decreases. See [Rot94] for exact values of this cut.

- If more than one T1T2 track associated with a T3T4 track passed all of the above cuts, only the one with the lowest χ^2 was retained.

- As of the previous cut, AUSCON has created a list of complete tracks containing all of the information from the associated T1T2 tracks and T3T4 tracks. T1T2 tracks associated with different T3T4 tracks are compared to determine if they share too many hits or too many modules. If this is found to be true, the track whose T1T2 track has the lowest χ^2 is given a good status. The other track is retained, but it is reported as having a bad status.

The ability to reconstruct T1T2 vectors without relying on the T3T4 vector would be a great enhancement to the E859 spectrometer, especially for correlation studies. The reason that this ability would help is that the current algorithms necessarily construct the best possible T1T2 vector *from hits within a window around the T3T4 projection to the target.* There are many potential sources for T3T4 vectors other than the target, but tracks from these sources can be reconstructed to the target if there are enough hits on T1 and T2. The ability to reconstruct tracks that do not originate from the target would help us to reject such spurious tracks and would let us identify such sources of background. Two finely segmented wire chambers have been constructed for just this purpose [C+93b], for use in experiment E866.

3.8 PICD

3.8.1 Particle Identification Basics

Once a track has been reconstructed, its particle type needs to be identified. A PID code needs to combine information from TOF, charge (obtained from energy loss in the TOFW) and the GASČ/BACK detectors to determine whether a given track satisfies any particle type hypotheses. Tracks may be either unidentified, uniquely identified or ambiguously identified.

Unidentified tracks are usually the result of some reconstruction error, but, they can also be the result of confusion arising in a high multiplicity environment. For example, a valid kaon below the kaon GASČ threshold may remain unidentified if it shares a GASČ cell with a fast pion. When a track is ambiguously identified, the PID code can either choose between competing particle identities based on large differences in the yields of those particles, or decide that it cannot decide.

3.8.2 The PICD Algorithm

The E859 collaboration-standard particle identification (PID) code was developed by Shige Hayashi [H+93]. This code is known as PICD, named after the YBOS bank containing its output. The major features of PICD include:

- Parameters are stored in an ASCII file so that they may be changed without recompiling. This was important in the testing stage.
- The GASČ and BACK counters were incorporated into the algorithm from the start.
- A great deal of information is stored in the PICD YBOS bank. This allowed users to modify PID decisions according to particular analyses while maintaining standard definitions for any such changes.
- Cuts were made in the variable $(1/\beta)$. This variable has the advantage of being distributed as a Gaussian, with a parameterized momentum-dependent width, about the expected value. By avoiding mass cuts, the standard PID variable, PICD also avoids problems that arise when tring to calculate the mass for particles with $\beta > 1$.[13]
- All particle species created in our spectrometer are identified. This includes: $e^{\pm}$, $\pi^{\pm}$, $K^{\pm}$, p, $\bar{p}$, d, t, and ^{3}He.
- Parameters were chosen to err on the side of inefficiency and certainty of identification. Even so, Monte Carlo calculations have shown the efficiency to be $\approx$ 98% [Mor94] in regions where TOF information is unambiguous and $\approx$ 90% when GASČ/BACK information is required.

Figure 3-11 shows a flow chart of the PICD algorithm. Projection of a track to the TOF wall and the GASČ/BACK are first verified. Next, the charge of the track is determined from the

[13]Such "tachyons" arise naturally because of finite timing resolution on the TOF wall.

energy loss in the TOF wall. The TOF PID decision is then determined by testing the p and $1/\beta$ values of the track against all particle hypotheses. At high momentum the p *vs* $1/\beta$ bands of different particles begin to overlap and ambiguities arise in the TOF PID. These may be resolved with information from the GASČ/BACK. Results of all tests are returned in the PICD status word. Figure 3-13 shows the different PICD PID regions obtained using the standard cuts discussed throughout the rest of this section.

TOF Energy Loss

A particle's charge, Z, is calculated from a parameterized, momentum-dependent function of energy loss. But the Landau distribution of energy loss for a particle with a given Z has a very long high-energy tail. Because of this, a large fraction of $Z = 1$ particles are above the $Z = 2$ threshold. Since particles with $Z > 1$ are very rare in our spectrometer, the upper charge cut is ignored everywhere except in the vicinity of ^{3}He. To account for tracks which cross slat boundaries, energy loss values from two adjacent slats may be added. This is only done if all of the following conditions are satisfied:

- The track points *between* the centers of two slats.
- The second slat does not have another track pointing at it.
- The difference between the recorded TOF for the two slats must be less than 2 nsec.

TOF PID

TOF particle identification is best visualized in the variables p and $1/\beta$. A particle identification hypothesis is confirmed by TOF if a particle's value of $1/\beta$ lies within a momentum-dependent distance of the expected value of $1/\beta$.

The value for of $1/\beta^{obs}$ for a given particle is:

$$1/\beta^{obs} = \frac{ct}{L}, \tag{3.36}$$

where L and t are the particle's pathlength flight-time respectively. The value of $1/\beta^{exp}$ for a given particle is:

$$1/\beta^{exp} = \frac{E}{p}, \tag{3.37}$$

where p is the measured momentum and E is the energy of that particle calculated from a given

3.8. PICD

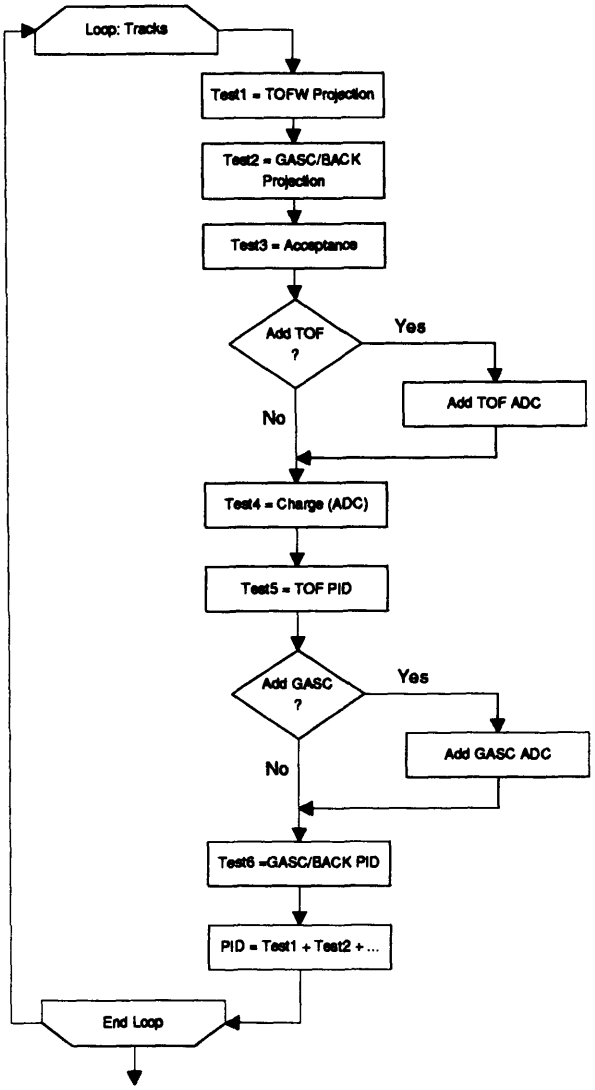

Figure 3-11: A flow chart of the PICD algorithm, courtesy of M. Cianciolo. See the text for details.

mass hypothesis. Given these equations, we can calculate the uncertainty on their difference:

$$\sigma\left(1/\beta\right) \equiv \sigma\left(1/\beta^{obs} - 1/\beta^{obs}\right) \tag{3.38a}$$

$$= \sqrt{\left(\frac{c}{L}\sigma_t\right)^2 + \left(\frac{m^2}{pE}\frac{\sigma_p}{p}\right)^2}. \tag{3.38b}$$

To calculate the momentum resolution term we first write the momentum, see equation 3.16, as:

$$p \approx p_{xz} = \frac{p_K}{2\sin\left(\alpha/2\right)}, \tag{3.39}$$

where α is the particle's bend angle as it traverses the magnet and p_K is the $p_\perp$-kick of the magnetic field (0.177 GeV/c for the 4 kG field setting). In the small-angle approximation this leads to:

$$\frac{\sigma_p}{p} = \frac{p}{p_K} d\alpha. \tag{3.40}$$

$d\alpha$ has contributions from instrumental resolution, position uncertainties and multiple scattering. The first two terms are momentum independent and we will combine them in the definition of a quantity, δ. We define the final term to be $\epsilon/p\beta$, where we have explicitly written the $(1/p\beta)$ dependence. Assuming that these two contributions add in quadrature, we obtain the following form for $d\alpha$:

$$d\alpha = \sqrt{\delta^2 + \left(\epsilon/p\beta\right)^2} \tag{3.41}$$

We can combine terms to obtain:

$$\sigma\left(1/\beta\right) = \sqrt{\left(\frac{c}{L}\sigma_t\right)^2 + \left(\frac{m^2}{pE}\right)^2 \left(\left(C_{res}\left(B\right)\cdot p\right)^2 + \left(\frac{C_{ms}\left(B\right)}{\beta}\right)^2\right)}. \tag{3.42}$$

We can write:

$$C_{res} = \frac{\delta}{p_K} \tag{3.43a}$$

$$\equiv \frac{1}{p_K}\frac{2\mu}{D}, \tag{3.43b}$$

where μ is the chamber's position resolution and D is distance separating T1 and T2 or T3 and T4. Here we have assumed that the four chambers contribute equally to track determination, that they all have the same resolution and that T1T2 and T3T4 are separated by the same

distance. To obtain an estimate for C_{res}, we write:

$$\mu \approx 200\mu\text{m} \tag{3.44a}$$

$$D \approx 50\,\text{cm} \tag{3.44b}$$

$$\Rightarrow C_{res} \approx 0.0045. \tag{3.44c}$$

To obtain an estimate for C_{ms}, we use [Hig75]:

$$C_{ms} = \frac{\epsilon}{p_K}, \tag{3.45a}$$

$$= \frac{1}{p_K}\frac{0.0175}{\sqrt{3}}\sqrt{\frac{X}{X_0}}\left(1+0.125\log_{10}\left(\frac{X}{X_0}\right)\right), \tag{3.45b}$$

$$\Rightarrow C_{ms} \approx 0.007. \tag{3.45c}$$

Here, $X/X_0 \approx 2.4\%$, is the average distance a particle travels between T1 and T4, in units of radiation lengths. The parameter values that were actually used are listed in table 3.1. These were obtained from proton data by fitting the above parameterization assuming $\sigma_t = 130\,\text{psec}$, see [Sak92] for more details.

Parameter	Value
σ_t	120 psec
C_{res}	0.006 GeV^{-1}
C_{ms}	0.012

Table 3.1: Parameter values used for PID at $B = 4\,\text{kG}$. See text for details of the parameterization and algorithm.

Figure 3-12 shows the relative importance of the three different terms in the formula for $\sigma\left(1/\beta\right)$, as a function of energy, for pions, kaons and protons. Note that the chamber resolution term never dominates.

GASČ and BACK PID

For any particle, regardless of mass, $\lim_{p\to\infty} 1/\beta = 1$. This means that above some momentum, p_{TOF}, TOF information cannot decide between two competing particle hypotheses. GASČ/BACK can decide between these two possibilities if the lighter candidate would fire the GASČ and the heavier candidate would not. At some momentum, $p_{\check{C}}$, the GASČ threshold of the heavier particle will be exceeded. This is the upper momentum limit for PID with the E859

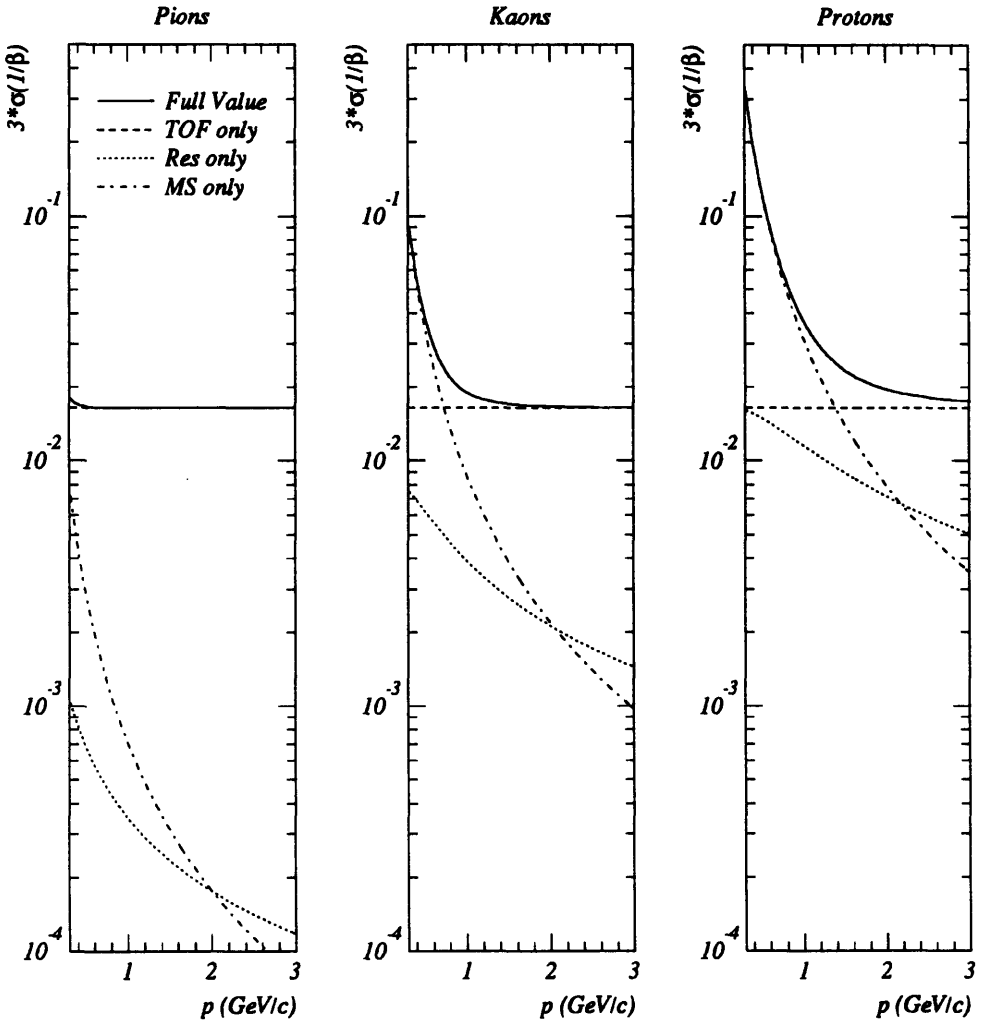

Figure 3-12: Contributions to $\sigma\left(1/\beta\right)$ from σ_t, $C_{ms} \cdot p$, and C_{res}/β, for pions, kaons and protons, as a function of momentum.

apparatus.

Some particle hypotheses require lack of a signal in the GASČ. In these cases, confirmation of the track on the BACK detector is necessary to know that it actually passed through the GASČ volume. The only exception to this rule is in the region where electrons and pions overlap. Demanding BACK confirmation for electrons would drastically reduce their PID efficiency since most electrons interact or are scattered in the GASČ and will not fire the predicted BACK pad.

There is a $\approx$ 10% inefficiency in GASČ and BACK PID. This is due to interactions in the GASČ material and low segmentation in the GASČ. The latter condition causes an inefficiency because if a track fires a GASČ cell, that cell is dead for any subthreshold particles that may hit it. Under certain conditions the light output from adjacent GASČ cells may be added together. This will tend to reduce the contamination of pions in the kaon sample at the cost of reduced efficiency for kaons. Light was added under the following conditions:

- The track projection crossed cell boundaries.
- The track projection at the mid-Z position of the cell passes within 5 mm of the cell wall.

Despite the lower efficiency of GASČ/BACK PID, agreement between TOF and GASČ/BACK PID was required for *all* particles above p_{TOF}. This is true even though particles outside the overlap region may still be uniquely identified by TOF. This procedure is used to avoid a $1/\beta$-dependent efficiency in addition to the momentum-dependent efficiency that would be hard to correct for in cross-section analyses. In correlation analyses single-particle efficiencies are not important and this analysis takes advantage of that fact to extend TOF identification beyond p_{TOF}, see section 4.2.2.

PICD Decisions

Figure 3-13 illustrates all of the different, *standard*, PICD particle identification regions. Curved lines indicate the $\pm 3\sigma$ $(1/\beta)$ values with the standard parameter values for the different particles, see table 3.1. Vertical bands show the different GASČ thresholds. Requirements for valid identification in each region are listed at the bottom right.

- All regions require an energy deposit in the TOF wall that exceeds the minimum ionizing threshold. The only regions that require a particle to pass an upper energy loss cut are those in which the ^{3}He TOF identification regions overlap TOF identification regions of other particles. See section 3.8.2.
- Low momentum regions of each particle merely require TOF identification.

- At higher momentum, the GASČ information needs to be used. Looking at momentum regions where two particle species overlap, we see several possibilities. For some values of $1/\beta$ the particle species are still uniquely identifiable by TOF. The GASČ information is still required for verification in these regions. If the GASČ and TOF information disagree, the particle is not identified. For values of $1/\beta$ in which TOF identification is ambiguous, the GASČ decision is accepted.

- For all regions where the GASČ information is required, BACK verification is also required. The exception to this rule is the e/π overlap region as detailed above.

- Above momenta where the GASČ information becomes ambiguous, identification can still be made in regions where the yields of the two particle species are quite different. For instance, all particles that fire the GASČ with $1.47\,\mathrm{GeV/c} < p < 5.2\,\mathrm{GeV/c}$ are identified as pions even though electrons at these momenta would also fire the GASČ. Protons and anti-protons are another example of such optimization. Above $p = 2.9\,\mathrm{GeV/c}$, p/K separation becomes ambiguous and the GASČ does not fire for either species. Any *positive* particle TOF identified as a proton in this region is called a proton. Anti-proton identification on the other hand has an upper momentum cutoff of $p = 2.9\,\mathrm{GeV/c}$.

Exceptions to these standard definitions made in this analysis are detailed in section 4.2.2.

3.9 E859 Monte Carlo

Since I spent a great deal of my personal time maintaining and upgrading the experiment's Monte Carlo program, I will spend a little time describing its features and limitations.

According to [Jam80], "A Monte Carlo technique is any technique making use of random numbers to solve a problem."[14] It is this element of randomness that earned the technique its name "Monte Carlo." In a show of Eurocentricity, [Jam80] also tells us that the name was chosen because

> ... the style of gambling in the Monte Carlo casino, not to be confused with the noisy and tasteless gambling houses of Las Vegas and Reno, is serious and sophisticated.

The prototypical Monte Carlo problem is an integral. For instance, figure 3-14 illustrates the calculation of the area of an arbitrarily complicated shape. One can pick a set of random

[14]This is stretching the definition a bit, because no one would consider the coin toss at the beginning of the SuperBowl to be a Monte Carlo technique.

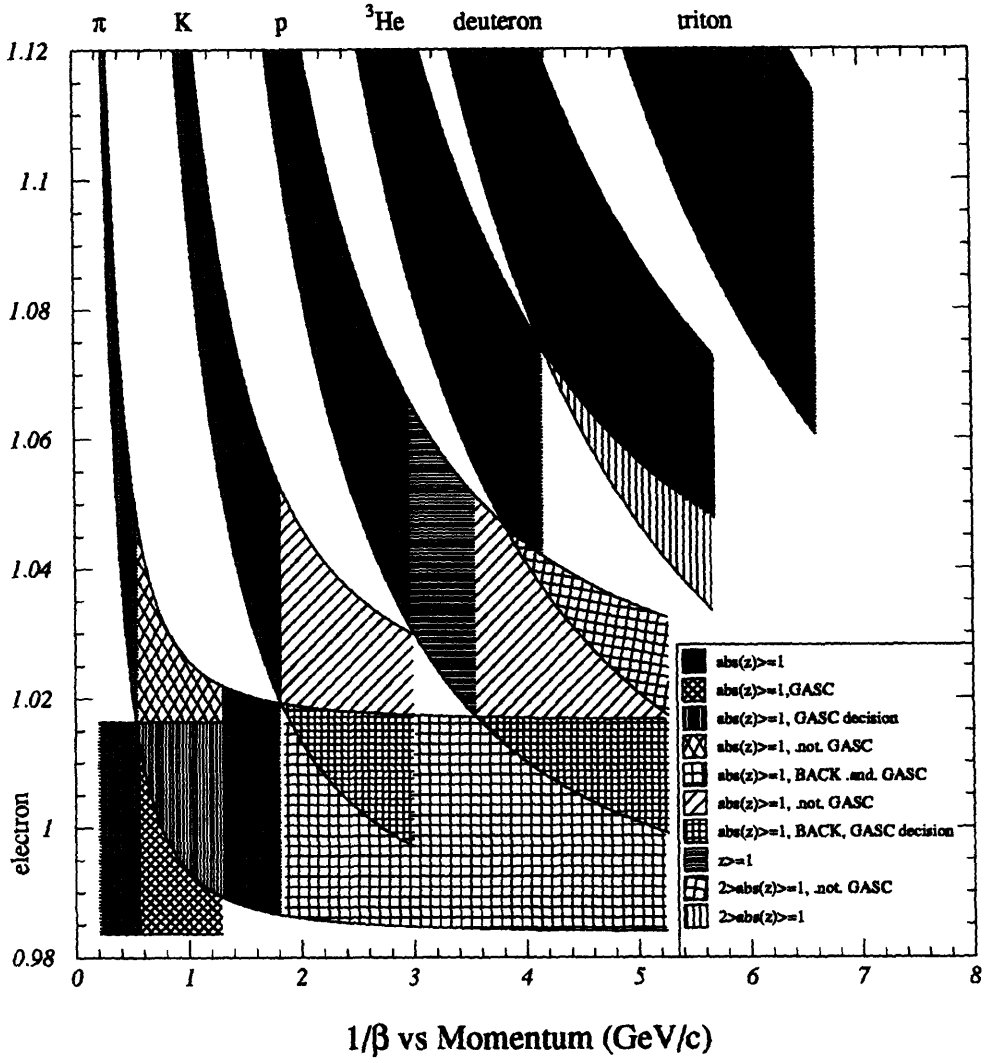

Figure 3-13: Plot of different particle identification regions in $(1/\beta)$ vs p. Requirements in the different regions are shown at the lower right. Parameter values are given in table 3.1. See text for details.

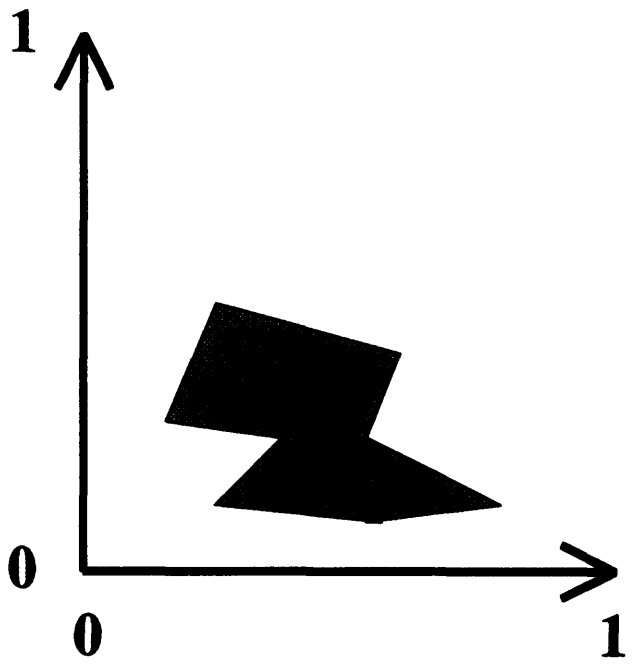

Figure 3-14: Illustration of a Monte Carlo area calculation.

(x, y) coordinates, and calculate the area from the fraction that fall inside of the shape. The information that we are trying to get from a Monte Carlo simulation of the experiment can also be considered to be a complicated, many-dimensional integral.

We would like to be able to compare our experimental data to theoretical predictions. But these predictions are for initial distributions that we never see. Rather, we see these distributions convoluted with our detector system response function, $\mathcal{R}\left(x_1, x_2, \ldots, x_n \rightarrow x_1^{'}, x_2^{'}, \ldots, x_n\right)$. This response function is an integral over such things as detector resolution, multiple scattering, etc. It is the role of a Monte Carlo simulation to reproduce $\mathcal{R}\left(x_1, x_2, \ldots, x_n \rightarrow x_1^{'}, x_2^{'}, \ldots, x_n^{'}\right)$ so that the theoretical predictions can be convoluted with the same response function that the experimental distributions were subjected to, see figure 3-15.

The E859 Monte Carlo has been at least partially successful in reproducing the experimental response function. This has been studied by comparing GEANT values for one- and two-particle AUSCON and PICD efficiencies to values obtained from the data. Results of these studies are detailed in 4.2.5.

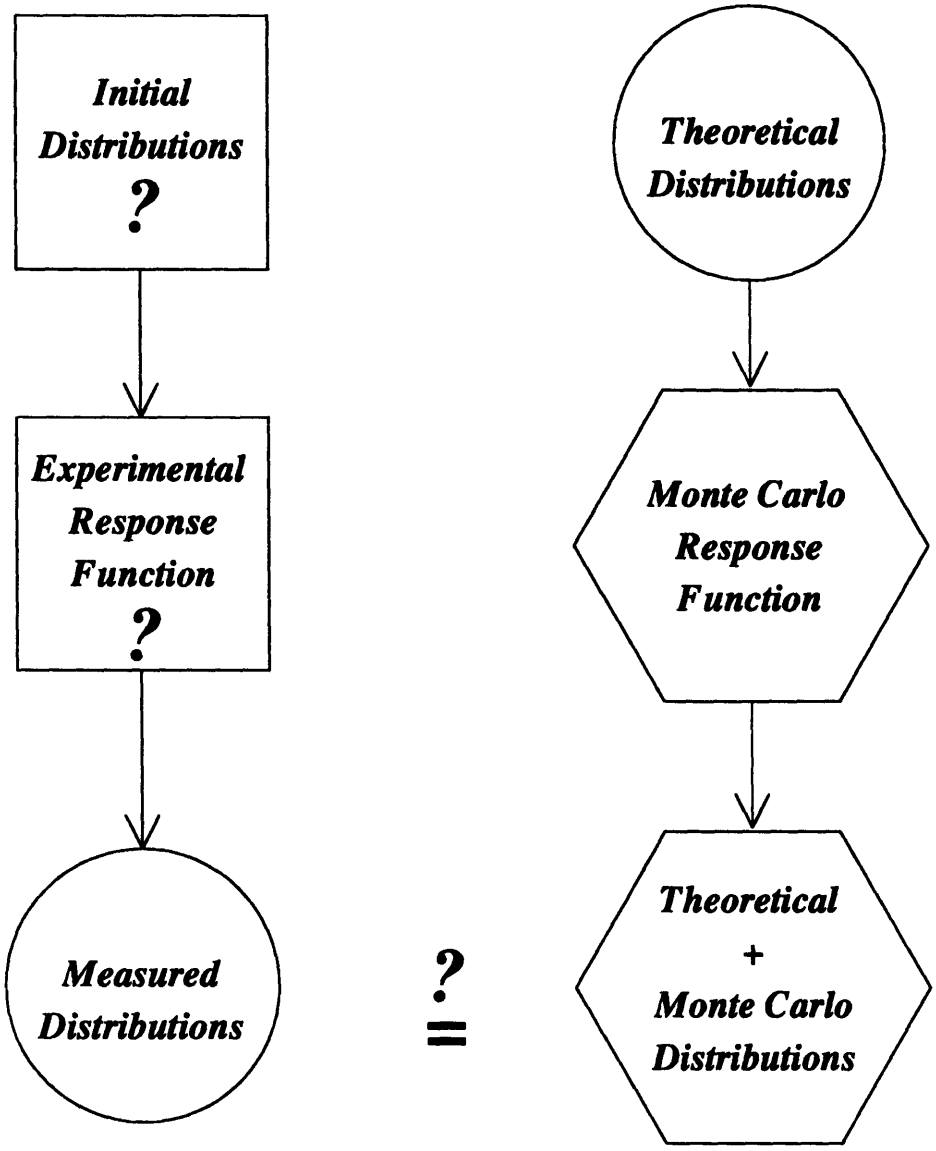

Figure 3-15: Illustration of the role of the experimental Monte Carlo simulation. Comparable items are aligned horizontally. Items we know are indicated with circles - the theoretical initial distributions and the measured experimental distributions. Items we cannot know are indicated by squares - the initial experimental distributions and the experimental response function. Items that we construct with the help of Monte Carlo simulation are indicated with hexagons. In order to make comparisons between theory and experiment, the Monte Carlo attempts to reproduce the experimental response function. Theoretical predictions can then be subjected to the same distortions as the measured data.

3.9.1 GEANT

The E859 Monte Carlo program is based on the CERN GEANT [GEA92] package, version 3.15. This package contains many powerful utility routines that allow the user to perform all of the tasks required of a detailed Monte Carlo simulation of a high-energy physics experiment.

The first task of an experimental simulation is to describe the geometry and materials (including values of the magnetic field) of all of the detector systems in the experiment. GEANT provides many shapes that allow the description of almost any experiment. Materials definitions exist for many elements and it is also possible to define new materials. GEANT provides routines that calculate the cross-sections for many supported physics processes in all materials used. Detailed descriptions of the algorithms used to simulate these processes can be found in [GEA92]. Those processes most important for our experiment are:

- Decay.
- Multiple scattering. The Moliere scattering option was used for all of this analysis.
- Ionization and δ-ray production.
- Hadronic interactions, for which we used the GHEISHA package [Fes85].

Once the boundary conditions (geometry and materials) have been defined, the "integration" needs to be performed. GEANT integrates the equations of motion for a particle traveling through the defined detector systems in a stepwise manner; this is known as "tracking." The step size is determined by both continuous processes (energy loss, multiple scattering, bending in a magnetic field) and discrete processes (decay, interaction, etc.). One also has to make sure that a step does not cross a material boundary.

The algorithm for determining the pathlength, λ_I, before a discrete interaction is very elegant. λ_I is obtained by random sampling for each selected, discrete process. The value of λ_I is given in units of the number of mean-free-paths traversed, N_λ. Since N_λ is *a medium-independent quantity*, λ_I can be determined *a priori*. A particle's actual pathlength before an interaction is the minimum λ_I of all the selected processes. GEANT decrements λ_I as the particle goes through the experimental apparatus. When $\lambda_I = 0$, the corresponding interaction takes place and final state particles and momenta are appropriately chosen. The new particles are then subjected to the above tracking algorithm which proceeds until all particles leave the experimental volume.

GEANT provides routines that will track particles through a properly defined detector system. These routines conveniently call user-written routines for every track and at every

step. This allows the user to store whatever information s/he desires (energy loss, position, etc.) for later digitization. This information is stored in ZEBRA [ZEB92] banks. Routines are provided to write and read these data structures. The following list describes the contents of the most important GEANT output banks:

- *HITS* - Stores user-selected information for tracks in a *sensitive volume* (TOFW slat, TR1 wire, etc.)
- *JXYZ* - Stores the space points of all tracks at every step along their trajectory.
- *KINE* - Stores the momentum 4-vector and the PID code for every primary particle. All secondary tracks above user-selectable kinetic energy cut (default = 0 GeV) are tracked, but only those above another user-selectable kinetic energy cut (default = 1 GeV) are stored in the KINE bank. The remainder are stored in the temporary STAK bank. The ability to store user-information has not been exploited in the E859 GEANT implementation.
- *VERT* - Stores the space-time 4-vector of the origin of every particle. Also stores pointers into the KINE bank for the parent track, the origin track and any daughter tracks. The ability to store user-information has been used to study secondary production processes.

After the particles in the event have been tracked through the detector systems, the experimental resolution needs to be applied and the data needs to be put into a format compatible with the programs used to analyze experimental data. This process is known as digitization. GEANT calls a user-written digitization subroutine. In E859, digitization routines are independent of routines in the rest of the Monte Carlo. So, for ease of maintenance and time considerations digitization was separated from the rest of the Monte Carlo into a program known as ZYBATCH. This program is described in more detail in section 3.9.2.

One final important task in an experimental simulation is that of visualization. Actually seeing what is happening during an event gives one a more intuitive understanding for a variety of things:

- Sources of background.
- Design weaknesses.
- Causes of reconstruction inefficiencies.

GEANT provides routines that allow the user to view any detector from any position in space. There are also routines which allow the display of simulated hits and tracks, or user-digitized

data. A program known as LOAD_DISPLAY processes the variety of data YBOS banks into a standard format readable by the display routines.

3.9.2 ZYBATCH

ZYBATCH is a program that processes GEANT ZEBRA output banks into YBOS banks appropriate for input to the analysis chain for "real" spectrometer data. This processing includes the menial task of format translation, the translation of absolute spatial coordinates of a track (this is the form of GEANT output) into geographical addresses (e.g., chamber, plane, wire) and the convolution of the GEANT output with instrumental resolution.

Accurate track reconstruction and PID demands careful matching between the physical locations of tracking and PID elements in the Monte Carlo, ZYBATCH and the analysis codes. These elements include every drift chamber and trigger chamber wire, every TOFW slat, every GASČ cell and every BACK pad. The procedure for determining the drift chamber wire positions is described in section 3.5.1. In this procedure the plane separation is allowed to vary. This is incompatible with our GEANT decription of the drift chamber volumes. Because of this a special geometry file was created in which the plane separations were forced to be equal to the design specifications. The internal consistency of the TR1/2 positions is enforced by obtaining the values from the same FORTRAN include file. The description of the TOFW is not entirely internally consistent because only the fat slats were surveyed. The experimental TOFW positions are obtained by minimizing track projection residuals to each slat. The surveyed fat slats are kept fixed and all slats in a panel are forced to lie in a line. The Monte Carlo TOFW is described as a series of panels, each tangent to *the same circle* with a radius and center fit to the surveyed positions of the fat slats. The maximum error on the position of any individual slat is $< 1\,\text{cm}$. The GASČ cells and BACK pads are each described by a plane and the angle of that plane with respect to the spectrometer axis. These quantities were determined for real data. But, I can find no documentation to indicate if this was done with survey values or a projection-residuals analysis similar to the positioning of the TOFW. The plane position and angle were difficult to extract from the relevant PID code, so their Monte Carlo positions were adjusted by minimizing projection residuals. The BACK counter is consistent to better than one pad and the GASČ position is consistent to within 3 mm [Sun94].

The drift chambers and the TOFW are the two most important examples of the application of instrumental resolution. Due to practical considerations we describe a drift chamber plane as a GEANT volume instead of each individual drift cell. We then use the known wire positions to predict which drift cells a track crossed. The total energy loss in a plane is divided into 100 eV

ionization events which are distributed randomly along the track's trajectory in that plane. A track will register a hit on the wires of every drift cell in which it has at least one ionization event. The width distribution of hits was taken from real data and peaked at 35 nsec. In order to simulate multi-hit blocking, two or more hits that overlap are combined into one wider hit. The position resolution distribution is a Gaussian with $\sigma = 200\mu$m. There are at least three drift chamber effects that are not taken into account:

- There is no simulation of electronic cross-talk. If included this effect would increase the local hit density creating more difficulties for reconstruction algorithms.
- The drift chamber wires are not included as separate volumes. Rather, their material is smeared out over the gas volume of the chamber. This affects the multiple scattering characteristics of the spectrometer.
- There are no systematic errors in the positioning of the wires in the Monte Carlo with respect to further analysis programs.

The TOFW has both ADC and TDC information. The arrival time of signals at both phototubes are independently smeared by $\sigma = 100/\sqrt{2}$ psec. The ADC output at each phototube is smeared according to a Poisson distribution with a mean given by the number of primary photoelectrons.

Finally, one must be careful to construct digitized Monte Carlo output banks with the same meaning as the corresponding experimental data output banks. Sometimes this means ignoring information available in the Monte Carlo that we have no access to in experimental data. As an example, consider the calculation of the drift time to a drift chamber wire. Inside ZYBATCH we have access to the distance each track passed from its struck wire and therefore the true drift time. In real data our timing information is limited to the sum of the drift time and the transit time, see section 3.5.2. We are forced to estimate the actual drift time assuming that the particle has $\beta = 1$ and make a transit time correction during reconstruction. To impose this ambiguity on Monte Carlo data, we have to pretend that we do not know the true drift time. Instead, we calculate the excess transit time due to $\beta < 1$,

$$\delta t = L\left(\frac{1}{v} - \frac{1}{c}\right), \tag{3.46}$$

and add it to the true drift time.

Chapter 4

Correlation Analysis

In this chapter, I will discuss all of the steps necessary to get from identified particles to extracted source parameters.[1] I will first summarize the HBT analysis environment. Next, I will discuss the $\pi^+\pi^+$ and K^+K^+ *Actual* distributions.[2] This will include a discussion of the cuts applied to the data, and a presentation of the number of pairs in the final data sets. It will also include a description of the two-particle acceptance correction (TPAC), made to account for spectrometer/tracking/PID inefficiencies that are dependent on two-particle quantities. Next, I will discuss generation of the *Background* distributions. This will include details of our implementation of the event-mixing procedure and details of how the resulting distributions are modified in order to correct for the Coulombic distortion of phase space in the data. Next, I will summarize the correlation function parameterizations used in this analysis and present the E859 acceptance for the different relative momentum projections. Finally, I will discuss the procedure used to fit correlation function histograms and extract source parameters.

4.1 HBT Analysis Environment

A great deal of effort went into creating a flexible HBT analysis environment. Demands on this environment were many and diverse:

- *Actual* and *Background* distributions must be stored in flexible data structures. A detailed listing of the quantities stored in these data structures is given in appendix D.

[1] If I were as literary-minded as my adviser, I could make an intelligent reference to Dante's journey in reverse.

[2] Throughout this chapter, *Actual* and *Background* are used in the sense of the correlation function numerator and denominator. See section 1.4.

- Cuts on the data, (e.g., track quality, multiplicity, momentum, etc.,) must be easy to make.
- Modifications for Coulombic phase-space distortion and two-particle acceptance must be taken into account.
- Source parameterizations must be trivial to add.
- Fit parameters must be estimated along with associated errors and correlations.

We decided to implement this environment within the framework of a VMS shareable-image version of the powerful CERN PAW [B+89b] program. Chuck Parsons developed the shareable-image version of PAW in order to allow the user to conveniently incorporate specialized additions into PAW.[3]

PAW is based on the KUIP [KUI91] command-line interpreter. KUIP allows subroutines (e.g., plot a histogram, fit a correlation function, etc.) to be called from within the PAW session. We used this feature repeatedly:

- A wide variety of cuts could be interactively defined.
- Histograms could be generated for different relative momentum projections, using different binning, different rapidity, different weighting (e.g., Gamow correction), etc., all defined on the command-line.
- Correlation functions of any dimensionality could be fit. The fit function and various MINUIT [JR92] options were declared on the command line.

KUIP also provides menu-driven on-line help which will hopefully make this environment usable for the next heavy ion HBT graduate student.

PAW also supports COMIS [COM92]; an interpreter, written in FORTRAN, that allows source-code to be directly executed from the command-line. COMIS has taught those of us spoiled by VMS the headaches that accompany a buggy compiler. But, despite the many expletives directed towards this software package over the years [Ste], it has been enormously useful. In the HBT analysis, the subroutines used to generate histograms and fit correlation functions each had the capability to call a user-defined COMIS function. With these functions, additional cuts could be made, or a new fit function could be tested.

In order to generate our three-dimensional correlation results, we needed to augment PAW with the capability to manipulate three-dimensional histograms. This was based on work

[3]This was an enormous time-saver because changes to the user's specialized additions could be made without having to relink all of PAW. It was also an important space-saver, since each group member could maintain his/her own modifications (small) and use one, standard, PAW executable (big).

initiated by Richard Morse, extended so that all standard histogram operations were nearly transparent to the user.

A more detailed writeup of all the programs used in this analysis can be found in [CSed].

4.2 *Actual* Distributions

In the following subsections I will discuss each of the cuts used to define a *good pair* for the *standard* $\pi^+\pi^+$ and K^+K^+ data sets and I will discuss additional cuts used to estimate systematic errors and to obtain information on the $\langle p^{pair} \rangle$-dependence and rapidity cut-dependence of the extracted source parameters. A description of the TPAC is included in section 4.2.5. Table 4.1 lists the names and purposes of all standard cuts. Table 4.2 lists the names and purposes of each of the non-standard cuts. Tables 4.3 and 4.4 list the numbers of pairs and events for the $\pi^+\pi^+$ and K^+K^+ *Actual* data sets respectively.

4.2.1 BTOF, INTPRE and INTFOL Cuts

As discussed in section 2.14.1, there is beam-counter logic to eliminate events which follow a preceeding event within 100 nsec (PRE), and to flag events which are followed by a succeeding event within 100 nsec (FOLLOW). It was also noted that there are windows in this logic, such that if a particle is preceded or followed within ≈ 3 nsec, it will be recorded as a valid event. This is a problem since these events will have distorted start-time information. Both beam particles in such an event will be within the BTOT ADC gate, producing a characteristically large BTOT signal. So, the standard technique for eliminating such events is to make a cut on the BTOT ADC spectrum.

Unfortunately, for at least some of the E859 run period, BTOT had an unidentified problem that severely distorted its ADC spectrum. For this reason, a cut was instead placed on the BTOF ADC spectrum. The arguments made for BTOT also apply to the BTOF, but the charge resolution is worse. Figure 4-1 shows the BTOF ADC spectrum for a subset of the K^+K^+ data. The top panel shows the spectrum for all events, and those events in which the FOLLOW bit was set. The bottom panel shows the spectrum for those events in which the FOLLOW bit was not set. From this second distribution one can clearly see two peaks corresponding to one and two beam particles within the BTOF ADC gate. These peaks are well described by Gaussians with $\sigma_Z \approx 1$. The mean of the second peak, $\mu_{Z=2} \approx 21.8$, is exactly the value predicted for two $Z = 14$ particles using $\Delta E = Z^{1.56}$, see section 3.2. The cut placed at $Z = 18$ eliminates unwanted events at the 3σ level.

	Name	Purpose
Event Cuts	BTOF	This cut is used to eliminate events in which the beam particle responsible for the recorded event is accompanied by a second beam particle so close in time that neither the PRE nor FOLLOW bits are set.
	INTPRE	This cut is used eliminate events in which the recorded event follows a second interaction within 1 μsec.
	INTFOL	This cut is used eliminate events in which the recorded event is followed by a second interaction within 1 μsec.
Track Cuts	TOFID	These cuts are my variation of the standard (PICD) PID decision.
	TR1·TR2	This cut eliminated tracks in which AUSCON failed to find a hit on both trigger chambers (TR1 *and* TR2).
Pair Cuts	Δ-Slat	This cut eliminates pairs whose tracks use the same TOFW slat.
	Scale Angle	This cut eliminates pairs whose angular separation in front of the magnet is small enough to guarantee hit sharing.

Table 4.1: Names and purposes of cuts used to define a *good event* for the *standard* data sets. See text for more details and actual cut values.

	Name	Purpose
Event Cuts	TMA	A software TMA cut was applied to the $\pi^+\pi^+$ and K^+K^+ data sets in order to examine the source parameters for the most central data sets possible.
Track Cuts	GASČ	GASČ information was used to verify the PID decision in the appropriate momentum regions.
	Rapidity	Kaons are much more massive than pions and therefore have a large tail of low-rapidity in our spectrometer acceptance. This cut was used to eliminate kaon tracks with $y < 1.3$ in order to optimize the K^+/π^+ acceptance overlap.
Pair Cuts	$\langle p^{pair} \rangle$	The HBT source parameters may depend on the the pair momentum, $\langle p^{pair} \rangle = \lvert\vec{p}_1 + \vec{p}_2\rvert$. This cut divided the $\pi^+\pi^+$ and K^+K^+ data sets into several bins with approximately equal numbers of pairs.
	Scale Angle	We doubled and tripled the standard scale angle cut in order to study systematic errors in the TPAC.

Table 4.2: Names and purposes of non-standard cuts. See text for more details and actual cut values.

$\pi^+\pi^+$	Pairs	Events
Standard	108283	95825
TMA	18400	16144
GASČ	96939	86519
$\langle p^{pair} \rangle$(GeV/c) < 650	30861	27502
650 < $\langle p^{pair} \rangle$(GeV/c) < 850	35192	31239
$\langle p^{pair} \rangle$(GeV/c) > 850	42230	37084
Scale Angle (radians) < 0.022	101483	89770
Scale Angle (radians) < 0.033	92313	81671

Table 4.3: Number of pairs in different $\pi^+\pi^+$ *Actual* data sets.

K^+K^+[a]	Pairs	Events
Standard	48840	47762
TMA	17771	17334
GASČ	38747	37793
$y > 1.3$	29453	28930
$\langle p^{pair} \rangle$(GeV/c) < 1050	22231	21727
$\langle p^{pair} \rangle$(GeV/c) > 1050	26609	26035
Scale Angle (radians) < 0.022	46228	45096
Scale Angle (radians) < 0.033	42785	41814

Table 4.4: Number of pairs in different K^+K^+ *Actual* data sets.

[a]The K^+K^+ data set is composed of two roughly equal data sets taken in February 1991 and March 1992. The Feb91 and Mar92 data sets were taken with a 1% and 2% interaction-length targets respectively. The TMA response was also somewhat different.

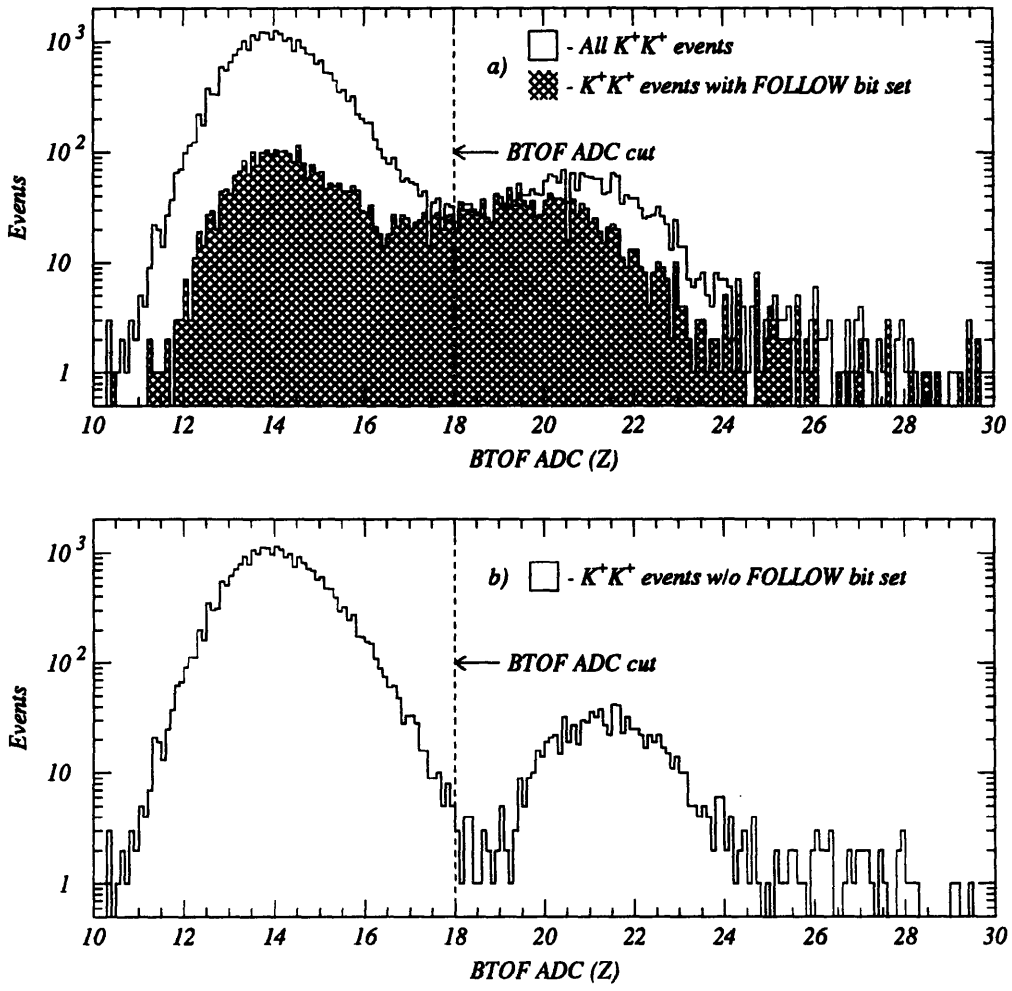

Figure 4-1: BTOF spectrum for K^+K^+ events. The top panel shows the BTOF spectrum for events with 2 K^+'s and for the subset of such events with the FOLLOW bit set. The bottom panel shows the same distribution for the subset of K^+K^+ events in which the FOLLOW bit was not set. The two clearly separated peaks indicate events in which one and two ^{28}Si nuclei pass through the BTOF counter within the ADC gate. The cut on BTOF < 18 is indicated by the dashed lines.

We decided to keep those FOLLOW events that passed the BTOF cut. We wanted to include such events since microstructure in the beam spill caused the FOLLOW bit to be set in as many as 1/3 of all events in the March 1992 data set. We justify this decision on the following grounds:

- If the energy deposited in the BTOF indicates that there was only one ^{28}Si nucleus within the ADC gate, then the second particle must have come late enough to avoid interfering with the start-time measurement. Recall that the beam counters use leading-edge discriminators and the rise-time until threshold is ≈ 1 nsec.
- The ratio of events with and without the FOLLOW bit set is identical for K^+K^+ events and minimum bias events.

Depending on target thickness, a second target interaction will occur in 1-2% of those events with the FOLLOW bit set. Such events need to be eliminated from consideration since any resulting particles will distort those detectors with relatively long response time (e.g., TMA, drift chambers) and those without multi-hit capability (e.g., TOFW). Because of the large FOLLOW rate in the March 1992 run, INTPRE and INTFOL were installed into the beam-counter logic. These signals flagged events in which an interaction occurred within 1μsec of the current event. Cutting on these bits eliminated 5-10% of the events during the time in which it was installed.

4.2.2 TOFID

HBT measurements are sensitive to misidentified particles. The presence of nonidentical particles in an *Actual* distribution will manifest itself as an apparent reduction in the correlation strength, i.e., the coherence parameter λ. In principle this should not affect the extracted radius parameters, but λ and the radius parameters are correlated in the fit procedure. Section 3.8 details the standard PID decisions. Three modifications were made to satisfy the specialized needs of this analysis. In this section I will list and justify those modifications. Figure 4-2 is a modified version of figure 3-13, showing my PID decisions. In appendix A, I will estimate the impact on this analysis of contamination due to misidentification.

- π^+'s which fail to fire the GASČ will be misidentified as K^+'s in those $1/\beta$ vs p region where the pion and kaon TOF identification regions overlap. In this region, π^+ contamination of the K^+ sample can reach as high as 5%, see [Mor94]. In order to avoid this, regions where pion and kaon TOF identification regions overlap beyond 3σ are eliminated.

- As shown on page 41, single-particle efficiencies cancel in the correlation function determination. Thus, it was not important that the PID decision be symmetric around $\delta\beta = 0$. Because of this, and since multidimensional HBT analyses place a premium on statistics, it was decided accept particles with momentum greater the $\pi/\mathrm{K}\ 3\sigma$ overlap momentum ($p = 1.8\mathrm{A} \cdot \mathrm{GeV/c}$) if they were in a region uniquely identified by TOF.

- Under conditions discussed in section 3.8, PICD adds the energy from adjacent GASČ cells when using the GASČ in a PID decision. This will change the GASČ efficiency for two close tracks. [Sol94]. GASČ information was ignored since Monte Carlo work needs to be performed to understand any contribution this may make to the TPAC. This does not affect kaons since they were only identified in regions where the TOFW information was unambiguous. For pions above 0.5 GeV/c this results in e^+ contamination of the π^+ sample which is less than 7% everywhere, and much less at lower momenta.

4.2.3 TR1·TR2 Cut

We eliminated tracks for which AUSCON failed to find a hit on both trigger chambers (TR1, TR2). Such tracks should not have satisfied the trigger. But, they could have been preferentially accepted or rejected depending on some event characteristic. As an example, consider a pair of tracks, one of which failed to fire its corresponding TR2 wire. If, and only if, the tracks are close together (within the programmed search width on TR2) the *LVL2* tracking algorithm would have been able to verify both tracks by reusing the TR2 wire that did fire. This particular type of trigger bias is especially dangerous since it distorts the low-relative momentum phase space vital to the HBT measurement.

4.2.4 Δ-Slat Cut

Pairs were eliminated if both tracks used the same TOFW slat. Such tracks were likely to be ghosts. If they were real, their time-of-flight would be distorted since the TOFW does not have multihit capability. Tracks were kept if they shared a slat with a non-identical particle, but this was rare.

4.2.5 Scale Angle Cut, Two-Particle Acceptance Correction (TPAC)

As discussed in section 3.7, reconstruction becomes difficult when tracks are very close to one another. The local hit density becomes very high. And, despite careful design of the drift-

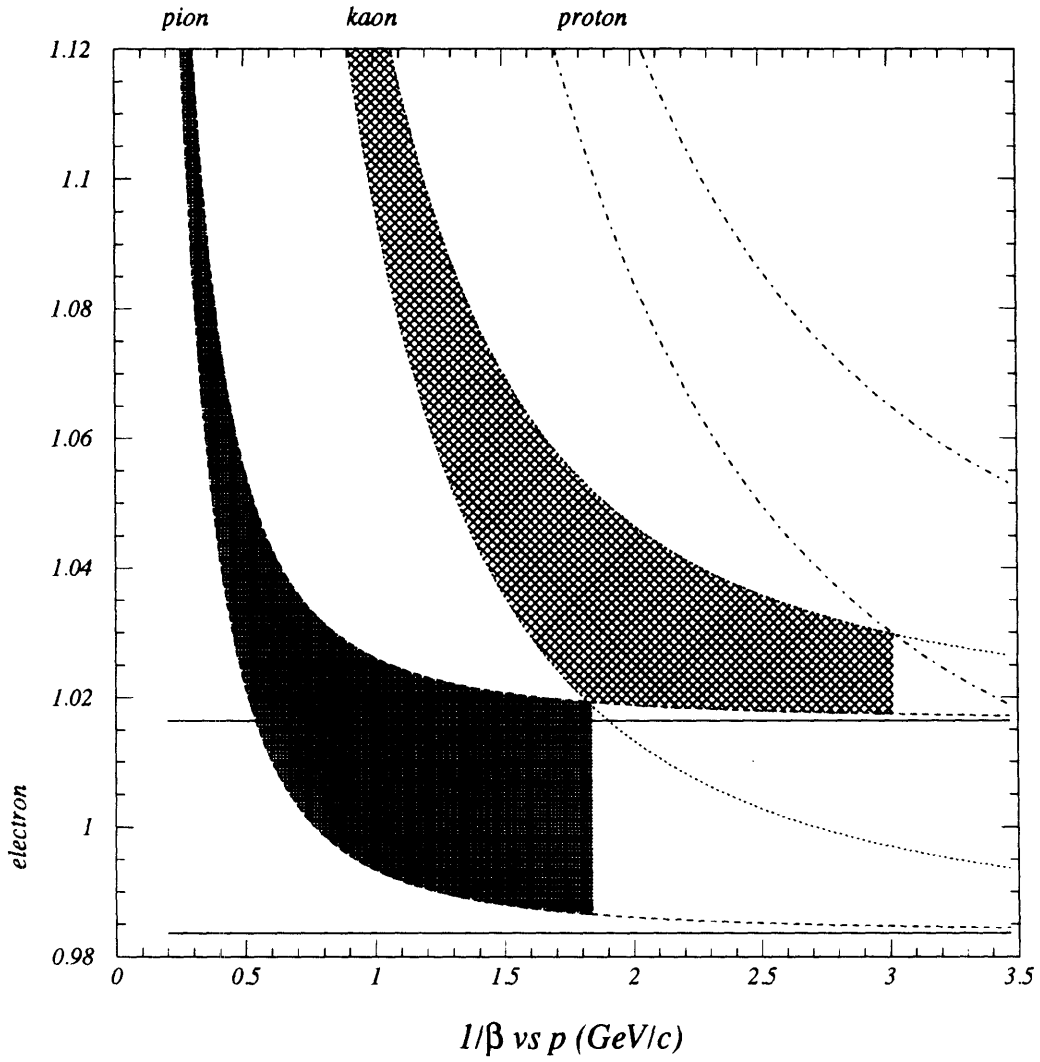

Figure 4-2: Illustration of the PID decisions used in this analysis. Valid kaons and pions must be within their respective TOF identification regions and must pass the standard energy-loss cut. GASČ information is ignored.

chamber readout electronics, see section 2.8, two hits within 2 mm along a given view direction will be recorded as one hit with the lead-time of the closer particle. This second effect is known as multihit-blocking. These problems are greatly magnified in front of the magnet since tracks that are close at one z-plane will be close throughout their entire trajectory. Section 1.4 showed that while single-particle inefficiencies do not affect correlation measurements, such two-particle inefficiencies must be accounted for.

This effect was examined by Ron Soltz using the Si+Au$\rightarrow 2\pi^-$ data set. An *Actual* distribution was generated in which all π^- pairs, and thus the bulk of the Bose-Einstein correlations in this data set, were eliminated. No attempt was made to correct for Coulombic distortion, but since same-sign and opposite-sign pairs were included, this effect is expected to cancel. The corresponding event-mixed *Background* distribution was generated, and the ratio of these two distributions was formed. This ratio should be flat everywhere since all known correlations have been removed.

Figure 4-3 shows this ratio as a two-dimensional histogram in the variables δy vs δx, where:

$$\delta x \equiv z_{T1}\left(\frac{p_{x1}}{p_{z1}} - \frac{p_{x2}}{p_{z2}}\right), \tag{4.1a}$$

$$\delta y \equiv z_{T1}\left(\frac{p_{y1}}{p_{z1}} - \frac{p_{y2}}{p_{z2}}\right), \tag{4.1b}$$

are the projections of the angular separation at the mid-plane of T1. There is a pronounced, elliptical dip in the region around $\delta x = \delta y = 0$ indicating the expected inefficiency for close tracks. The depleted region extends about 1 cm in δx and about 2 cm in δy. The reason the ellipse is elongated in the δy-direction is not firmly established. I believe that the reason is a combination of the AUSCON algorithm, which searches for T1T2X tracks and T1T2Y tracks independently, and the fact that there are more T1T2 x-planes (7) than y-planes (5). It may also be due to the fact that, because of their angles, the UV planes give primarily X information.

This same distribution was generated for a Monte Carlo data set, see section 3.9 for a detailed discussion of the E859 implementation of the GEANT Monte Carlo package. 200,000 events were generated with $2\pi^-$'s[4] chosen according to

$$\frac{dn}{dm_\perp} \sim m_\perp \exp\left(-m_\perp/A\right), \tag{4.2}$$

where A was obtained from fits to E802 data [Par92]. The target was 1.5% interaction lengths

[4]We expect the close-pair inefficiency in the chambers to be largely due to reconstruction problems and thus independent of particle type.

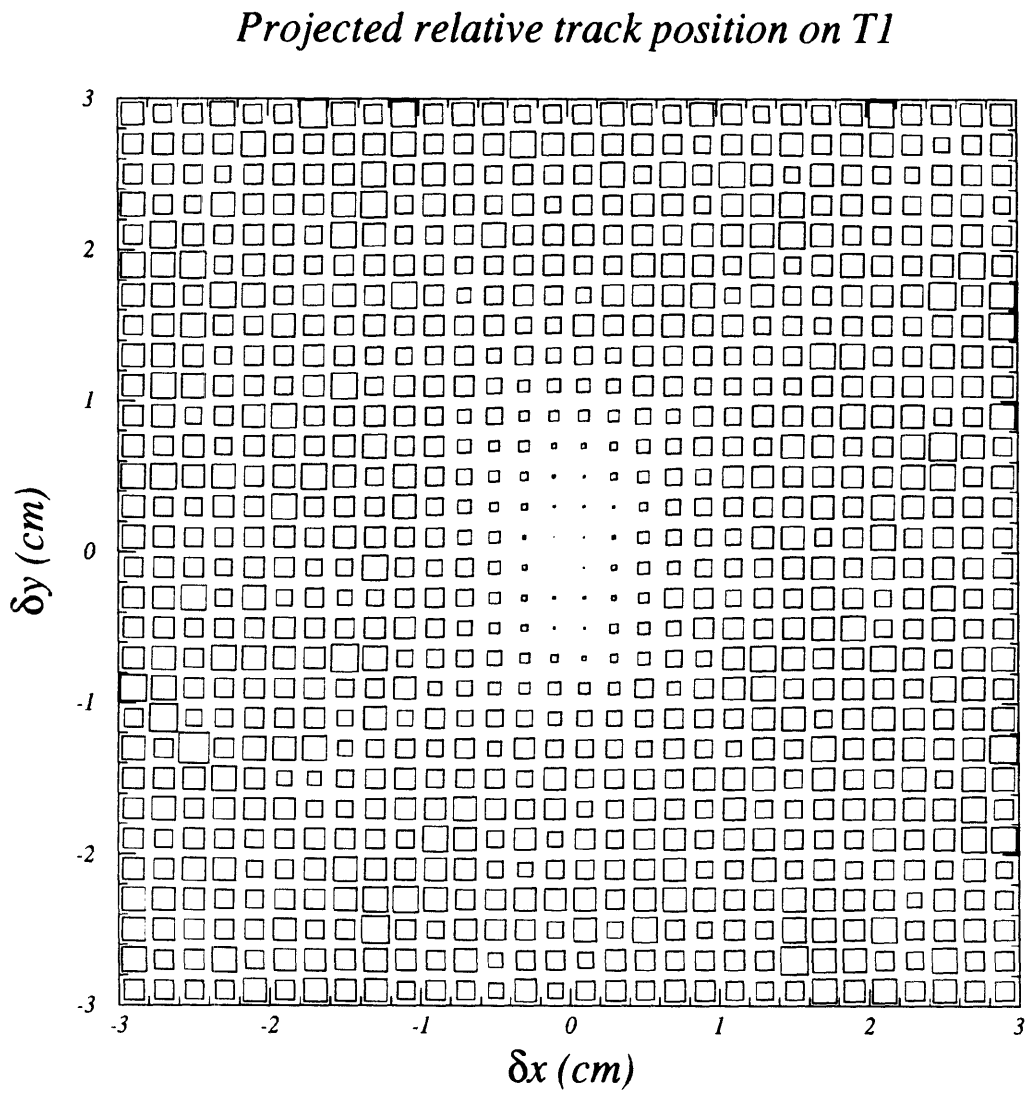

Figure 4-3: Correlation function for non-identical particles as a function of δy vs δx. This shows the inefficiency for spatially close pairs. From [Sol94]. See text for details.

of gold in order to interpolate between the Feb91 and Mar92 target thicknesses. All physics processes were turned on. The Moliere multiple scattering option was selected. Digitized events were analyzed with the same AUSCON and PICD executables as the spectrometer data.

This distribution, for both spectrometer data and Monte Carlo data, was fit with a two-dimensional Gaussian:[5]

$$A/B = N\left[1 - \lambda \exp\left(-\frac{\delta x^2}{2\sigma_x^2} - \frac{\delta y^2}{2\sigma_y^2}\right)\right]. \tag{4.3}$$

N is an overall normalization to account for the different number of pairs in the *Actual* and *Background* distributions. λ is a parameter to take into account partial efficiency at the smallest separations. σ_x and σ_y are the widths of the distribution in the x- and y-directions. Fit parameters for both distributions are given in table 4.5. These fit values were found to

Parameter	Data	Monte Carlo
σ_x	0.46 ± 0.01	0.45 ± 0.02
σ_y	1.26 ± 0.03	1.30 ± 0.06
λ	0.89 ± 0.02	1.00 ± 0.01

Table 4.5: Two-Particle Acceptance Correction parameters, from [Sol94]. See text for details.

be insensitive to elimination of pairs which shared a TOFW slat and elimination of pairs with spatial separation small enough to be in a region where the efficiency was below 50%.

σ_x and σ_y for spectrometer and Monte Carlo data are remarkably similar, indicating that the Monte Carlo provides a good description of the spectrometer response function. The value of λ is smaller for spectrometer data than it is for Monte Carlo data. This indicates a lower efficiency in the Monte Carlo data at smallest separations. This is more clearly shown in figure 4-4 where slices of these distributions ($|\delta x| < 0.6$ cm and $|\delta y| < 0.6$ cm) are plotted along with the fit functions evaluated at the centers of these slices.

This discrepency can be qualitatively explained by noting that the Monte Carlo data set was generated without any tracks besides the pair of interest and electronic noise was not simulated. Two tracks can be so close together that their hits *should* be completely blocked leaving AUSCON with no way to reconstruct both of them. This is precisely what is seen in the Monte Carlo. But, in real life, there are sources of hits (extra tracks, cross-talk, etc.) that are not associated with the reconstructed track. AUSCON can use these extra hits to find a second

[5]For historical reasons the TPAC is applied to the *Actual* distribution. As a result, the applied correction is the inverse of this fit function.

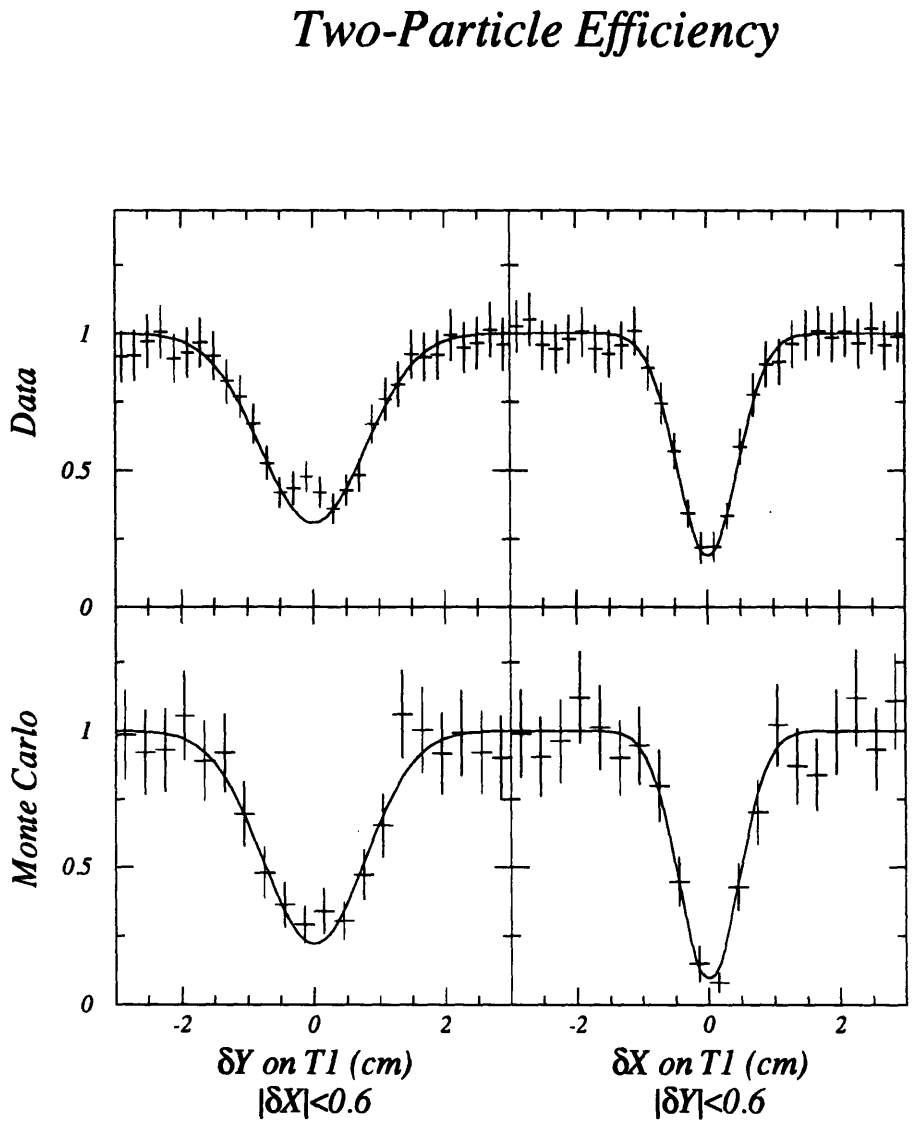

Figure 4-4: TPAC $|\delta x| < 0.6\,\text{cm}$ and $|\delta y| < 0.6\,\text{cm}$ slices. The top and bottom panels show the distribution for spectrometer data and Monte Carlo data respectively. From [Sol94]. See text for details.

track.

Two tracks that are spatially separated by an amount less than some value, ϵ, must necessarily be reconstructed using incorrect hits. For this reason we apply a cut to the data, known as the *scale angle cut*. This cut eliminates regions in δy vs δx where equation 4.3 falls below 50%, or equivalently, regions where the TPAC rises above 2. The δx value of a pair is scaled by $\sigma_x/\sigma_y = 2.75$, and the applied cut is of the form:

$$(2.75\,\delta x)^2 + (\delta y)^2 < (0.011 \cdot z_{T1})^2 \,. \tag{4.4}$$

Heated discussion surrounded the decision to parameterize the TPAC and scale angle cut in terms of the angular separation. This parameterization fails to take into account the pair separation at the target. It is therefore not a direct measure of pair separation at the drift chamber planes — the quantity in which we expect to see the inefficiency manifested. An argument was made to instead use the measured spatial separation at each chamber z-plane. But, the chosen parameterization was simple and it worked well. In the end, its use was rationalized in the following manner:

> The only pairs that are affected are those which are close on *all* planes in front of the magnet. These *must* be pairs with the smallest angular separation. Some fraction of these parallel pairs are spatially separated, and this could be seen by examining their target separation. But, this will simply result in an incomplete inefficiency when parameterized in terms of the angular separation.

Projections of the TPAC into various relative momentum projections are given in appendix A.

4.2.6 TMA Cut

The expectation of a dependence of extracted parameters on the centrality can be motivated by simple geometry. One expects the size of the particle production zone to increase with decreasing impact parameter as more and more nucleons participate in the collision. Such a dependence has indeed been observed by E859 in a variety of heavy ion collisions, see [Sol94] and references therein.

The details of how to set the hardware TMA threshold are discussed in section 2.14.2. For the data used in this analysis, the hardware TMA threshold was set to accept roughly the upper 10–15% of the minimum bias TMA distribution. Representative minimum bias TMA distributions, and the TMA distributions accepted by the TMA trigger are shown in figure 4-5. The hardware threshold is not sharp, and the triggered centrality varied by up to 5% [Wan].

As a test, we applied sharp, ultra-central software TMA cuts to the data. We want to avoid averaging over different centralities as this may result in distorted source parameters. It is interesting to examine the most central data set possible to see if anything interesting (e.g., the QGP) shows up.

The TMA cut was applied to the standard data sets such that only the most central 20,000 $\pi^+\pi^+$ and K^+K^+ pairs were accepted. For the $\pi^+\pi^+$ data set this is straightforward. The K^+K^+ data set was taken over two different run periods for which the TMA response was slightly different. A different TMA cut was applied to the Feb91 and Mar92 K^+K^+ data sets such that the same fraction of the K^+K^+ pairs in each data set were kept. Table 4.6 shows the TMA cuts applied to the different data sets. Figure 4-6 shows the TMA distributions for the different data sets and the applied cuts.

$\pi^+\pi^+$	K^+K^+ (Feb91)	K^+K^+ (Mar92)
147	139	117

Table 4.6: Minimum TMA values applied in ultra-central tests.

4.2.7 GASČ Cut

We wanted to examine the effect of contamination that results from ignoring the GASČ information in regions of ambiguous TOF PID. To do this, we merely needed to use the standard PICD PID decisions. Even in this test we eliminated kaons which were in the π/K TOF identification overlap region. Estimates of the systematic errors resulting from particle misidentification are given in appendix A.

4.2.8 Rapidity Cut

Figure 4-7 shows the accepted phase space, in y vs $p_\perp$, for pions and kaons in the standard data sets. The low-y tail in the kaon distribution is a result of their large mass relative to the pion. We wanted to optimize the acceptance overlap of pions and kaons so that we were comparing apples to oranges.[6] Low-y particles preferentially contribute to low-q, and we wanted to be sure that including these particles in the K^+K^+ data set did not distort the extracted parameters.

[6]Yes, this is correct. We want to compare apples to oranges (pions to kaons), but not apples to oranges *and* bananas (pions to low-y *and* high-y kaons).

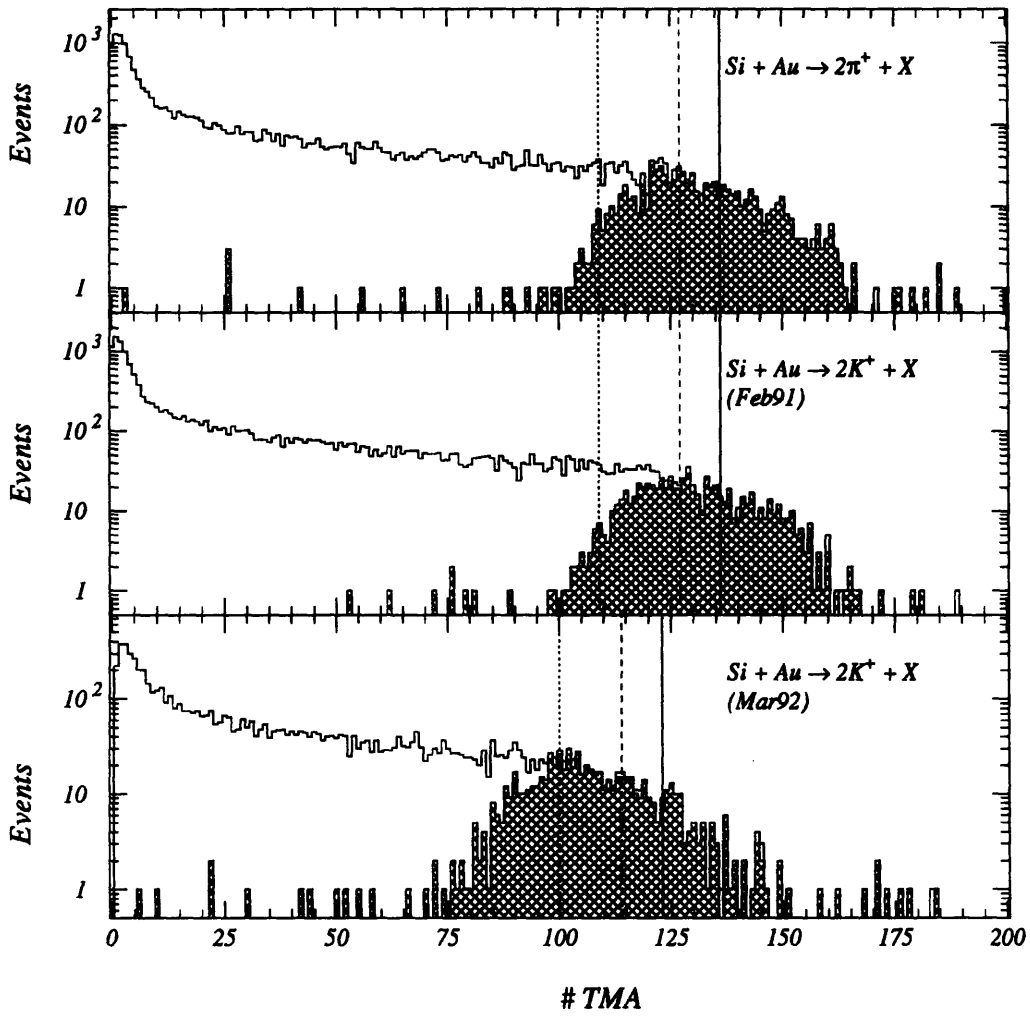

Figure 4-5: TMA distribution for *INT* triggers and TMA triggers (hatched regions) for sample runs in the three run periods. These distributions have not been target-out corrected. Vertical lines indicate the upper 4% (solid), 7% (dashed) and 15% (dotted) of the minimum bias TMA distributions determined offline [Wan].

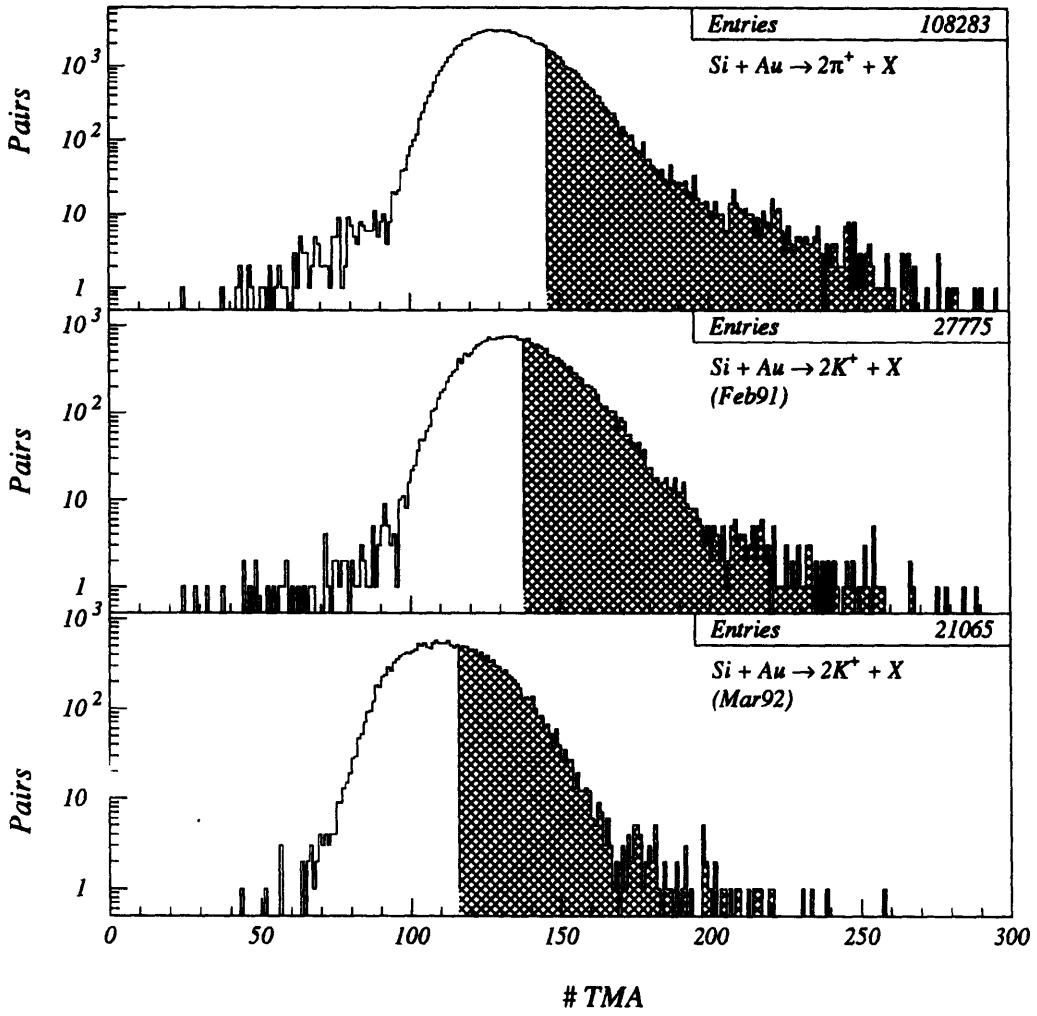

Figure 4-6: TMA distributions for different pair data sets. Hatched regions indicate the applied software TMA cuts.

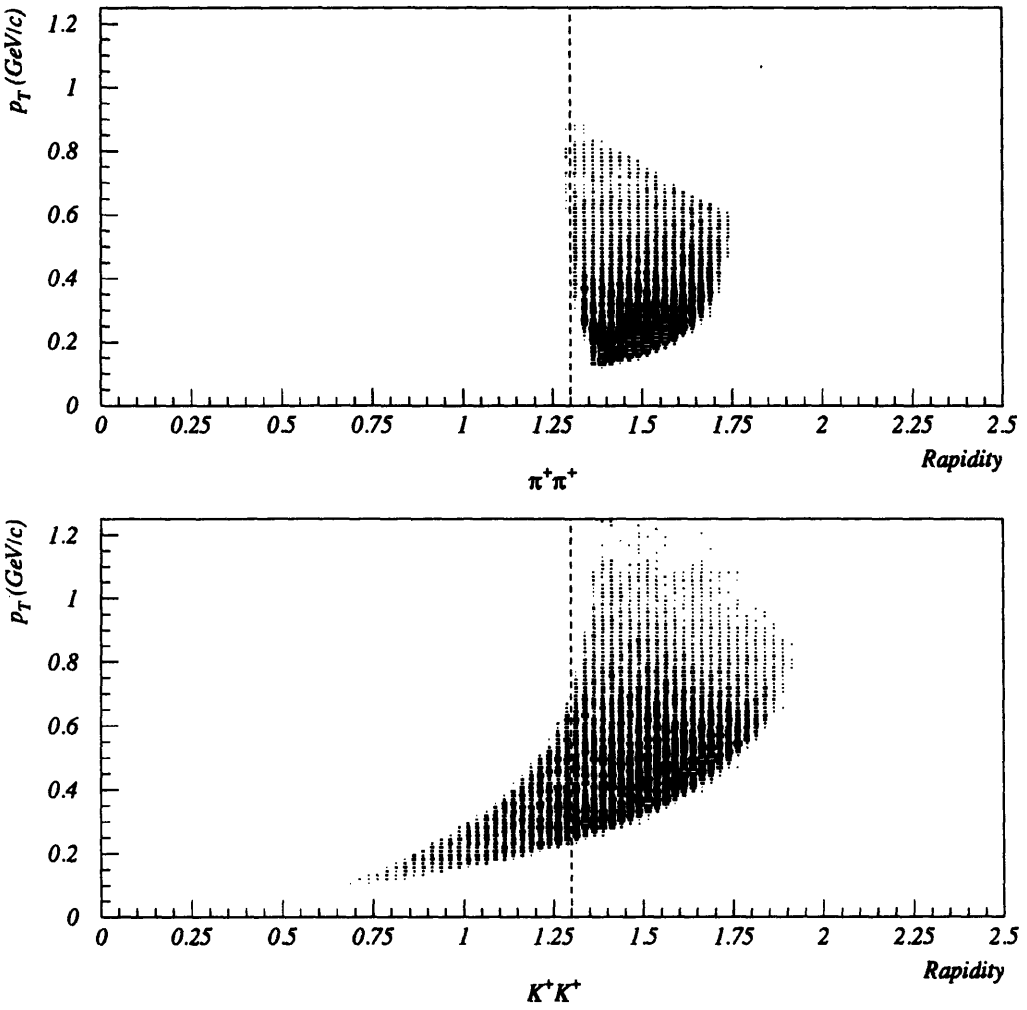

Figure 4-7: y vs $p_\perp$ phase space for pions and kaons in the *standard* data sets. The cut applied to the kaons, $y > 1.3$, is indicated by the dashed line.

4.2.9 $\langle p^{pair} \rangle$ Cut

Extracted source parameters may depend on the average monentum of the pair:

$$\langle p^{pair} \rangle \equiv \frac{\vec{p}_1 + \vec{p}_2}{2}. \tag{4.5}$$

Pratt [Pra84] suggests a $\langle p^{pair} \rangle$-dependence arising from an exploding source. A $\langle p^{pair} \rangle$-dependence could also arise from different momentum distributions of directly produced particles compared to resonance products. $\langle p^{pair} \rangle$ and $\vec{q}$ are correlated such that low-$\langle p^{pair} \rangle$ pairs do not populate high-$\vec{q}$ phase space and vice-versa. Despite these difficulties, we were able to divide the $\pi^+\pi^+$ data set into three $\langle p^{pair} \rangle$-bins and the K^+K^+ data set into two $\langle p^{pair} \rangle$-bins. Figure 4-8 shows the $\langle p^{pair} \rangle$-distributions for the two different standard data sets and the applied cut values. The cut values were chosen such that bins for each particle species have an approximately equal number of pairs.

4.3 *Background* Distributions

Some specific details of our implementation of the event-mixing algorithm are worth special note:

- Pairs in the *Background* distribution are taken from completely randomly selected events.
- Pairs in the *Background* distribution are allowed to repeat.
- Fluctuations in the *Background* distributions are assumed to be described by Poisson statistics.
- Pairs in the *Background* distributions are only selected from valid pairs in the corresponding *Actual* distribution.
- Coulomb distortion of phase space is incorporated into the *Background* distributions with the standard Gamow correction.
- Residual correlations in the *Background* distributions have been examined and found to be negligible.

Each of these items will be discussed in detail below.

Once the *Background* distributions are generated they must be cut identically to the corresponding *Actual* distributions. The cuts are described in section 4.2. Table 4.8 and Table 4.7 give the number of *Background* pairs for the different data sets.

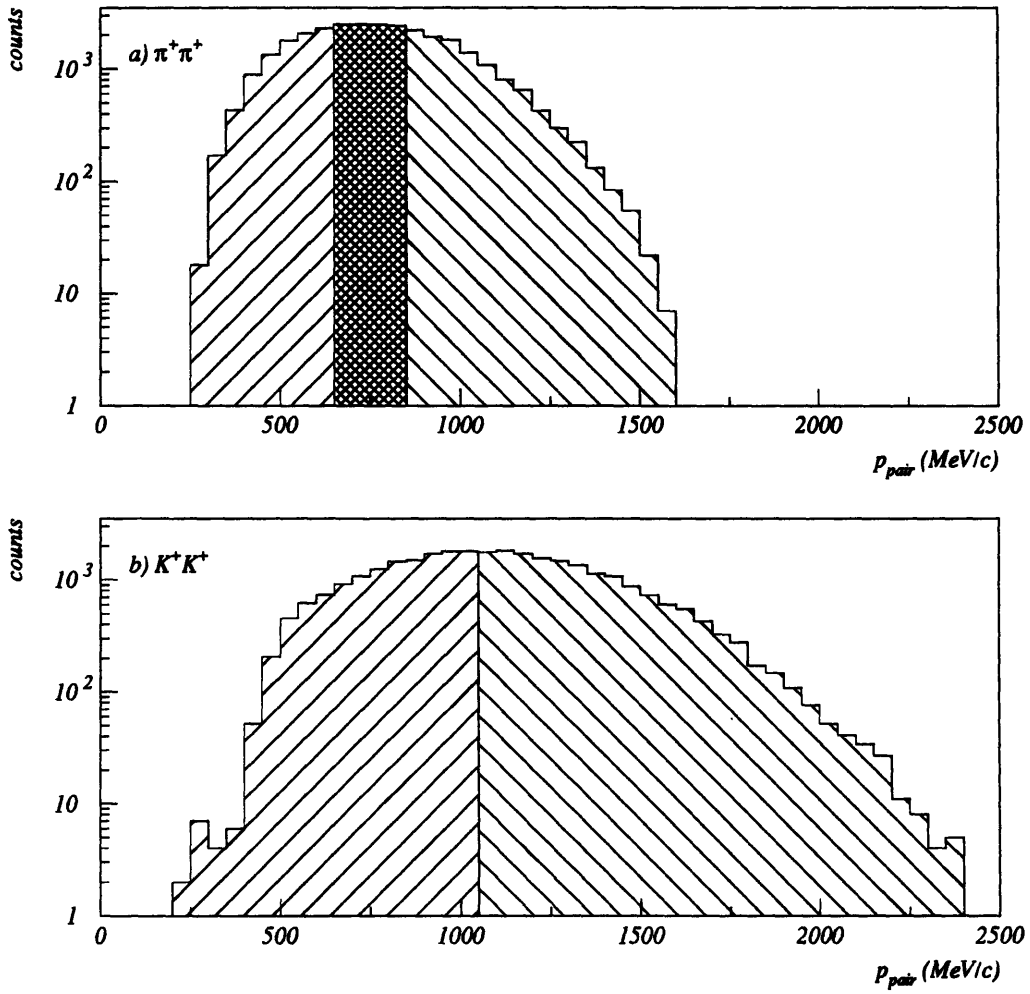

Figure 4-8: Illustration of different $\langle p^{pair} \rangle$ bins used to study the $\langle p^{pair} \rangle$-dependence of extracted source parameters. Cuts were selected so that bins for each particle species have an approximately equal number of pairs.

$\pi^+\pi^+$	Pairs
Standard	600000
TMA	300000
GASČ	600000
$\langle p^{pair} \rangle$(GeV/c) < 650	179403
650 < $\langle p^{pair} \rangle$(GeV/c) < 850	183598
$\langle p^{pair} \rangle$(GeV/c) > 850	236999
Scale Angle (radians) < 0.022	557953
Scale Angle (radians) < 0.033	508866

Table 4.7: Number of pairs in different $\pi^+\pi^+$ *Background* data sets.

K^+K^+	Pairs
Standard	300000
TMA	150000
GASČ	300000
$y > 1.3$	183847
$\langle p^{pair} \rangle$(GeV/c) < 1050	134567
$\langle p^{pair} \rangle$(GeV/c) > 1050	165433
Scale Angle (radians) < 0.022	282605
Scale Angle (radians) < 0.033	261763

Table 4.8: Number of pairs in different K^+K^+ *Background* data sets.

4.3.1 Random vs Serial Sampling

We mix bosons from completely random events. This is different than mixing serial events, e.g., mixing a boson from one event with bosons from the next N events. The motivation behind this choice was the presence of super-Poisson fluctuations in an event-mixed *Background*. This was first noted in [Zaj82, Z+84] which examined a simplified problem - the calculation of the area of a square box using a Monte Carlo event-mixing technique. As described in section 3.9, the standard technique for such a calculation consists of picking a set of N random coordinate pairs, and calculating the area from the fraction that fall inside of the box. In the event-mixing technique, we choose $M = \sqrt{N}$ random numbers and form all N unique coordinate pairs. Taking the binomial nature of the problem into account, the errors on the determination of the area can be written as:

$$\frac{\sigma_{N\Omega}}{N\Omega} = \frac{\sqrt{2\left(1-\Omega^{1/2}\right)}}{(N\Omega)^{1/4}} \tag{4.6}$$

This indicated that, for the box model, the *Background* fluctuations could *never* be small compared to the *Actual* fluctuations, and would have to deviate very rapidly from Poisson.

This model was extended to the more general case in which $N < M^2$ pairs are mixed [Sol94].[7] In this case, the formula for the error on the determination of the area was found to be:

$$\frac{\sigma_{N\Omega}}{N\Omega} = \sqrt{\frac{2\left(1-\Omega^{1/2}\right)}{M\Omega^{1/2}} + \frac{1-\Omega^2}{N\Omega}\left(1-\frac{1}{N}\right)} \tag{4.7}$$

It is easy to verify that equation 4.7 reduces to equation 4.6 for $\lim_{N\to M^2, M\to\infty}$. It is also easy to verify its Poisson nature for $\lim_{N\to 0}$.

Random mixing was chosen over serial mixing because, in Monte Carlo studies with this model, random mixing was found to retain Poisson fluctuations for larger values of N [Sol94]. To get an intuitive feeling for this consider the following, admittedly handwaving, argument. Both serial and random mixing use the same particles in more than one pair. This means that the relative-momenta of different pairs are not independent — this is the origin of the super-Poisson fluctuations. In serial mixing there is even less independence. Table 4.9 shows a few pairs generated in the two different mixing schemes. In the serial mixing case, the pairs that use events 1,2 and 1,3 are not independent, and the pair that uses events 2,3 is related to both of these pairs. Let us contrast this with the random mixing case. The pairs that use events 1,11769 and 1,66721 are not independent, but the pair that uses 11769,66721 is not

[7] This is more relevant to our analysis since we cannot hope to use all, $\frac{(10^5)^2}{2} = 5 \times 10^9$, possible *Background* pairs.

likely to be chosen if we are only mixing a small fraction of the available pairs.

Serial Mixing	Random Mixing
1 , 2	1 , 11769
1 , 3	1 , 66721
.	.
.	.
.	.
2 , 3	~~11769 , 66721~~

Table 4.9: Comparison of pairs used in serial and random mixing techniques. The event number for two pairs which use event 1 are shown. With serial mixing the third pair in this correlated triplet is always used. With random mixing this pair is almost never used.

4.3.2 Fluctuations

Despite the concerns expressed in the previous section, *Background* fluctuations were assumed to be Poisson distributed. This decision was based on:

- Simplicity.
- Extension of the box model, discussed above, to a geometry more closely resembling relative momentum. Results of this study suggested that deviations from Poisson fluctuations are not as severe in relative momentum bins as they are for the simple box model.
- Calculations showed fluctuations in the data to have negligible deviations from Poisson.

Figure 4-9 shows the geometry used in the extension of the box model. This geometry is the closest we were able to get to the elusive goal of extending the box model to a general expression for *Background* fluctuations in a relative momentum bin. For this geometry, it was found that fluctuations *could* be reduced below those of the parent distribution with the limiting value given by the bin size [Sol94].

Fluctuations in the data were studied using a technique similar to that in [Mor90]. First, the *Actual* distribution was split into several subsets. Each subset was used to generate an ensemble of *Background* distributions. Histograms were made of the number of counts in each relative momentum bin for every *Background* distribution. These histograms were well-fit by Gaussians. For the case in which a given pair in the *Actual* distribution is used ≈ 10 times,[8]

[8]This case corresponds well to the fraction of possible pairs used in the real analysis.

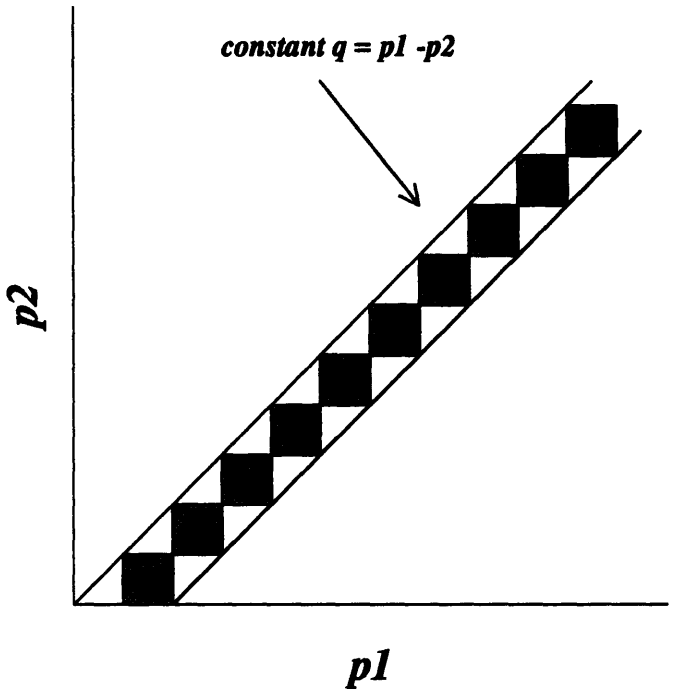

Figure 4-9: Illustration of the super-Poisson box model extended to a relative momentum-like geometry. If we consider each axis to represent a momentum component from a different particle, then a diagonal slice corresponds to relative momentum ($q = p_1 - p_2 = constant$). For reasons discussed in [Sol94] we had to restrict ourselves to the hatched regions which consist of squares with their corners touching.

the fitted variances were found to agree with those predicted for Poisson fluctuations. For the case in which all $N^2/2$ *Background* pairs were formed the fitted variances were found to significantly deviate from those predicted for Poisson fluctuations. Figure 4-10 compares the Poisson and box-model predictions for these two cases. The reader is directed to [Sol94] for many more details.

4.3.3 Repeating Pairs

For convenience, our event-mixing technique allows the same *Background* pair to be repeated. The effect of this is expected to be negligible since 10^5 events gives 2×10^{10} unique pairs, of which we use only $\approx 10^6$. Pairs which use tracks from the same event are not allowed.

4.3.4 Pair Selection

All particles in the *Background* distribution use tracks from valid pair events in the *Actual* distribution. This has the advantage of insuring identical event character (e.g., centrality) in the *Actual* and *Background* distributions.

4.3.5 Gamow Correction

We correct our *Background* distributions for the Coulomb distortion of phase space with the standard Gamow factor. The Gamow factor is correct in the limit of a point-like source. Zajc [Zaj82] expresses the low-Q limit[9] of the true Coulomb correction, C, in terms of the Gamow factor, G, and a power series in $<r> /\alpha_0$:

$$C = G\left(1 + \langle r\rangle/\alpha_0 + \mathcal{O}\left(\langle r\rangle/\alpha_0\right)^2 + \cdots\right) \tag{4.8}$$

where $\langle r\rangle$ is the average radius of the emitting source, and α_0 is the Bohr radius.

In principle, the Gamow factor could be modified in an iterative procedure. In practice, this effect is usually ignored since for pions, $\alpha_0 = 194.3\,\text{fm}$, and for kaons, $\alpha_0 = 55.1\,\text{fm}$. Systematic studies have found the effect of not using the full Coulomb correction to be small.

4.3.6 Residual Correlations

The phase space in event-mixed *Background* distributions is distorted by an integration over unobserved Bosons. This effect, known as *residual correlations*, was first noted in [Zaj82].

[9] In the high-Q limit, both corrections converge to 1.

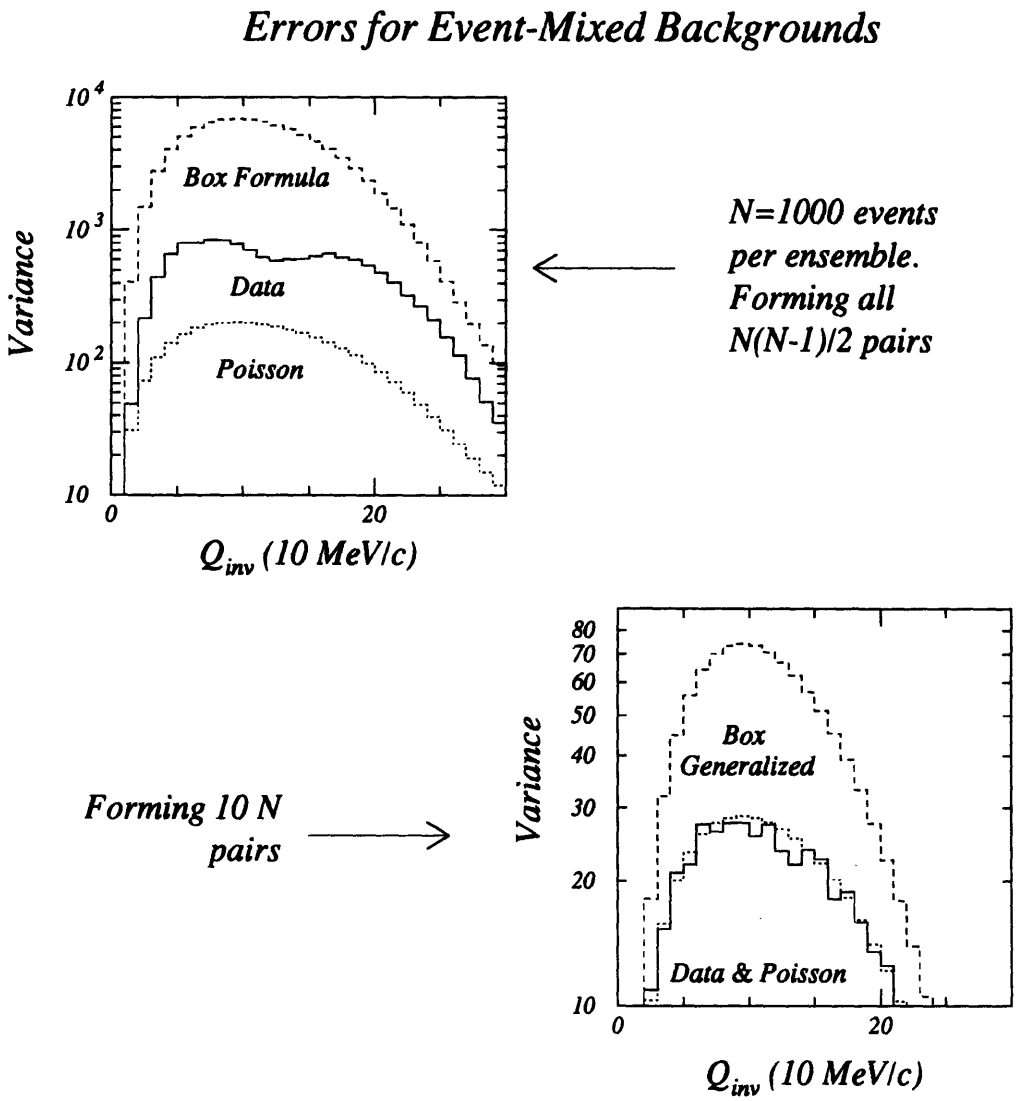

Figure 4-10: These two plots compare the calculated variance for event-mixed *Background* distributions, as a function of Q, to predictions from Poisson statistics and the box-model described in the text. The top panel shows the case in which all $N^2/2$ possible *Background* pairs are generated from each *Actual* pair. The observed variances are observed to be significantly greater than those predicted by Poisson statistics, but significantly less than those predicted by the box-model. The bottom panel shows the case in which only 10 *Background* pairs are generated from each *Actual* pair. The observed variances are well described by Poisson statistics. From [Sol94].

A detailed derivation of this effect, and results of a study performed for the E859 acceptance is given in appendix B. The impact of residual correlations on this analysis is small.

4.4 Relative Momentum Acceptances

Figures 4-11— 4-20 show the E859 acceptance for the different relative momentum projections. In these figures and throughout this analysis, all relative momenta are calculated at $y = 1.25$. This is the ^{28}Si + ^{197}Au participant center-of-mass rapidity, which is expected to be the source-rapidity for central collisions.

4.5 Fitting

Let's assume we have chosen a fit parameterization, and generated the corresponding correlation function histogram. We are left with the problem of extracting the source parameters and estimating the errors on these parameters. Both of these problems are solved by minimizing the difference between the correlation function parameterization and the experimental data. Simple to say, not so simple to do.

In this analysis, parameter estimation is performed with the CERN MINUIT [JR92] software package. This package minimizes any multi-parameter user-function. We used the MINI option which first minimizes with the MIGRAD algorithm, defaulting to the SIMPLEX algorithm if MIGRAD fails to find a minimum. MINUIT returns parabolic error estimations given by the change in the function value which results in a change in the user-function, $\Delta f = 1$. With the MINOS option, the errors are calculated while reminimizing with respect to all variables other than the ones examined. This method was used to calculate the confidence contours, shown in chapter 5, in order to remove cross-correlations.[10] Any bins for which there were no counts in either the *Actual* or *Background* distribution were eliminated.

The rest of this section is devoted to motivating and deriving the user function minimized for parameter estimation. For most of this discussion I will follow the notation in [Zaj90].

The standard function used in parameter estimation is the chi-squared distribution, given by:

$$\chi^2_C \equiv \sum_{i=1} N \frac{(C_i - A_i/B_i)^2}{\sigma^2_{A_i/B_i}}. \tag{4.9}$$

[10] A cross correlation occurs when variables i and k are correlated, variables j and k are correlated, but variables i and j are not correlated. If this is the case, and we plot a confidence contour of i vs j while reminimizing with respect to k, i and j will appear correctly uncorrelated.

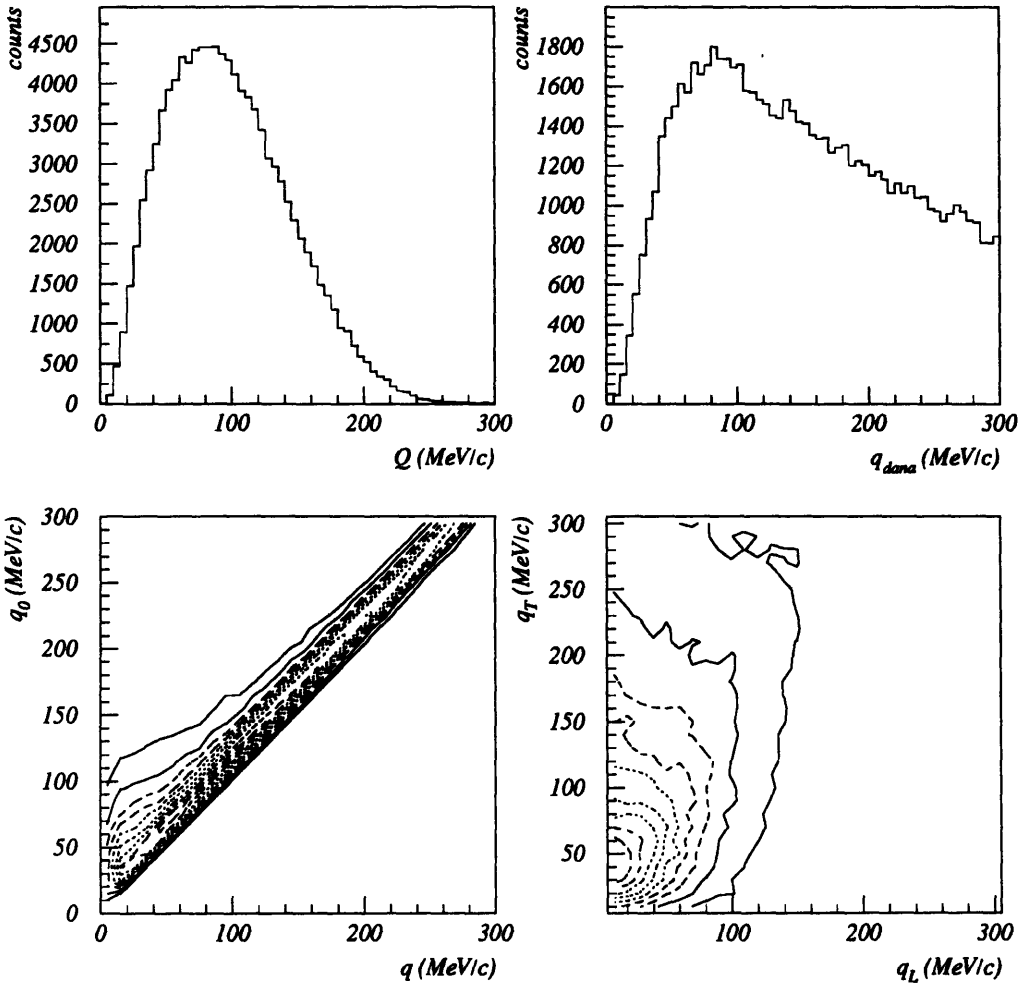

Figure 4-11: Illustration of E859 1D (Q, q_{dana}) and 2D (q_0 vs q, q_T vs q_L), phase space for pions.

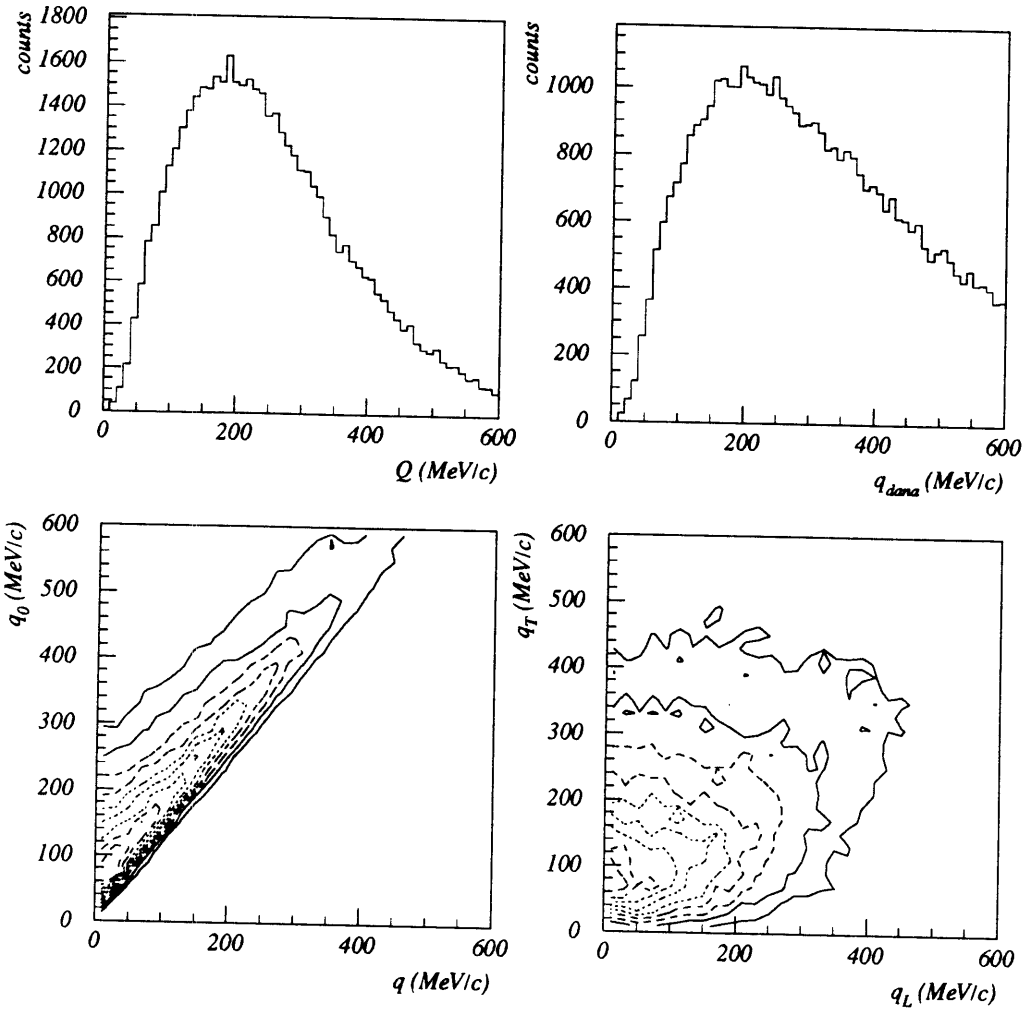

Figure 4-12: Illustration of E859 1D (Q, q_{dana}) and 2D (q_0 vs q, q_T vs q_L), phase space for kaons.

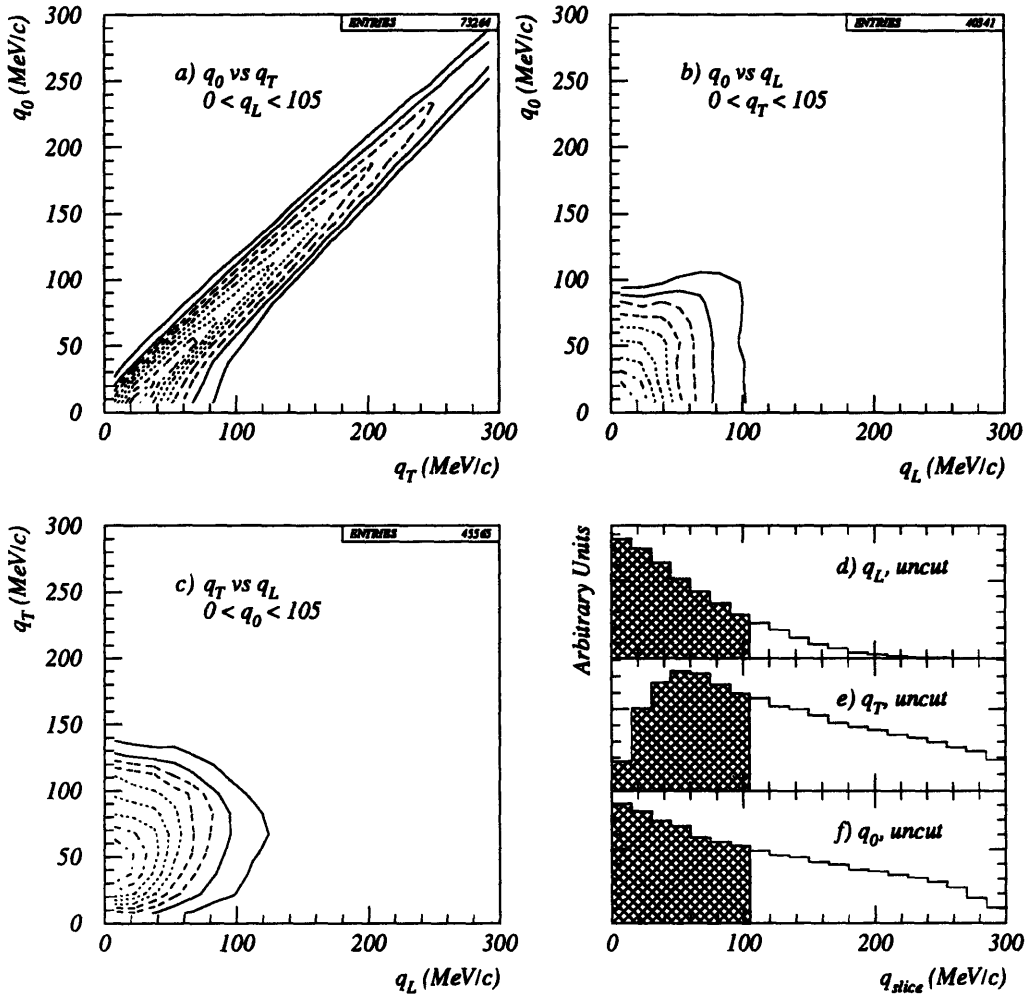

Figure 4-13: Illustration of E859 (q_L vs q_T vs q_0) phase space for pions. The first three panels show the three possible 2D combinations of these three variables. The data plotted are cut on the unplotted third variable, in order to show the available phase space in the region of correlation function enhancement. The final panel shows the 1D projections of each of these relative momentum variables. The hatched regions show the cuts used to generate the 2D projections.

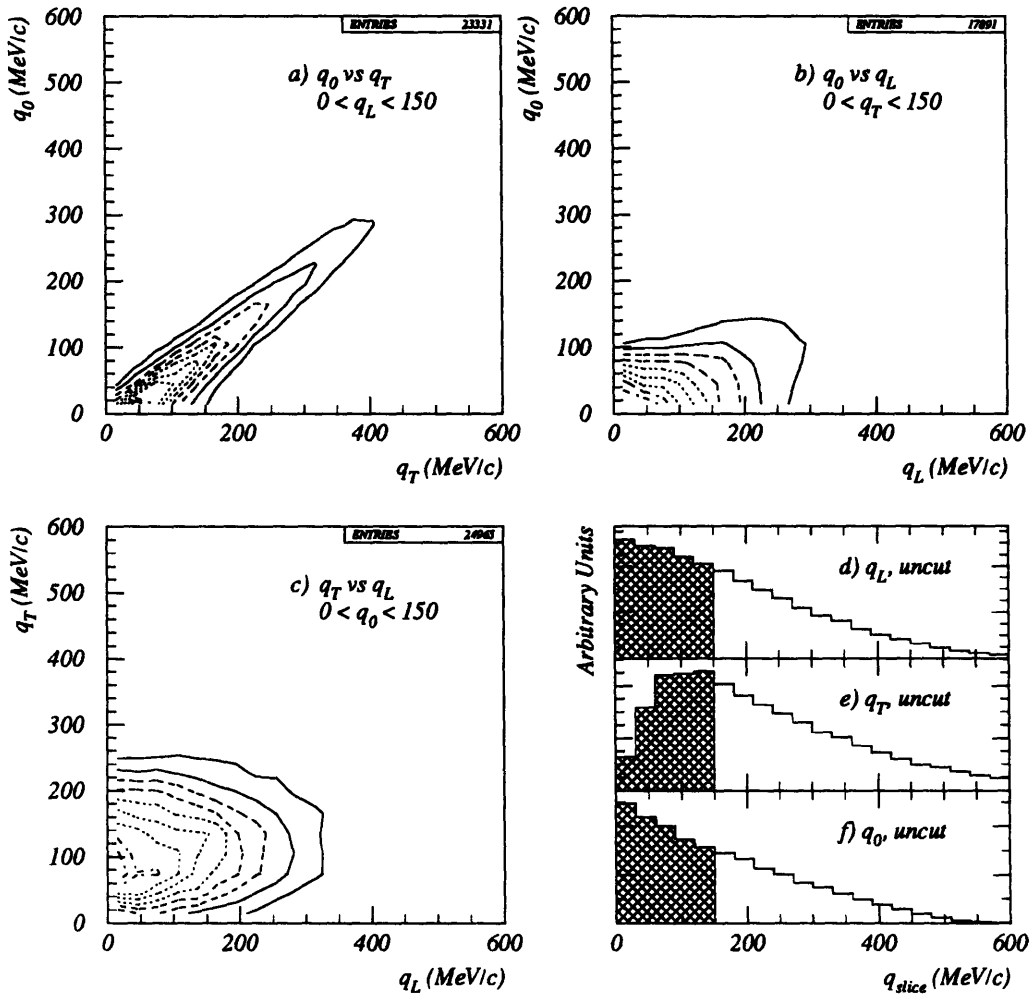

Figure 4-14: Illustration of E859 (q_L vs q_T vs q_0) phase space for kaons. The first three panels show the three possible 2D combinations of these three variables. The data plotted are cut on the unplotted third variable, in order to show the available phase space in the region of correlation function enhancement. The final panel shows the 1D projections of each of these relative momentum variables. The hatched regions show the cuts used to generate the 2D projections.

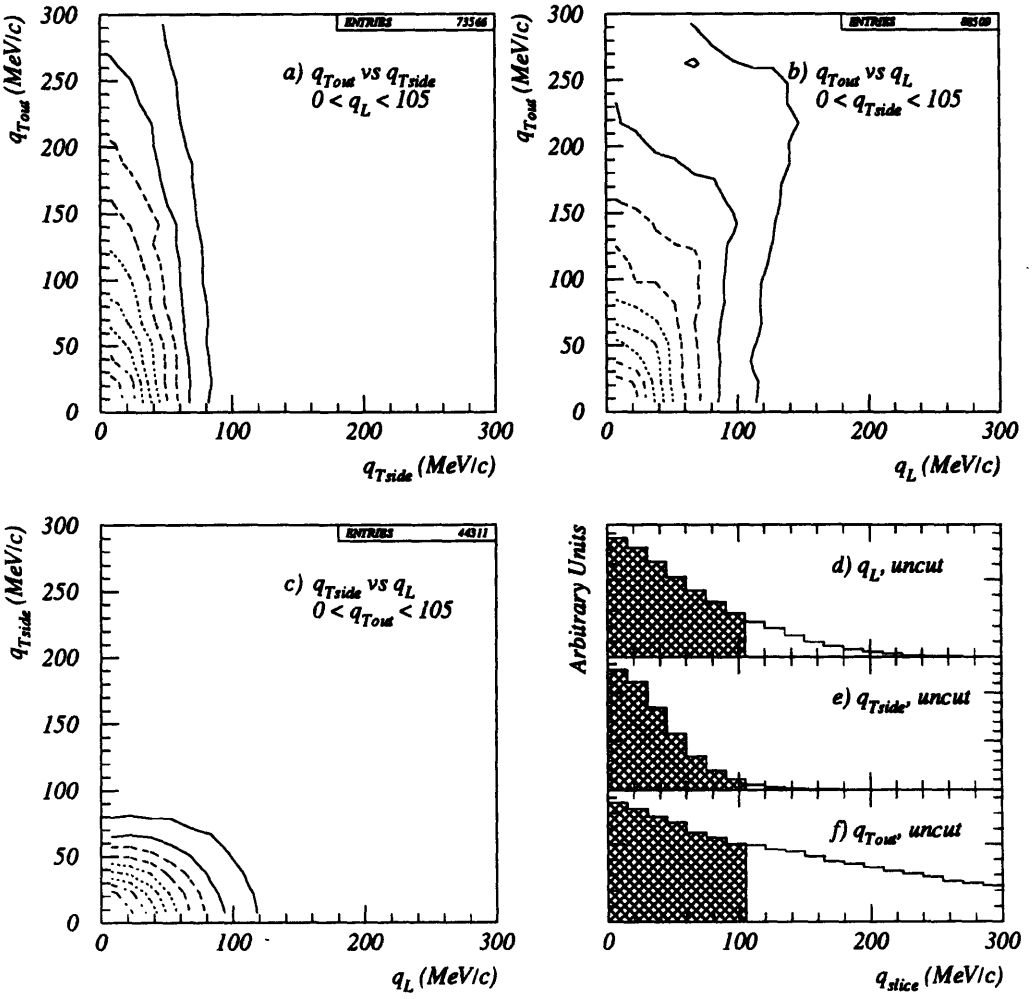

Figure 4-15: Illustration of E859 (q_L vs q_{Tside} vs q_{Tout}) phase space for pions. The first three panels show the three possible 2D combinations of these three variables. The data plotted are cut on the unplotted third variable, in order to show the available phase space in the region of correlation function enhancement. The final panel shows the 1D projections of each of these relative momentum variables. The hatched regions show the cuts used to generate the 2D projections.

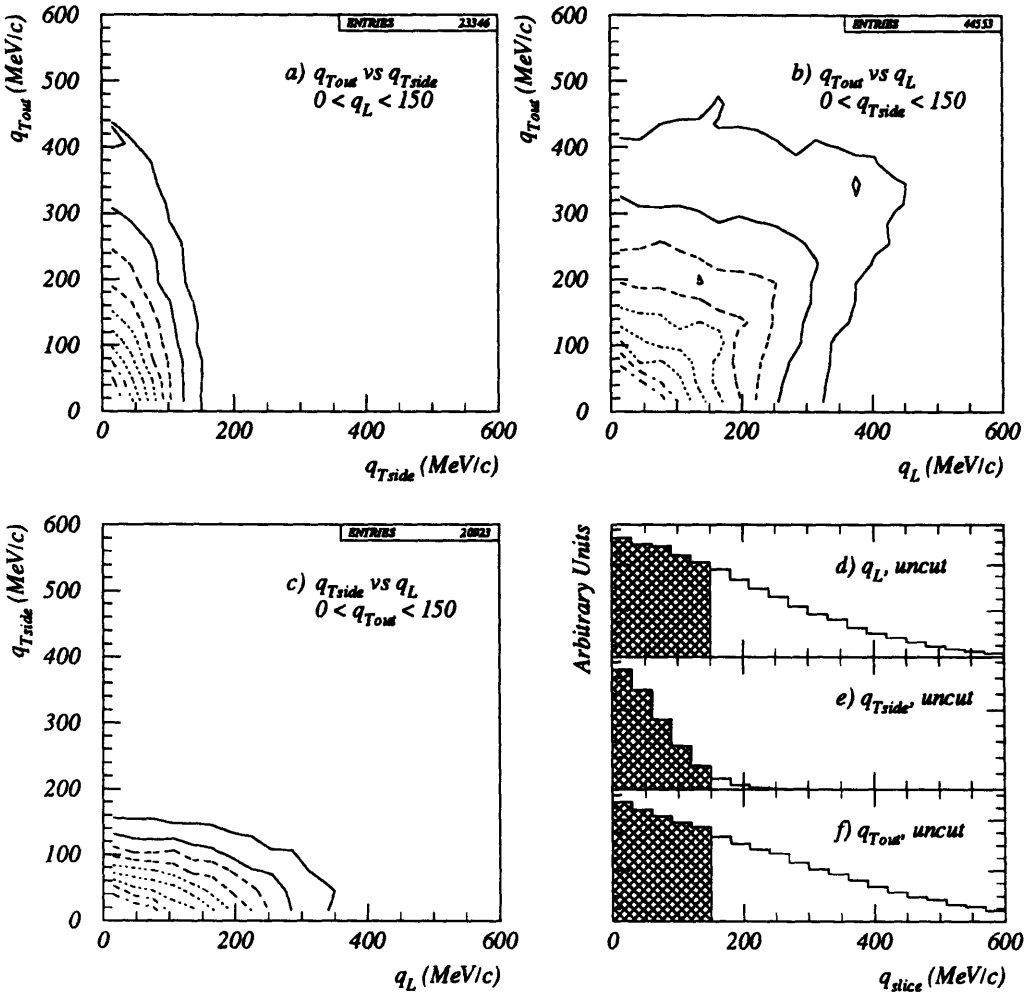

Figure 4-16: Illustration of E859 (q_L vs q_{Tside} vs q_{Tout}) phase space for kaons. The first three panels show the three possible 2D combinations of these three variables. The data plotted are cut on the unplotted third variable, in order to show the available phase space in the region of correlation function enhancement. The final panel shows the 1D projections of each of these relative momentum variables. The hatched regions show the cuts used to generate the 2D projections.

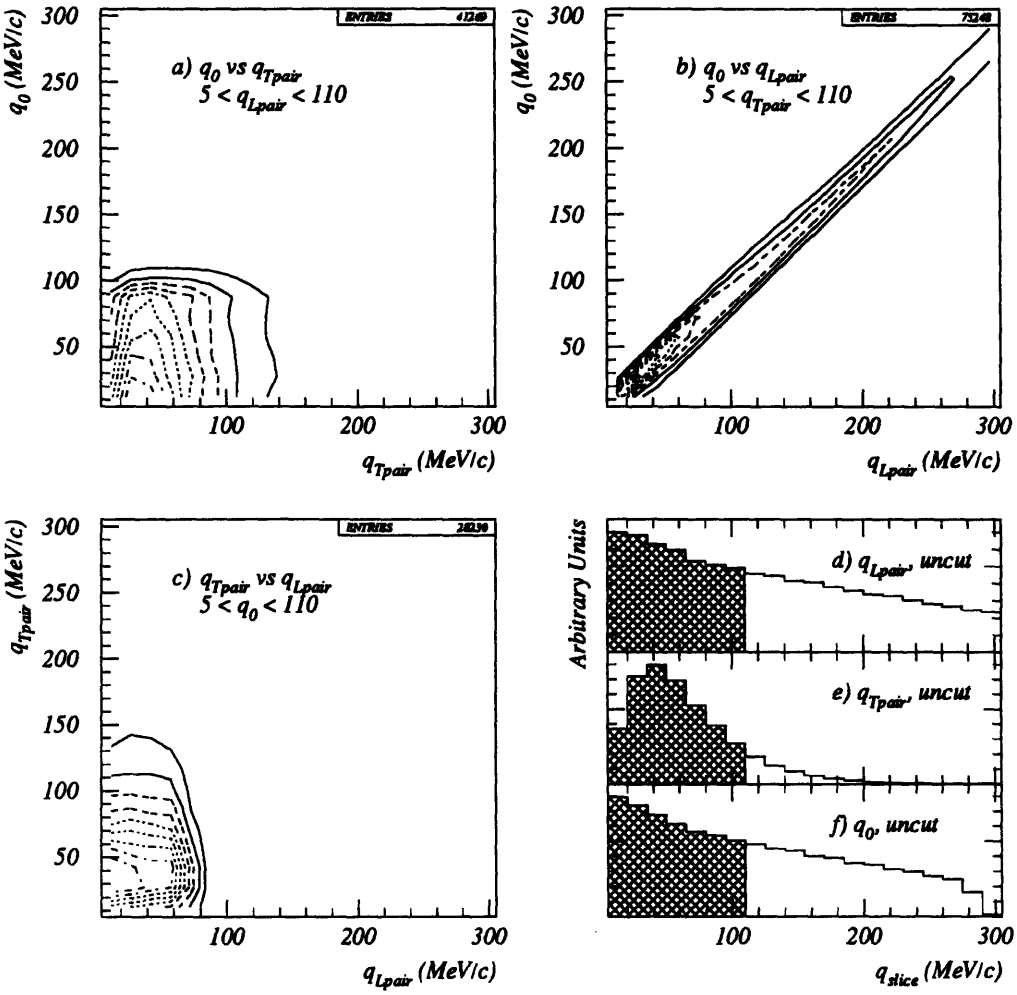

Figure 4-17: Illustration of E859 (q_{Lpair} vs q_{Tpair} vs q_0) phase space for pions. The first three panels show the three possible 2D combinations of these three variables. The data plotted are cut on the unplotted third variable, in order to show the available phase space in the region of correlation function enhancement. The final panel shows the 1D projections of each of these relative momentum variables. The hatched regions show the cuts used to generate the 2D projections.

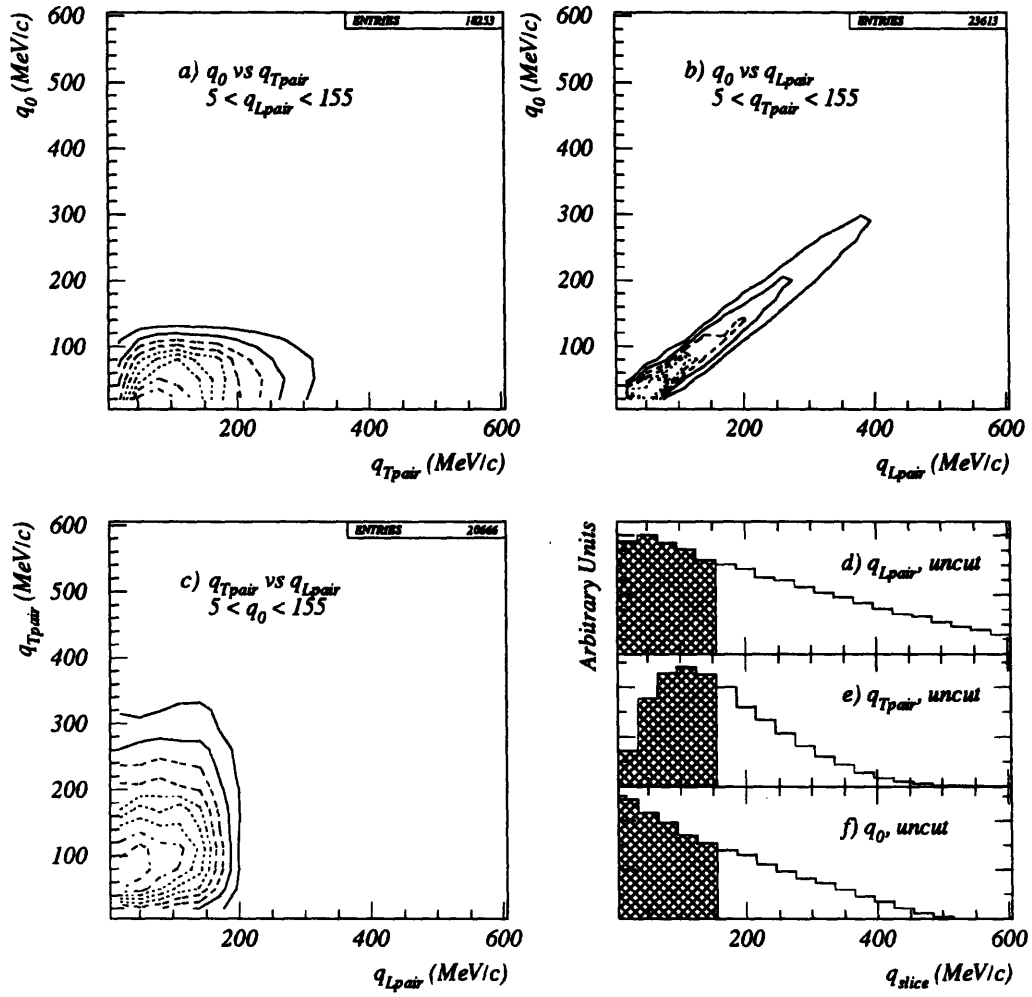

Figure 4-18: Illustration of E859 (q_{Lpair} vs q_{Tpair} vs q_0) phase space for kaons. The first three panels show the three possible 2D combinations of these three variables. The data plotted are cut on the unplotted third variable, in order to show the available phase space in the region of correlation function enhancement. The final panel shows the 1D projections of each of these relative momentum variables. The hatched regions show the cuts used to generate the 2D projections.

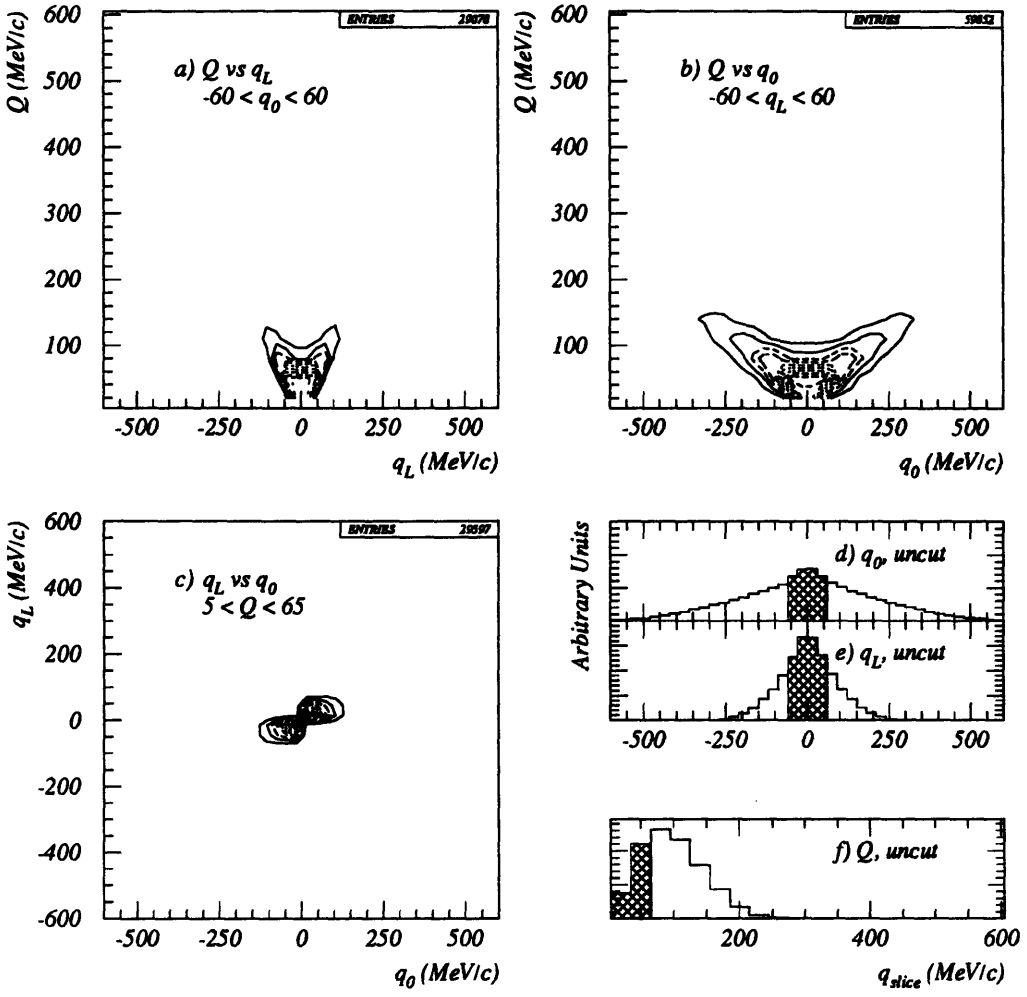

Figure 4-19: Illustration of E859 (q_0 vs q_L vs Q) phase space for pions. The first three panels show the three possible 2D combinations of these three variables. The data plotted are cut on the unplotted third variable, in order to show the available phase space in the region of correlation function enhancement. The final panel shows the 1D projections of each of these relative momentum variables. The hatched regions show the cuts used to generate the 2D projections.

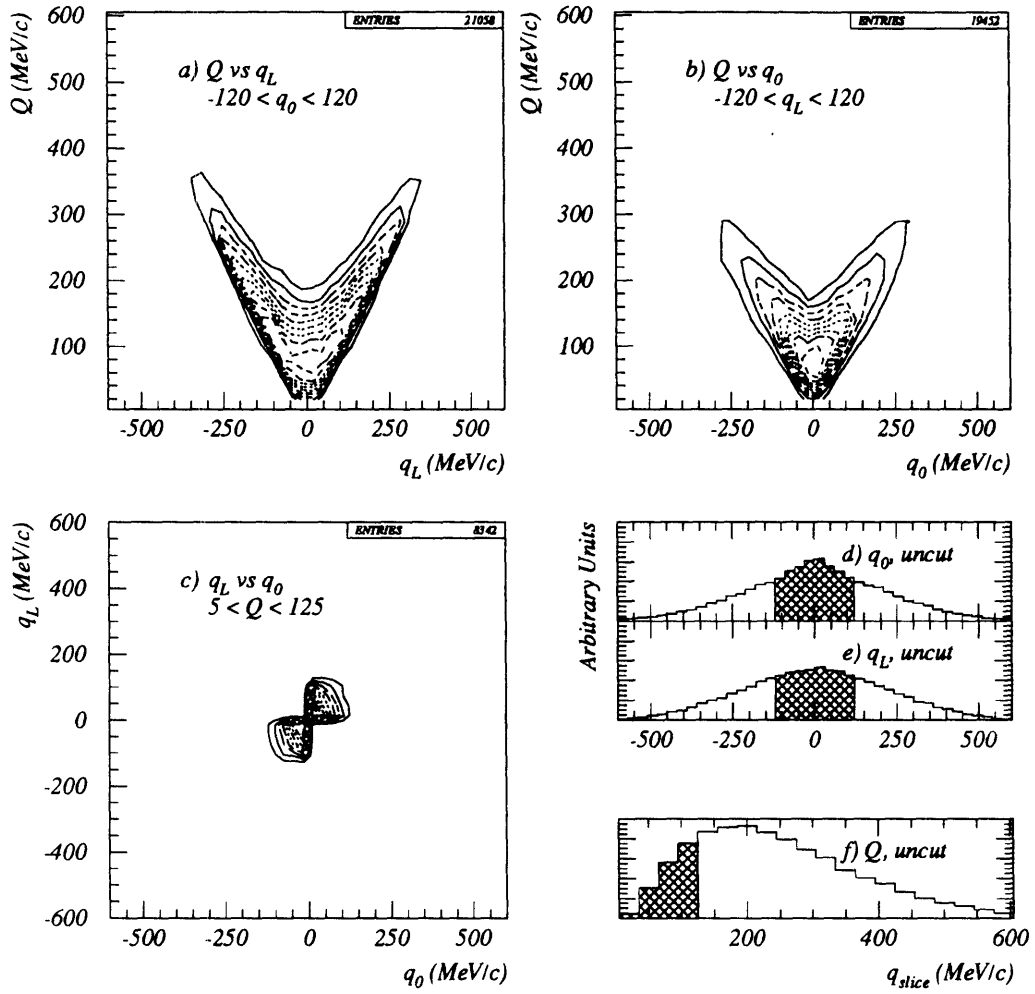

Figure 4-20: Illustration of E859 (q_0 vs q_L vs Q) phase space for kaons. The first three panels show the three possible 2D combinations of these three variables. The data plotted are cut on the unplotted third variable, in order to show the available phase space in the region of correlation function enhancement. The final panel shows the 1D projections of each of these relative momentum variables. The hatched regions show the cuts used to generate the 2D projections.

The sum is over the i bins of the correlation function histogram. C_i is the value of the correlation function at the middle of the i^{th} bin given the estimated fit parameter values. A_i and B_i are the values of the i^{th} bin of the *Actual* and *Background* distributions respectively. $\sigma^2_{A_i/B_i}$ is the error of the i^{th} bin of the measured correlation function histogram. There is an implicit assumption in equation 4.9 that $\sigma^2_{A_i/B_i}$ is Gaussian distributed. This assumption is not explicitly satisfied for the ratio of two numbers, and it is badly violated for the ratio of small numbers [JR80].

One way to circumvent this difficulty is to instead minimize the function:

$$\chi^2_A \equiv \sum_{i=1} N \frac{(C_i B_i - A_i)^2}{\sigma^2_{A_i} + \sigma^2_{C_i B_i}}. \tag{4.10}$$

Unfortunately, this function also has difficulties for small values of A_i and B_i where the Gaussian approximation to a Poisson distribution is not good.

To obtain the optimization function for Poisson distributed data one must use the Principle of Maximum Likelihood (PML) method. To begin this derivation, we first neglect errors on the *Background* distribution so that the number of counts in the i^{th} bin of the *Actual* distribution, A_i, is Poisson distributed about the expected number, $\bar{A}_i \equiv C_i B_i$. The probability for obtaining the measured set of A_i's given the varied set of $\bar{A}_i$'s is given by:

$$\mathcal{P}\left(A_i|\bar{A}_i\right) = \prod_{i=1}^{N} \frac{\bar{A}_i^{A_i}}{A_i!} \exp^{-\bar{A}_i} \tag{4.11}$$

To find correct source parameters we need to maximize this probability. It is convenient to instead minimize the negative logarithm of this probability. We also multiply by two for later comparison to equation 4.9:

$$PML_0 \equiv -2 \ln \left(\prod_{i=1}^{N} \frac{\bar{A}_i^{A_i}}{A_i!} \exp^{-\bar{A}_i} \right), \tag{4.12a}$$

$$= 2 \sum_{i=1}^{N} \left(\bar{A}_i - A_i \ln\left(\bar{A}_i\right) + \ln(A_i!) \right), \tag{4.12b}$$

$$= 2 \sum_{i=1}^{N} \left(\bar{A}_i - A_i - A_i \ln\left(1 + \frac{\bar{A}_i - A_i}{A_i}\right) \right). \tag{4.12c}$$

To obtain equality in the last line we invoke Stirling's approximation and absorb higher-order terms into the definition of PML_0[11] so that $\lim_{A_i \to \infty} PML_0 = \chi^2_C$.

Zajc [Zaj90] suggested an augmentation to PML_0 in order to account for cases in which the

[11] We can do this because these terms are constants in the minimization procedure.

errors in the *Background* distribution are not negligible:

$$PML_A \equiv 2\sum_{i=1}^{N}\left(\bar{A}_i - A_i - \left(A_i + \sigma^2_{C_iB_i}\right)\ln\left(\frac{\bar{A}_i + \sigma^2_{C_iB_i}}{A_i + \sigma^2_{C_iB_i}}\right)\right). \tag{4.13}$$

The motivation for this optimization function is to obtain a formula which is correct for Poisson distributed numbers and for which $\lim_{A_i\to\infty} PML_A = \chi^2_A$.

One can work backwards and derive the probability distribution which would give rise to this optimization function. Let us rewrite equation 4.13, restricting our attention to only one bin and defining $\sigma^2 \equiv A + \sigma^2_{CB}$:

$$PML_A \equiv 2\left(\bar{A} - A - \sigma^2\ln\left(\frac{\bar{A} - A + \sigma^2}{\sigma^2}\right)\right). \tag{4.14}$$

To obtain the probability distribution we need to first restore terms lost in Stirling's approximation:

$$\begin{aligned}
PML_A &= 2\left(\bar{A} - A - \sigma^2\ln\left(\frac{\bar{A} - A + \sigma^2}{\sigma^2}\right)\right), && \text{(4.15a)}\\
&= 2\left(\bar{A} - A - \sigma^2\ln\left(\bar{A} - A + \sigma^2\right) + \sigma^2\ln\left(\sigma^2\right)\right), && \text{(4.15b)}\\
&\approx 2\left(\bar{A} - A - \sigma^2\ln\left(\bar{A} - A + \sigma^2\right) + \sigma^2\ln\left(\sigma^2\right) + \sigma^2 - \sigma^2 + \mathcal{O}\left(\ln\left(\sigma^2\right)\right)\right) && \text{(4.15c)}\\
&\approx 2\left(\bar{A} - A + \sigma^2 - \sigma^2\ln\left(\bar{A} - A + \sigma^2\right) + \ln\left(\sigma^2!\right)\right). && \text{(4.15d)}
\end{aligned}$$

Next, we need to multiply by $-\frac{1}{2}$ and exponentiate:

$$\begin{aligned}
\mathcal{P}\left(A|\bar{A}\right) &= \exp\left(\frac{-PML_A}{2}\right), && \text{(4.16a)}\\
&= \frac{\left(\bar{A} - A + \sigma^2\right)^{(\sigma^2)}}{\sigma^2!}\exp\left[-\left(\bar{A} - A + \sigma^2\right)\right]. && \text{(4.16b)}
\end{aligned}$$

This distribution is neither Gaussian nor Poisson, although it should be noted that we do recover a Poisson distribution in the limit of negligible *Background* errors:

$$\lim_{A\to\infty, B\to\infty, \sigma_{C_iB_i}\to 0} \mathcal{P}\left(A|\bar{A}\right) = \frac{\bar{A}_i^A}{A!}\exp^{-\bar{A}}. \tag{4.17}$$

We sought a way to introduce *Background* errors into the probability distribution function

in a more natural fashion. The first step was to unwittingly invoke Bayes' Postulate [F+79].[12] Given the number of counts in the i^{th} bin of the *Actual* histogram, A, we wrote the probability that the the parent distribution was Poisson distributed with a mean, μ as:

$$\mathcal{P}\left(\mu|A\right) = \mathcal{P}\left(A|\mu\right) \equiv \frac{\mu^A \exp\left(-\mu\right)}{A!}. \tag{4.19}$$

We assume that the *Background* is Poisson distributed with mean, ν, and that the correlation function, $C = \mu/\nu$. This allows us to write:

$$\begin{aligned}
\mathcal{P}(C|A,B) &= \iint \left(\frac{\mu^A \exp\left(-\mu\right)}{A!}\right)\left(\frac{\nu^B \exp\left(-\nu\right)}{B!}\right)\delta\left(C-\mu/\nu\right)d\mu\, d\nu, && \text{(4.20a)}\\
&= \int \left(\frac{(C\nu)^A \exp\left(-C\nu\right)}{A!}\right)\left(\frac{\nu^{B+1} \exp\left(-\nu\right)}{B!}\right)d\nu, && \text{(4.20b)}\\
&= \frac{C^A}{A!B!}\int \nu^{A+B+1}\exp\left(-\left(C+1\right)\nu\right)d\nu, && \text{(4.20c)}\\
&= \frac{C^A}{A!B!}\frac{(A+B+1)!}{(C+1)^{A+B+2}}. && \text{(4.20d)}
\end{aligned}$$

We want to maximize this probability. But, as in equation 4.12, it is more convenient to minimize the negative logarithm of this probability. We also multiply by two for comparison to equation 4.10 in the high-count limit. Using Stirling's approximation and absorbing higher-order terms into the definition of PML_P, we can write:

$$\begin{aligned}
PML_P &\equiv -2\ln\left(\frac{C^A}{A!B!}\frac{(A+B+1)!}{(C+1)^{A+B+2}}\right), && \text{(4.21a)}\\
&= -2\left[(A+B+1)\ln(A+B+1) - A\ln A - B\ln B - 1 + \right.\\
&\qquad \left. A\ln C - (A+B+2)\ln(C+1)\right]. && \text{(4.21b)}
\end{aligned}$$

Equation 4.21 would have been the function optimized for parameter estimation in this analysis,

[12] Bayes' Theorem is an equation for the posterior probability in terms of the prior probabilities:

$$\mathcal{P}\left(\theta_i|x\right) = \frac{\mathcal{P}\left(x|\theta_i\right)\mathcal{P}\left(\theta_i\right)}{\sum_{j=1}^{N}\mathcal{P}\left(x|\theta_j\right)\mathcal{P}\left(\theta_j\right)},$$

where,

$$\sum_{j=1}^{N}\mathcal{P}\left(\theta_i\right) = 1\,,\ \sum_{j=1}^{N}\mathcal{P}\left(x|\theta_i\right) = 1. \tag{4.18}$$

Bayes' Postulate states that if the prior probabilities are completely unknown, then one may assume they are equal:

$$\mathcal{P}(\theta_1) = \mathcal{P}(\theta_2) = \cdots \mathcal{P}(\theta_N) = \frac{1}{N}.$$

except for an error in the original derivation discovered only recently by Mark Baker. As a result, the function actually optimized was:

$$\begin{aligned} PML_{p\prime} &= -2\left[(A+B)\ln(A+B) - A\ln A - B\ln B + \right. \\ &\qquad \left. A\ln C - (A+B+1)\ln(C+1)\right]. \end{aligned} \tag{4.22}$$

Equations 4.21 and 4.22 are only different in the very low count limit. Since fit results obtained with equation 4.22 were found to be nearly identical to those obtained with equation 4.13, the error associated with the mistake in equation 4.22 is estimated to be negligible.

To examine the behavior of equation 4.21 in the high-count limit, we drop the term $\ln(C+1)$ and rearrange:

$$\lim_{A\to\infty,B\to\infty} PML_P \approx -2\left[A\ln\left(\frac{A+B}{A}\frac{C}{C+1}\right) + B\ln\left(\frac{A+B}{B}\frac{1}{C+1}\right)\right], \tag{4.23a}$$

$$= -2\left[A\ln\left(1+\left(\frac{CB-A}{A(C+1)}\right)\right) + B\ln\left(1-\left(\frac{CB-A}{B(C+1)}\right)\right)\right] \tag{4.23b}$$

We expand $\ln(1+x) \approx x - x^2/2$, linear terms cancel, and we are left with:

$$\lim_{A\to\infty,B\to\infty} PML_P \approx \frac{(CB-A)^2}{AB(C+1)^2/(A+B)}. \tag{4.24}$$

It is straight-forward to show that equation 4.24 has the correct high-count behavior:

$$\lim_{A\to\infty,B\to\infty} PML_P \approx \chi^2_A, \tag{4.25a}$$

$$\lim_{A\to\infty,B\to\infty,\sigma_{CB}\to 0} PML_P \approx \chi^2_C. \tag{4.25b}$$

As a final note, the probability distribution given in equation 4.20d shows that A/B is a biassed estimator of the correlation function. To see this, we find the value of the correlation function obtained by maximizing the probability function given in equation 4.20d:

$$\frac{dPML_P}{dC} = PML_P \cdot \left(\frac{A}{C} - \frac{A+B+2}{C+1}\right) = 0, \tag{4.26a}$$

$$\Rightarrow C = \frac{A}{B+2}. \tag{4.26b}$$

The source of this unexpected result is not well established. We believe it is a consequence of the fact that while the true correlation function in a given bin is the ratio of the means of the parent distributions, the measured correlation function is more nearly given by the ratio of

the most-probable-values of the parent distributions. In the low-count limit, these are not the same. In any case, this bias is negligible over most of phase space.

Chapter 5

Results

In this chapter I discuss the final fit results for all source parameterizations of the $\pi^+\pi^+$ and K^+K^+ *standard* data sets. In addition, I will discuss results of fits to the data sets cut on the individual particle rapidity and on the total pair momentum. I will briefly discuss how well the parameterizations describe the data. And, I will summarize our efforts to understand the systematic uncertainty associated with the quoted fit parameters.

The final fit parameters and goodness-of-fit values are presented in table 5.1 — table 5.8. These same results are graphically summarized in figure 5-1. The most striking feature of this data is that every extracted fit parameter, in every source parameterization, indicates that the π^+ source is $\approx 50\%$ larger than the K^+ source.

Q, q_{dana} Parameterizations

Plots of the 1D (Q, q_{dana}) parameterizations of the *standard* K^+K^+ and $\pi^+\pi^+$ data sets are shown in figure 5-3. Fit parameters are presented in table 5.1 and table 5.2.

The very large difference between the R and R_{dana} fit parameters is mostly due a mundane, but non-intuitive kinematic effect: Bose-Einstein correlations measure Lorentz extended radii. This effect is described in more detail in appendix C. R_{dana} is not kinematically suspect, and the fit values indicate that the $\pi^+\pi^+$ source is significantly larger than the K^+K^+ source. Recall that this parameterization assumes that $\tau = R$. The validity of this assumption is discussed below.

$q_0 q$ Parameterization

The two lowest q_0 slices of $C_2(q_0, q)$, for the *standard* K^+K^+ and $\pi^+\pi^+$ data sets, are shown

	$\pi^+\pi^+$	K^+K^+
R_Q	5.00 ± 0.18	2.19 ± 0.10
λ	0.59 ± 0.04	0.84 ± 0.07
χ^2/dof	43.4/56	70.4/56

Table 5.1: Q fit results for the *standard* data sets.

	$\pi^+\pi^+$	K^+K^+
R_{dana}	2.78 ± 0.10	1.81 ± 0.10
λ	0.63 ± 0.03	0.84 ± 0.07
χ^2/dof	69.9/56	57.1/56

Table 5.2: q_{dana} fit results for the *standard* data sets.

	$\pi^+\pi^+$	K^+K^+
R_L	2.52 ± 0.18	1.63 ± 0.12
R_T	3.56 ± 0.13	2.10 ± 0.12
λ	0.64 ± 0.04	0.84 ± 0.07
χ^2/dof	729.3/759	874.2/854

Table 5.3: $q_L q_T$ fit results for the *standard* data sets.

	$\pi^+\pi^+$	K^+K^+
R	2.84 ± 0.09	1.83 ± 0.07
τ	2.94 ± 0.30	0.01 ± 0.94
λ	0.67 ± 0.04	0.78 ± 0.07
χ^2/dof	467.6/434	456.8/393

Table 5.4: $q_0 q$ fit results for the *standard* data sets.

	$\pi^+\pi^+$	K^+K^+
R_L	2.75 ± 0.15	1.71 ± 0.14
R_{Tside}	2.95 ± 0.19	2.09 ± 0.20
R_{Tout}	3.77 ± 0.13	2.07 ± 0.16
λ	0.65 ± 0.02	0.83 ± 0.08
χ^2/dof	2605/2711	2374/2402

Table 5.5: $q_L q_{Tside} q_{Tout}$ fit results for the *standard* data sets.

	$\pi^+\pi^+$	K^+K^+
R_L	2.57 ± 0.15	1.65 ± 0.08
R_T	3.15 ± 0.15	2.05 ± 0.07
τ	2.78 ± 0.21	0.00 ± 0.56
λ	0.67 ± 0.02	0.80 ± 0.04
χ^2/dof	1817/2110	2541/2738

Table 5.6: $q_L q_T q_0$ fit results for the *standard* data sets.

	$\pi^+\pi^+$	K^+K^+
R	2.80 ± 0.17	2.11 ± 0.04
τ	2.99 ± 0.39	0.00 ± 0.52
y_{source}	1.43 ± 0.11	1.55 ± 0.11
λ	0.60 ± 0.03	0.85 ± 0.04
χ^2/dof	1480/1538	4182/4765

Table 5.7: *Koonin* fit results for the *standard* data sets, fit at $y = 1.25$.

	$\pi^+\pi^+$	K^+K^+
R_{Lpair}	3.82 ± 0.16	2.08 ± 0.09
R_{Tpair}	2.78 ± 0.14	1.89 ± 0.07
τ	0.00 ± 0.43	0.00 ± 0.51
λ	0.66 ± 0.03	0.87 ± 0.04
χ^2/dof	809.8/825	1332/1442

Table 5.8: $q_{Lpair} q_{Tpair} q_0$ fit results for the *standard* data sets.

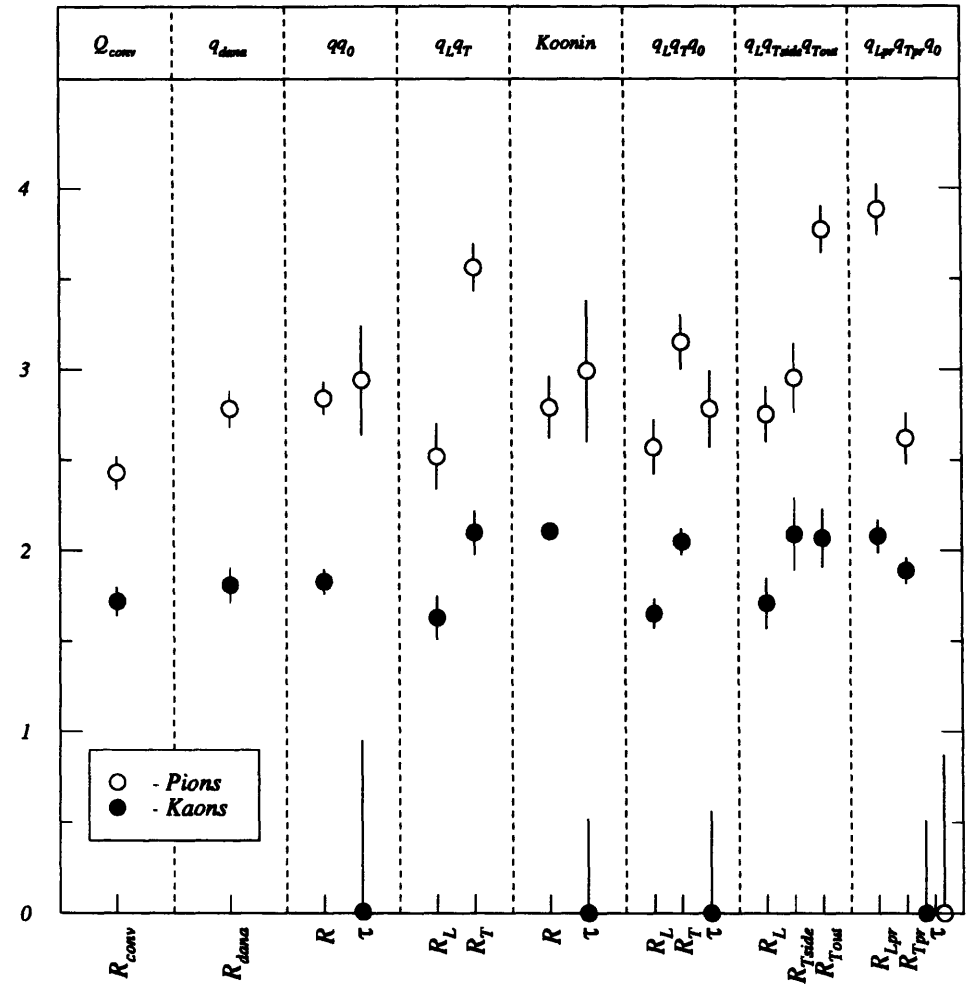

Figure 5-1: Summary of source-size fit results for all source parameterizations for the *standard* $\pi^+\pi^+$ and K^+K^+ data sets. Error bars represent statistical errors only. Multidimensional source parameterizations were fit over the entire phase space. Data in the lowest relative momentum bins, $q_{slice} \leq 5$ MeV/c, were omitted from the fits.

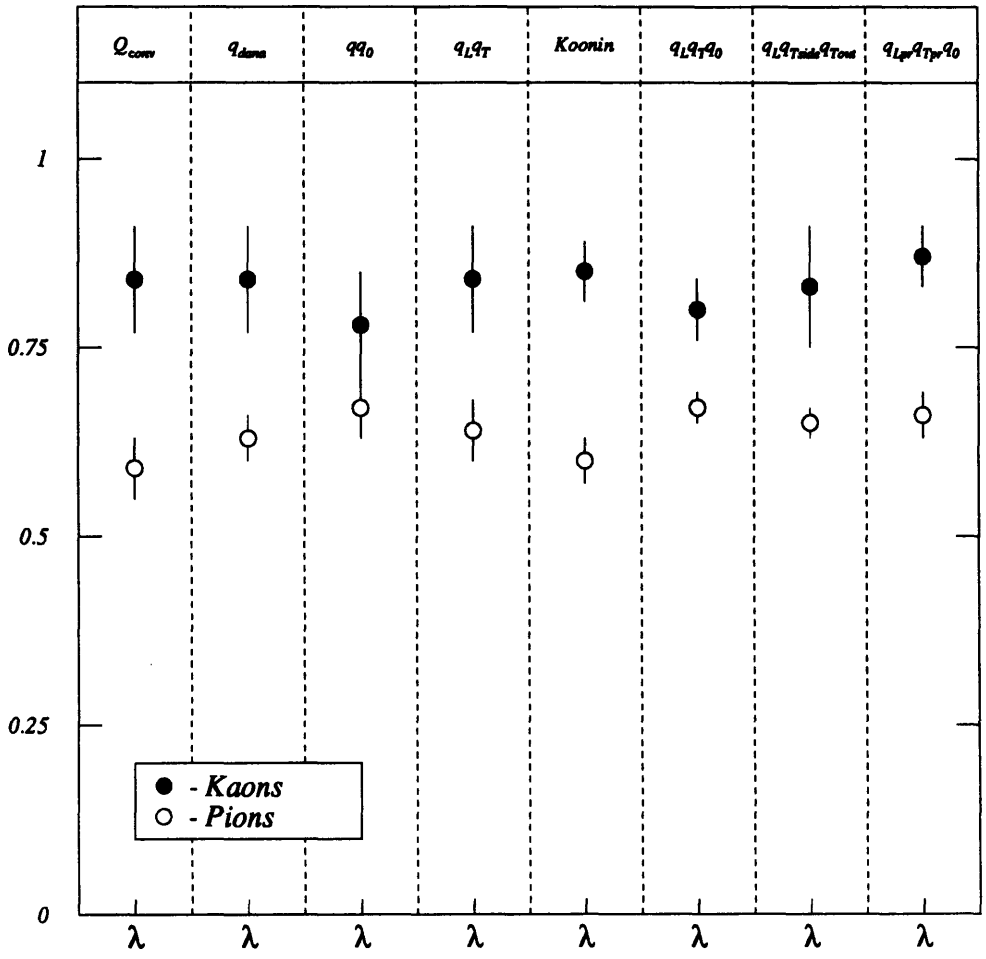

Figure 5-2: Summary of λ fit results for all source parameterizations for the *standard* $\pi^+\pi^+$ and K^+K^+ data sets. Error bars represent statistical errors only. Multidimensional parameterizations were fit over the entire phase space. Data in the lowest relative momentum bins, $q_{slice} \leq 5$ MeV/c, were omitted from the fits.

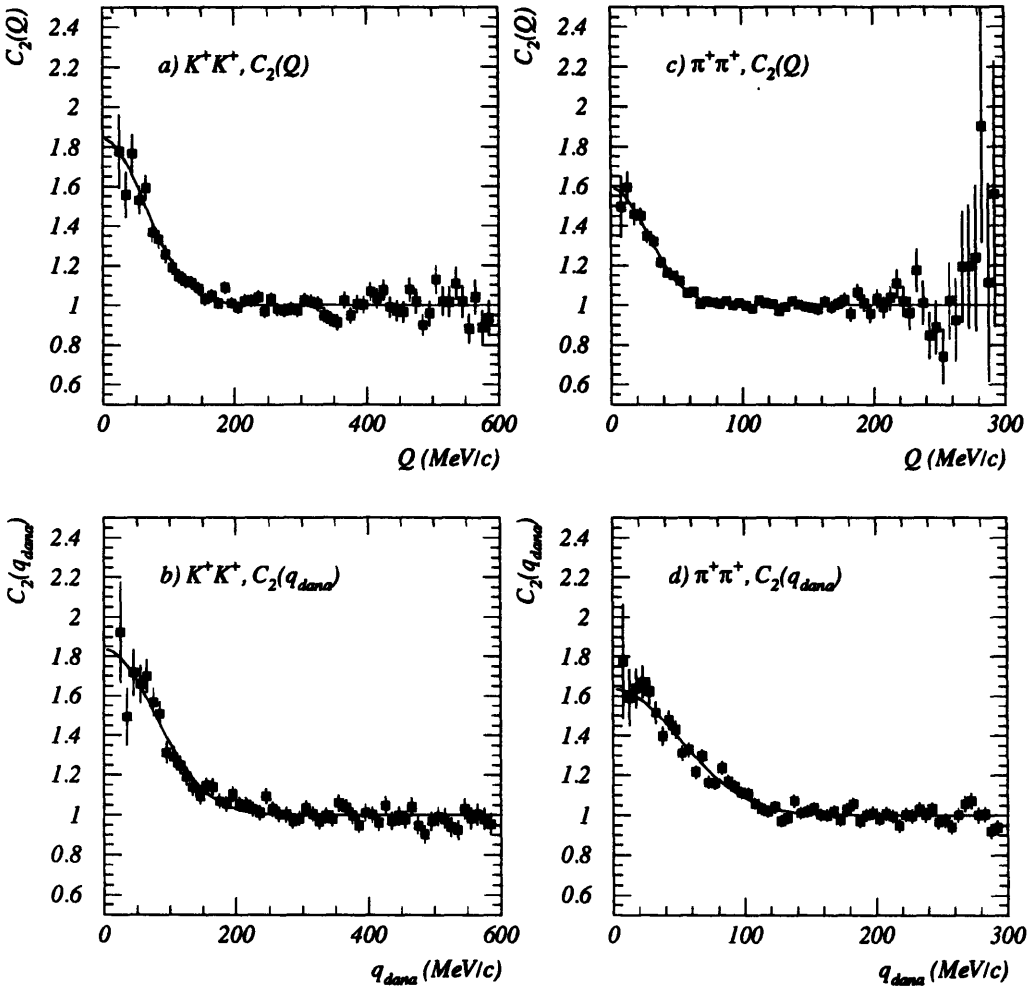

Figure 5-3: Plots of the 1D (Q, q_{dana}) parameterizations of the *standard* K^+K^+ and $\pi^+\pi^+$ data sets. Note the difference in the horizontal scale between the π^+'s and K^+'s. Solid lines are the fits to the data. Fit parameters are presented in table 5.1 and table 5.2.

in figure 5-4.[1] Fit parameters are presented in table 5.4. 1-, 2- and 3-σ confidence contours are shown in figure 5-7a.

The $\pi^+\pi^+$ source is consistent with $\tau = R$. It is also consistent with pion sources measured for ^{28}Si+^{197}Au central collisions at the spectrometer's 14° setting [A+92a, Sol94]. The extracted *rms* radius of the $\pi^+\pi^+$ source, $R_{rms} = \sqrt{3}R = 4.92 \pm 0.16$ fm, is significantly larger than the ^{28}Si projectile radius, $R^{Si}_{rms} = 3.04$ fm. The K^+K^+ source is consistent with $\tau = R$ *and* with $\tau = 0$. The problems with extracting the emission time duration have been discussed in section 1.4. The extracted *rms* radius of the K^+K^+ source, $R_{rms} = \sqrt{3}R = 3.17 \pm 0.12$ fm, is consistent with R^{Si}_{rms}.

$q_L q_T$ Parameterization

The two lowest q_L and q_T slices of $C_2(q_L, q_T)$, for the *standard* $\pi^+\pi^+$ data set, are shown in figure 5-5. The equivalent slices for the K^+K^+ data set are shown in figure 5-6. Fit parameters are presented in table 5.3. 1-, 2- and 3-σ confidence confidence contours are shown in figure 5-7b.

The $\pi^+\pi^+$ source is consistent with pion sources measured for ^{28}Si + ^{197}Au central collisions at the spectrometer's 14° setting [A+92a, Sol94]. Both the $\pi^+\pi^+$ and K^+K^+ sources are oblate with a major axis perpendicular to the beam axis, and a minor axis parallel to the beam axis. Care must be taken in interpreting these results for two reasons:

1. As discussed in section 1.4, a non-zero emission duration will contribute primarily to R_T as measured in our spectrometer.

2. Dynamical correlations may limit the amount of the source that one can see with Bose-Einstein correlations. As will be shown in section 6.3.2, at least one model predicts this effect to be much more severe along the beam axis.

$q_L q_T q_0$ Parameterization

q_L, q_T and q_0 slices of $C_2(q_L, q_T, q_0)$, for the *standard* $\pi^+\pi^+$ data set, are shown in figure 5-8. The slices are cut on the lowest relative momentum bins of the two unplotted variables. The actual cut values are indicated in the figure. The equivalent slices for the K^+K^+ data set are shown in figure 5-9. Fit parameters are presented in table 5.6.

With the $q_L q_T q_0$ parameterization, we avoid the integration over different values of q_0 implicit in the $q_L q_T$ parameterization. This removes most of the distortion of R_L and R_T

[1] Slices in q are not shown because of the kinematic constraint that limits phase space to $q \geq q_0$.

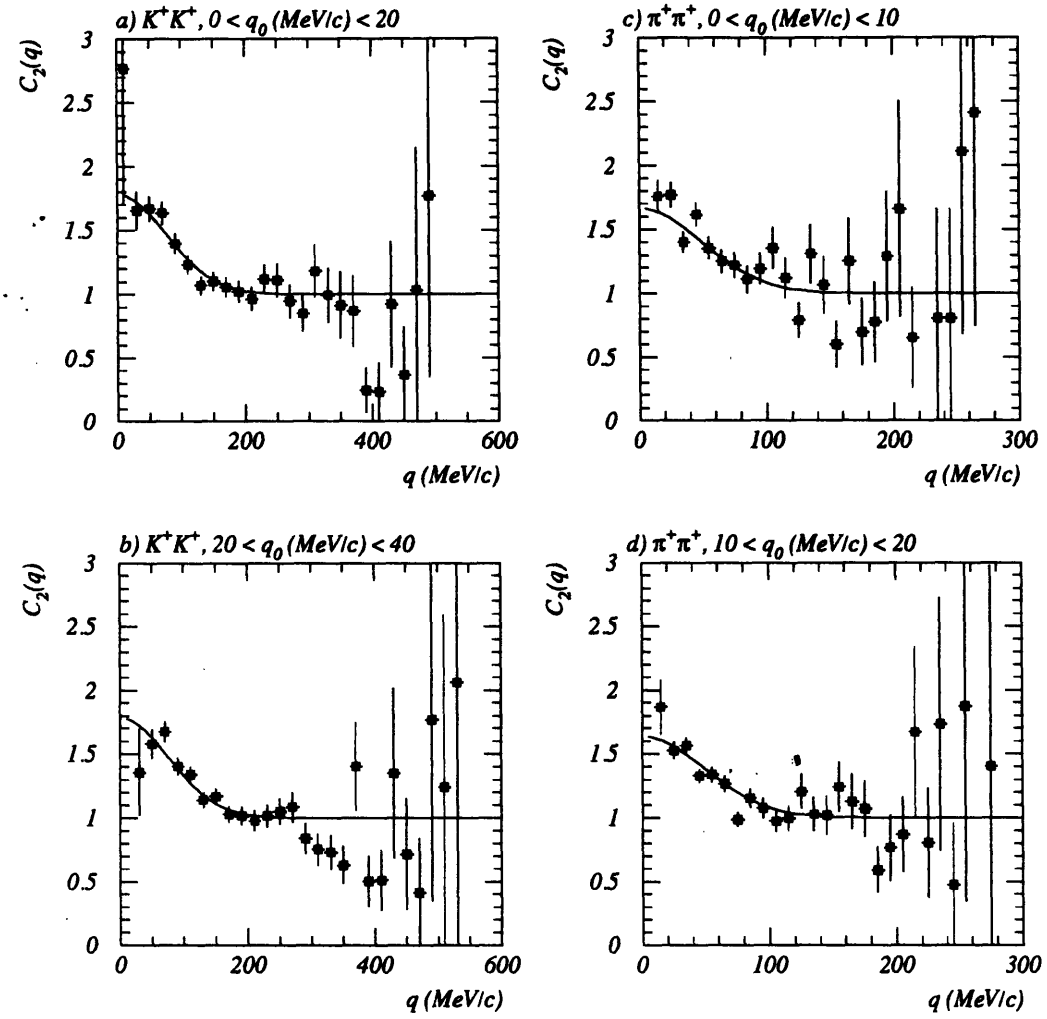

Figure 5-4: Low relative momentum slices of the $q_0 q$ parameterization of the *standard* K^+K^+ and $\pi^+\pi^+$ data sets. Note the difference in the horizontal scale between the π^+'s and K^+'s. Solid lines are the fits to the data over the full 2D phase space, evaluated at the center of the relative momentum slice of the unplotted variable. Fit parameters are presented in table 5.4.

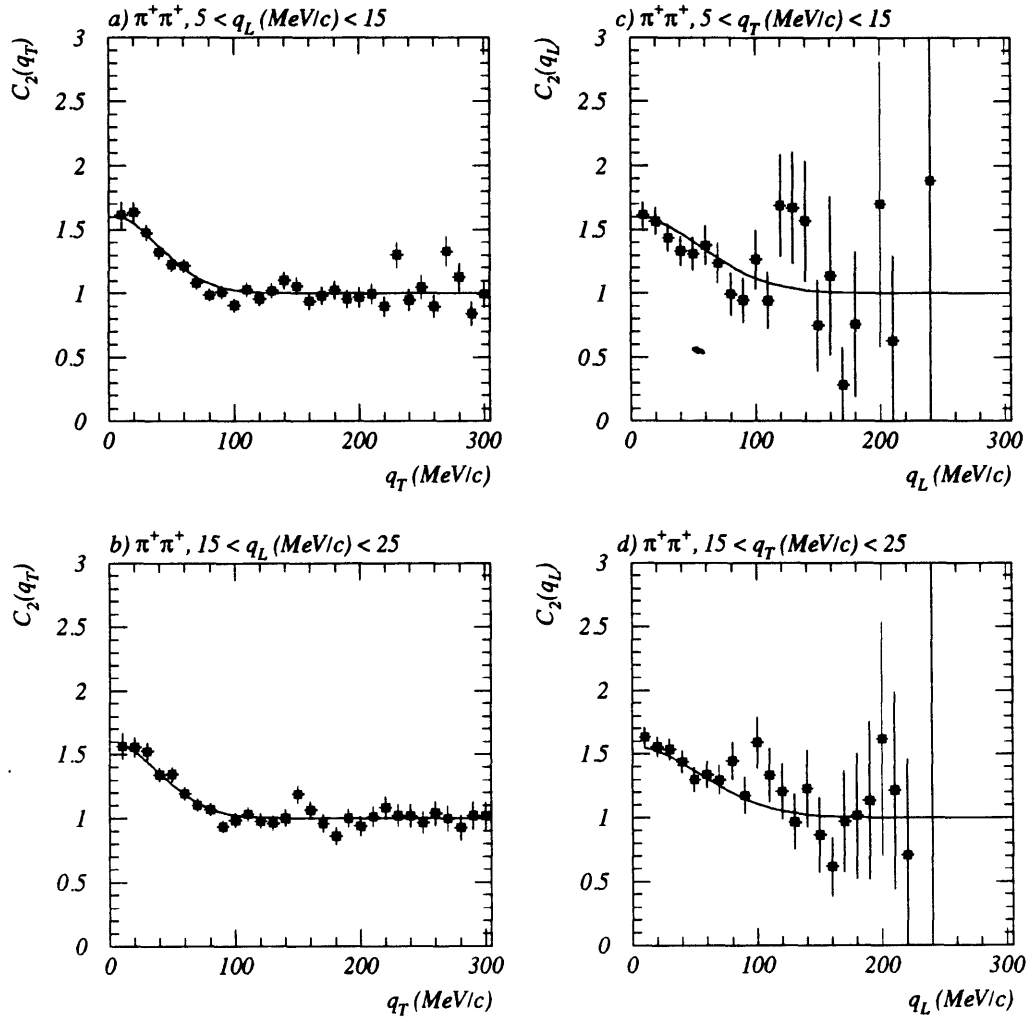

Figure 5-5: Low relative momentum slices of the $q_L q_T$ parameterization of the *standard* $\pi^+\pi^+$ data set. Solid lines are the fits to the data over the full 2D phase space, evaluated at the center of the relative momentum slice of the unplotted variable. Fit parameters are presented in table 5.3.

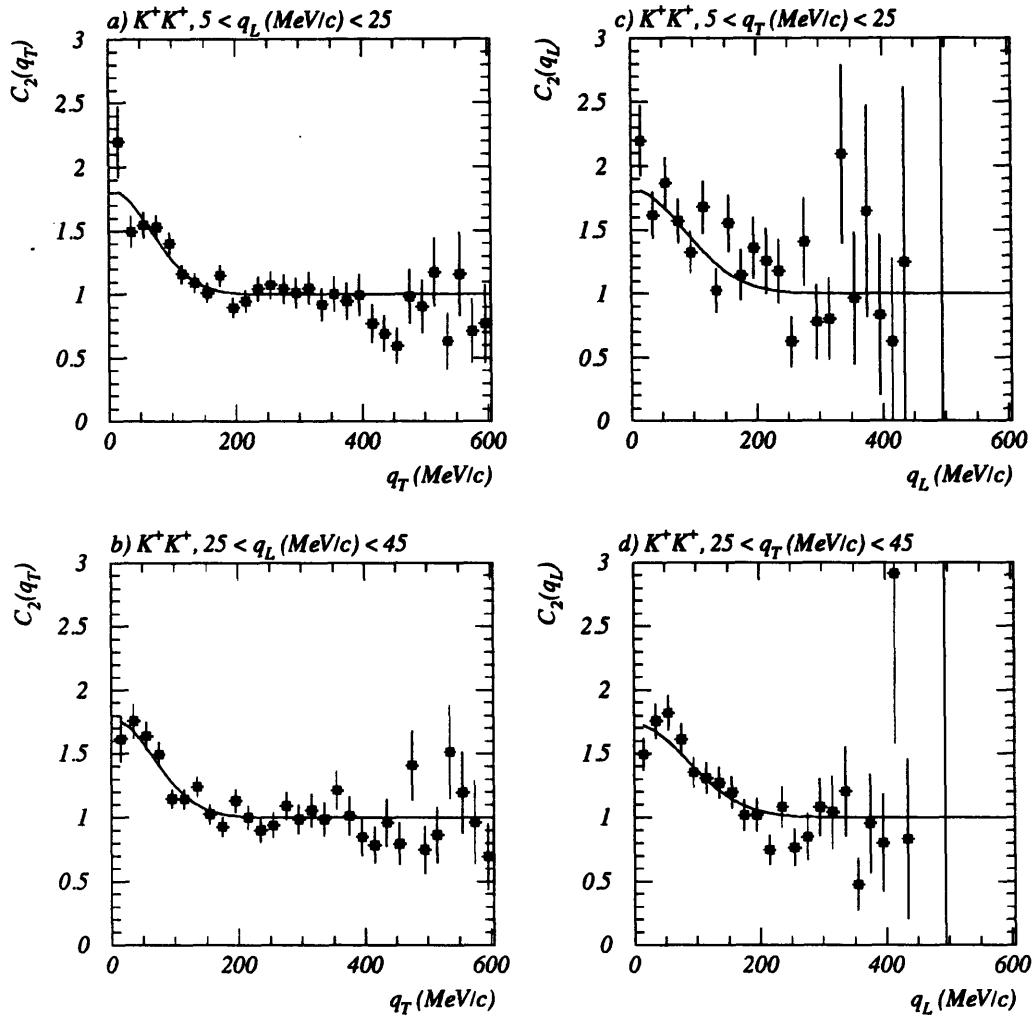

Figure 5-6: Low relative momentum slices of the $q_L q_T$ parameterization of the *standard* K^+K^+ data set. Solid lines are the fits to the data over the full 2D phase space, evaluated at the center of the relative momentum slice of the unplotted variable. Fit parameters are presented in table 5.3.

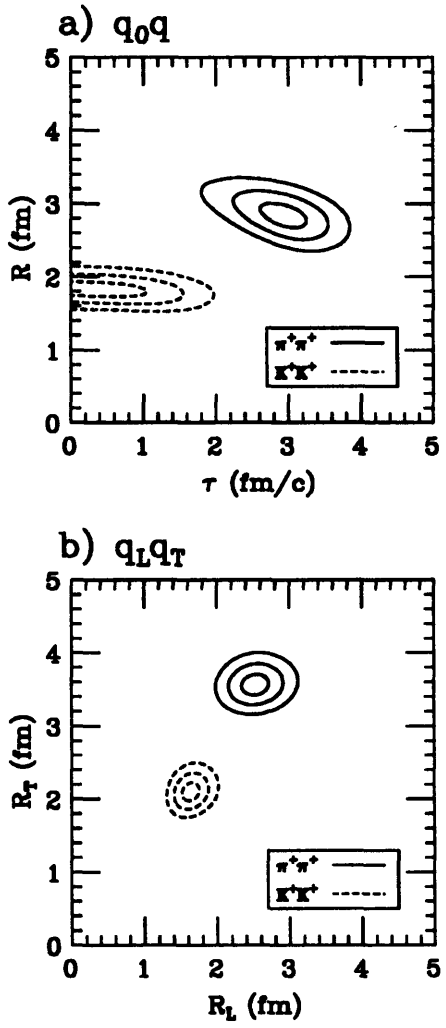

Figure 5-7: Confidence contours for the q_0q and q_Lq_T parameterizations of the *standard* K^+K^+ and $\pi^+\pi^+$ data sets. Parameters are obtained from fits to the full 2D phase space. The optimization function is re-minimized with respect to the unplotted variables in the parameterization. Fit parameters are presented in table 5.4 and table 5.3.

caused by a non-zero emission duration (see section 1.4 for more details). Similarly, we remove most of the distortion of τ caused by any asymmetry of the source size relative to the direction of p^{pair}.

The fits seem rather poor for the τ parameter, but this is an example of the dangers of integrating over different relative momentum variables. We have to use rather large slices in q_L and q_T (180 MeV/c for kaons, 90 MeV/c for pions) in order to get dynamic range for q_0.[2] The reasons for this are clearly illustrated in figure 4-13 and figure 4-14, where the tight correlation between q_T and q_0 can be seen. This means that a large slice in q_T, projected onto the q_0 axis, will artificially increase the correlation function observed along that axis.

For the $\pi^+\pi^+$ source, we see a significant decrease in the value of R_T and almost no change in the value of R_L relative to the values obtained from the $q_L q_T$ parameterization. We also see a reduction in the value of τ relative to the value found in the $q_0 q$ parameterization. These results are consistent with our expectations given the measured, non-zero emission duration of the pion source, and the relationship between q_L, q_T, and p^{pair} in our spectrometer. For the K^+K^+ source, we see almost no change in the values of R_L and R_T relative to those obtained from the $q_L q_T$ parameterization. τ fits to zero. Given the known problems with fitting τ, these results are not too surprising.

Another test we can make with the results of this parameterization is to add R_L and R_T in the appropriate fashion:

$$R_{LT} = \sqrt{\frac{R_L^2 + 2R_T^2}{3}}, \tag{5.1}$$

and compare R_{LT} to the value of R obtained from the $q_0 q$ parameterization. The results of this comparison are given in table 5.9.

	$\pi^+\pi^+$	K^+K^+
R	2.84 ± 0.09	1.83 ± 0.07
R_{LT}	2.97 ± 0.12	1.93 ± 0.10

Table 5.9: Comparison of radius parameters extracted from the $q_0 q$ and $q_L q_T q_0$ parameterizations of the $\pi^+\pi^+$ and K^+K^+ *standard* data sets.

$q_L q_{Tside} q_{Tout}$ Parameterization

q_L, q_{Tside} and q_{Tout} slices of $C_2(q_L, q_{Tside}, q_{Tout})$, for the *standard* $\pi^+\pi^+$ data set, are shown

[2]For the $q_0 q$ parameterization I do not plot any slices in q_0 for this exact reason. The slices are retained here for illustrative purposes.

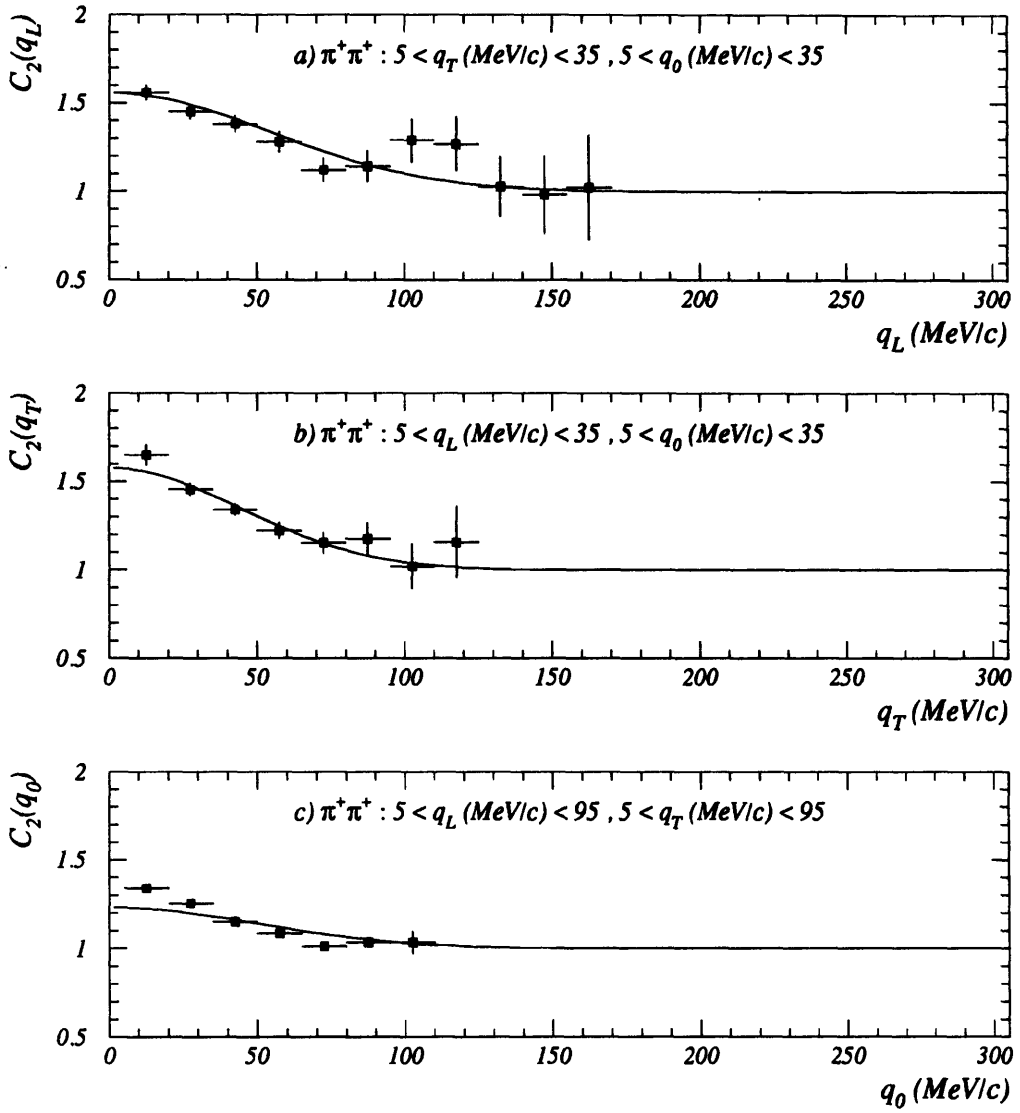

Figure 5-8: Low relative momentum slices of the $q_L q_T q_0$ parameterization of the *standard* $\pi^+\pi^+$ data set. Solid lines are the fits to the data over the full 3D phase space, evaluated at the center of the relative momentum slices of the unplotted variables. Fit parameters are presented in table 5.6.

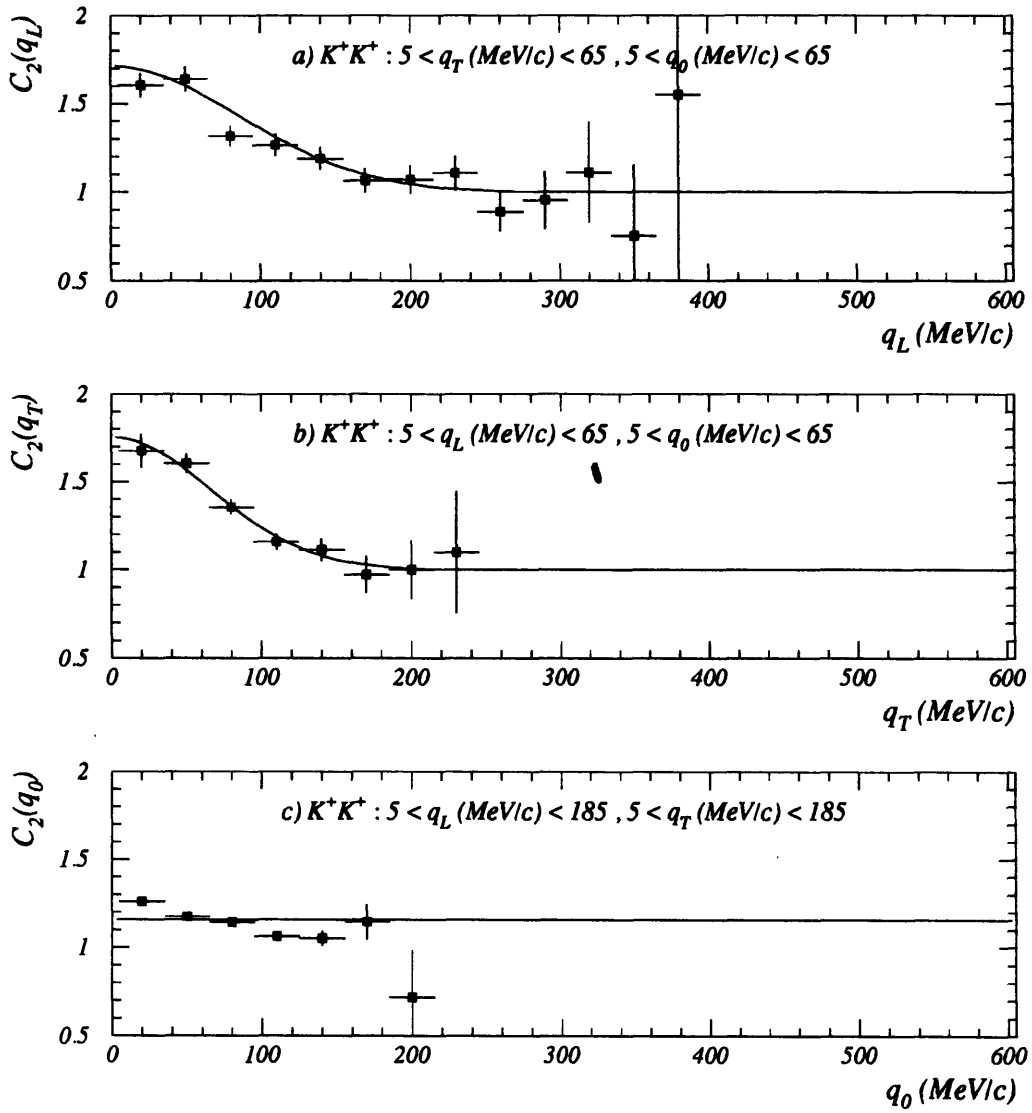

Figure 5-9: Low relative momentum slices of the $q_L q_T q_0$ parameterization of the *standard* K^+K^+ data set. Solid lines are the fits to the data over the full 3D phase space, evaluated at the center of the relative momentum slices of the unplotted variables. Fit parameters are presented in table 5.6.

in figure 5-10. The slices are cut on the lowest relative momentum bins of the two unplotted variables. The actual cut values are indicated in the figure. The equivalent slices for the K^+K^+ data set are shown in figure 5-11. Fit parameters are presented in table 5.5.

For the $q_L q_{Tside} q_{Tout}$ parameterization of both the $\pi^+\pi^+$ and K^+K^+ *standard* data sets, we obtain values for R_L that are nearly identical to those obtained from the $q_L q_T$ and the $q_L q_T q_0$ parameterizations. As stated several times earlier, we expect nearly all of the emission duration dependence of the source size to be incorporated into R_T. By definition, R_{Tout} contains all of the emission duration dependence of R_T, and R_{Tside} contains no such dependence. Given this, we can calculate a value for $\beta_{pair}\tau = \sqrt{R^2_{Tout} - R^2_{Tside}}$. For the pions, $\beta_{pair}\tau = 2.35 \pm 0.31$ fm/c, roughly consistent with the value of τ obtained from the $q_0 q$ parameterization. It may be interesting that the K^+K^+ source has $R_{Tside} < R_{Tout}$ by 0.02 fm. This is may *may* indicate a truly small emission duration of the K^+K^+ source since this parameterization does not suffer from the same phase space difficulties as those parameterizations that explicitly fit τ.

$q_{Lpair} q_{Tpair} q_0$ Parameterization

q_{Lpair}, q_{Tpair} and q_0 slices of $C_2\left(q_{Lpair}, q_{Tpair}, q_0\right)$, for the *standard* $\pi^+\pi^+$ data set, are shown in figure 5-12. The slices are cut on the lowest relative momentum bins of the two unplotted variables. The actual cut values are indicated in the figure. The equivalent slices for the K^+K^+ data set are shown in figure 5-13. Fit parameters are presented in table 5.8.

The fit through the q_0 slices are not mistakes. This is just a much more dramatic illustration of a point mentioned in the discussion of the $q_L q_T q_0$ parameterization: limited phase space can be dangerous. We have to use 90 MeV/c slices in q_{Lpair} and q_{Tpair} in order to get dynamic range for q_0. But, as shown in figure 4-17, q_0 and q_{Lpair} are *very* highly correlated, especially for pions (this is directly related to the limited range of β_π in the spectrometer). This means that q_0 and q_{Lpair} are effectively interchangeable as far as any fitting procedure is concerned. In fact, the dashed line through the q_0 slices use the q_{Lpair} fit parameters.

R_{Lpair} should be comparable to R_T. In fact, with τ fit to zero, we expect R_{Lpair} to absorb *all* of the time dependence, and be equivalent to R_{Tout}. The values for these two parameters are, in fact, nearly identical. We are also comforted by the tight consistency between R_{Tpair} and the values of R_L obtained from other parameterizations.

Koonin Parameterization

We have the made the first attempt that this author is aware of to fit experimental data to the Yano-Koonin Lorentz invariant correlation function for a space-time Gaussian source.

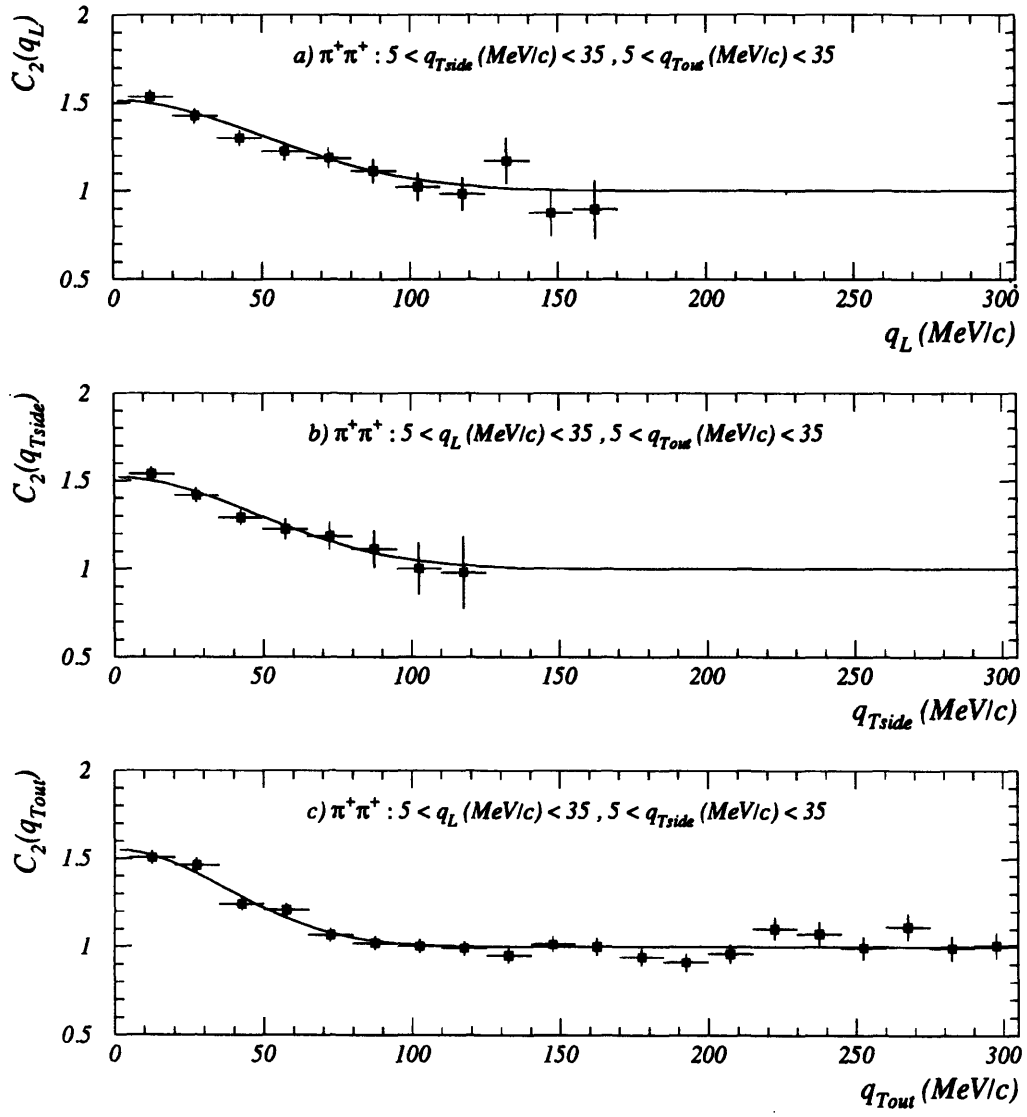

Figure 5-10: Low relative momentum slices of the $q_L q_{Tside} q_{Tout}$ parameterization of the *standard* $\pi^+\pi^+$ data set. Solid lines are the fits to the data over the full 3D phase space, evaluated at the center of the relative momentum slices of the unplotted variables. Fit parameters are presented in table 5.5.

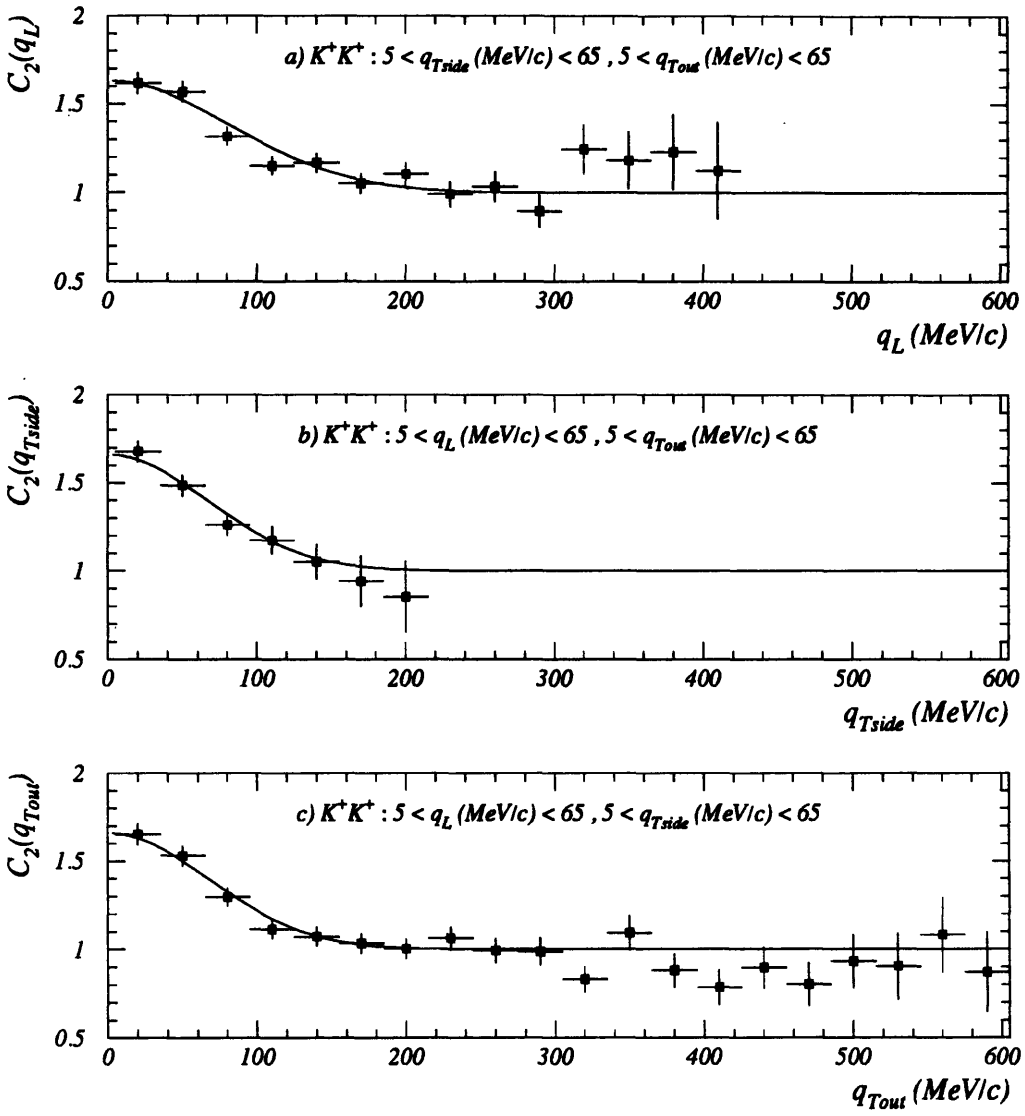

Figure 5-11: Low relative momentum slices of the $q_L q_{Tside} q_{Tout}$ parameterization of the *standard* K^+K^+ data set. Solid lines are the fits to the data over the full 3D phase space, evaluated at the center of the relative momentum slices of the unplotted variables. Fit parameters are presented in table 5.5.

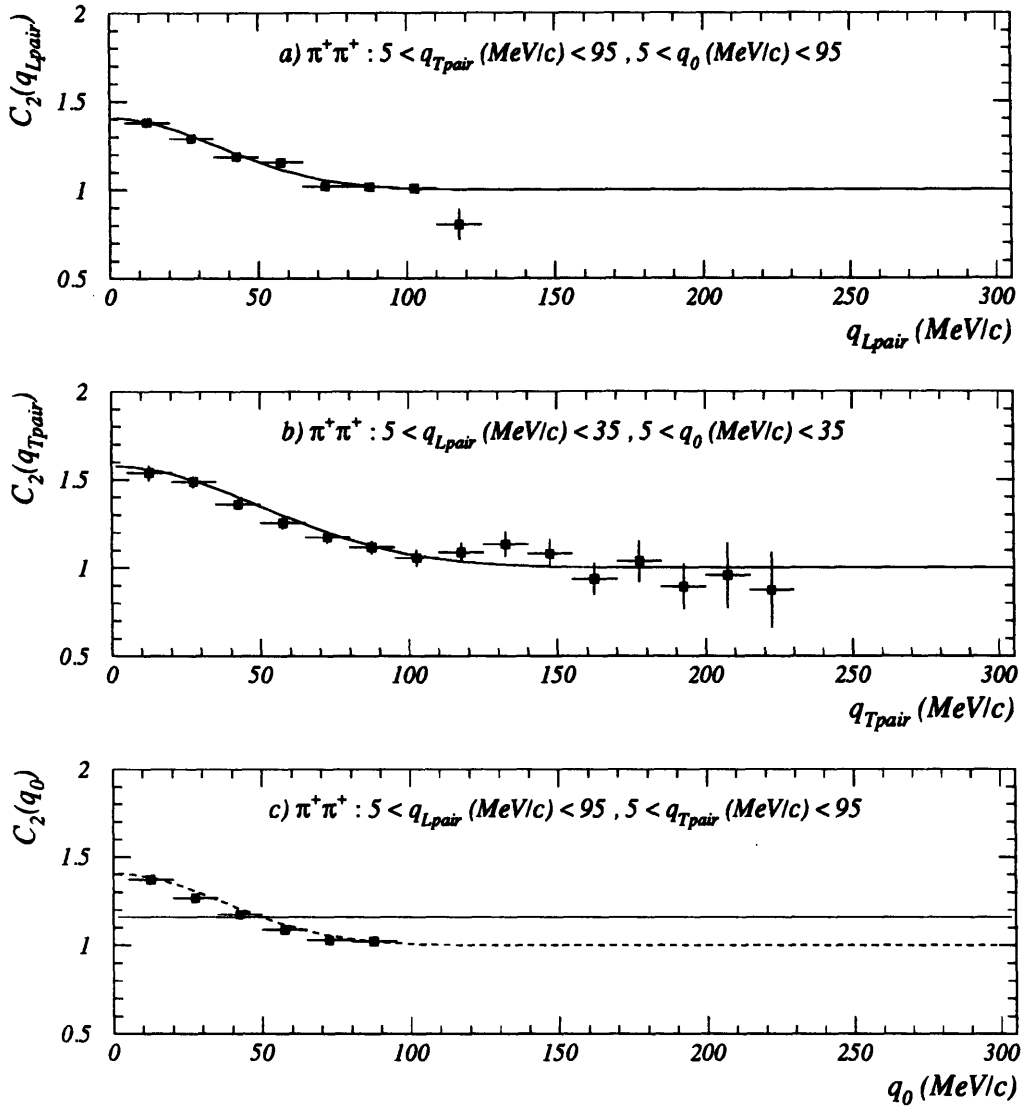

Figure 5-12: Low relative momentum slices of the $q_{Lpair}q_{Tpair}q_0$ parameterization of the *standard* $\pi^+\pi^+$ data set. Solid lines are the fits to the data over the full 3D phase space, evaluated at the center of the relative momentum slices of the unplotted variables. The dashed line in the q_0 slice is the fit function for R_{Lpair}, see text for explanation. Fit parameters are presented in table 5.8.

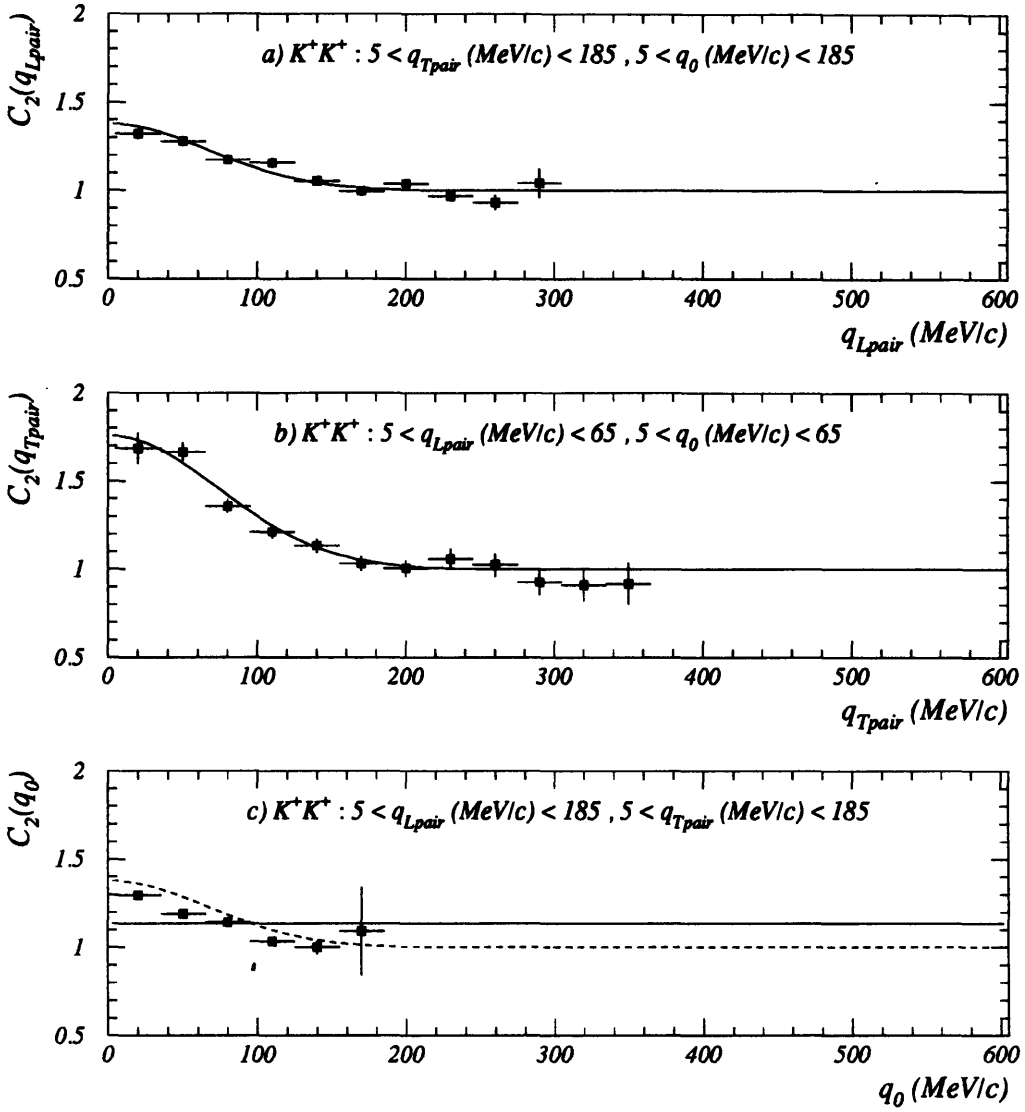

Figure 5-13: Low relative momentum slices of the $q_{Lpair}q_{Tpair}q_0$ parameterization of the *standard* K^+K^+ data set. Solid lines are the fits to the data over the full 3D phase space, evaluated at the center of the relative momentum slices of the unplotted variables. The dashed line in the q_0 slice is the fit function for R_{Lpair}, see text for explanation. Fit parameters are presented in table 5.8.

We have been forced to make the (reasonable) assumption that the source velocity is along the beam axis. With this assumption, the correlation function becomes:

$$C_2 = 1 + \lambda \exp\left(-\left(R^2 + \tau^2\right)\left(\gamma_s[q_0 - \beta_s q_L]\right)^2 - (QR)^2\right) \tag{5.2}$$

This parameterization is explicitly Lorentz invariant, but we find that the fit results depend on the frame in which we calculate the relative momenta. The results of fits to this correlation function, with the relative momenta projected at rapidities $y = 0.0$, and $y = 1.25$), are listed in table 5.10.

y_{fit}	Parameter	$\pi^+\pi^+$	K^+K^+
0.00	R	3.05 ± 0.06	2.06 ± 0.06
	τ	0.07 ± 0.40	0.09 ± 0.20
	λ	0.60 ± 0.04	0.85 ± 0.05
	y_s	0.91 ± 0.02	1.25 ± 0.08
	χ^2/dof	1257/1391	4031/4504
1.25	R	2.80 ± 0.17	2.11 ± 0.04
	τ	2.99 ± 0.39	0.00 ± 0.52
	λ	0.60 ± 0.03	0.85 ± 0.04
	y_s	1.43 ± 0.11	1.55 ± 0.11
	χ^2/dof	1480/1538	4182/4765

Table 5.10: Rapidity dependence of fits to the *Koonin* parameterization for the $\pi^+\pi^+$ and K^+K^+ *standard* data sets. See text for details.

These results *must* be considered work in progress since we do not understand this frame dependence. But we can make an attempt to extract some information. For the K^+'s, the size parameters are nearly independent of the fit frame and are consistent with the same parameters obtained from the q_0q parameterization. Both values for y_{source} seem reasonable. For the pions, the results when the fit is performed at $y = 1.25$ seem to make more sense than those obtained from the fit at $y = 0$. At this rapidity, the values of R and τ are both consistent with values for the same parameters obtained from the q_0q parameterization. There may be justified suspicion of the results obtained when the fit is performed at $y = 0$. In the lab frame, $p_z \gg p_\perp$. This distorts phase space in two ways. First, q_0 and q_L become quite correlated. From the discussion of the $q_{Lpair}q_{Tpair}q_0$ parameterization above, the reader should be suspicious of correlated relative momentum variables. Second, because of the increasing single particle momentum, the relative momentum distributions become much broader. Having used the

same bin size, this may mean that the Bose-Einstein enhancement was spread out over too many bins. With E859 data, we have the data to extract information from this interesting parameterization, but more work needs to be done.

$\langle p^{pair} \rangle$ Dependence

Dependence of the source parameters on the average pair momentum can arise for several reasons. A cooling source emits the fastest particles first, at a smaller radius. In an exploding source, the fastest particles are most likely to be emitted along the explosive direction. The greater dynamical correlations makes the effective source size smaller [Pra84]. RQMD predicts a larger resonance contribution at low $p_\perp$ in 200A · GeV/c heavy ion collisions [S+93b]. But, this effect is not predicted to be as severe at AGS energies [Mor94].

We have been able to divide the K^+K^+ data set into two $\langle p^{pair} \rangle$ bins, and the $\pi^+\pi^+$ data set into three $\langle p^{pair} \rangle$ bins. It should be reiterated that p^{pair} is calculated at $y = 1.25$. This means that the cut is in a variable that is nearly $\left\langle p_\perp^{pair} \right\rangle$. Confidence contours are plotted for the $\pi^+\pi^+$ data sets in figure 5-14. The analogous contours are plotted for the K^+K^+ data sets in figure 5-15. The fit parameters are listed in table 5.11 — table 5.14.

We see a generally downward trend in the size parameters with increasing momentum although the mid-$\langle p^{pair} \rangle$ cut goes against this trend in both R_T and R. For the pions, the value of λ is largest for the mid-$\langle p^{pair} \rangle$ data set. For the kaons, λ is largest for the low-$\langle p^{pair} \rangle$ data set. This is certainly not what one would expect from a hypothesis in which resonances dominate low-$\langle p^{pair} \rangle$.

Rapidity Dependence

We wanted to verify that kaons from the low rapidity tail were not unduly biasing our extracted source parameters. In order to test this, we cut the kaon distribution, demanding $y > 1.3$. In general, the source parameters were seen to decrease by $\approx$ 10%. R_L shrank by $\approx$ 20%.

The results of this study prompted us to divide the pion distribution into rapidity slices, $y < 1.5, y > 1.5$. Note that dividing the single particle distribution in half leaves only $\approx 1/4$ of the pairs in each of the two bins since half of the pairs have a particle in each bin. The behavior of the parameters in this study was less systematic for all variables except R_L. This parameter was observed to be significantly smaller in each bin than it was for the entire data set. For a data set in which particles were demanded to come from opposite sides of $y = 1.5$, R_L was seen to be significantly larger than for the uncut data set. These results are listed in table 5.15.

$\pi^+\pi^+$	$p^{pair} < 650$ (MeV/c)	$650 < p^{pair} < 850$ (MeV/c)	$p^{pair} > 850$ (MeV/c)
R_L	3.38 ± 0.35	2.73 ± 0.29	2.05 ± 0.24
R_T	3.61 ± 0.18	3.81 ± 0.31	3.01 ± 0.26
λ	0.68 ± 0.06	0.78 ± 0.10	0.71 ± 0.10
χ^2/dof	482.5/456	696.0/596	720.3/759

Table 5.11: $q_L q_T$ fit results for the different $\pi^+\pi^+$ $\langle p^{pair} \rangle$ data sets.

$\pi^+\pi^+$	$p^{pair} < 650$ (MeV/c)	$650 < p^{pair} < 850$ (MeV/c)	$p^{pair} > 850$ (MeV/c)
R	3.14 ± 0.11	3.25 ± 0.26	2.54 ± 0.22
τ	2.70 ± 0.57	2.52 ± 0.62	1.71 ± 0.67
λ	0.67 ± 0.05	0.85 ± 0.11	0.73 ± 0.09
χ^2/dof	167.8/167	256.9/251	473.4/435

Table 5.12: $q_0 q$ fit results for the different $\pi^+\pi^+$ $\langle p^{pair} \rangle$ data sets.

K^+K^+	$p^{pair} < 1050$ (MeV/c)	$p^{pair} > 1050$ (MeV/c)
R_L	1.94 ± 0.16	1.17 ± 0.17
R_T	2.30 ± 0.16	1.76 ± 0.20
λ	0.98 ± 0.10	0.69 ± 0.10
χ^2/dof	808.1/761	927.5/848

Table 5.13: $q_L q_T$ fit results for the different K^+K^+ $\langle p^{pair} \rangle$ data sets.

K^+K^+	$p^{pair} < 1050$ (MeV/c)	$p^{pair} > 1050$ (MeV/c)
R	1.95 ± 0.14	1.54 ± 0.07
τ	2.47 ± 0.59	0.00 ± 0.79
λ	0.96 ± 0.22	0.67 ± 0.09
χ^2/dof	328.8/300	361.4/364

Table 5.14: $q_0 q$ fit results for the different K^+K^+ $\langle p^{pair} \rangle$ data sets.

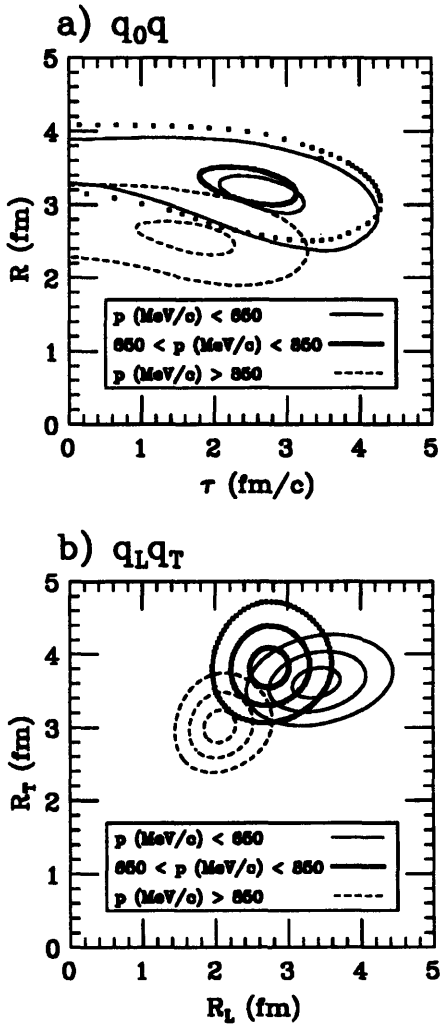

Figure 5-14: Confidence contours for the q_0q and q_Lq_T parameterizations of the different $\langle p^{pair} \rangle$ $\pi^+\pi^+$ data sets. The 2σ contour for the q_0q parameterization has been eliminated for clarity. Parameters are obtained from fits to the full 2D phase space. The optimization function is re-minimized with respect to the unplotted variables in the parameterization. Fit parameters are presented in table 5.11 and table 5.12.

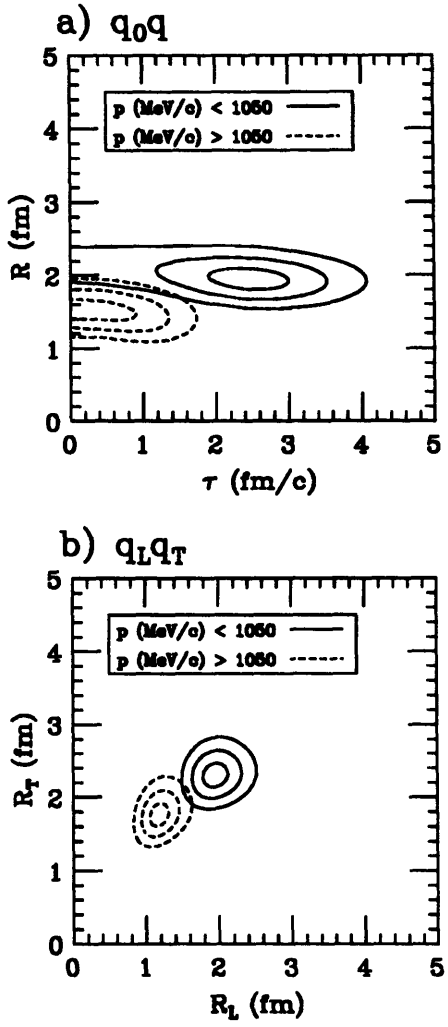

Figure 5-15: Confidence contours for the q_0q and q_Lq_T parameterizations of the different $\langle p^{pair} \rangle$ K^+K^+ data sets. Parameters are obtained from fits to the full 2D phase space. The optimization function is re-minimized with respect to the unplotted variables in the parameterization. Fit parameters are presented in table 5.13 and table 5.14.

This is an unambiguous sign of longitudinal dynamical correlations — the smaller the rapidity slice, the less of the source we actually observe. We have two working hypotheses for the origin of this behavior:

1. A velocity gradient imposed by a longitudinally expanding source.

2. Longitudinal shadowing. We think our spectrometer acceptance is centered near the source rapidity — the particle at lower rapidity may preferentially come from the back of the source and the higher rapidity particle may preferentially come from the front of the source [Ste].

	standard	$y_1, y_2 < 1.5$	$y_1, y_2 > 1.5$	$y_1 < 1.5 \wedge y_2 > 1.5$
R_L	2.52 ± 0.18	1.67 ± 0.40	1.41 ± 0.18	2.98 ± 0.19
R_T	3.56 ± 0.13	3.71 ± 0.19	3.53 ± 0.16	3.37 ± 0.14
λ	0.64 ± 0.04	0.74 ± 0.07	0.59 ± 0.04	0.59 ± 0.03
χ^2/dof	729.3/759	512.8/499	330.0/362	770.1/759

Table 5.15: $q_L q_T$ fit results for different rapidity slices of the $\pi^+\pi^+$ data set. See text for details.

Chaoticity

The values for the chaoticity parameter, λ, for all parameterizations of the $\pi^+\pi^+$ and K^+K^+ *standard* data sets, are graphically summarized in figure 5-2. λ is a delicate parameter, both in terms of its experimental measurement and in terms of its theoretical interpretation. As summarized below, and detailed in appendix A, and appendix B, we estimate a systematic uncertainty of 10% on the values of λ. But, any systematic change in λ is likely to affect both species in the same direction. As a result, the observed difference in λ, between the two species, is probably real. This is probably mostly due to differences in resonance production. In [A+92a], the resonance contribution to pion production is estimated, from pp collisions at 12 GeV/c [B+74], to be no more than 15%. This value is almost enough to account for the deviation of λ from one for the $\pi^+\pi^+$ data set. Given the systematic error associated with λ, there is certainly no evidence for any source coherence. The fact that the values of λ, for each species, are consistent across all different parameterizations gives confidence in the entire fitting procedure.

Fit Quality

Quality of fits to data are usually reported as χ^2/dof. As reported in table 5.1 - table 5.8, the values of χ^2/dof indicate that the *standard* data sets are well fit by each of the examined parameterizations. The authors of [Gyu93] warned against the possibility that testing a fit with this *average* quantity may hide pathological behavior in the data, interesting new physics, or both. Motivated by this work, we examined the relative momentum distributions of χ^2 for the 1D and 2D parameterizations. These distributions are plotted for pions in figure 5-16, and for kaons in figure 5-17. These distributions show no sign of systematic deviation from the chosen fit functions.

Another method for examining the quality of multidimensional fits was suggested by George Stephans. In this method, we calculate the deviation between the fit and the data at every bin:

$$\chi = \frac{{C_2}^{obs} - {C_2}^{exp}}{\sigma_{C_2^{obs}}}. \tag{5.3}$$

If the correlation function errors are Gaussian, χ should be Gaussian with $\mu = 0, \sigma = 1$. These distributions, for every fit parameterization of the *standard* $\pi^+\pi^+$ data set, are shown in figure 5-18. The corresponding distributions for the *standard* K^+K^+ data set are shown in figure 5-19. The solid curves in these figures are the expected Gaussian distributions, *not* fits to the data.

The non-Gaussian nature of the correlation function fluctuations has been discussed in section 4.5. But, this deviation from Gaussian is only expected for bins with a small number of counts. There are few bins with a small number of counts in the 1D parameterizations. Indeed, we see that the distribution of χ is Gaussian for the 1D *and* 2D parameterizations. But, for most of the 3D parameterizations, the distribution of χ is distinctly non-Gaussian.

Some of this difference may be due to non-Gaussian fluctuations in the relatively large number of small-count bins. The fact that C_2 is a biassed estimator, see section 4.5, may also contribute to this difference. There is also a bias introduced into this distribution by the necessary elimination of bins with no counts in the *Actual* or *Background* distributions. (Such bins, of course, give a singularity in the value of χ.) This bias gives a dip at small, negative values of χ.[3] More work needs to be done to verify that the observed deviations from Gaussian distributions are due to effects that we understand.

[3]The dip is at small negative values because our *Background* distribution has many more pairs than our *Actual* distribution. As a result, most of the eliminated bins have zero counts in the *Actual* distribution, for which ${C_2}^{obs} - {C_2}^{exp} < 0$.

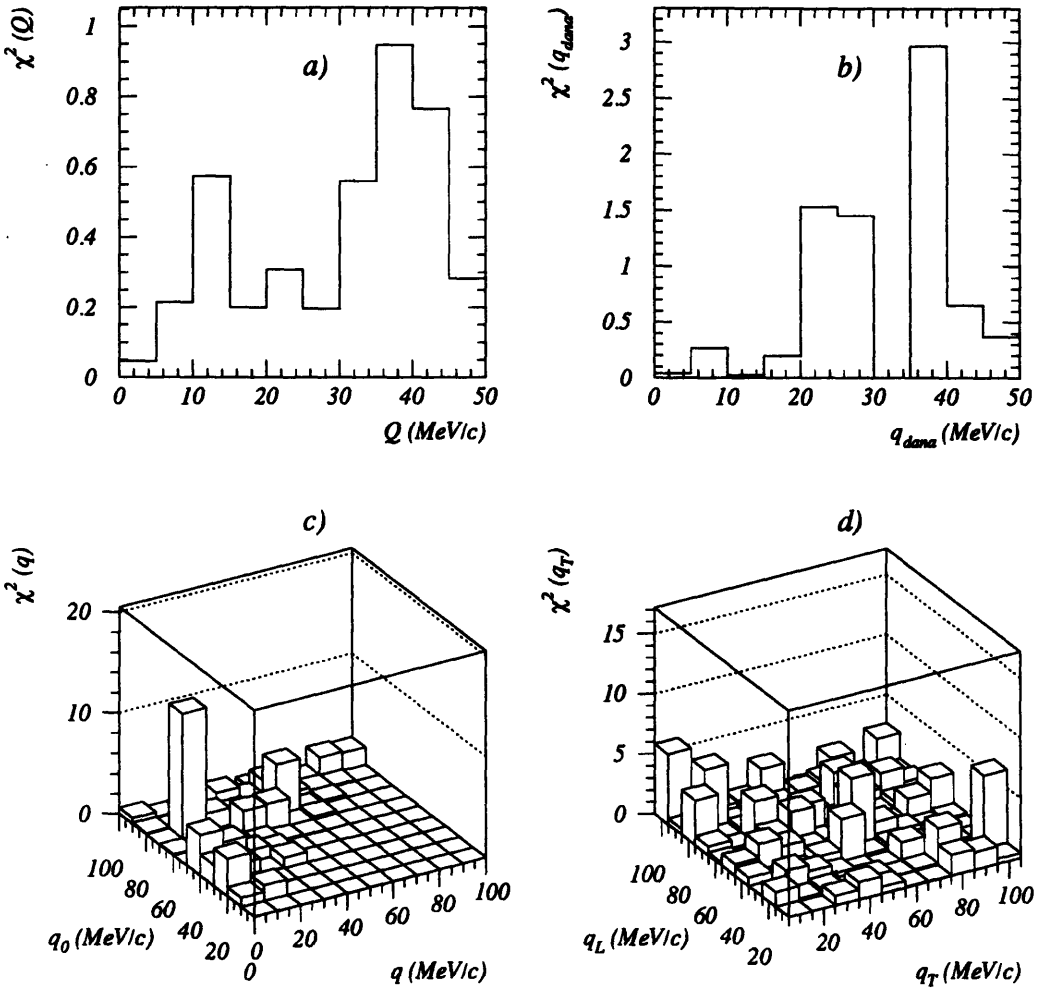

Figure 5-16: Relative momentum distributions of χ^2 for the 1D and 2D fit parameterizations of the *standard* $\pi^+\pi^+$ data set. These figures concentrate on the lower relative momentum bins for clarity. The distributions have been examined at higher values of relative momentum with no sign of systematic behavior.

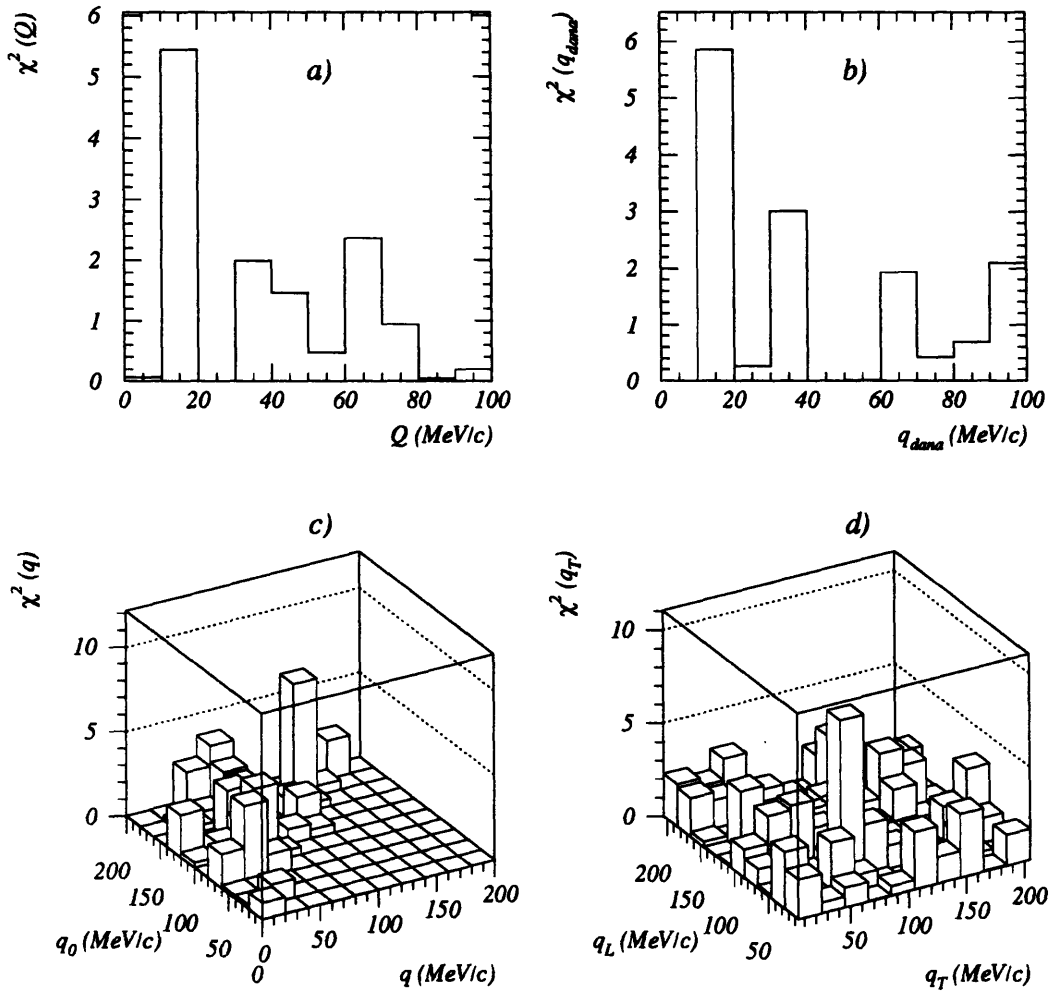

Figure 5-17: Relative momentum distributions of χ^2 for the 1D and 2D fit parameterizations of the *standard* K^+K^+ data set. These figures concentrate on the lower relative momentum bins for clarity. The distributions have been examined at higher values of relative momentum with no sign of systematic behavior.

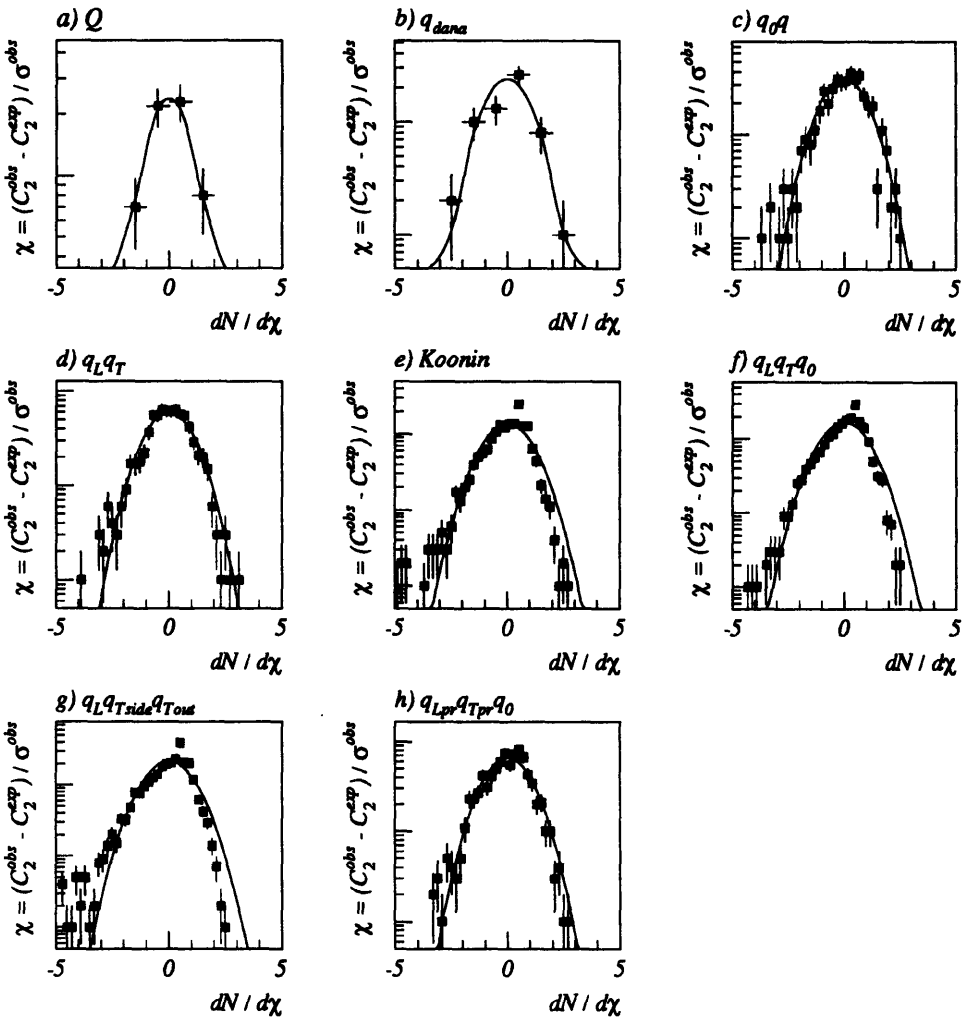

Figure 5-18: Normalized binwise error distributions for all source parameterizations of the *standard* $\pi^+\pi^+$ data set. These distributions should be Gaussian, with $\mu = 0$ and $\sigma = 1$ and this is the function plotted with a solid line. The apparently non-Gaussian tails in the plotted function are due to roundoff errors in the plotting package. This is one of a number of features collectively referred to as "pawology."

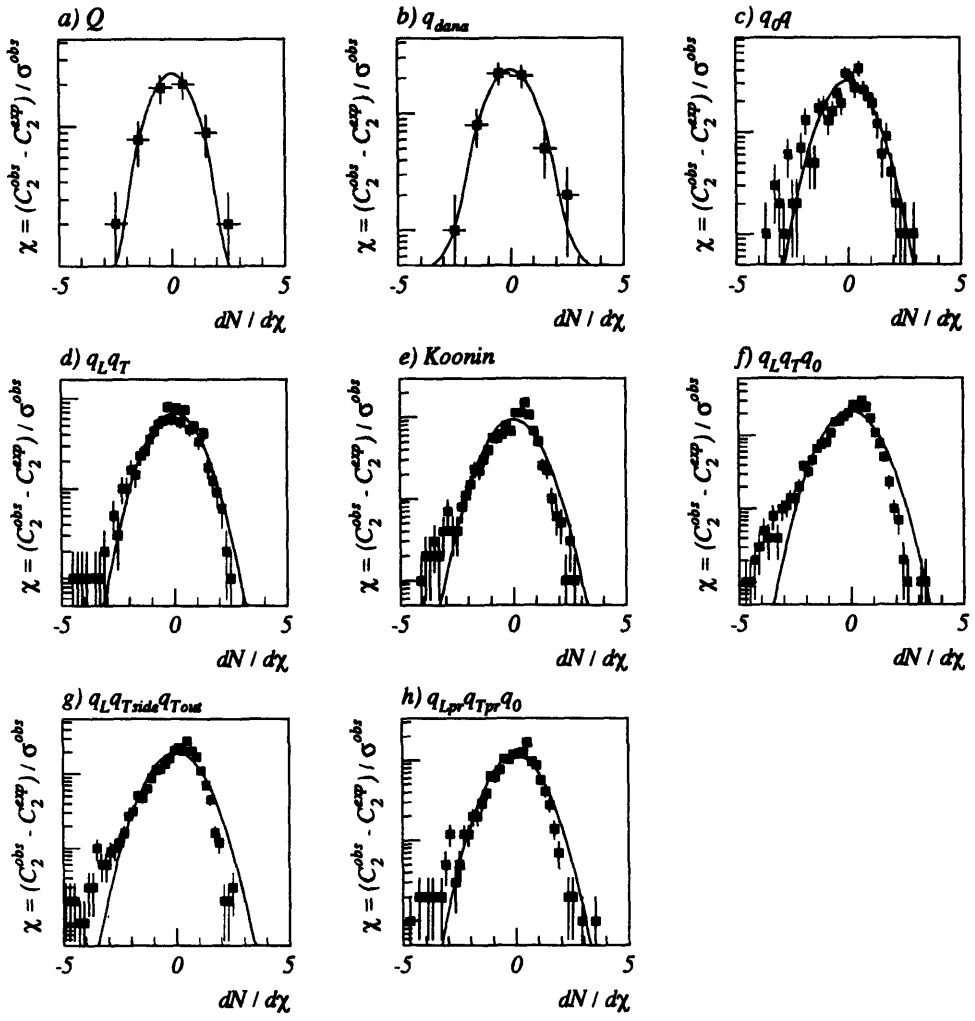

Figure 5-19: Normalized binwise error distributions for all source parameterizations of the *standard* K^+K^+ data set. These distributions should be Gaussian, with $\mu = 0$ and $\sigma = 1$ and this is the function plotted with a solid line. The apparently non-Gaussian tails in the plotted function are due to roundoff errors in the plotting package. This is one of a number of features collectively referred to as "pawology."

Systematic Error Summary

We have examined various systematic effects on the extracted source parameters. The range of values taken on by the various parameters is summarized in appendix A. The different data sets used in these studies are detailed in section 4.2.

The overall systematic error on the various parameters, except the K^+K^+ τ parameter, is estimated to 5–10%. These numbers are comparable to the statistical errors. The K^+K^+ τ parameter is fit to zero, so a fractional error makes no sense. In several of the systematic studies, the K^+K^+ τ parameter was fit to values as large as 1 fm/c. We therefore estimate the systematic error for this parameter to be 1 fm/c. Perhaps not surprisingly, this is comparable to the statistical errors on this parameter.

Here I summarize the results of these studies:

- Low relative momentum bins were incrementally eliminated to determine the importance to the fit parameters of these regions which have the largest systematic uncertainty associated with them. This had somewhat different effects on different source parameters. But, overall, the effects were small.

- Relative momentum bins necessarily have a finite size. If this size is too big, the fit parameters will be distorted. In order to estimate the distortion due to our minimum bin size, we systematically increased the bin sizes. For all but the 3D fits, this was seen to have a negligible effect. For the 3D fits, a doubling of the standard bin size (30 MeV/c for kaons, 15 MeV/c for pions) reduced λ and the radius parameters by 5-10%. The minimum bin size on the 3D fits is already large, so doubling it is a significant change. We estimate the effect of the standard bin size to be negligible.

- Fits were performed without any correction for the Coulomb distortion of phase space. For the kaons, this reduced λ by 50% and for the pions this reduced λ by 30%. It affected different radius parameters differently. Since we feel that we know the correction to within a few percent, we estimate the systematic errors associated with using the Gamow factor instead of the full Coulomb correction to be quite small.

- The importance of potential errors in the TPAC was studied by tripling the size of the scale angle cut to 3.3 mrad. With a cut this big, the TPAC is effectively unity. This study showed negligible change in the parameters.

- The effect of particle contamination was studied by fitting correlation functions in which particles were required to satisfy the GASČ in TOF ID overlap regions, see section 4.2.2.

This was found to have negligible effect.

- Residual correlations were studied in some detail as reported in appendix B. Taking them into account increases λ by 2-5%, and decreases the radius parameters by the same fraction.

- Ultra-central TMA software cuts were applied. This was to reduce averaging over event character, and to see if anything interesting occurred in the most violent collisions. The effect is negligible for kaons. There was some difference seen for pions. Values for λ and R_L were both reduced. These variations are not very statistically significant. And, when a slightly looser TMA cut was made, the effect went away. This same study was performed for the very large statistics $2\pi^-$ sample taken at 14° [Sol94]. Negligible change was seen for the different source parameters.

Chapter 6

Bose-Einstein Correlations in Models

There is no calculable theory of relativistic heavy ion collisions. Instead, several types of phenomenological models are used to gain insight, and to provide a baseline against which to determine if measured behavior indicates the presence of new physics. Theorists from higher and lower energy regimes have joined their experimental colleagues in the quest to understand the extreme states of nuclear matter produced in these collisions. Fluid dynamic and cascade type models have evolved out of descriptions of lower energy nucleus-nucleus collisions. String models have evolved out of descriptions of e^+e^- collisions, deep-inelastic scattering data, and hadron-hadron collisions, all at higher energies. These models have successfully predicted (and postdicted) a wide variety of quantities measured in relativistic heavy ion collisions. A review of such predictions is beyond the scope of this thesis. The interested reader is directed to the proceedings of the most recent Quark Matter conference [Str94, Gus94, S+94a].

As discussed in section 1.4, the interplay between the source size and dynamics complicates the interpretation of extracted source parameters. At this point, the only model-independent statements one can make are highly qualified. With a model, one *knows* the spatial size of the source as well as the dynamics. With this knowledge, one can observe how different dynamics change the source size as predicted by a correlation function calculation. This is the biggest motivation for studying model predictions of Bose-Einstein correlations.

We can remove ourselves even further from the data,[1] and try to use Bose-Einstein correla-

[1] And offend many experimentalists.

tions to differentiate between models. Bose-Einstein correlations are sensitive to the space-time description of the source. By demanding agreement between the data and model predictions, we constrain all six phase-space dimensions.

In section 6.1, we will describe the Wigner density technique developed by Pratt for the *post hoc* incorporation of Bose-Einstein correlations into various models. In section 6.2, we will describe the development of a spectrometer response function to account for experimental resolution on the model predictions. In section 6.3, we will present some details of RQMD, the specific cascade code used for model comparisons in this analysis. Finally, in section 6.3.2, we will present some results; both a characterization of the source directly from the final space points and a Bose-Einstein analysis.

6.1 The Pratt Wigner Density Function Technique

All of the currently available models are classical. None produce a final state wave function, let alone a symmetrized wave function. As a result, none contain Bose-Einstein correlations. Pratt has developed a technique in which one identifies Wigner density functions with the classical phase space distributions output by models [Pra94, and references therein]. With this identification, one is left with the task of calculating the squared magnitude of the two-particle wave function for identical particle pairs produced by the model.

This technique, embodied in a computer code that has been made freely available, has been widely used in the relativistic heavy ion community.[2] Data have been compared to correlation functions predicted by fluid dynamic models [B+93b], cascade models [Pra94, and references therein] and string models [M+92].

In the remainder of this section, we will present a brief derivation of the technique, review the technique's algorithm, and document a change we made in the standard impact parameter selection prescription.

6.1.1 Derivation and Justification

A detailed derivation of this technique can be found in [P+90b]. More approachable derivations can be found in [Zaj93, Pra94]. The following discussion will borrow heavily from these latter two sources.

[2]The code is accompanied by its author who offers his enthusiastic assistance and invaluable insight to anyone who asks for it.

6.1. THE PRATT WIGNER DENSITY FUNCTION TECHNIQUE

Writing the correlation function in terms of Wigner density functions requires three assumptions:

1. Particle emission is independent. A consequence of this condition is that there can be no higher-order correlations. Examples of such correlations include Coulomb interaction with the nuclear residue and three-particle Bose-Einstein correlations.

2. The source distribution that we are trying to measure, $S(\mathbf{r}, \mathbf{p})$, varies slowly with $\mathbf{p}$.

3. Particles in a pair are emitted at equal times. In this technique, equal time emission is explicitly enforced by propagating the particles to the positions that they will occupy at the average of their true emission times.

With these assumptions, the correlation function can be written as:

$$C_2(\mathbf{p}_1, \mathbf{p}_2) \equiv \frac{\mathcal{P}_2(\mathbf{p}_1, \mathbf{p}_2)}{\mathcal{P}_1(\mathbf{p}_1)\,\mathcal{P}_1(\mathbf{p}_2)}, \tag{6.1a}$$

$$= 1 + \frac{\int d\mathbf{r}_1\, d\mathbf{r}_2\, |\Psi(\mathbf{q}, \Delta)|^2\, \rho_W(\mathbf{r}_1, \mathbf{K})\, \rho_W(\mathbf{r}_2, \mathbf{K})}{\left[\int d\mathbf{r}_1\, \rho_W(\mathbf{r}_1, \mathbf{p}_1)\right]\left[\int d\mathbf{r}_2\, \rho_W(\mathbf{r}_2, \mathbf{p}_2)\right]}, \tag{6.1b}$$

where $\mathbf{K} \equiv \frac{1}{2}(E_1 + E_2, \vec{p}_1 + \vec{p}_2)$ is the average four-momentum of the pair, $q \equiv (E_1 - E_2, \vec{p}_1 - \vec{p}_2)$ is the relative four-momentum of the pair, and $\Delta \equiv (0, \vec{r}_1 - \vec{r}_2 - \vec{\beta}_{pair}(t_1 - t_2))$ is the average-time separation of the pair. In the correlation computer code, C_2 is evaluated in the pair center-of-mass frame, where $\vec{\beta}_{pair} = 0$. Equation 6.1 is also evaluated in the low-relative momentum limit,[3] where $\mathbf{K} \to \mathbf{p}_1, \mathbf{p}_2$:

$$C_2(\mathbf{p}_1, \mathbf{p}_2) = 1 + \frac{\int d\mathbf{r}_1\, d\mathbf{r}_2\, |\Psi(\mathbf{q}, \Delta)|^2\, \rho_W(\mathbf{r}_1, \mathbf{p}_1)\, \rho_W(\mathbf{r}_2, \mathbf{p}_2)}{\left[\int d\mathbf{r}_1\, \rho_W(\mathbf{r}_1, \mathbf{p}_1)\right]\left[\int d\mathbf{r}_2\, \rho_W(\mathbf{r}_2, \mathbf{p}_2)\right]}. \tag{6.2}$$

The Wigner density function is defined in terms of the one-body density matrix [Zaj93]:

$$\rho(\mathbf{x}, \mathbf{x}') = \int d(\mathbf{x}_2, \ldots, \mathbf{x}_A)\, \Psi^*(\mathbf{x}, \mathbf{x}_2, \ldots, \mathbf{x}_A)\, \Psi(\mathbf{x}', \mathbf{x}_2, \ldots, \mathbf{x}_A), \tag{6.3}$$

$$\rho_W(\mathbf{r}, \mathbf{p}) = \langle \mathbf{r} | \rho(\mathbf{x}, \mathbf{x}') | \mathbf{p} \rangle. \tag{6.4}$$

Zajc [Zaj93] notes the *apparently* classical nature of the Wigner density function:

$$\mathcal{P}(\mathbf{p}) = \int d\mathbf{r}\, \rho_W(\mathbf{r}, \mathbf{p}), \tag{6.5a}$$

[3] This is the limit of interest for Bose-Einstein correlations.

$$\mathcal{P}(\mathbf{r}) = \frac{1}{(2\pi\hbar)^3}\int d\mathbf{p}\,\rho_W(\mathbf{r},\mathbf{p}). \tag{6.5b}$$

Pratt's key insight was identifying the Wigner density function, $\rho_W(\mathbf{r},\mathbf{p})$, with the classical phase space distributions, $\rho(\mathbf{r},\mathbf{p})$, produced as model output. This should, and does, set off warning sirens - "What about the uncertainty principle? How can we use the model output, which specifies the position and momentum of each particle?" Zajc [Zaj93] reveals the key to interpreting this violation of the uncertainty principle:

> ...$\rho_W(\mathbf{r},\mathbf{p})$ is not positive definite, which prohibits a one-to-one mapping between ρ_W and a truly classical phase space distribution.

Zajc [Zaj93] also presents an exercise that facilitates a quantitative understanding of when Pratt's technique begins to break down. Consider a source that is Gaussian in space and momentum:

$$\rho(\vec{r},\vec{p}) \sim \exp\left(-\frac{|\vec{r}|^2}{2R^2} - \frac{|\vec{p}|^2}{2P^2}\right). \tag{6.6}$$

If the Wigner density is identified as the classical density given in equation 6.6, and one solves for the correlation function by equation 6.1, *the predicted source radius does not equal the input radius*:

$$R_W = R\sqrt{1-\left(\frac{\hbar/2}{RP}\right)^2}. \tag{6.7}$$

This shows that violation of the uncertainty principle, implicit in Pratt's technique, shows up as incorrect predictions of the source parameters when $RP \not\gg \hbar/2$.

Gyulassy has argued that violation of the uncertainty principle should be explicity avoided by smearing the spatial positions produced by the models [P+90a]. Pratt has argued against such smearing on two grounds [Praa]:

1. The input to cascade codes, such as RQMD, are measured cross sections and momentum distributions. The processes that result in these quantities obey the uncertainty principle. In some sense then, the codes "know about the uncertainty principle." Thinking in terms of equation 6.7, we have $RP \gg \hbar/2$ in relativistic heavy ion collisions.

2. Models can still locally violate uncertainty principle if they predict very strong dynamical correlations. Pratt argues that smearing a model's position distributions merely hides a violation of the uncertainty principle. Such a violation should instead be exposed by the resulting, incorrect, source parameters.

6.1.2 The Algorithm

The algorithm for imposing correlations onto model output has been given in some detail in [Pra94]. Here I give a brief summary:

1. Run the model of your choice in order to get final 8-dimensional phase space points for the produced particles. The model must be run with a fixed spatial orientation of the projectile with respect to the target (the *reaction plane*).

2. Pass model events through a simulation of the experimental centrality trigger conditions. This will be discussed in section 6.3.1.

3. For those events which pass the centrality cut, force the decay of resonances which contribute to the particles of interest. For RQMD the only the resonances left undecayed are the following, weak-force moderated, resonances: $K^0_s, \Lambda, \Sigma^+, \Sigma^-$.

4. Record the phase space points and impact parameter for those particles of interest that lie within the $p\theta$ acceptance of the spectrometer.

5. Bin the particles in impact parameter. This is different than the standard prescription, in which impact parameters are selected from a series of impact parameter δ-functions. Implications of this are discussed in section 6.1.3.

6. Loop over the phase space points for a given impact parameter bin to form random pairs (an event-mixing procedure). The number of pairs must be properly generated for each impact parameter bin. This is discussed in section 6.1.3. Care must be taken to not overmix.

7. Make a rough check on the pair opening angle, $\delta\phi$. If $\delta\phi > \delta\phi_{max}$ (where $\delta\phi_{max}$ is the largest ϕ separation allowed in the spectrometer), this pair can be eliminated from consideration without any further acceptance calculation.

8. If a pair passes the $\delta\phi$ cut, rotate the position and momentum of ***both particles*** by a random angle α. We perform this rotation in order to increase statistics. By rotating the pairs together, we preserve the reaction plane orientation. α is chosen such that $\langle p^{pair} \rangle$ varies randomly across a ϕ sector just large enough to contain the entire ϕ-acceptance of the spectrometer. The rotated particles are each checked against the full spectrometer acceptance.

9. Boost the particles to their center-of-mass frame and calculate the squared wave-function. This is the factor by which each pair will be weighted throughout the rest of the analysis.

10. We must now smear the momenta according to the spectrometer resolution. We also need to correct for efficiency and particle decay in the spectrometer. Both of these topics are discussed in section 6.2. At this point, we have an *Actual* distribution, completely compatible with subsequent stages of the standard analysis described in chapter 4.

6.1.3 Impact Parameter Selection

As discussed in the previous section, we want to mix particles from different events in order to form the correlation function. But, we do not want to average over event characteristics, such as impact parameter. For this reason, the standard input to the Pratt algorithm are particles from events thrown at a series of impact parameter δ-functions. The only particles mixed come from events with the same impact parameter.

Unfortunately, RQMD is a *very* CPU intensive code.[4] Because of this, we wanted to generate only one data set for use in both single-particle analyses [Mor94, Sun94, Zac94], and two-particle analyses. Although we were worried about event-class averaging in the two-particle analyses, we were also worried that discrete impact parameters could produce subtle biases in the single-particle analyses. Because the preferred method for the two-particle analyses was the unorthodox method,[5] the burden of proof was on us - Would a correlation analysis really be sensitive to the use of impact parameter bins as opposed to impact parameter δ-functions?

Our first impression was that, at least for central collisions, it should not make much of a difference. In E859, the source has been shown to scale with the number of projectile participants, $A_{pp}^{1/3}$ [Sol94]. But, for ^{28}Si + ^{197}Au collisions with $b < 5$ fm, there is not much change in A_{pp}. No change in the extracted source parameters was observed for different TMA bins of the central ^{28}Si+^{197}Au $\rightarrow 2\pi^+\pi^+$ data set (defined by the forward-going energy deposited in the ZCAL) [Sol94].

We confirmed this expectation by examining our ability to know the impact parameter. In RQMD, the impact parameter is defined to be the distance between the center-of-mass of the projectile and that of the target. Due to the finite number of nucleons, this quantity was observed to have an uncertainty of ≈ 0.4 fm. Since this was about the size of the impact parameter bins that we wanted to use, we decided to bin the data. We used 0.5 fm bins for kaons and 0.2 fm bins for pions. In a way, event-mixing necessarily imposes the position smearing advocated by Gyulassy (see section 6.1).

Due to memory considerations, we wanted to process one impact parameter at a time. In

[4] One central ^{28}Si + ^{197}Au event takes ≈ 1.5 CPU minutes on a DEC ALPHA 3000/400.
[5] And because there were more, and larger, people performing single-particle analyses.

order to do this, the number of pairs that get mixed for each impact parameter needs to be precalculated. Since our events are generated with correct geometrical weighting of impact parameters, we can write this number as:

$$P_b = \frac{(P_{tot})\left(\frac{S_b}{E_b}\right)^2 (A_b)}{\sum_{b=1}^{N}\left(\frac{S_b}{E_b}\right)^2 (A_b)}, \tag{6.8}$$

where,

$P_{tot} \equiv$ The total number of pairs to mix.

$P_b \equiv$ The number of pairs for impact parameter b.

$S_b \equiv$ The number of single-particle phase space points for impact parameter b.

$A_b \equiv$ The area corresponding to impact parameter b.

$E_b \equiv$ The number of events at impact parameter b.

$N \equiv$ The total number of impact parameters.

6.2 E859 Spectrometer Response Function ($\mathcal{R}_p$)

Ideally, weighted pairs generated by the procedure described in section 6.1 would be passed through the E859 Monte Carlo program, in order to impose the experimental response function, $\mathcal{R}\left(x_1, x_2, \ldots, x_n \rightarrow x_1', x_2', \ldots x_n'\right)$. The Monte Carlo output would then be passed through the rest of the analysis chain described in chapter 3 and chapter 4. Only after all this would the model contain the effects of decay, multiple scattering, energy loss, efficiency, and acceptance, and thereby be comparable to spectrometer data. Unfortunately, even with today's computational abilities, it is not feasible to generate the millions of Monte Carlo events needed to make model comparisons to all of the data sets of interest.[6]

Inspired by the work of Vutsadakis [Vut92], we set out to use the results of a limited Monte Carlo simulation of the detector to generate an analytic response function. In [Vut92], the response function was formulated as a single histogram in the relative momentum variable, Q: $\mathcal{R}_Q\left(Q_i \rightarrow Q_1, Q_2, \ldots, Q_n\right)$. This formulation is appropriate for the proton correlations studied in [Vut92], since there is only one relative momentum variable of interest. But, the formulation of $\mathcal{R}_Q$ in terms of relative momentum variables is cumbersome for the studies in this analysis,

[6]It takes roughly one CPU minute on a VAX Model 4000-60 computer to process one complete two-track event through the E859 Monte Carlo program.

since we want to examine the correlation function for different relative momentum projections and different binning schemes. Such a formulation would force us into one of two bad situations. Either we would have to store some large data structure on disk and use it to generate a new response function for every different relative momentum histogram (different in projection *or* binning) that we wanted to examine. Or, we would have to develop a functional form for the response function in every relative momentum variable analyzed.

We realized that formulating the response function in terms of the single-track momenta, $\mathcal{R}_p\left(\vec{p}, \rightarrow \vec{p}'\right)$, would be a very flexible approach. With a reasonable functional form for $\mathcal{R}_p$, we would have a single algorithm which could generate relative momentum distributions of model output, smeared by the spectrometer, for any projection or binning scheme desired. We would simply smear the model-output momentum for each track in a pair with $\mathcal{R}_p$. We would then use these smeared momenta to calculate the relative momentum bin to increment for that pair. We have obtained such a form and this is the subject of the remaining discussion in this section.

6.2.1 $\mathcal{R}_p$ Monte Carlo Data Set

The Monte Carlo data set used for this analysis is the same used in the TPAC study described in section 4.2.5. 200,000 events were generated with $2\pi^-$'s chosen according to:

$$\frac{dn}{dm_\perp} \sim m_\perp \exp\left(-m_\perp/A\right), \tag{6.10}$$

where A was obtained from fits to E802 data [Par92]. The target was 1.5% interaction lengths of gold in order to interpolate between the Feb91 and Mar92 target thicknesses. Target-z interaction points were chosen according to a flat distribution coincident with the extent of the target volume. All physics processes were turned on, the Moliere multiple scattering option was selected, and the full magnet map was enabled. Digitized events were analyzed with the same AUSCON and PICD executables as the spectrometer data. For the response function study we needed to make a few additional cuts:

- We will address the effects of decay separately, see section 6.2.4, so we eliminate any decay products from this analysis by using only those GEANT tracks whose origin, $r_0 < 4\,\text{cm}$ from the target.
- We demand that both tracks in an event be satisfactorily reconstructed.
- We demand that both GEANT tracks survive to T4, the final tracking chamber.

- We demand that there be a unique mapping between GEANT and AUSCON tracks. An AUSCON track is mapped to the GEANT track with which it has the smaller magnitude of relative momentum, $|\vec{q}|$.

6.2.2 $\mathcal{R}_p$ Parameterization

$\mathcal{R}_p$ $(\vec{p}, \rightarrow \vec{p}')$ is theoretically a six-dimensional quantity. This quantity would be very time-consuming to generate and would most likely not provide any insight into the processes which effect our momentum determination. Therefore we reached into the physicist's bag of tricks and came up with *simplification* and *experimentation*. We considered the different components of $\mathcal{R}_p$ in an effort to factorize it into independent variables. The paramaterization of $\mathcal{R}_p$ is described in the remainder of this section. Figure 6-1 shows the different distributions used to define $\mathcal{R}_p$ and fits to these distributions. Table 6.1 lists the fit values used.

Variable	Fit Parameter	Value
$\beta p\omega$	$A_1^{\beta p\omega}/A_1^{\beta p\omega}$	1.0
	$A_2^{\beta p\omega}/A_1^{\beta p\omega}$	6.6×10^{-1}
	$A_3^{\beta p\omega}/A_1^{\beta p\omega}$	8.0×10^{-3}
	$A_4^{\beta p\omega}/A_1^{\beta p\omega}$	8.0×10^{-4}
	$\sigma_1^{\beta p\omega}$ (GeV·mrad)	2.37
	$\sigma_2^{\beta p\omega}$ (GeV·mrad)	4.72
	$\sigma_3^{\beta p\omega}$ (GeV·mrad)	7.81
	$\sigma_4^{\beta p\omega}$ (GeV·mrad)	20.2
δp	$A^{\delta p}$ (MeV/c)	5.14
	$B^{\delta p}$ (MeV/c)	106.0
	$C^{\delta p}$ (MeV/c)	230.0
σp	$A^{\sigma p}$	0.01
	$B^{\sigma p}$ (MeV/c)$^{-1}$	9.31×10^{-7}

Table 6.1: This table lists the fit parameters for the different variables used to parameterize the spectrometer response function. The parameterization is described in the text. The comparison of these fit values to the data are plotted in 6-1.

We first factorize the change in a track's momentum into a change in the momentum

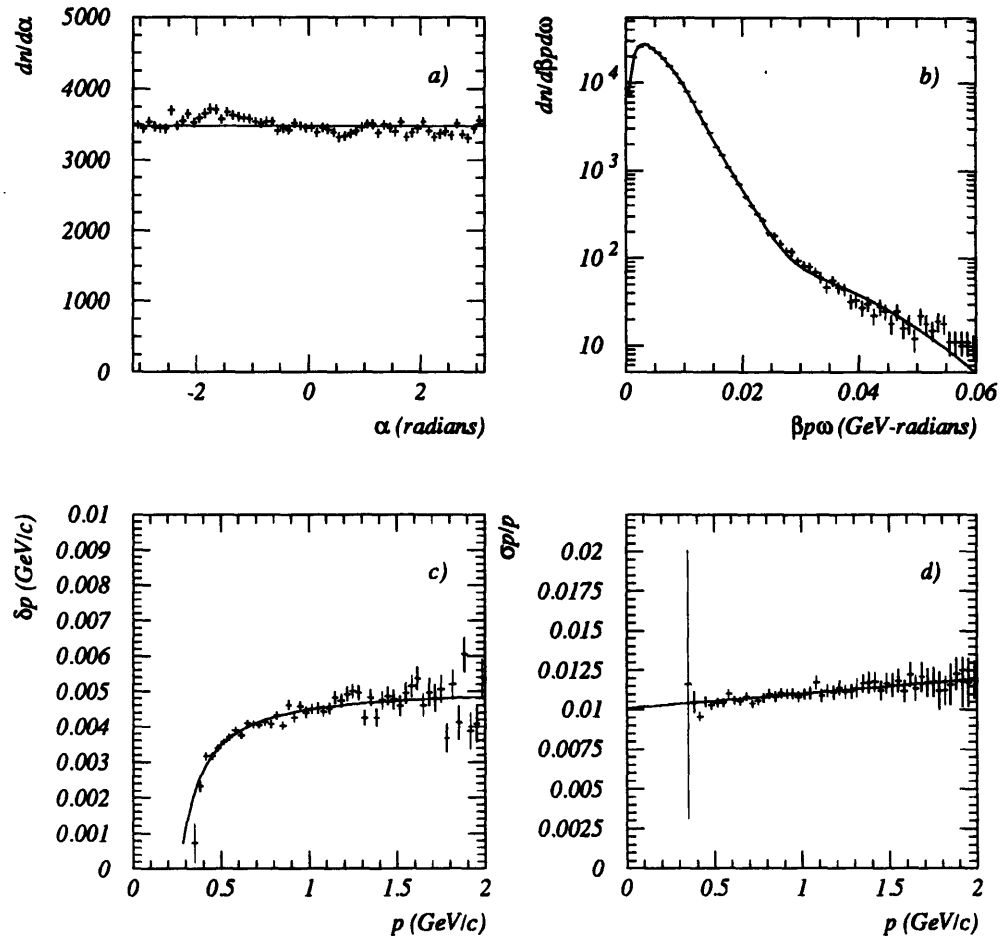

Figure 6-1: The different panels show fits to the different variables used to parameterize the spectrometer response function, $\mathcal{R}_p$. The parameterization is described in the text. The fit values are listed in table 6.1.

magnitude, and a change in the momentum angle. A track's angle is solely determined by information in front of the magnet.[7] The target represents the majority of material in front of the magnet, see table 6.2, and so it will have the biggest effect on the determination of the track's angle. In contrast, the target will have very little effect on the magnitude of the momentum since this quantity is determined by the change in a track's angle as it passes through a magnet:

$$p \approx p_{xz} = \frac{eB}{c} \frac{D}{2 \sin\left((\theta_1 + \theta_2)/2\right)}. \tag{6.11}$$

After several false starts, we realized that the change in a track's reconstructed angle was best described in a coordinate system in which the z-axis is defined by the GEANT track. The polar and azimuthal angles of the reconstructed track in this coordinate system are called α and ω respectively.

We expect reconstructed tracks to be azimuthally symmetric in this coordinate system. This expectation was verified by the flat distribution of α shown in figure 6-1a. We expect the distribution of polar deviations in this coordinate system to be described by the standard equation for the multiple scattering angle deviation formula [Hig75]:

$$\sigma^{\beta p\omega} = \frac{17.5}{\sqrt{3}} \sqrt{\frac{X}{X_0}} \left(1 + 0.125 \log_{10}\left(\frac{X}{X_0}\right)\right), \tag{6.12}$$

where $\beta p\omega$ is in units of GeV-mrad. Here, X/X_0, is the distance a particle travels in units of radiation lengths, and we explicitly incorporate βp into $\sigma^{\beta p\omega}$ in order to obtain a quantity described by a Gaussian with a momentum-independent width. For an ensemble of tracks, we expect this distribution to be described by an infinite sum of Gaussians, with a distribution of widths given by the different amount of material that a track can go through. This distribution, uncorrected for the 2-dimensional Jacobian factor of $\beta p\omega$, is plotted in figure 6-1b. The solid line represents a fit to this distribution with the sum of four Gaussians:

$$dN/d\beta p\omega = \beta p\omega \sum_{i=1}^{4} A_i^{\beta p\omega} \exp\left(-\frac{1}{2}\left(\frac{\beta p\omega}{\sigma_i^{\beta p\omega}}\right)^2\right). \tag{6.13}$$

The actual parameters are listed in table 6.1. These numbers are consistent with estimates obtained using known radiation lengths of material in the spectrometer listed in table 6.2.

The reconstructed momenta were observed to be systematically lower than the thrown

[7] As described in section 3.7, the AUSCON algorithm uses T3T4 information to generate a T1T2 hit-possibilities list. But, the T1T2 vector (which gives the track's angle) is reconstructed ignoring any T3T4 information.

momenta by ≤ 5 MeV/c. This is shown in figure 6-1c. The functional form fit to this distribution was:

$$\delta p = A^{\delta p} \exp\left(\frac{B^{\delta p}}{C^{\delta p} - p}\right). \tag{6.14}$$

The values used are listed in table 6.1. This effect can be largely explained by energy loss. From the values listed in table 6.2, we can calculate the average energy loss of a minimum-ionizing particle traveling to the center of the magnet, $\Delta E \approx 5$ MeV. This is consistent with the high-momentum asymptotic value of the energy difference.

Contrary to expectations for an effect due to energy loss, the deviation decreases at lower momenta. This is not rigorously understood, but we have a hypothesis — multiple scattering. Multiple scattering will systematically raise the value of the reconstructed momentum since $\delta\theta$ is a uniform deviate, not momentum. So, this effect somewhat cancels the effects of energy loss. Unfortunately, the magnitude of this effect is difficult to estimate. For a given value of $\delta\theta$, the effect is more severe for higher momentum tracks. But, lower momentum tracks suffer larger values of $\delta\theta$. Also lumped into this offset are any inconsistencies between the GEANT magnetic field map and the effective edge approximation used by AUSCON.

The width of the momentum spread about its average value, shown in figure 6-1d, was found to behave like:

$$\sigma(p)/p = A^{\sigma p} + B^{\sigma p} p. \tag{6.15}$$

Table 6.1 gives the parameters used for this fit function.

6.2.3 $\mathcal{R}_p$ Results

The effect of $\mathcal{R}_p$ is shown in figure 6-2. The plotted distribution is the ratio of the $\pi^+\pi^+$ correlation functions with and without application of $\mathcal{R}_p$. The effect is generally less than 10%. The effect on extracted parameters is small, as quantified in appendix A.

The single-track approach used in this analysis implicitly assumes that the resolution is independent of any two-track quantity. The only situation in which one might expect a violation of this assumption, is that in which a pair is spatially close in front of the magnet. These are the same pairs addressed in connection with the TPAC. To investigate our sensitivity to errors in the TPAC parameterization, we performed a study in which the scale angle cut was incrementally tripled to 3.3 mrad. The results of this study (little change was observed in extracted parameters) give us confidence that we are not sensitive to any two-particle component in the response function.

The alert reader will have noticed that only pions were used in the response function anal-

	Material	Thickness (g/cm^2)	X_0 (%)	dE_{min} MeV
Target	^{197}Au	2.85 (1.5% λ_I)	43.5	3.27
F0	Scintillator	0.660	1.56	1.29
T1	^{40}Ar	0.0065	0.033	0.01
	Isobutane	0.0065	0.014	0.01
	Mylar	0.032	0.08	0.06
	^{27}Al	0.038	0.16	0.06
	^{184}W	0.002	0.03	0.00
			0.317	0.14
T2	^{40}Ar	0.0165	0.084	0.02
	Ethane	0.0165	0.036	0.03
	^{63}Cu	0.031	0.24	0.04
	Mylar	0.028	0.07	0.05
	^{184}W	0.0007	0.01	0.00
			0.440	0.14
T3	^{40}Ar	0.017	0.087	0.02
	Ethane	0.017	0.037	0.02
	^{63}Cu	0.021	0.16	0.03
	Mylar	0.028	0.07	0.05
	^{184}W	0.0004	0.006	0.00
			0.360	0.12
T4	^{40}Ar	0.017	0.087	0.02
	Ethane	0.017	0.037	0.02
	^{63}Cu	0.019	0.15	0.03
	Mylar	0.028	0.07	0.05
	^{184}W	0.0004	0.006	0.00
			0.350	0.12
Air - Before Magnet Center		0.335	0.854	0.61
Air - After Magnet Center Before T4		0.225	0.575	0.41

Table 6.2: Spectrometer materials list, taken directly from the E859 Monte Carlo code.

ysis. This should make no difference in the angular deviation parameterization since the azimuthal deviation is flat and the polar deviation takes the particle's β into account explicitly. Since the absolute momentum offset distribution is nearly flat, differences in this parameterization should leave the relative momentum unchanged. The resolution of the momentum magnitude, σ_p, as obtained from pions, is an overly optimistic prediction of this quantity for kaons. This error in this prediction should be everywhere less than $1/\sqrt{\delta\beta} \approx 20\%$. In figure 6-3, we show the ratio of the the $\pi^+\pi^+$ correlation functions with no $\mathcal{R}_p$, and with application of $\mathcal{R}_p$ with the parameters $A_i^{\beta p\omega}$ multiplied by a factor of ten. As expected, the effect is seen to be larger in this case. But, the difference is small enough to give confidence in using $\mathcal{R}_p$ extracted from pion data for the kaons.

Some technical details of application of $\mathcal{R}_p$ could not be addressed in time for this writeup. For this reason, and the fact that the overall effect appeared to be small, no response function was used for model comparisons in this thesis.

6.2.4 Spectrometer Efficiency

The efficiency of the spectrometer, including decay probability, needs to be taken into account to compare model predictions to data. We parameterized this efficiency using single-track Monte Carlo data sets of the relevant particles, as described in [Mor94]. We chose to separate the reconstruction efficiency from the decay probability. In figure 6-4 we show the reconstruction efficiencies for pions and kaons and fits to these distributions of the form:

$$\mathcal{F}(p) = A \exp\left(-\frac{B}{C-p}\right). \tag{6.16}$$

Because of the non-standard PID definitions used in this analysis, see section 4.2.2, the total efficiency for kaons above the pion/kaon 3σ overlap-momentum ($p = 1.82\,\text{GeV/c}$) is multiplied by the fraction of kaons that are unambiguously TOF identified. The pion PID efficiency is assumed to be flat.[8] Both pion and kaon efficiencies are multiplied by the known decay factor.

6.3 RQMD

RQMD [Sor93] is one of the cascade codes available to compare with relativistic heavy ion collisions. In general, cascade codes begin by constructing a nucleus according to measured

[8]Because of my non-standard PID definitions, the pion efficiency is not complicated by GASČ efficiency. This is in contrast to the analysis found in [Mor94].

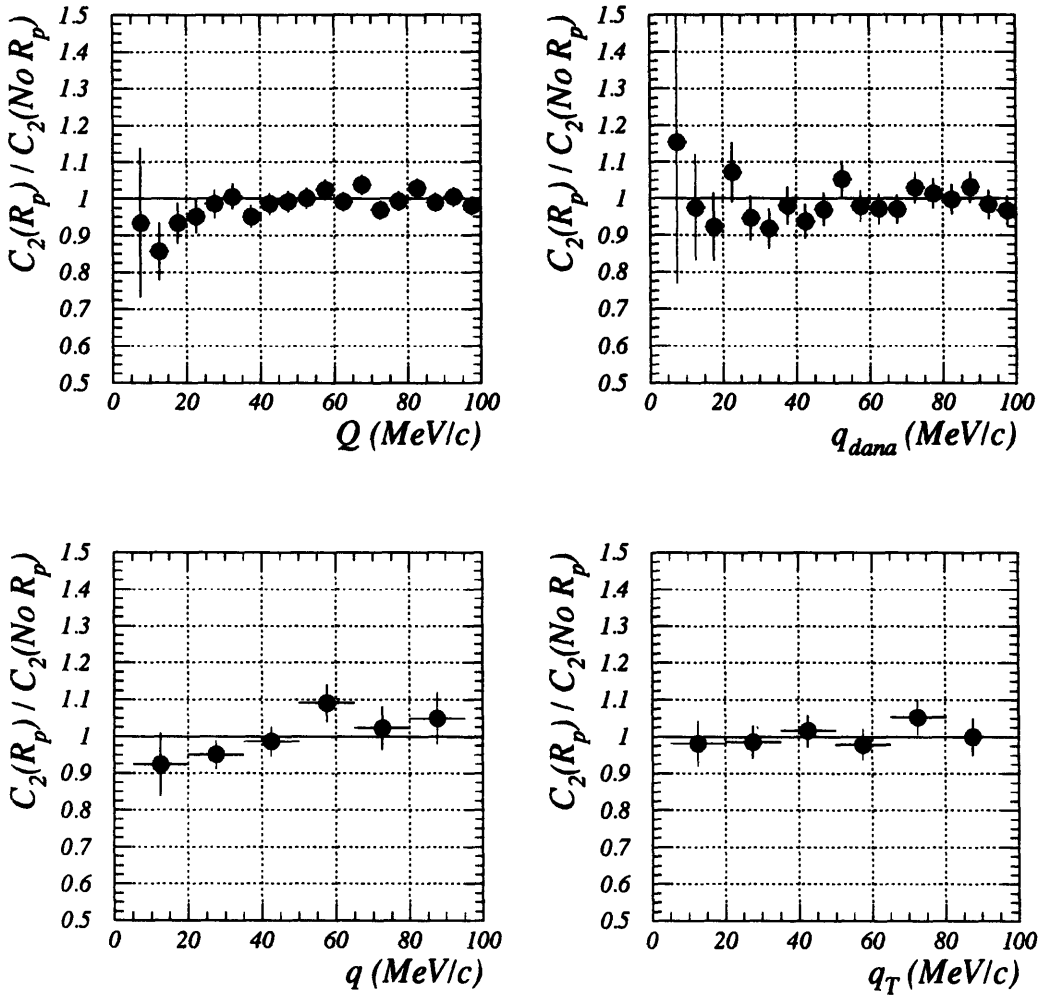

Figure 6-2: Correlation function modification due to $\mathcal{R}_p$. The plotted distributions are the ratios of different relative momentum projections of the correlation function, for the *standard* $\pi^+\pi^+$ data set, with and without application of $\mathcal{R}_p$.

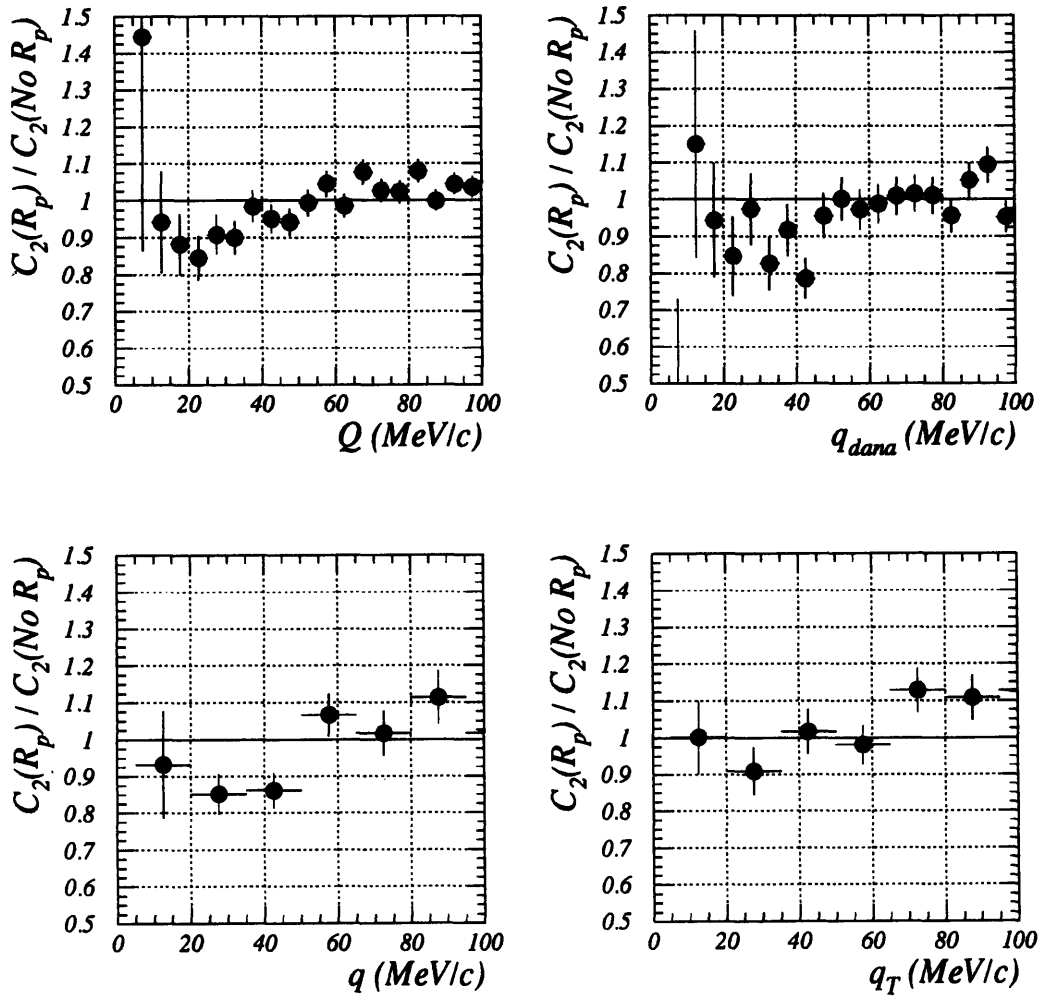

Figure 6-3: Correlation function modification due to artificially worsened $\mathcal{R}_p$. The plotted distributions are the ratios of different relative momentum projections of the correlation function, for the *standard* $\pi^+\pi^+$ data set, without application of $\mathcal{R}_p$, and with application of $\mathcal{R}_p$ in which the $A_i^{\beta p\omega}$ parameters are multiplied by a factor of ten..

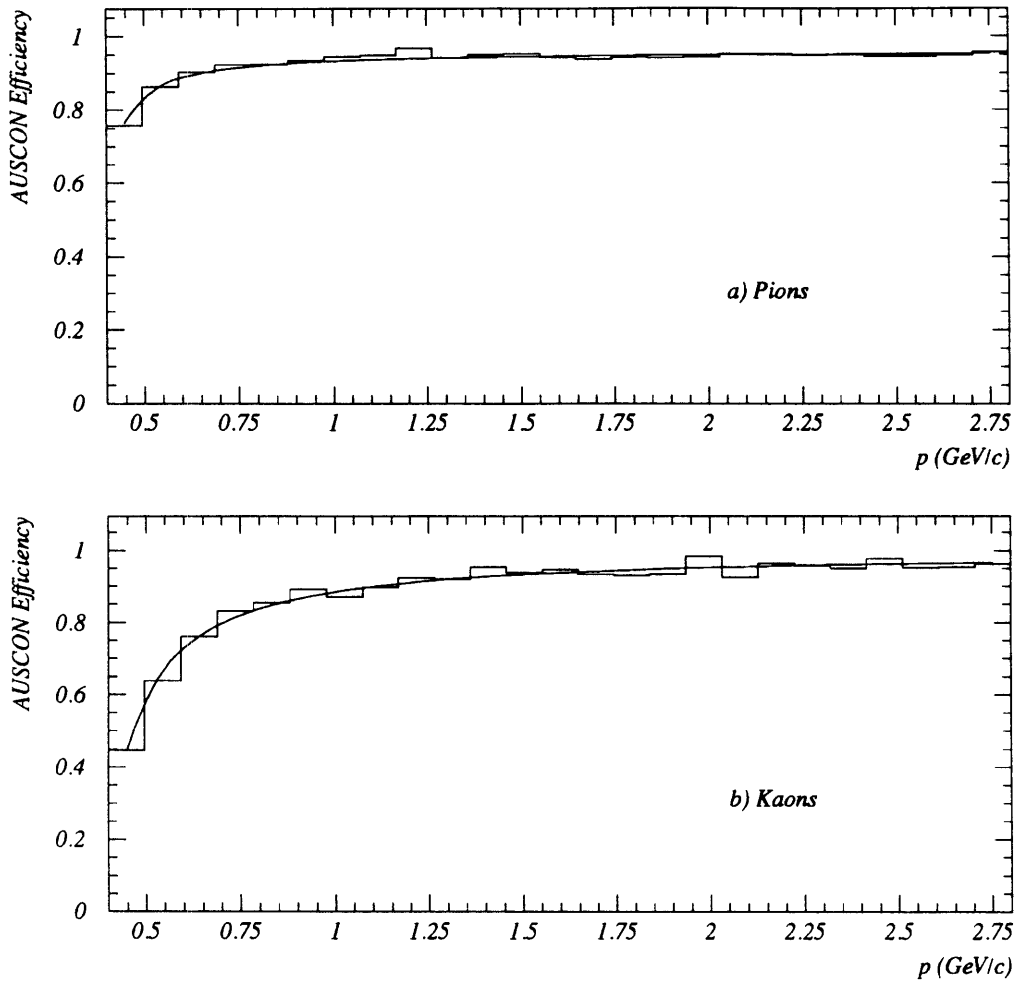

Figure 6-4: Parameterized AUSCON efficiencies for pions and kaons. These efficiencies get multiplied by the known decay factor. There is an additional term (not shown) for the kaons to account for the fraction of kaons that are not ambiguously TOF identified above the pion/kaon 3σ-overlap momentum ($p = 1.82\,\mathrm{GeV/c}$).

density and Fermi energy distributions. Individual nucleons are propagated in time until an interaction, triggered by an approach distance $r < \sqrt{\sigma/\pi}$, occurs.[9] The difference between cascade codes is embodied in different cross-section and branching ratio parameterizations, and different allowed processes.

RQMD is a very permissive code and the reader is directed to [Sor93] for a more complete description of the allowed processes. These include:

- Standard meson-meson, meson-baryon and baryon-baryon interactions.
- $q\bar{q}$ and qq interactions.
- String formation and decay (overlapping strings are known as *ropes*). These processes play a very small role at AGS energies.
- Objects in a collision can interact with the mean field of surrounding objects. This was observed to have little effect on particle abundances at AGS energies. It was therefore switched off in these comparisons due to CPU considerations.

It is important to note that no parameters in the model were optimized for comparison to E859 data.

6.3.1 RQMD Data Sets

The RQMD data set used in this analysis was generated using RQMD version 1.08. A complete list of selected switch settings can be found in [Sol94]. 30,837 ^{28}Si + ^{197}Au collisions were generated with impact parameters in the range $b \in (0, 5)$ fm, randomly selected according to $dN/db \sim b$.

We used a simplified geometrical simulation of the TMA, developed by Ron Soltz, in order to match the experimental centrality trigger (the upper 20% of the minimum bias TMA multiplicity distribution). For a particle to count as a TMA hit, it needed to be electrically charged, have $E_{kin} > 25$ MeV, and lie within the geometrical acceptance of the TMA (see section 2.6). Of the events with $b < 5$ fm, $\approx$ 95% passed the TMA cut.

We wanted to study the effects of the spectrometer acceptance on the extracted source parameters. So, we needed to write out files for the particle species of interest with and without cuts on the spectrometer acceptance. For these cuts, we used a slightly modified

[9] Note that time-ordering of collisions, common to all cascade codes, necessarily violates relativity. A frame can be found in which the time-ordering is different. For the cascade code ARC, it has been reported that less than 5% of the collisions are affected by this [K$^+$93].

version of the cross-section standard acceptance routine, written by Dave Morrison and Chuck Parsons [Mor94]. The geometrical input to this code was taken from YBOS geometry files for the Mar92 run period. We only used the p and θ information returned from this code. Particles inside the spectrometer $p\theta$ acceptance, but beyond the ϕ limits, could be rotated in ϕ to increase statistics. This is discussed in more detail in section 6.1.2. We also needed to impose an upper momentum cutoff due to particle identification limits (3.0 GeV/c for kaons and 1.8 GeV/c for pions).

The final number of particles in each data set are given in table 6.3. The final number of pairs in each data set are listed in table 6.4.

	K^+	π^+
Acceptance cut	2,521	21,815
No acceptance cut	121,810	1,307,530

Table 6.3: Number of pairs in different RQMD data sets.

	K^+	π^+
Actual, Acceptance cut	150,000	300,000
Actual, No acceptance cut	1,000,000	1,000,000
Background, Acceptance cut	300,000	600,000
Background, No acceptance cut	1,000,000	1,000,000

Table 6.4: Number of particles in different RQMD data sets.

6.3.2 RQMD Results

RQMD predictions have been compared to single-particle kaon data taken by E859 [Mor94]. Predicted K^+ and K^- yields are observed to 10-15% low. Predicted slope parameters, from an $m_\perp$ fit, are 10–20 MeV low for K^+, and $\approx$ 70 MeV high for K^-. Comparisons of predicted RQMD Bose-Einstein correlations have been made by E814 [X+94] (pions) and by NA44 [S+94b, S+93b] (kaons). Both E814 and NA44 found excellent agreement between data and RQMD predictions for pions. NA44 found some discrepency between data and RQMD for both K^+'s and K^-'s, with RQMD predicting a smaller source than observed for both sign kaons.

A comparison of extracted fit parameters for E859 and RQMD is presented in table 6.5. The alert reader will notice the very large values of χ^2/dof for the fits to the RQMD correlation

functions. This is *not* an indication of non-Gaussian correlation functions predicted by RQMD. In fact, the E859 and RQMD correlation functions, plotted for corresponding relative momentum projections in figure 6-5 and figure 6-6, agree very well. A close examination of the RQMD data points reveals *very* small error bars compared to the observed fluctuations. This is a result of badly over-mixing our phase-space point inputs to the Pratt Wigner-density technique and assuming Poisson errors, see section 6.1. These results are still usable, but we need to realize that the quoted errors on fit parameters extracted from RQMD are unrealistically small.

The fully qualified message that comes out of this analysis is that RQMD Bose-Einstein correlation function predictions closely match the E859 results, for central π^+ and K^+ at mid-rapidity. There is some discrepency in the chaoticity parameter λ. But, this is within any reasonable estimate of the systematic error on our determination λ. The difference in λ for pions and kaons, observed in the data, is reproduced by RQMD.

Does this mean that the RQMD K^+ source is 50% smaller than the π^+ source? Does this mean that the RQMD π^+ and K^+ sources are distinctly oblate? Does this mean that the RQMD K^+ source really does have an emission duration of 0 fm/c? The answer to these questions, and all questions concerning the interpretation of parameters extracted from a Bose-Einstein correlation analysis, is a resounding "...maybe, maybe not."

Let us step into RQMD and look at the source. This is the advantage of having a model. Note that all of the positions and momenta presented in this section are calculated in the participant center-of-mass frame, $y = 1.25$.

First, in figure 6-7, we compare the final scattering positions of *all* π^+'s and K^+'s in RQMD. The π^+ source is significantly larger than the K^+ source in every parameter. This is somewhat due to the larger meson-baryon cross-section of the π^+, and somewhat due to a greater contribution of long-lived resonances to π^+ production. A detailed analysis of the origins of the particles in the tails of the pion distributions has not been performed. We also note that these distributions seem very large compared to the source parameters typically extracted. To understand this apparent contradiction, we need to return to the discussion of dynamical correlations.

Recall that in order to be able to interpret an extracted source parameter in terms of a physical source size, we assume that the emission function factorizes into functions of space and momentum, $g(\mathbf{r}, \mathbf{p}) = f(\mathbf{r})\,\rho(\mathbf{p})$. In order to test the validity of this assumption, we first examined the distribution of the angle between the final-state position and momentum vectors [Vos]:

$$cos\,(\alpha) = \hat{r} \cdot \hat{p}. \tag{6.17}$$

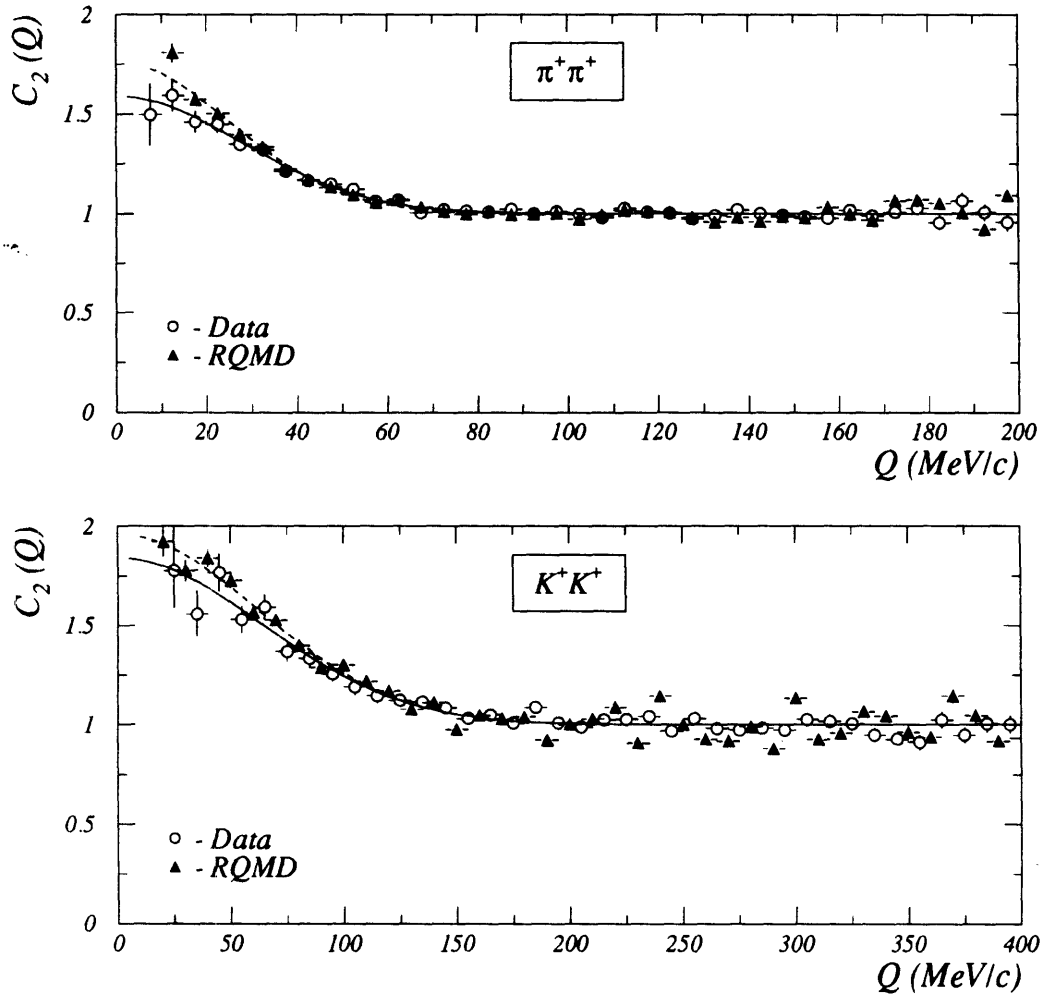

Figure 6-5: Comparison of E859 and RQMD correlation functions for $\pi^+\pi^+$ and K^+K^+ (Q parameterization). Fit results are summarized in table 6.5, see text for details.

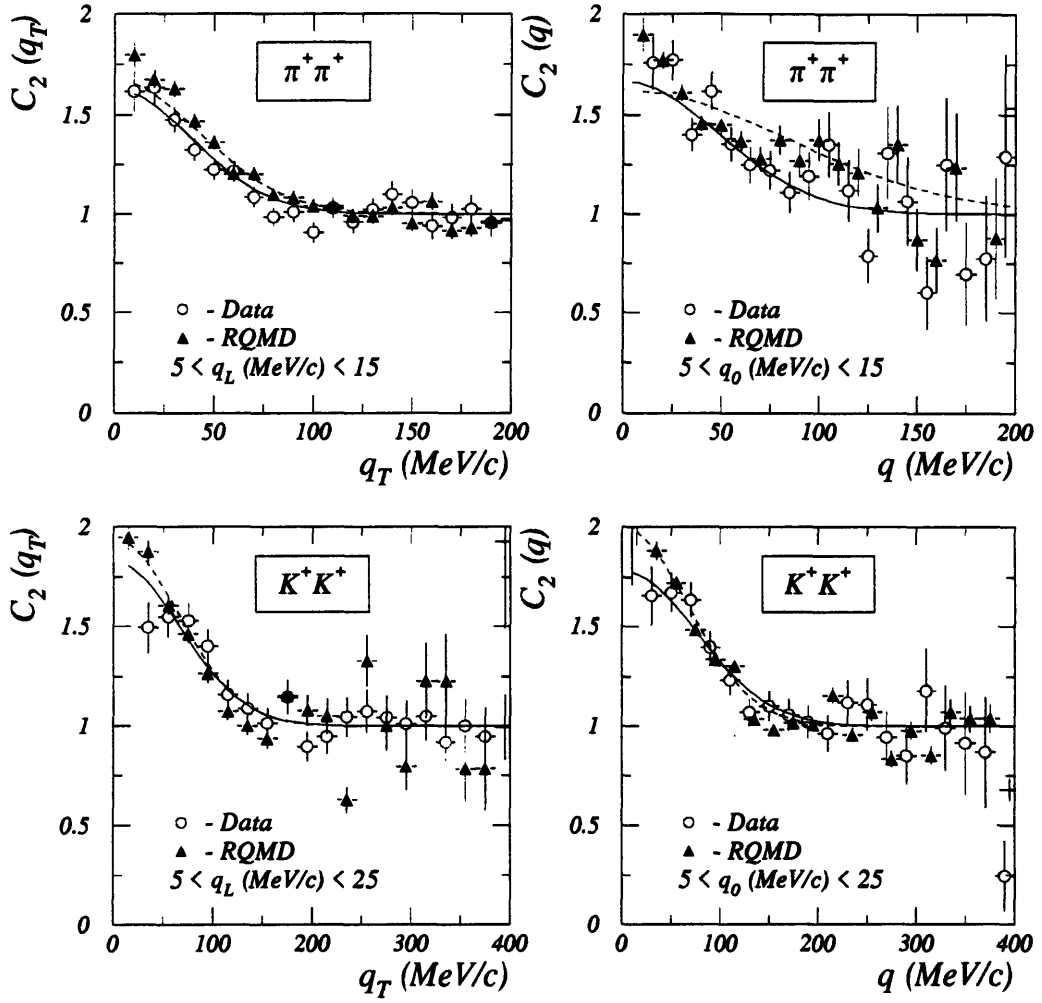

Figure 6-6: Comparison of E859 and RQMD correlation functions for $\pi^+\pi^+$ and K^+K^+ ($q_{0}q$ and q_Lq_T parameterization). The plotted distributions are slices of 2D distributions. The cut values are indicated on the figure. Fit results were obtained from a fit over the full 2D phase space and are summarized in table 6.5, see text for details.

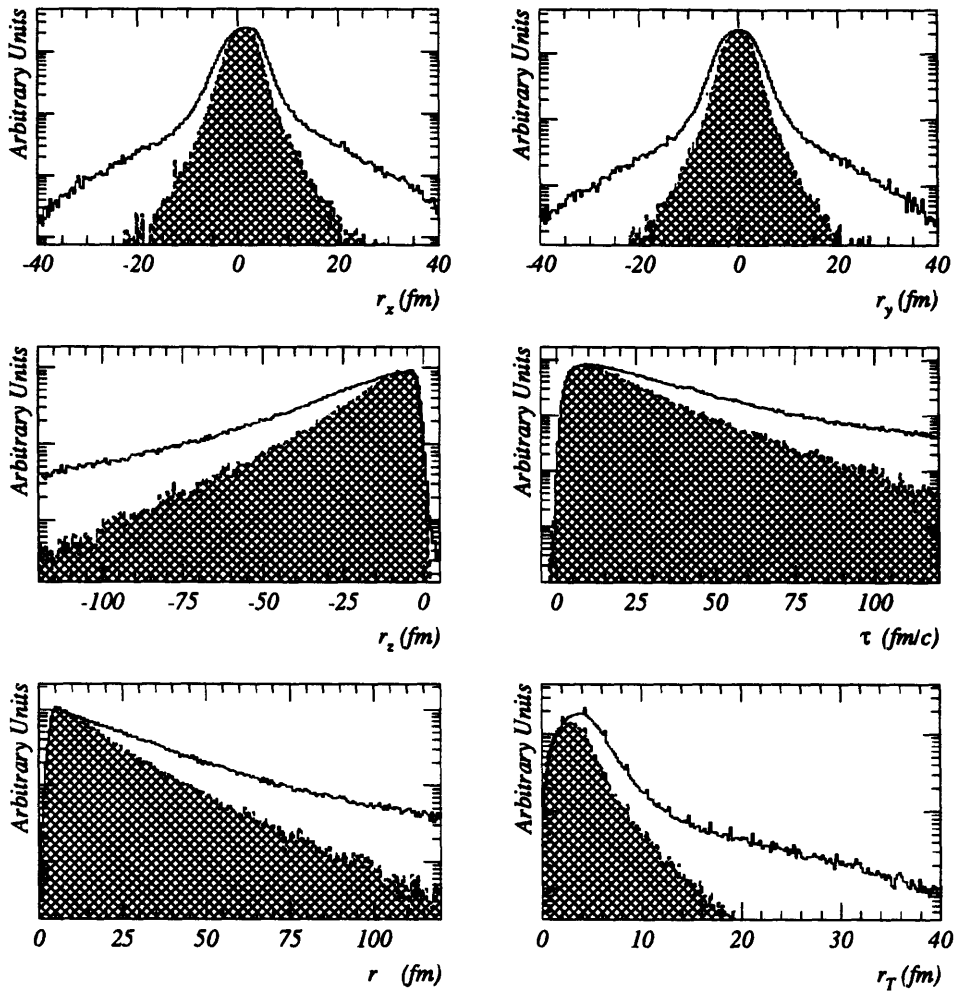

Figure 6-7: Comparison of final-state spatial distributions for π^+'s and K^+'s produced by RQMD. The hatched areas are K^+'s. The distributions have been normalized such that the peak of each K^+ distribution matches the corresponding π^+ distribution in that histogram bin.

Fit	Parameter	E859 $\pi^+\pi^+$	RQMD $\pi^+\pi^+$	E859 K^+K^+	RQMD K^+K^+
Q	R_Q	5.00 ± 0.18	5.55 ± 0.11	2.19 ± 0.10	2.26 ± 0.04
	λ	0.59 ± 0.04	0.76 ± 0.03	0.84 ± 0.07	0.96 ± 0.03
	χ^2/dof	45.5/57	162/57	70.5/57	429/57
q_{dana}	R_{dana}	2.78 ± 0.10	2.72 ± 0.06	1.81 ± 0.10	2.03 ± 0.04
	λ	0.63 ± 0.03	0.72 ± 0.02	0.84 ± 0.07	0.94 ± 0.03
	χ^2/dof	70.0/57	121/57	57.1/56	397/57
$q_0 q$	R	2.84 ± 0.09	1.64 ± 0.06	1.83 ± 0.07	2.08 ± 0.04
	τ	2.94 ± 0.30	4.07 ± 0.08	0.01 ± 0.94	0.00 ± 0.07
	λ	0.67 ± 0.04	0.65 ± 0.04	0.78 ± 0.07	1.00 ± 0.03
	χ^2/dof	468/434	1011/426	457/393	2628/367
$q_L q_T$	R_L	2.52 ± 0.18	2.83 ± 0.13	1.63 ± 0.12	1.96 ± 0.05
	R_T	3.56 ± 0.13	3.22 ± 0.07	2.10 ± 0.12	2.17 ± 0.06
	λ	0.64 ± 0.04	0.68 ± 0.02	0.84 ± 0.07	0.97 ± 0.03
	χ^2/dof	729/759	1011/426	874/854	5239/762

Table 6.5: Comparison of RQMD correlation function predictions versus E859 results. The very large values of χ^2/dof is due to overmixing of the model data. See text for details.

This distribution is plotted in figure 6-8, for RQMD π^+'s and K^+'s, with and without spectrometer acceptance cuts.

The first thing to notice about these distributions, is the fact that for both π^+'s and K^+'s, the distributions without acceptance cuts are sharply peaked at $\cos(\alpha) = 1$. As illustrated in figure 6-9, this seems physically intuitive. Particles with $\cos(\alpha) = -1$, must pass, unscattered, through the production zone.

The second thing to notice about these distributions, is that for both π^+'s and K^+'s, the distributions become much flatter when acceptance cuts are applied.[10] This is an indication that the E859 spectrometer is not seeing the entire source, since particles that contribute to the sharp spike at $\cos(\alpha) = 1$ are missing. If this corresponds to reality, then we may be able to interpret the extracted source parameters as the size of the source of those particles *seen by our detector*.

This blindness of the E859 spectrometer to portions of the particle source is more explicitly shown in figure 6-10. This plot shows the final state spatial distributions, of those K^+'s and π^+'s, accepted by the E859 spectrometer. Comparing figure 6-10 to figure 6-7, we see a dramatic

[10] Although note the logarithmic scale.

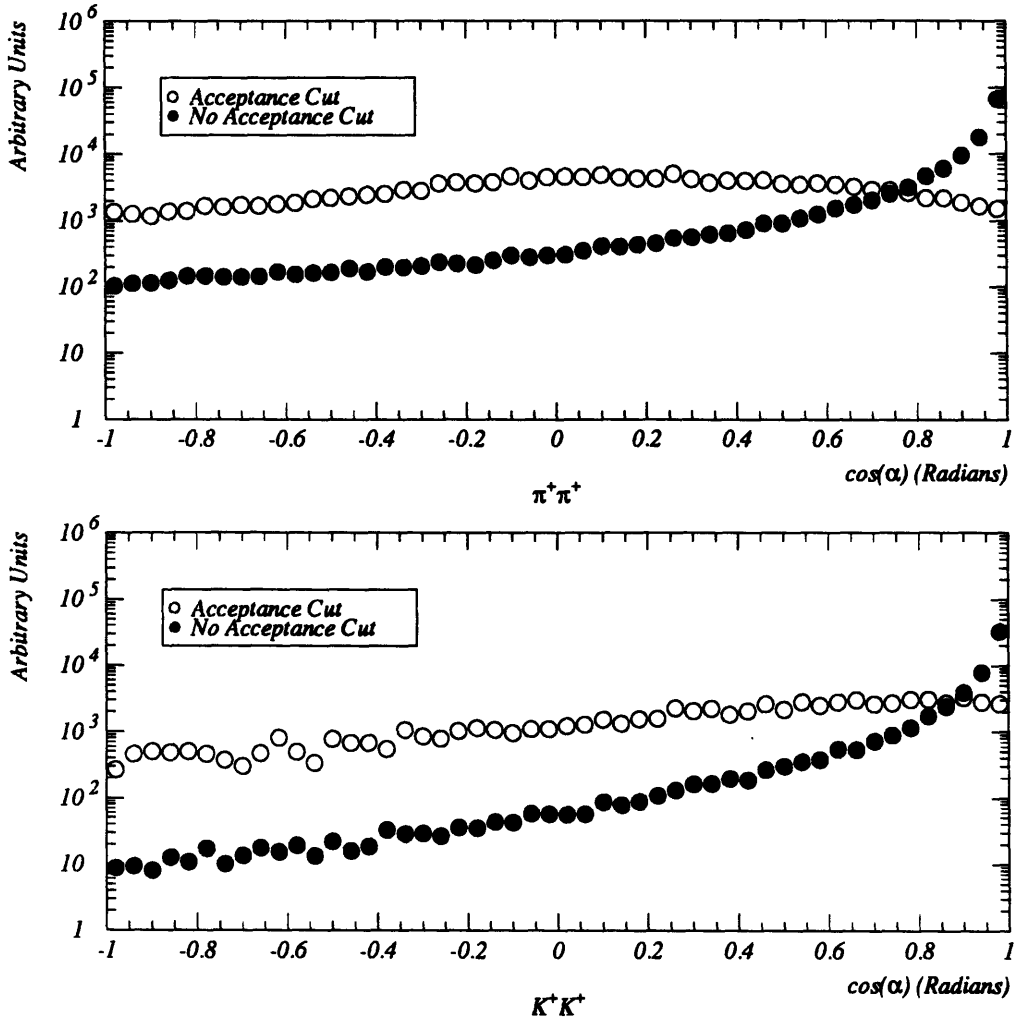

Figure 6-8: Correlation between the produced position and momentum directions of RQMD K^+'s and π^+'s. The plotted distributions show the cosine of the angle between the produced position and momentum vectors. See text for details.

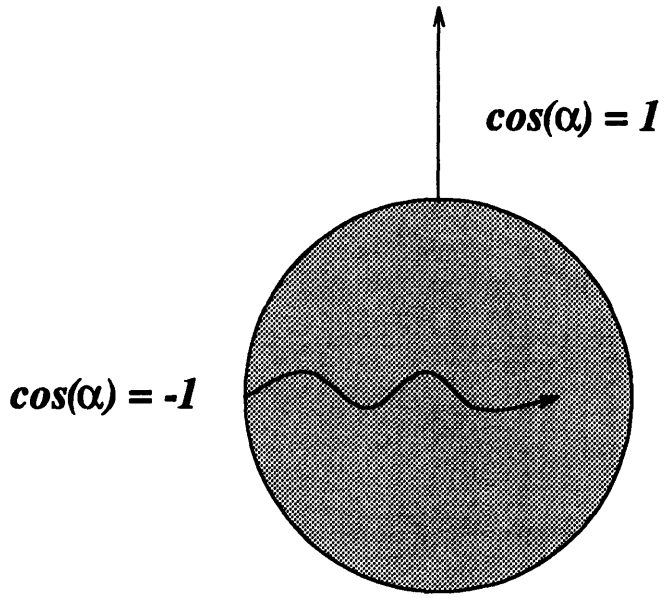

Figure 6-9: Schematic diagram of the origin of the observed dynamical correlations. This figure shows the requirements for producing a particle with $\cos(\alpha) = 1$ and a particle with $\cos(\alpha) = -1$. Particles with $\cos(\alpha) = -1$ must pass, unscattered, through the production zone.

reduction in the longitudinal and production-time extent of both the K^+ and π^+ the sources. In RQMD, both of these variables are tightly correlated with p_z. Therefore, we know that the upper rapidity cutoff of the E859 spectrometer is largely responsible for our inability to see such particles. The other dramatic feature of figure 6-10 is the large reduction of π^+'s with negative values of r_x. This becomes less mysterious when we realize that the E859 spectrometer is only in the positive x-direction. This shadowing effect is greater for the π^+'s than for the K^+'s, presumably because of the π^+'s greater meson-baryon cross-section. This is important, because it suggests that the observed difference in the K^+ and π^+ sources is a lower limit.

Another effect which distorts the picture of the source revealed by Bose-Einstein correlations is the fact that two-particle correlations are not sensitive to the shape of the distribution.[11] Figure 6-11 shows the separation distributions of the phase space points whose absolute position distribution was shown in figure 6-10.[12] Most indications that the distribution is exceedingly non-Gaussian have been erased. Much of the remaining information, in the form of long non-Gaussian tails, will also be erased. This is because the largest separations will show up as a component of the correlation function that is too narrow to measure. This may very well reduce

[11]The example of a spherical shell was discussed in section 1.4.

[12]The separations have been calculated at the time when the latter particle is emitted in order to reproduce the quantity that the Bose-Einstein correlation is sensitive to.

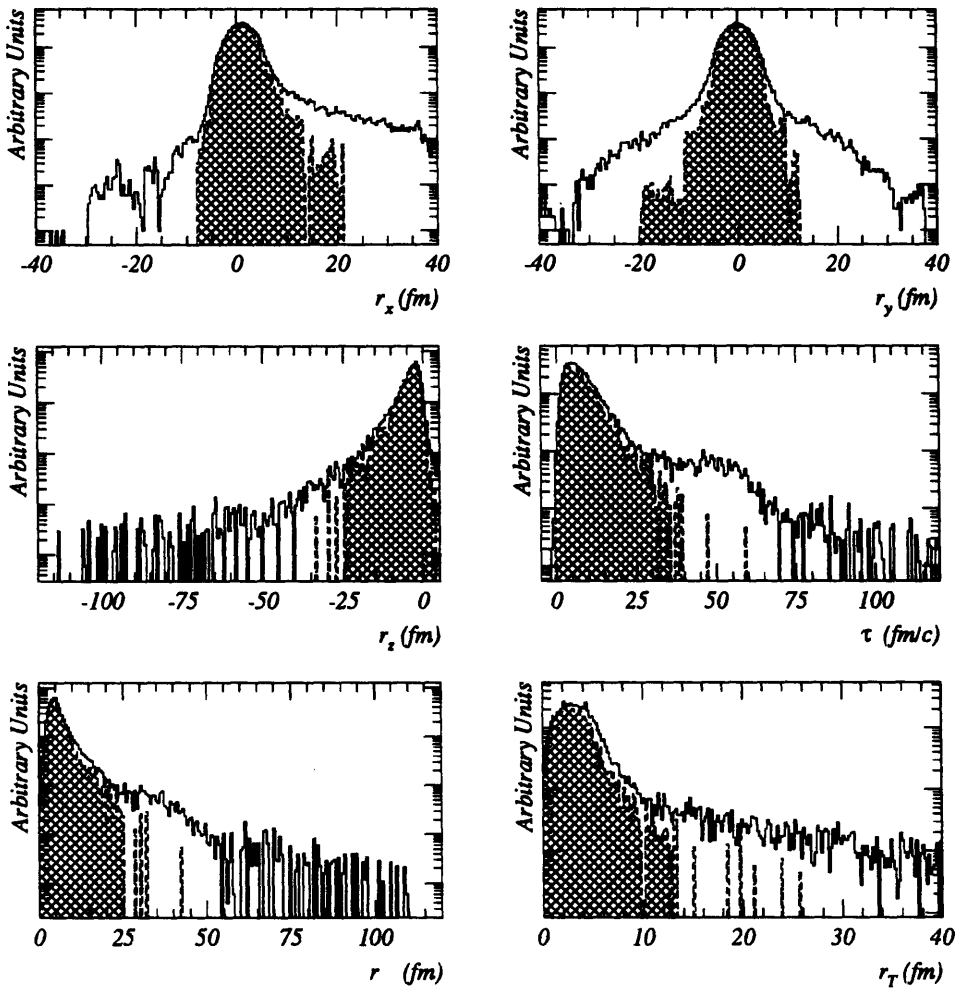

Figure 6-10: Comparison of final-state spatial distributions for π^+'s and K^+'s produced by RQMD in the E859 acceptance. The hatched areas are K^+'s. The distributions have been normalized such that the peak of each K^+ distribution matches the corresponding π^+ distribution in that histogram bin.

λ without giving a larger radius. Note that since these are distributions of separations, their size needs to be divided by $\sqrt{2}$ in order to compare them to the predicted size of the originating distribution.

Dynamical correlations can affect Bose-Einstein correlation functions in another way. It could be that the only particles with small enough relative momentum to have a measureable correlation function would also be very close spatially. If this were true then detector acceptance would not affect the extracted source parameters. *Any* detector would see a source size determined by the size of the patch of the source which could emit pairs with small relative momentum.

In figure 6-12, we see that RQMD predicts this effect to be negligible for E859. The plotted distributions are projections of the *rms* separation of RQMD π^+'s and K^+'s, in the E859 acceptance, as a function of the conjugate relative momentum variable. These distributions are very flat, indicating that particles at low relative momentum, *in the E859 acceptance*, see all of that portion of the source visible to the spectrometer.

In figure 6-13, we show that RQMD does predict this effect to be present for a hermetic detector. The plotted distributions are projections of the *rms* separation of *all* RQMD π^+'s and K^+'s, as a function of the conjugate relative momentum variable. It is clear that these distributions are not flat, indicating that even with a hermitic detector, we can not see the entire source with a Bose-Einstein correlation measurement. This has been referred to as:

> ...a fundamental limit of the technique, as opposed to a fundamental limit of the experimental apparatus. [Ste]

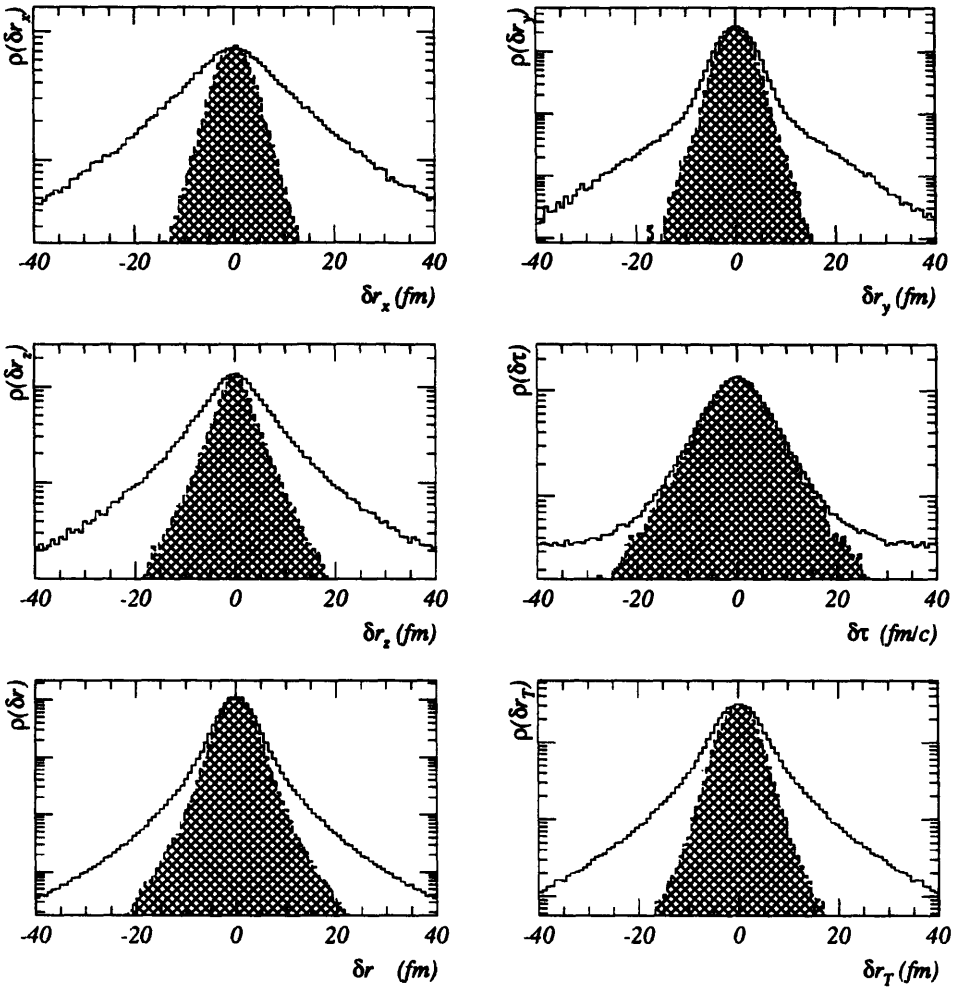

Figure 6-11: Comparison of final-state spatial *separations* for $\pi^+$and K^+pairs produced by RQMD in the E859 acceptance. The hatched areas are K^+'s. The distributions have been normalized such that the peak of each K^+ distribution matches the corresponding π^+ distribution in that histogram bin.

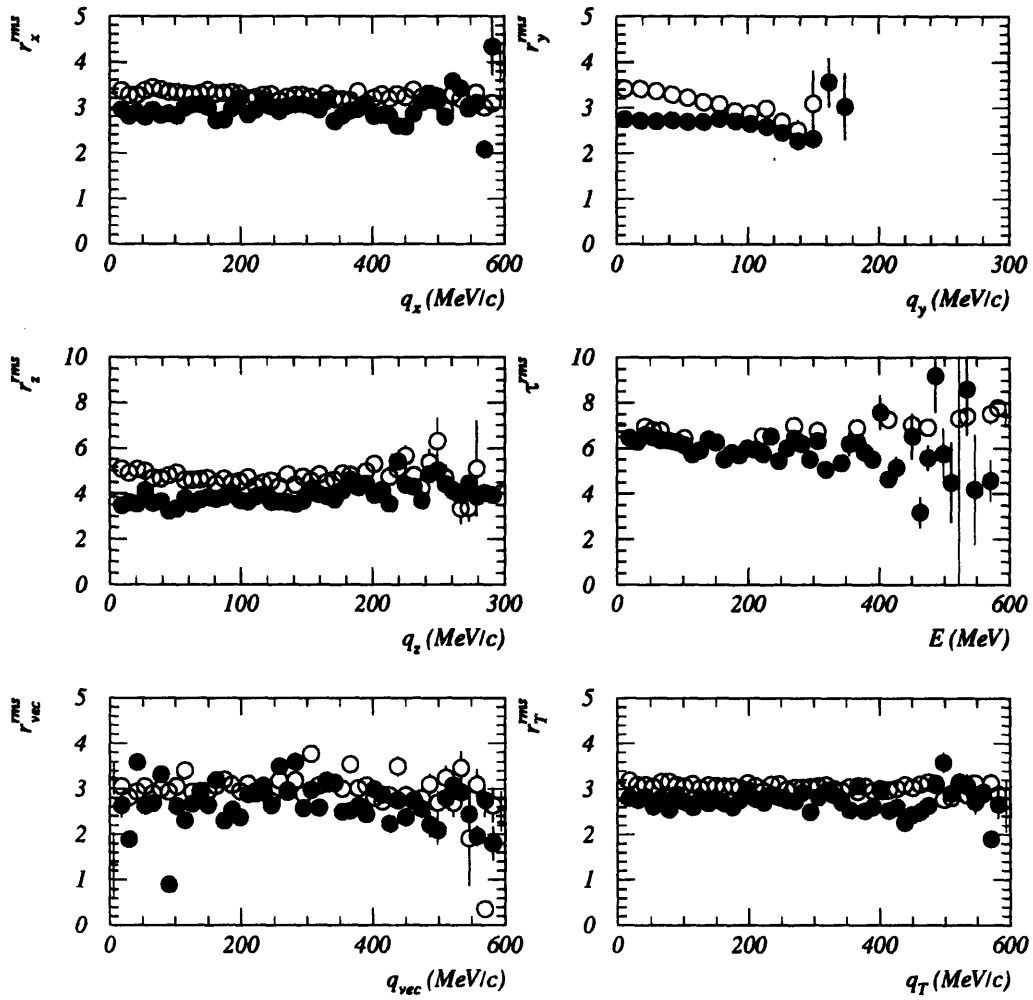

Figure 6-12: These distributions show the different projections of the *rms* separation of RQMD π^+'s (open symbols) and K^+'s (solid symbols), in the E859 acceptance, as a function of the conjugate relative momentum variable. Before calculating the *rms* value, the distributions are cut off at ± 20 fm, in an attempt to eliminate those pairs so far separated that their correlation function will be unmeasureable. Note that since these are distributions of separations, their size needs to be divided by $\sqrt{2}$ in order to compare them to the predicted size of the originating distribution.

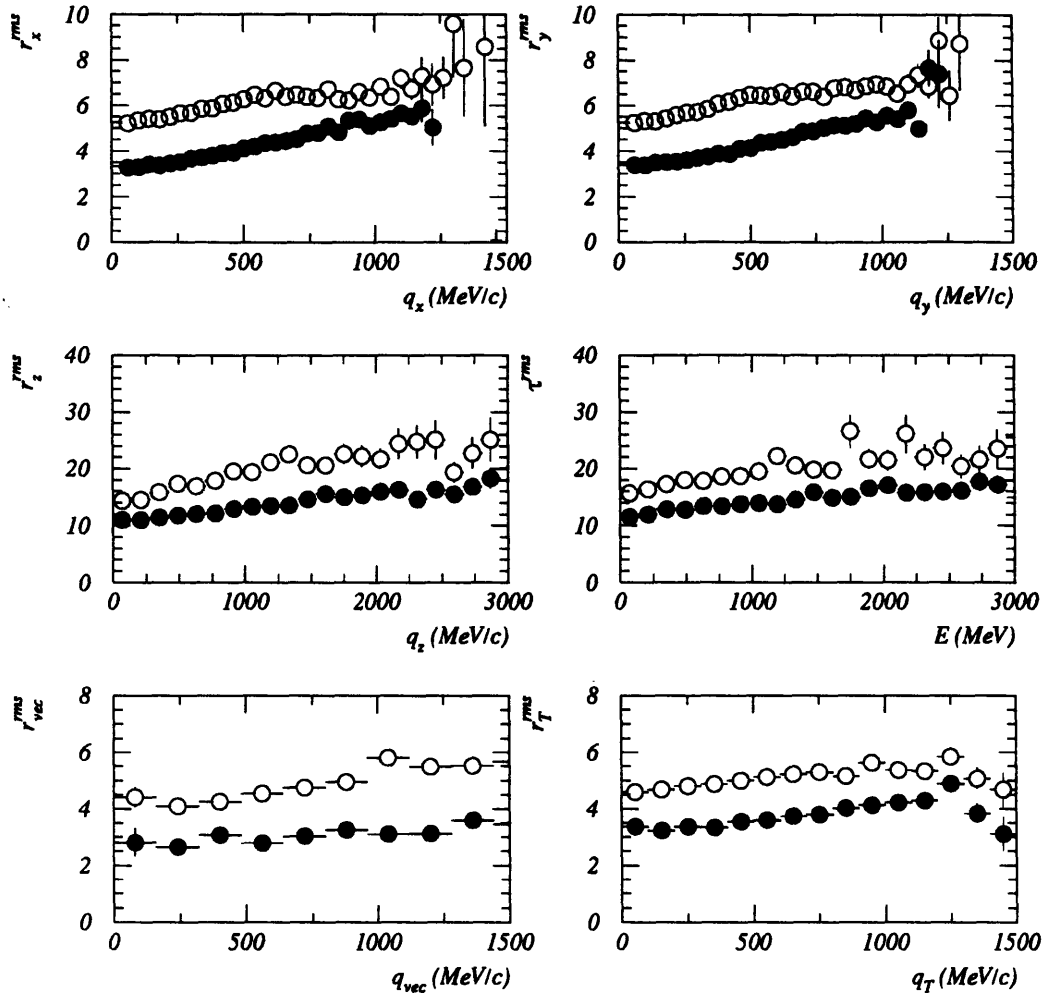

Figure 6-13: These distributions show the different projections of the *rms* separation of all RQMD π^+'s (open symbols) and K^+'s (solid symbols), as a function of the conjugate relative momentum variable. Before calculating the *rms* value, the distributions are cut off at ± 20 fm, in an attempt to eliminate those pairs so far separated that their correlation function will be unmeasureable. Note that since these are distributions of separations, their size needs to be divided by $\sqrt{2}$ in order to compare them to the predicted size of the originating distribution.

Chapter 7

Conclusions

E859 Data

This work reports the results of the first high-statistics measurements of the Bose-Einstein correlations of K^+'s for any system. Results presented in this work show no signs of QGP formation. However, these results do contribute to our understanding of the hot, dense matter created in heavy ion collisions at AGS energies. The highlights are summarized below:

- Every extracted size parameter of every source parameterization indicates that the π^+ source is $\approx 50\%$ larger than the K^+ source.
- R_{rms} for the K^+ source is consistent with R^{Si}_{rms}. R_{rms} for the π^+ source is significantly larger.
- The π^+ source is consistent with $\tau = R$. The K^+ source is consistent with $\tau = R$ *and* with $\tau = 0$.
- The $q_L q_{Tside} q_{Tout}$ parameterization also indicates that $\tau \approx 0$ for the K^+ source. This parameterization does not suffer from the same phase space difficulties as all parameterizations that directly fit τ, so this *may* indicate that the emission duration of the K^+ source is truly small.
- Both the π^+ and K^+ sources are oblate with the major axis (perpendicular to the beam) $\approx 25\%$ larger than the minor axis (parallel to the beam).
- The chaoticity parameter, λ, is observed to be ≈ 0.2 units larger for the K^+ source than for the π^+ source. The values of the parameters have an estimated systematic error of

0.1 unit, but any error is likely to be in the same direction for the two species. Thus, the difference is probably real.

- Single-particle rapidity cuts give unambiguous evidence for dynamical correlations. Longitudinal expansion and longitudinal shadowing are two hypotheses that explain this observation.

- Some systematic behavior is observed when the data sets are cut on $\langle p^{pair} \rangle$. The general trend is for reduced radius *and* reduced λ for larger values of $\langle p^{pair} \rangle$. The λ dependence is inconsistent with a hypothesis of resonance dominance of low $p_\perp$ production.

- 3D source parameterizations were successfully tested. Significantly, the fits were performed *over the full 3D phase space.*

- The first fits to the Yano-Koonin Lorentz invariant correlation function were performed. Work is still in progress to understand the observed frame dependence.

- The data are consistent with Gaussian correlation functions in every variable examined.

- The size and chaoticity parameters from all parameterizations are very consistent, lending confidence to their values.

- Parameters for the π^+ source are consistent with values obtained by E802 [Mor90, A+92a].

RQMD Results

Models, with their ability to provide final-state space-time coordinates, provide a unique laboratory in which to study Bose-Einstein correlations. Thanks to model studies, there is a growing understanding of the limits *and* power inherent in the observed sensitivity of Bose-Einstein correlations to the dynamics of the examined system. Hopefully, the model comparisons reported in this work will contribute to this understanding. The highlights are summarized below:

- RQMD 1D and 2D correlation functions, for π^+'s and K^+'s, are consistent with E859 results.

- Dynamics can limit the portion of the source visible to Bose-Einstein correlations. This effect may be more severe for small aperture devices. Due to the large meson-baryon cross-section of the π^+ relative to the K^+, any such effect is likely to *reduce* the observable difference between the π^+ and K^+ source size.

- Even though the model sources are highly non-Gaussian, the correlation functions are well described by Gaussian parameterizations. This reinforces the point that two-particle correlations are mostly sensitive to the pair *separation* along the examined projection, a quantity that approaches the Gaussian limit for many spatial distributions.

Final Summary

In central $^{28}Si + ^{197}Au$ collisions, we see that the Bose-Einstein source-size parameters for the π^+ source are significantly larger than those for the K^+ source. This conclusion is strengthened by the very consistent results from a wide variety of source parameterizations, and from the small statistical and systematic uncertainties on the extracted parameters.

Initial E859 results, presented in this analysis, seem to indicate the presence of dynamical correlations. Comparisons to the cascade code RQMD, also presented in this analysis, are vivid illustrations of the extent to which such correlations can distort a naive geometrical interpretation of Bose-Einstein correlation source parameters. These same results hint at the potential power of this technique to extract information on the dynamics of relativistic heavy ion collisions.

With our improved understanding of the Bose-Einstein correlation techique, we can look forward to characterizing matter in even more extreme conditions. Larger baryon densities have been made available with the acceleration of gold beams at the AGS. Larger energy densities will be available upon completion of the Relativistic Heavy Ion Collider. The sheer volume of available data will enable us to perform the systematic studies necessary to obtain both geometrical and dynamical information. Maybe, we will even see the QGP.

Appendix A

Systematic Studies

A list of the different systematic checks that have been performed, and a summary of their effect on the extracted source parameters, has been given on page 223. Figure A-1 presents a graphical summary of the range of values taken on by the different source-size parameters in these tests.[1] Figure A-2 presents a similar summary of the effects on the chaoticity parameter, λ. To give some concrete examples of the variation in the fit parameters, tables A.1 and A.2 present a tabular summary of all the different tests performed for the Q parameterization of the two particle species.

To illustrate the fact that the low relative momentum bins suffer from the greatest systematic uncertainty, we have included figures A-3 — A-6. These figures show the TPAC and Gamow corrections for several relative momentum projections of both particle species.

Also included in this appendix is a summary of the contamination of the different particle samples. Figure A-7 shows the contamination of pions by electrons (when the GASČ is ignored as it was in this analysis) to be less than 6%. Figure A-8 illustrates the technique used to estimate the contamination of kaons by pions and protons. The distribution of $\delta(1/\beta)/\sigma(1/\beta)$ for PICD identified particles should be Gaussian with $\sigma = 1$. We examine these distributions in momentum slices, near the TOFID overlap momentum of the respective particle species. From the amplitudes and widths obtained from these distributions, we can analytically calculate the contamination of kaons arising from the tails of the distributions of the more abundant particles. The amplitude of the pion distribution is roughly twice that of the kaon distribution. In this analysis, all identified kaons are farther than $3\sigma(1/\beta)$ from the pion peak. This corresponds to a 0.3% contamination of kaons by pions. The amplitude of the proton distribution is ten

[1] Note that systematic studies have not been performed for the $Koonin$ or the $q_{Lpair}q_{Tpair}q_0$ parameterizations.

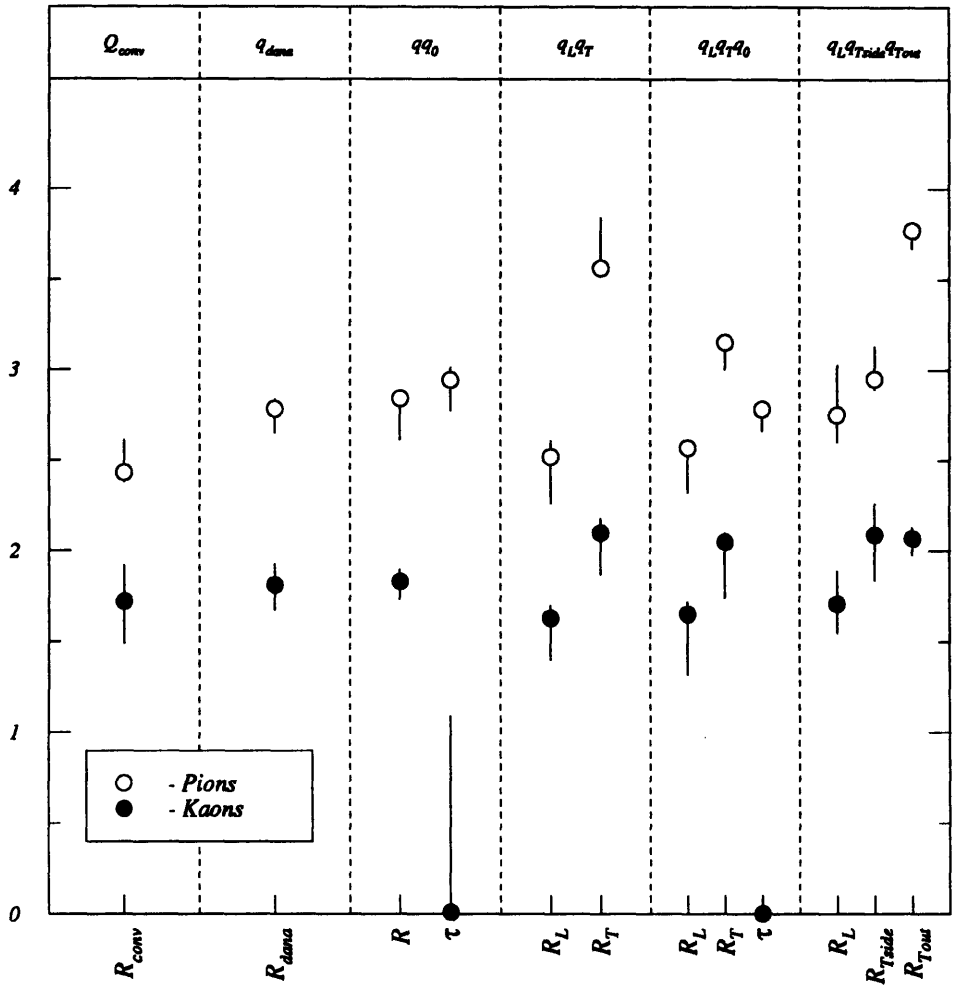

Figure A-1: Range of source-size parameter values obtained in the different systematic tests performed. Data points are the results of fits to the *standard* data sets, see figure 5-1.

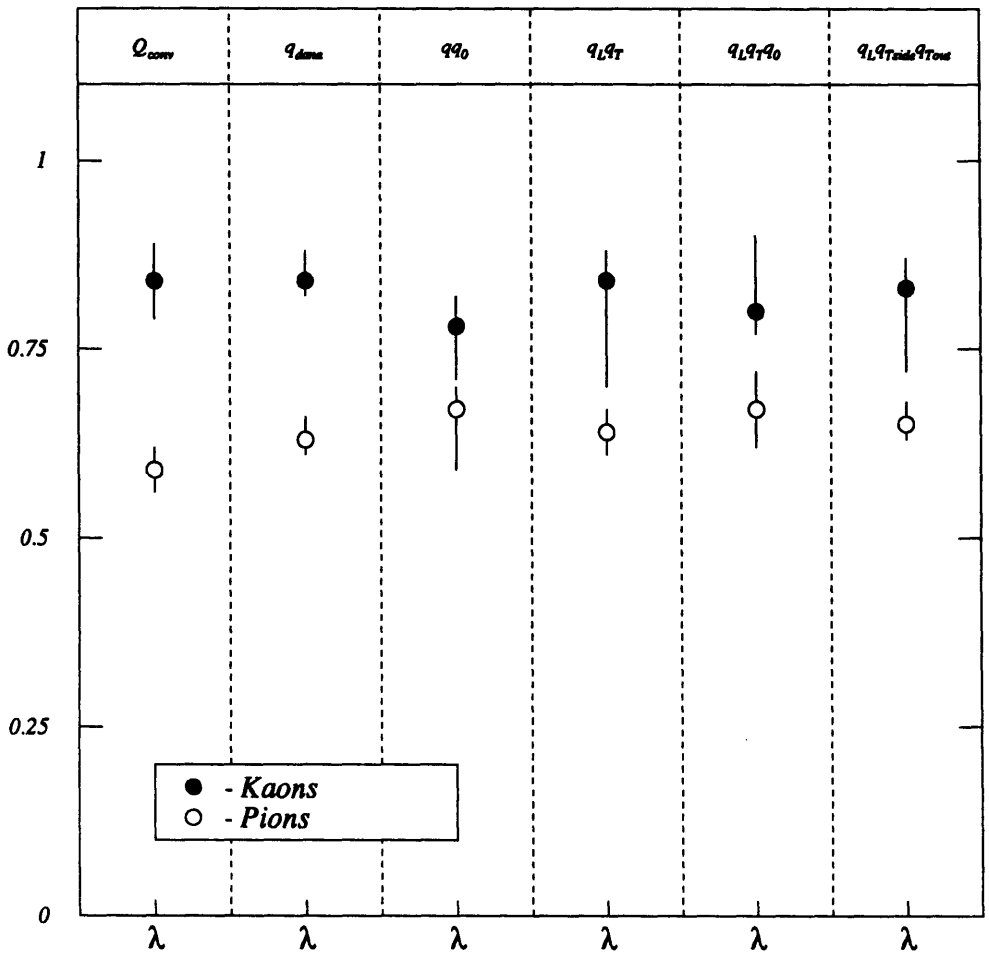

Figure A-2: Range of chaoticity parameter values obtained in the different systematic tests performed. Data points are the results of fits to the *standard* data sets, see figure 5-2.

Study	R_Q	λ	χ^2/dof
Standard	5.00 ± 0.18	0.59 ± 0.04	43.4/56
PICD	5.18 ± 0.19	0.62 ± 0.04	50.2/57
10 MeV start	5.02 ± 0.19	0.59 ± 0.04	43.3/55
15 MeV start	4.97 ± 0.20	0.58 ± 0.04	42.7/54
20 MeV start	5.01 ± 0.22	0.59 ± 0.05	42.5/53
25 MeV start	4.93 ± 0.23	0.57 ± 0.06	42.0/52
30 MeV start	4.97 ± 0.29	0.58 ± 0.08	42.0/51
35 MeV start	4.74 ± 0.31	0.50 ± 0.09	40.5/50
22 mrad scale	5.01 ± 0.19	0.67 ± 0.05	40.5/57
33 mrad scale	4.73 ± 0.20	0.64 ± 0.06	36.9/56
TMA > 140	5.15 ± 0.35	0.56 ± 0.09	80.7/56
TMA > 147	4.99 ± 0.43	0.56 ± 0.09	66.3/55
5 MeV bins[a]	4.81 ± 0.19	0.51 ± 0.03	56.7/57
7.5 MeV bins	4.76 ± 0.19	0.50 ± 0.03	35.8/37
10 MeV bins	4.76 ± 0.19	0.50 ± 0.03	26.7/27

[a]The bin size study was performed with the scale angle cut not applied to the *Background*. These numbers should therefore only be compared with each other.

Table A.1: Q systematic study results for the $\pi^+\pi^+$ data set.

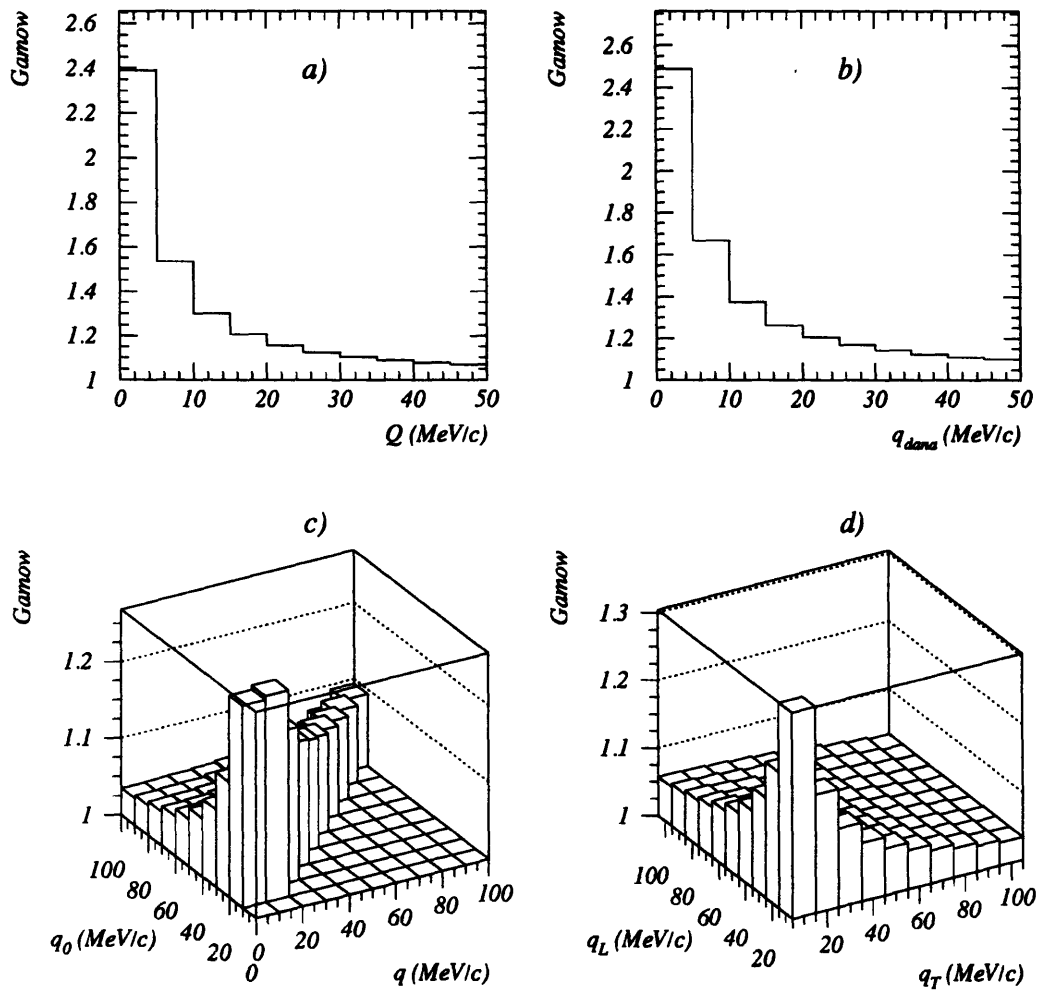

Figure A-3: Gamow correction for the *standard* $\pi^+\pi^+$ data set, binned in different relative momentum variables.

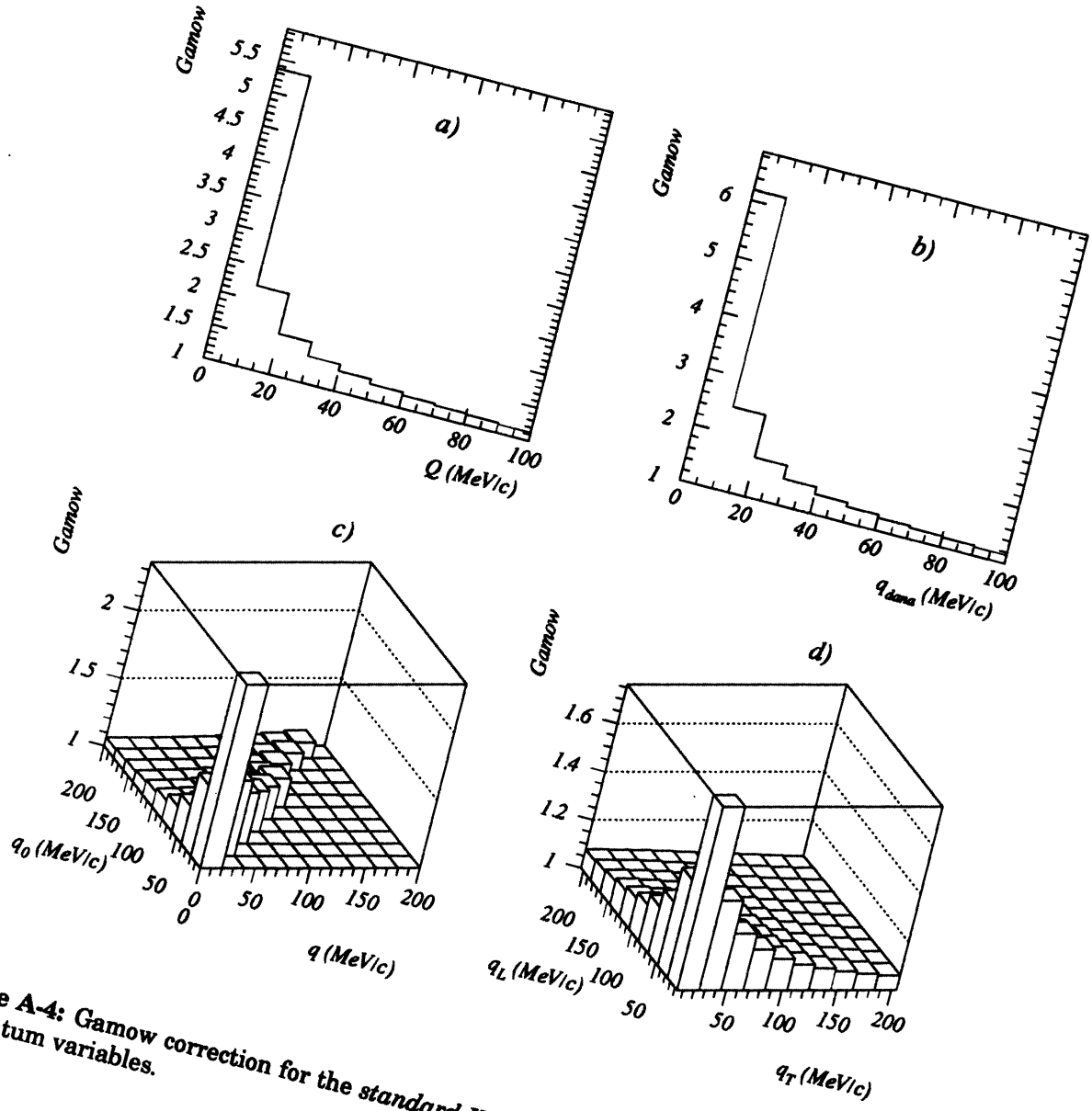

Figure A-4: Gamow correction for the *standard* K^+K^+ data set, binned in different relative momentum variables.

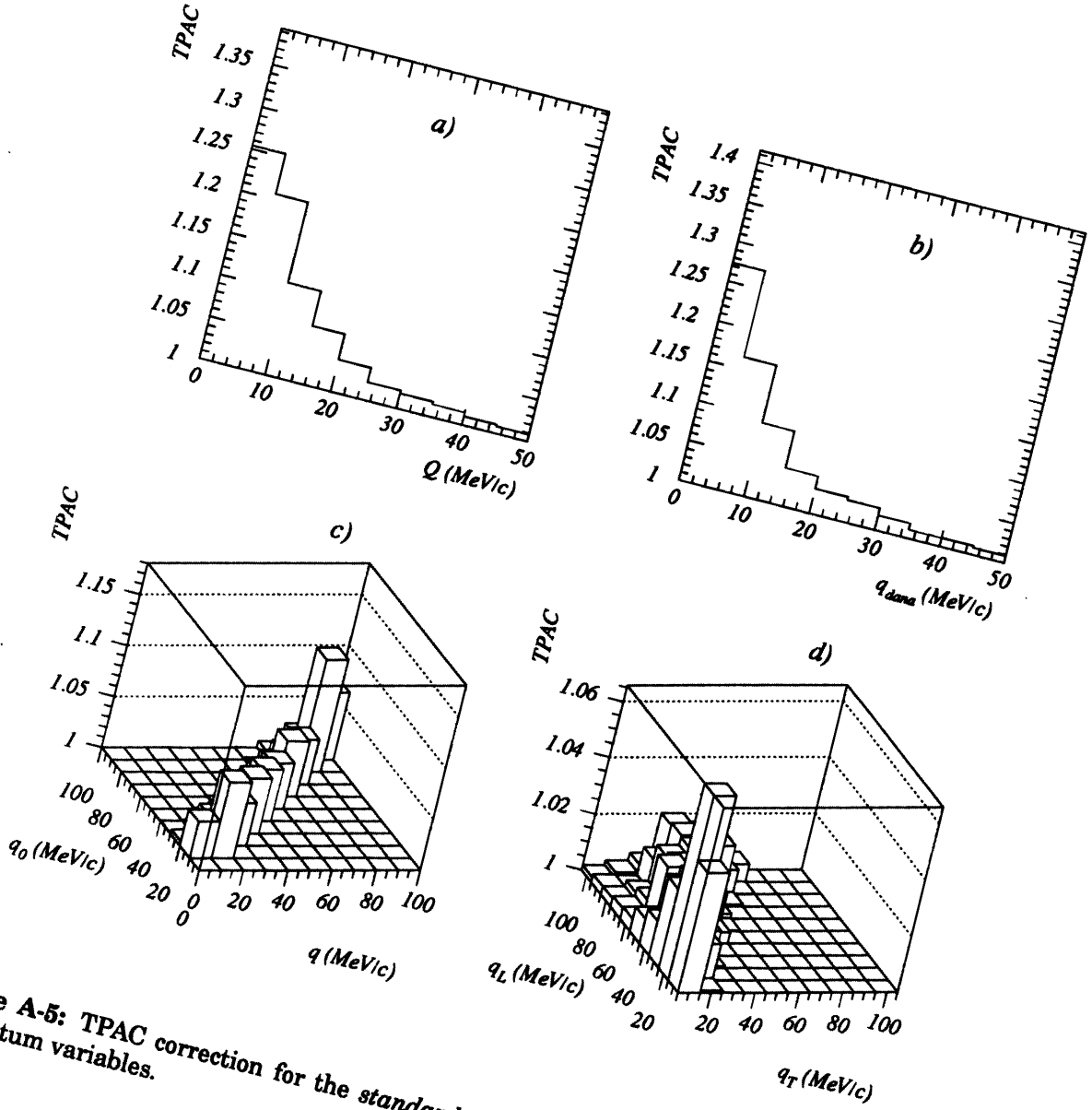

Figure A-5: TPAC correction for the *standard* $\pi^+\pi^+$ data set, binned in different relative momentum variables.

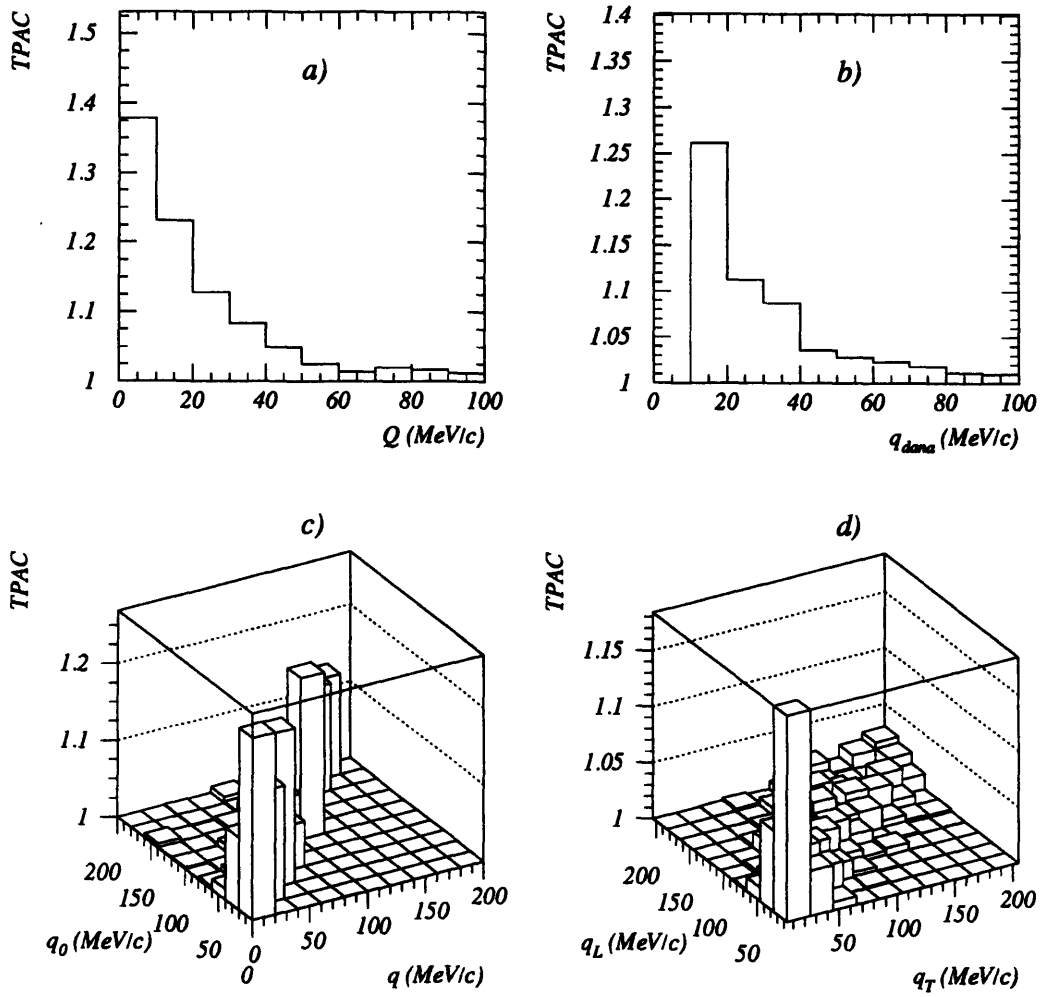

Figure A-6: TPAC correction for the *standard* K^+K^+ data set, binned in different relative momentum variables.

Study	R_Q	λ	χ^2/dof
Standard	2.19 ± 0.10	0.84 ± 0.07	70.4/56
PICD	2.31 ± 0.12	0.89 ± 0.07	62.6/57
20 MeV start	2.15 ± 0.10	0.81 ± 0.06	64.7/55
30 MeV start	2.15 ± 0.11	0.81 ± 0.07	64.6/54
40 MeV start	2.20 ± 0.12	0.85 ± 0.08	63.0/53
50 MeV start	2.13 ± 0.12	0.79 ± 0.09	61.0/52
60 MeV start	2.16 ± 0.15	0.81 ± 0.11	60.9/51
70 MeV start	1.96 ± 0.16	0.63 ± 0.16	55.6/50
22 mrad scale	2.18 ± 0.05	0.84 ± 0.04	73.7/56
33 mrad scale	1.98 ± 0.13	0.85 ± 0.10	70.6/56
TMA cut	2.36 ± 0.20	0.89 ± 0.13	60.5/57
15 MeV bins	2.18 ± 0.10	0.83 ± 0.06	51.5/37
20 MeV bins	2.16 ± 0.10	0.81 ± 0.06	44.6/27
$y < 1.3$	2.03 ± 0.13	0.76 ± 0.07	96.6/57

Table A.2: Q systematic study results for the K^+K^+ data set.

times that of the kaon distribution. This corresponds to a 1.5% contamination of kaons within $3\sigma(1/\beta)$ of the proton peak. But, the momentum at which the kaon-proton overlap reaches this value is the momentum above which kaons are no longer identified. The proton contamination decreases rapidly below this momentum.

Kaons are rare enough that we need to examine the contamination by "noise" (non-identified particles).[2] Figure A-9 shows $\delta(1/\beta)/\sigma(1/\beta)$ vs p for all particles, assuming a kaon mass hypothesis. The kaons are the flat band centered at $\delta(1/\beta) = 0$. Pions have $\delta(1/\beta) < 0$, protons and deuterons can be seen with $\delta(1/\beta) > 0$. The outlined areas are at least $5\sigma(1/\beta)$ from any valid mass hypothesis. We define particles in these regions to be noise. This noise has been found to be roughly uniformly distributed in this space. Given this, we can calculate the contamination of kaons by noise, as a function of momentum. We simply need to normalize the counts in each distribution by the contributing area in this space. The results of this analysis are shown in figure A-10. The contamination of kaons by noise is seen to be generally less than 2%.

[2]Such particles can arise from resonstruction errors, shared TOFs slats, decay, etc.

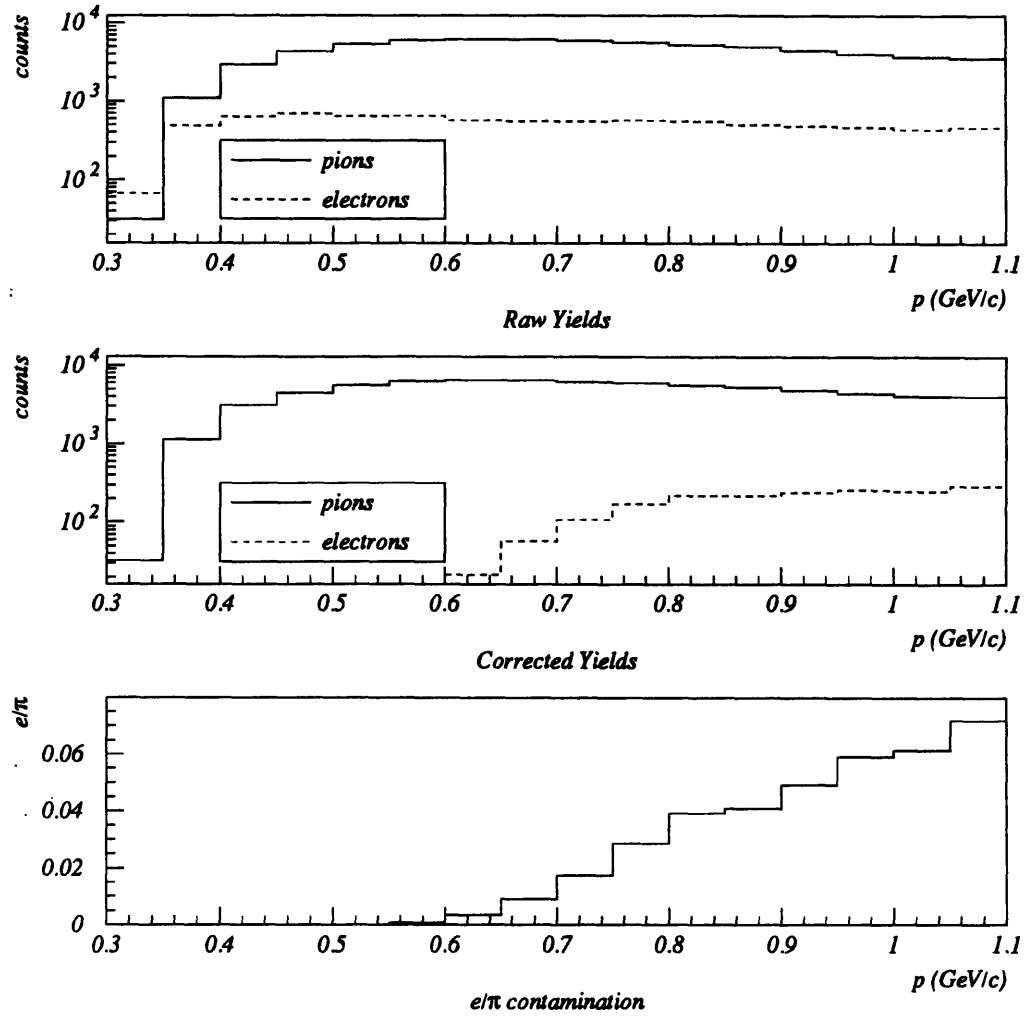

Figure A-7: Electron contamination of pions. The top panel shows the total number of PICD identified electrons and pions for momenta below the μ GASČ threshold. The middle panel shows the number of electrons and pions, in the pion TOFID region, corrected for GASČ inefficiency (for electrons, the GASČ fails to fire $\approx$ 5% of the time) and overefficiency (for pions the GASČ fires for reasons not associated with the pion $\approx$ 5% of the time). A more careful analysis of the GASČ response to electrons and pions can be found in [Rat94]. The bottom panel is merely a division of the two histograms in the middle panel, and shows that the contamination of pions by electrons (when the GASČ information is ignored) is less than 6%.

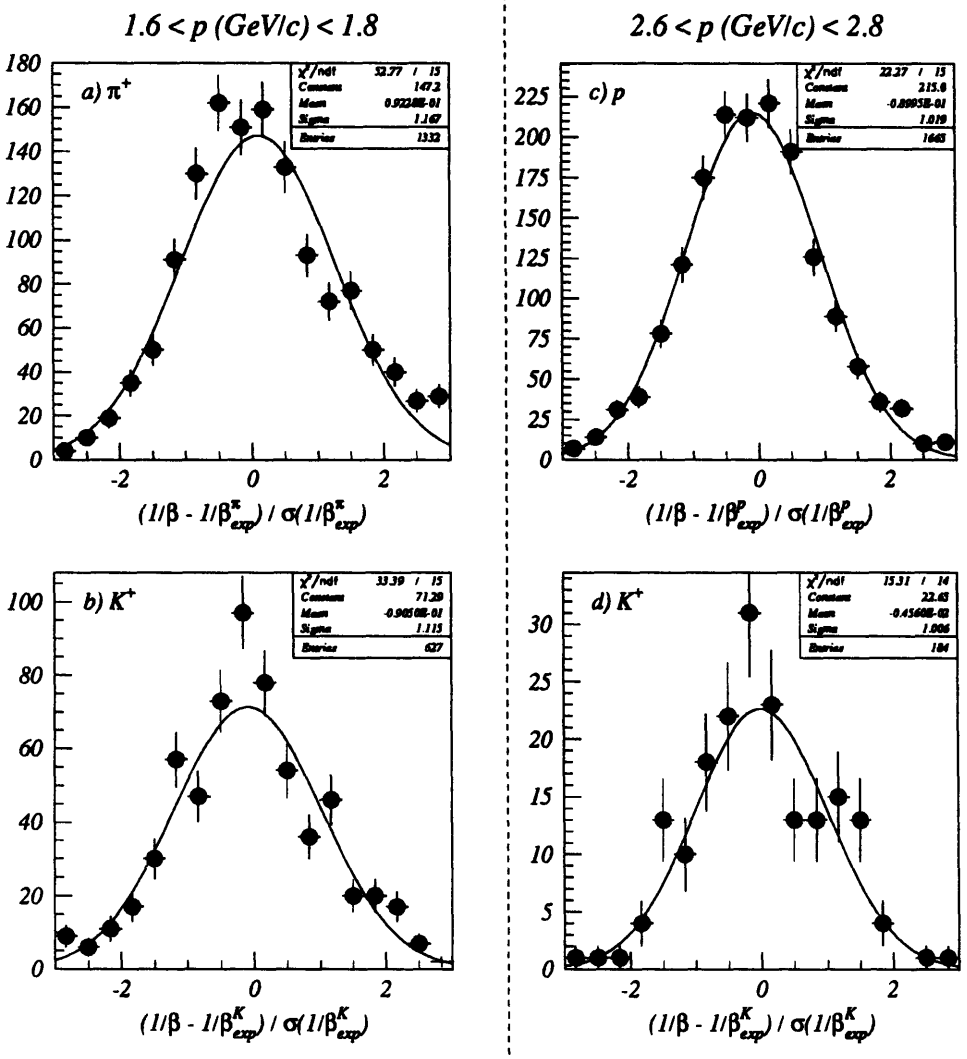

Figure A-8: Contamination of K^+'s by π^+'s and protons. We examine momentum slices just below the $3\sigma(1/\beta)$ overlap region. From the yield ratios (note the number of entries printed in each panel), and the fitted Gaussian width, we can calculate the overlap fraction. See text for details.

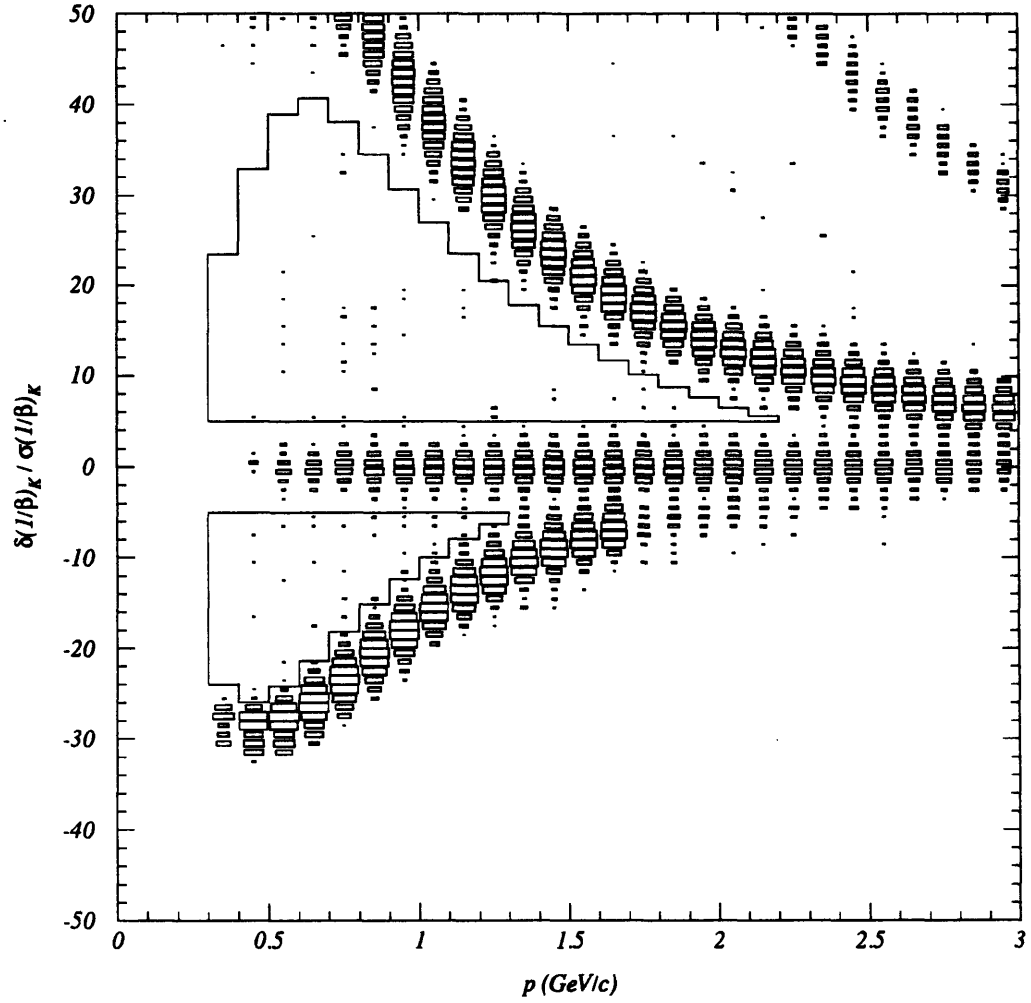

Figure A-9: $\delta(1/\beta)/\sigma(1/\beta)$ vs p for all particles, assuming a kaon mass hypothesis. The outlined regions are at least $5\sigma(1/\beta)$ from any valid mass hypothesis. See text for details.

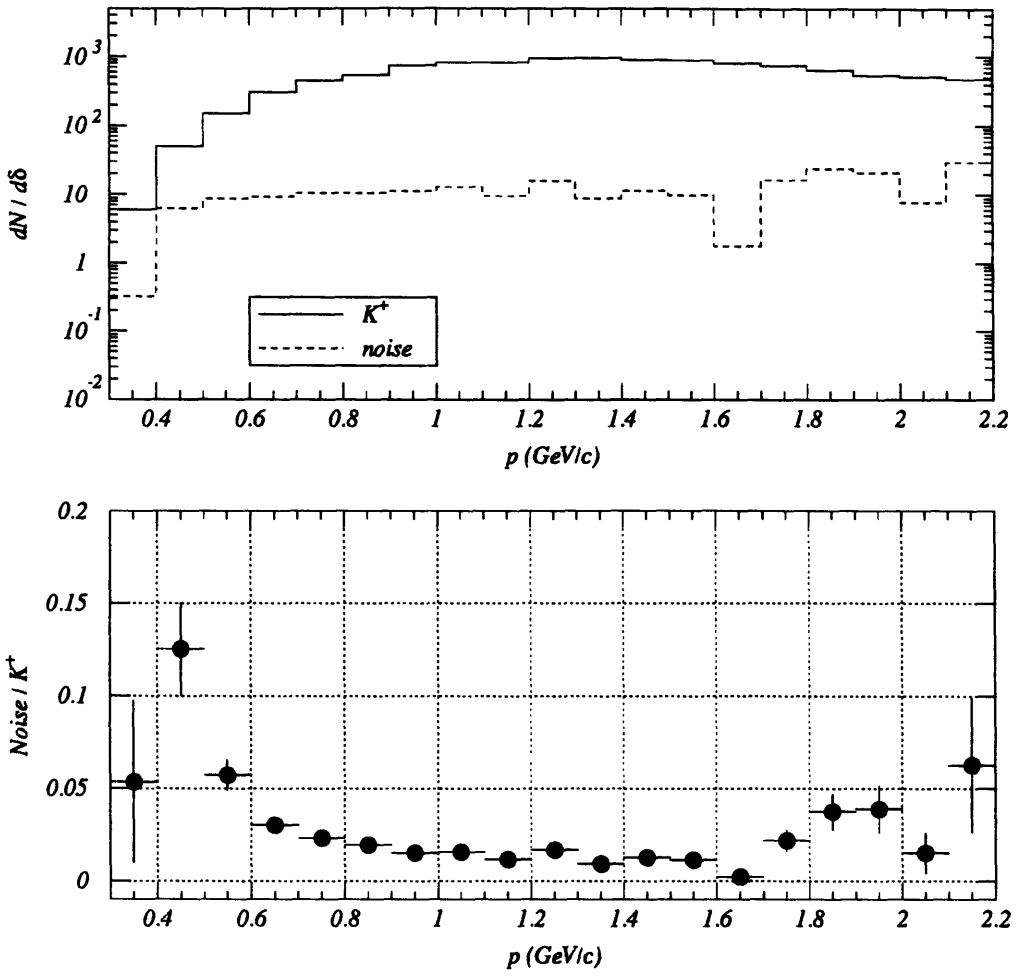

Figure A-10: Ratio of PICD identified K^+'s to noise. The top panel shows the total number of K^+'s, and of noise, per unit $\delta(1/\beta)$, as a function of momentum. The bottom panel is the ratio of these two distributions, showing the contamination of K^+'s, by non-identified particles, to be generally less than 2%.

APPENDIX A. SYSTEMATIC STUDIES

Appendix B

Residual Correlations

Residual correlations were first discussed in Zajc [Zaj82, Z+84]. This effect arises in the event-mixing procedure because the single-particle momentum distribution is obtained by an integration over the observed, correlation function-distorted, two-particle momentum distribution. This results in an enhancement of the event-mixed *Background* distribution relative to the *true Background* distribution. The relative momentum dependence of this enhancement is necessarily similar to the relative momentum dependence of the parent correlation function. Since the *Background* is artificially enhanced by residual correlations, the resulting correlation function is artificially reduced. This effect can be dramatically worsened if the measuring apparatus has a "small" two-particle phase space.[1]

To demonstrate this more rigorously, I will borrow heavily from the derivations found in [Mor90] and [Zaj82]. For clarity, this derivation begins with the correlation function for an individual pair (indicated by the subscript a) with momenta $\mathbf{p}_1$ and $\mathbf{p}_2$:

$$C_2\left(\mathbf{p}_{1a},\mathbf{p}_{2a}\right) \equiv \frac{\mathcal{P}_2\left(\mathbf{p}_{1a},\mathbf{p}_{2a}\right)}{\mathcal{P}_1\left(\mathbf{p}_{1a}\right)\mathcal{P}_1\left(\mathbf{p}_{2a}\right)}. \tag{B.1}$$

$\mathcal{P}_1$ and $\mathcal{P}_2$ are the correctly normalized *inclusive* one- and two-particle production probabilities respectively. In reality we construct the correlation function as:

$$C_2{}^m\left(\mathbf{p}_{1a},\mathbf{p}_{2a}\right) \equiv \frac{Actual}{Background} \equiv \frac{\mathcal{P}_2\left(\mathbf{p}_{1a},\mathbf{p}_{2a}\right)}{\mathcal{P}_1{}^m\left(\mathbf{p}_{1a}\right)\mathcal{P}_1{}^m\left(\mathbf{p}_{2a}\right)}. \tag{B.2}$$

The superscript m indicates that the single-particle probabilities are obtained from the event-

[1] Here "small" means that the Bose-Einstein enhancement is essentially flat across the entire acceptance [Zaj82, Z+84].

mixing procedure:

$$\mathcal{P}_1{}^m(\mathbf{p}_{1a}) = \sum_{i=1}^{N} \mathcal{P}_2(\mathbf{p}_{1a}, \mathbf{m}_i) \tag{B.3a}$$

$$= \mathcal{P}_1(\mathbf{p}_{1a}) \sum_{i=1}^{N} C_2(\mathbf{p}_{1a}, \mathbf{m}_i)\, \mathcal{P}_1(\mathbf{m}_i) \tag{B.3b}$$

$$= \mathcal{P}_1(\mathbf{p}_{1a}) \frac{1}{N} \sum_{i=1}^{N} C_2(\mathbf{p}_{1a}, \mathbf{m}_i) . \tag{B.3c}$$

Here the last step follows from having properly normalized the single particle probability.

So, the event-mixed probability for a given momentum is enhanced by the value of the correlation function for that momentum averaged over the accepted momentum distribution. It is now easy to see why this effect can be much worse for a "small" detector. If a detector is so small that a given single-particle momentum is tightly associated with a value of relative momentum, then the event-mixed *Background* distribution will be just as correlated as the actual distribution. The effect is minimized with a 4π detector with infinite momentum particle identification capability, but, it is not eliminated. A pernicious single-particle momentum distribution could still cause the effect since it is the average correlation function achievable for a given pair that is important.

We define the residual correlation weight for the a^{th} pair to be:

$$W(\mathbf{p}_{1a}, \mathbf{p}_{2a}) \equiv C_2(\mathbf{p}_{1a}, \mathbf{p}_{2a}) / C_2{}^m(\mathbf{p}_{1a}, \mathbf{p}_{2a}) = \frac{1}{N^2} \sum_{i=1}^{N} \sum_{j=1}^{N} C_2(\mathbf{p}_{1a}, \mathbf{m}_i)\, C_2(\mathbf{p}_{2a}, \mathbf{m}_j) . \tag{B.4}$$

Making the usual assumption that $C_2 = C_2(Q \equiv \mathbf{p}_1 - \mathbf{p}_2)$, we can write the above equation as:

$$W(Q_{12a}) = \frac{1}{N^2} \sum_{i=1}^{N} \sum_{j=1}^{N} C_2(Q_{1ai})\, C_2(Q_{2aj}) . \tag{B.5}$$

To cast equation B.5 in terms of relative momentum bins, we average over the M pairs that have $|Q_{12a} - Q| \leq \delta Q$, to obtain:

$$W(Q) = \frac{1}{MN^2} \sum_{a=1}^{M} \sum_{i=1}^{N} \sum_{j=1}^{N} C_2(Q_{1ai})\, C_2(Q_{2aj}) \tag{B.6}$$

So, we are left with the following (unappealing) situation: if we knew the correlation function, we could solve for the residual correlation weight; but, we need to know the residual correlation

weight to calculate the correlation function. In [Zaj82] it was noted that the above expression may be solved iteratively. First, make a good guess at the correlation function fit parameters. Next, derive the residual correlation weights. Finally, obtain new fit parameters for the re-weighted correlation function. Continue this process until the fit parameters converge. This process has been observed to converge within a few iterations [Zaj82, Z+84, Mor90].

In [Mor90] it was noted that the value of the correlation function determined by the fit parameters, ${C_2}^{fit}(Q)$, is *not* the correct value to use in the above sums. This is because determining ${C_2}^{fit}(Q)$ requires removing contributions to the measured correlation function from the Coulomb interaction and the two-particle acceptance. These factors must be restored to the correlation function used in the above sums:

$$C_2(Q) = {C_2}^{fit}(Q)\frac{Gamow(Q)}{TPAC(Q)}, \tag{B.7}$$

Our calculation of the residual correlation weights differs from previous calculations in that we never fit the correlation function in the iterative process. Rather, we interrogate the correlation function *histogram*, uncorrected for Coulomb interactions or two-particle acceptance. The final weights obtained are then used in the correlation function fit. This procedure is valid because residual correlations in the Henry Higgins spectrometer are not severe [Mor90]. This means that our original correlation function histograms are good first guesses at their final values.[2]

Equation B.6 leaves us with an exact expression for the residual correlation weight for a particular relative momentum bin. But, it is in terms of a sum over the *four-dimensional* correlation function of contributing pairs. Unfortunately, this is statistically impossible to calculate. To get beyond this point, previous analyses have made the implicit assumption that the correlation function for an individual pair is independent of the relative momentum projection in which it is calculated [Zaj82, Mor90]. This seems like an intuitively reasonable assumption. But, it is not explicitly true, since to obtain different relative momentum projections of the correlation function one must perform different integrations over the contributing single-particle momenta. [3]

In order to test the assumption of relative momentum projection independence, we generated

[2]To see the problems that can arise when a bad first guess is made, consider the limit where residual correlations completely mask the Bose-Einstein signal. In this limit, the original correlation function histogram would be flat and the residual correlation weights calculated in equation B.4 will all be equal to one. The procedure will have rapidly converged, but to the wrong value.

[3]This is "a trivial binning effect" [Zaja], but we will see that it has a non-zero effect on the determination of the residual correlation weights.

equation B.4 for each pair in the K^+K^+ data set with N=100, using six iterations. The results of the calculation using three standard source parameterizations ($Q, q_O q, q_L q_T$) are shown in figure B-1. It is clear that these distributions are not the same, violating our assumption. Since we have no other way to proceed, we will ignore this result and see if it matters in the end.

Before moving on, a relevant question would be, "Why were the sums in equation B.4 limited to N=100 in this calculation?" To answer this, we first note that calculating the sum rigorously would require $\approx (10^5)^2$ terms for each of our 10^5 *Background* pairs. So, the question becomes "How big does N *need* to be?" In order to answer this question, we created an ensemble of residual correlation weights with $N = 1$ for several pairs. The RMS values of these ensembles was $\approx$ 10-20% depending on the source parameterization. Since the error on the mean is reduced by $\sqrt{N}$, using $N = 100$ results in an error of $\approx$ 1-2%. Figure B-2 shows the distribution of the uncertainty on the residual correlation weight value for individual pairs.

Since each relative momentum bin contains M pairs, we expect the uncertainty on the residual correlation weight for each bin to be reduced by a further factor of $\sqrt{M}$. Figure B-1 shows the distribution of individual-pair residual correlation weights contributing to arbitrary bins of the different relative momentum projections. The means of the distributions are the residual correlation weights of the corresponding bins, see equation B.6. The uncertainty of this value, given by $rms/\sqrt{M}$, is seen to be very small. It is interesting to note that the rms of these distributions is $\approx 2-3\%$, somewhat larger than the rms of the contributing pairs. This shows that there is an intrinsic distribution in the residual correlation weights of pairs in a relative momentum bin that is of order 2%.

To quantify the convergence of our iterative procedure, we examined the change in the residual correlation weights of a relative momentum bin from one iteration to the next. The results for the Q-parameterization for six iterations are shown in figure B-4. The data are plotted in units of δ_{bin}, the uncertainty of the residual correlation weight for that bin. So, convergence would be indicated by a distribution randomly scattered about zero with an average scatter of one. It can be seen that even at iteration six, we have not reached this ideal. But, notice that the systematic change has been vastly reduced from the first iteration. Notice too, that the value of δ_{bin} is typically 10^{-3}, so that the systematic effect left after six iterations is very small. To show this explicitly, we compare ${C_2}^{iter=6}/{C_2}^{iter=0}$ to ${C_2}^{iter=6}/{C_2}^{iter=5}$. The results for all source parameterizations are shown in figure B-5. We conclude that the residual correlation weights have converged.

After performing this iterative procedure, we have three different determinations of the residual correlation weight of each pair. We have assumed that each pair's weight is the same

for all three of these determinations. To test this assumption, we can compare correlation functions that use these different determinations of the residual correlation weights. For each source parameterization, two correlation function ratios are generated. The numerator in every case is the correlation function in which the residual correlation weights were obtained using that parameterization. The denominators are correlation functions in which the residual correlation weights were determined using one of the other two source parameterizations. Figure B-6 shows the results of this comparison. One can see that there are systematic errors arising from this assumption that are similar in magnitude to the residual correlations.

The bottom line is, "How do residual correlations affect the source parameters?" Figure B-7 shows the cumulative change in the source parameters for different iterations in the residual correlation correction. This figure shows that the radius parameters are systematically reduced by $2-5\%$ and λ is increased by a similar amount. The last two points in the three panels of figure B-7 show the difference between parameter-values calculated using residual correlation weights for different source parameterizations after six iterations. From these points, we estimate that systematic uncertainties on the change in the extracted source parameters due to residual correlations to be about half the magnitude of the actual changes.

The uncertainties on the source parameters plotted in figure B-7 are the uncertainties reported by the fitting routine divided by 10. The uncertainty on the source parameters represents the change in the fit parameter if the contributing data points are jittered by their uncertainty. But, when we iterate the value of the residual correlation weights we use the same *Actual* and *Background* distributions; the only jitter we introduce is the uncertainty in the residual correlation weight. The uncertainty in the residual correlation weight of the i^{th} bin, $\sigma^i_{rc} = \sigma^i_{A/B}/\sqrt{N} = \sigma^i_{A/B}/10$, where $N = 100$ is the number of samples used to determine the residual correlation weight for each pair. This is the factor of ten by which the reported parameter uncertainties are divided.

As a final note, consider distortions of the two-particle correlation function by three-particle and higher-order correlations. Residual correlations arise when using event-mixed backgrounds because of an integration of the correlation function over the second boson. The correlation function is expressed in terms of inclusive production probabilities. For the $\pi^+\pi^+$ data set, this may integrate over fifty or more unobserved bosons in a similar fashion. This fact was first noted in [GKW79] as one objection to the formulation of the correlation function in terms of an integral over an explicitly two-particle wave function. In that work, the distortion

of the two-particle correlation function due to higher-order terms is calculated to be:

$$C_2{}^d\left(\mathbf{p}_1,\mathbf{p}_2\right) = C_2\left(\mathbf{p}_1,\mathbf{p}_2\right)\left[1-\delta\left(\mathbf{p}_1,\mathbf{p}_2\right)\right]. \tag{B.8}$$

It is argued that

$$\delta\left(\mathbf{p}_1,\mathbf{p}_2\right) \sim \mathcal{O}\left(r_f/R_0\right) \sim \mathcal{O}\left(1/A\right), \tag{B.9}$$

where A is the number of participating nucleons. For all systems studied in this thesis, this will be smaller than a 1% effect. Zajc [Zaj87] points out that in the high-density limit, the distortion will contain many terms of the size $\mathcal{O}\left(1/A\right)$, and argues for a correction as a power series in the phase space density, $\mathcal{N} = (n_\pi/pR)^3$. If we take $n_\pi = 50, p = 600\,\mathrm{MeV/c}$, and $R = 4.5\,\mathrm{fm}$, $\mathcal{N} \approx 2\%$ and the effect is still small.

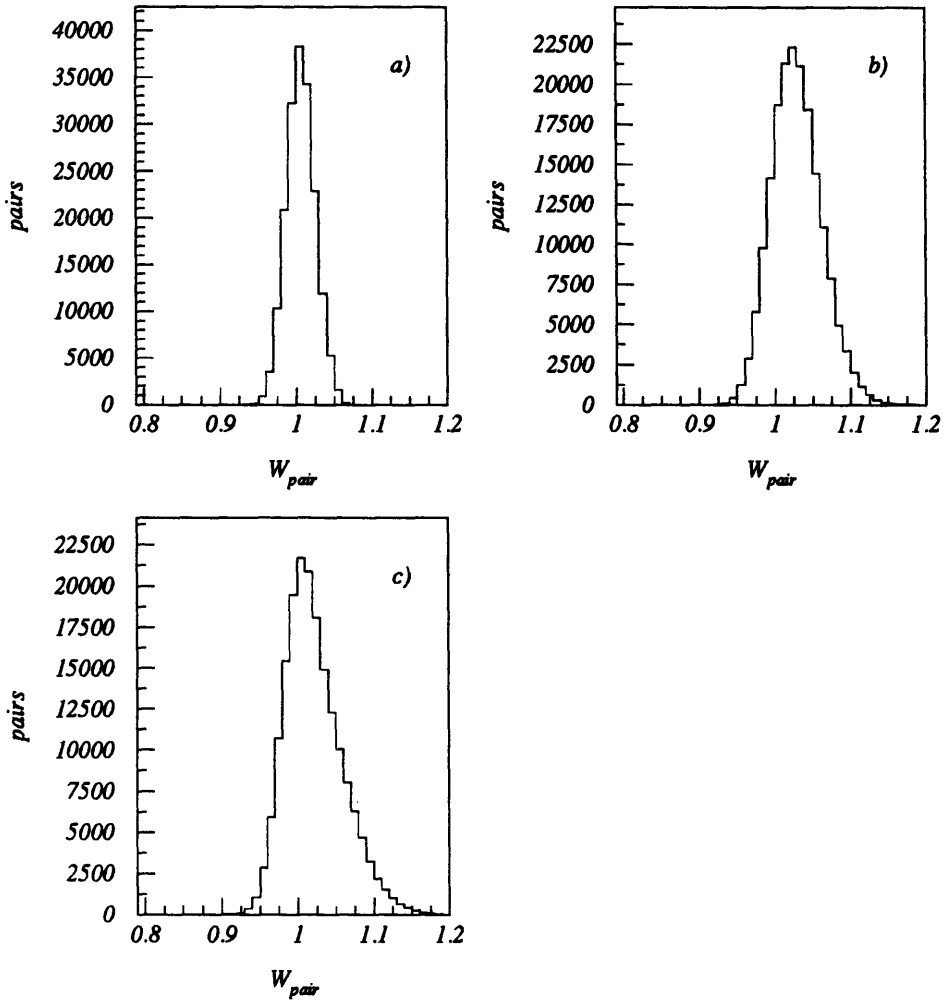

Figure B-1: Distribution of individual-pair residual correlation weights for a) Q, b) $q_O q$, and c) $q_L q_T$ parameterizations. The extent to which these distributions are different is the extent to which the assumption of projection-independent residual correlation weights is violated on a pair-by-pair basis. The fact that the Q-projection weights are more tightly clustered about their average than the weights for other projections indicates that single-particle momenta are more loosely correlated to Q than to the other projections.

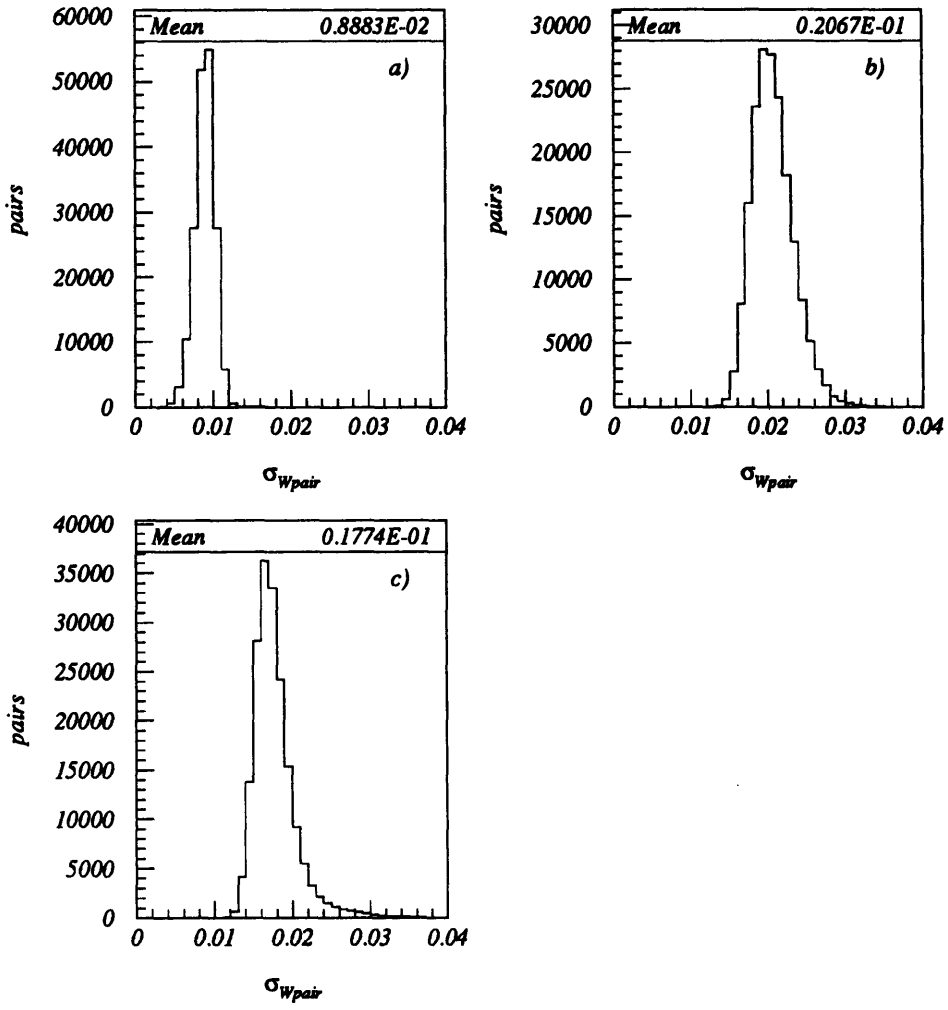

Figure B-2: Distribution of individual-pair residual correlation weight uncertainties for a) Q, b) $q_0 q$, and c) $q_L q_T$ parameterizations. Operationally, we fill a histogram with $N = 100$ samples of the residual correlation function weight for each pair. The mean of these distributions are accumulated for every pair and plotted in figure B-1, the variance of these distributions are accumulated and plotted in this figure.

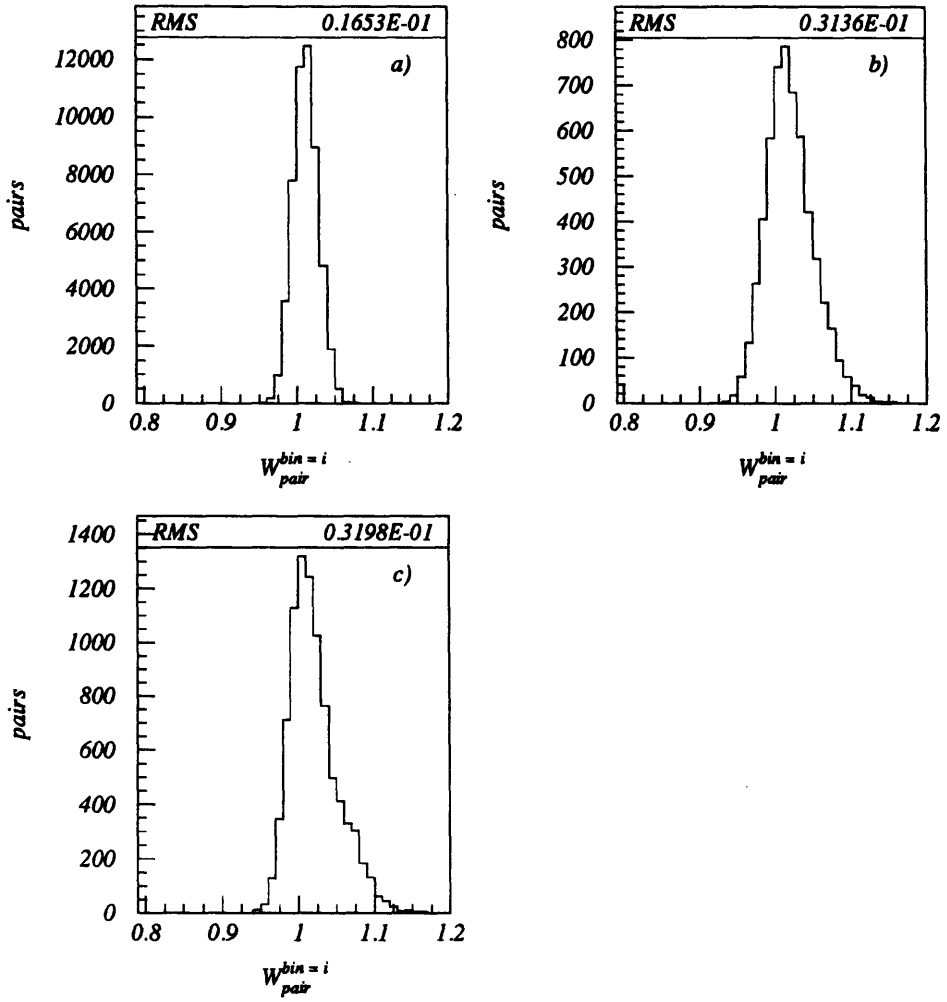

Figure B-3: Distribution of residual correlation weights for arbitrary bins of a) Q, b) $q_0 q$, and c) $q_L q_T$ parameterizations. The uncertainty on the weight for a given bin is given by $rms/\sqrt{M}$ and is quite small. The rms values of these distributions are somewhat larger than the rms values of the individual pairs, indicating that there is an intrinsic width of residual correlation weights for the pairs in a given bin.

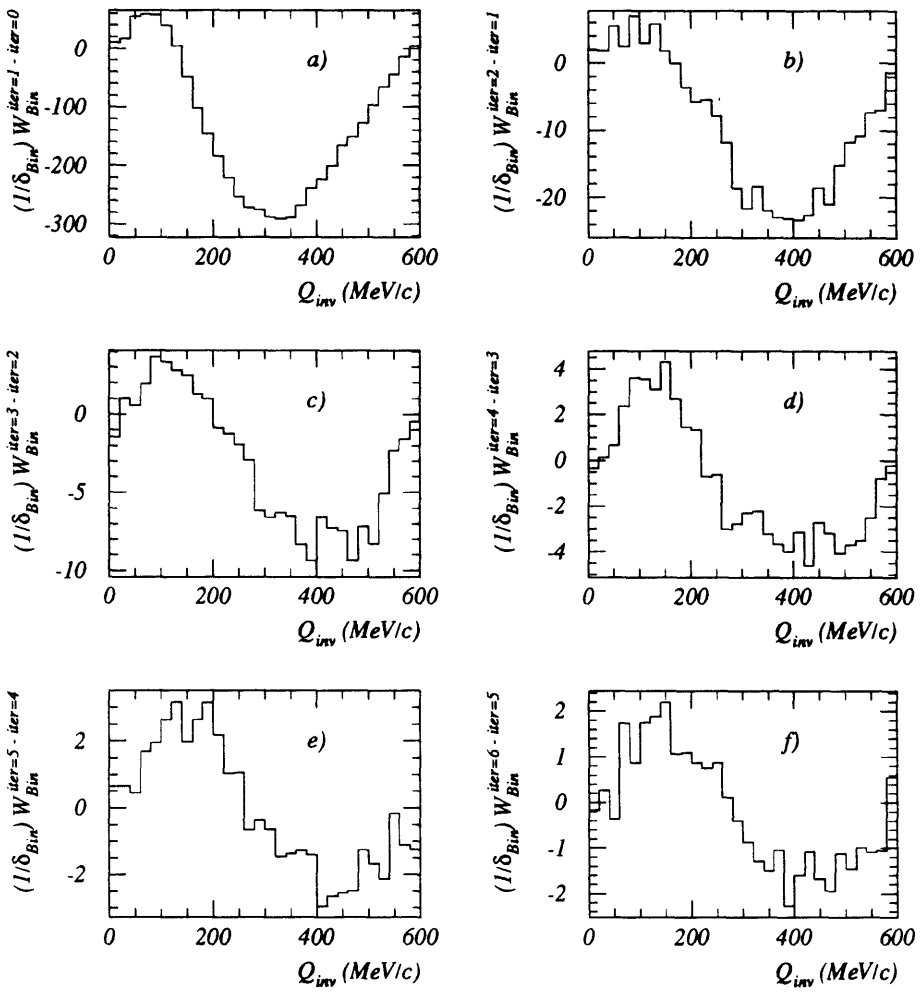

Figure B-4: Distributions of six iterations of the relative change in the residual correlation weights for the Q-parameterization. There are still systematic changes occuring after six iterations, but these are very small, $\mathcal{O}(10^{-3})$.

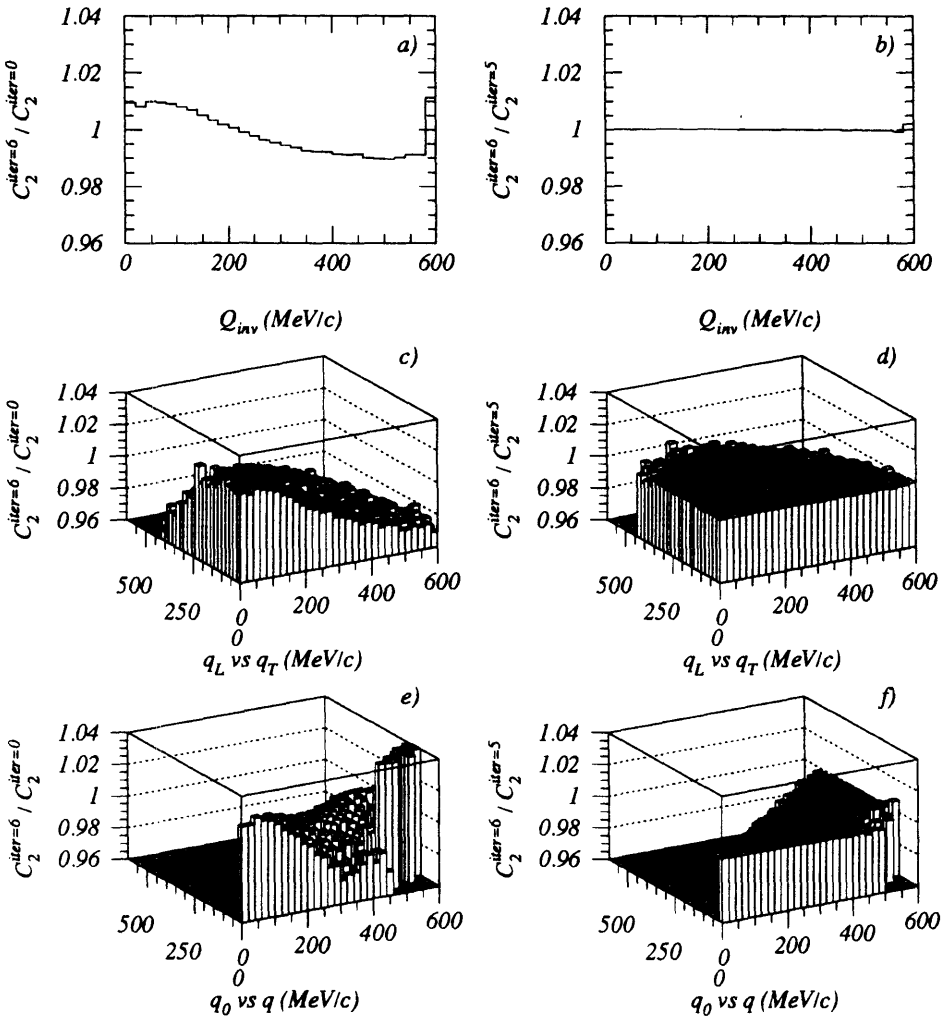

Figure B-5: Ratios of $C_2^{iter=6} : C_2^{iter=0}$ and $C_2^{iter=6} : C_2^{iter=5}$ for the examined source parameterizations. $C_2^{iter=6} : C_2^{iter=0}$ shows the total magnitude of residual correlations to be no more than a few percent in any bin. Distributions of $C_2^{iter=6} : C_2^{iter=5}$ show the weights have essentially converged after six iterations.

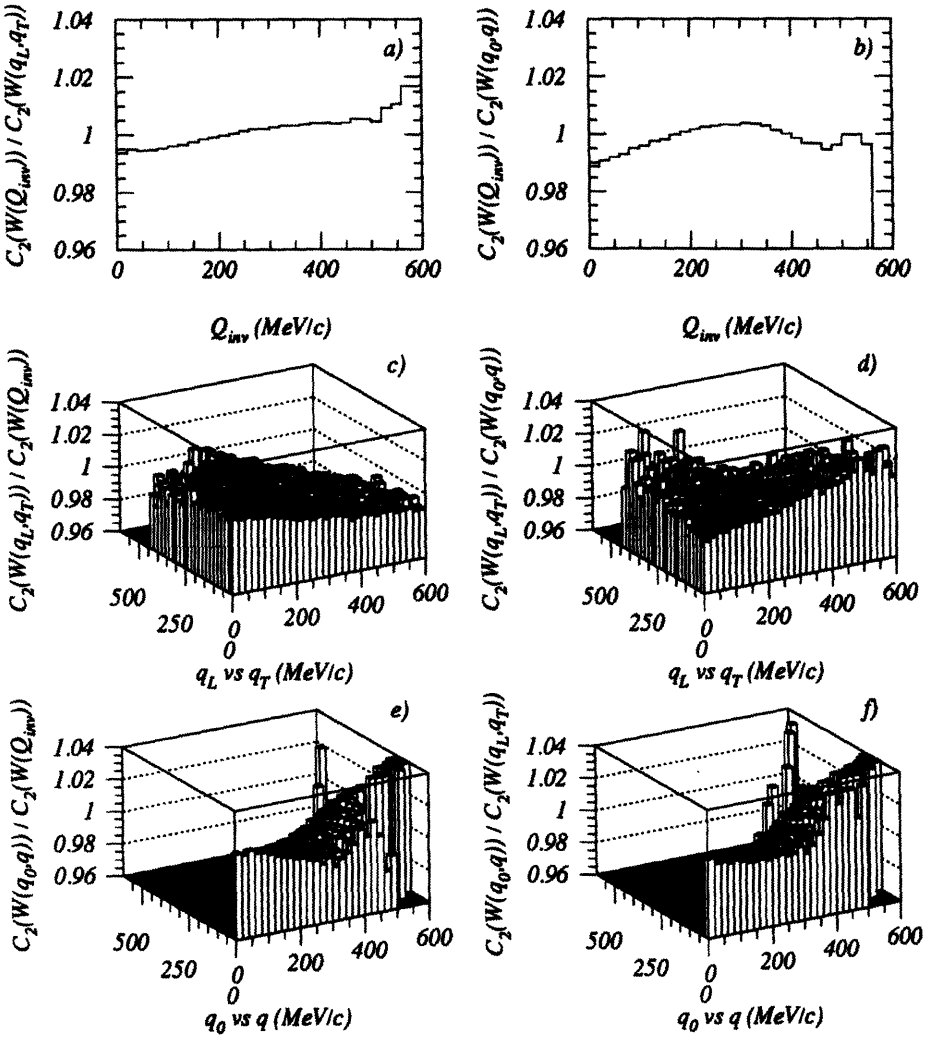

Figure B-6: Ratios of correlation functions for the examined source parameterizations when residual correlation function weights are calculated from different source parameterizations. These distributions show that there are uncertainties in the residual correlation weights arising from our assumption of relative momentum projection independence. These uncertainties are similar in magnitude to the weights themselves.

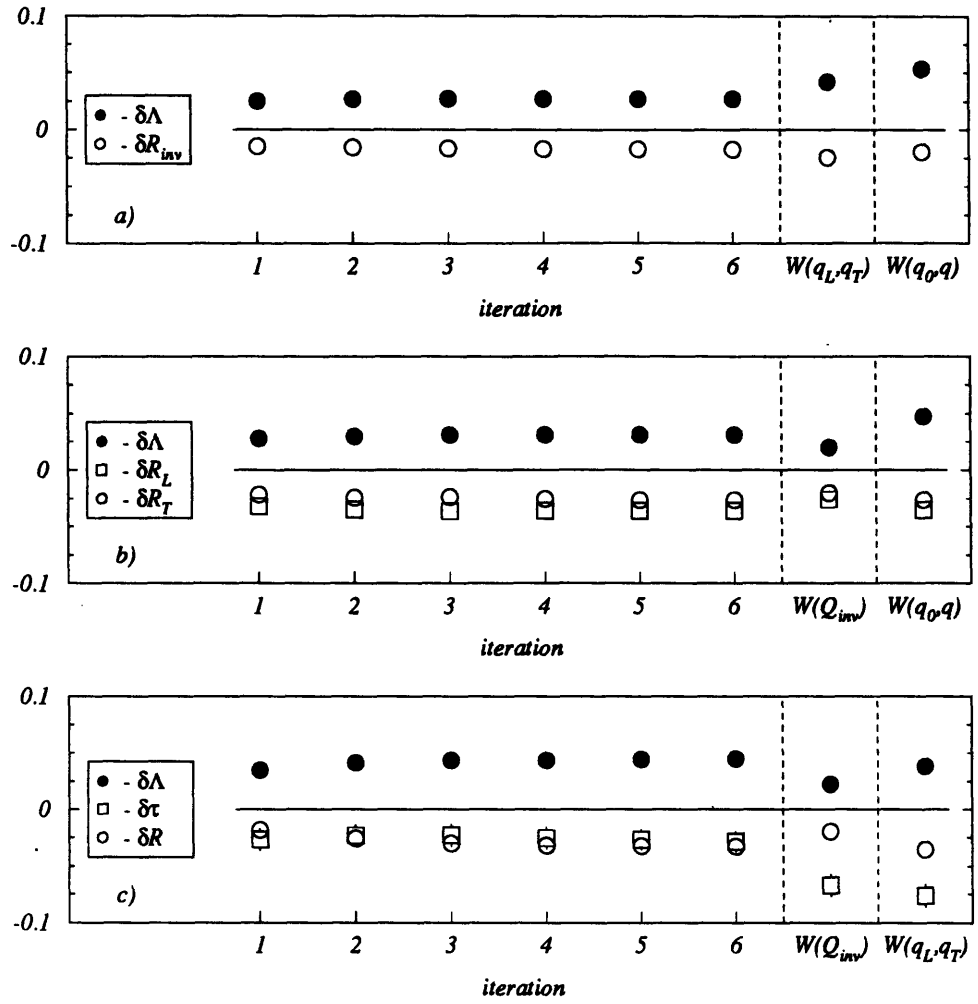

Figure B-7: Plot of the cumulative change in extracted source parameters, for the examined source parameterizations, as a function of residual correlation iteration number. The error bars are typically smaller than the data points, see the text for details of their calculation. The radius parameters systematically increase by 2-5%, λ decrease by a similar amount. The final two points in all panels show the change in parameters when the correlation function is fitted with residual correlation weights obtained from other source parameterizations. This indicates that systematic errors on the changes in the extracted parameters are similar in magnitude to the changes themselves.

APPENDIX B. RESIDUAL CORRELATIONS

Appendix C

Lorentz Extensions in E859

Consider a standard relativity problem, in which a train of proper length, L_0, moves past an observer on a stationary platform with velocity, β. Lightning bolts strike both ends of the train *simultaneously in the observer's rest frame.* The lightning bolts also strike the platform, creating scorch marks that can be used to measure the length of the train in the observer's rest frame. This is the standard prescription for measuring distance, and the scorch marks will be a Lorentz-contracted distance apart, L_0/γ, as expected.

Let us change the problem so that the lightning bolts strike both ends of the train *simultaneously in the train's rest frame.*[1] This is exactly what HBT measures - the pair separation *when the second particle is emitted* [Koo77]. To solve this problem we have to recall the effects of relativity on simultaneity:

> If two clocks are synchronized in the frame in which they are at rest, they will be out of synchronization in another frame. In the frame in which they are moving, the "chasing clock" leads by an amount $\Delta t_s = \beta L_0/c$, where L_0 is the proper distance between the clocks.

In the rest frame of the platform the lightning bolt at the rear of the train will hit first. The train will then travel a distance of

$$x = \beta c\tau, \tag{C.1a}$$

$$= \beta c\gamma\,(\Delta t_s)\,, \tag{C.1b}$$

[1] I agree - this seems like a very silly way of measuring distance. Even without relativity complicating things it is easy to see that a distance measured in this fashion will have to be corrected for the velocity of the object. This is probably why this example is never discussed in class.

$$= \gamma\beta^2 L_0, \tag{C.1c}$$

before the other lightning bolt strikes the front of the train. The front of the train starts out a Lorentz-contracted distance, L_0/γ, ahead of the rear of the train. So, the distance between the lightning marks on the platform will be given by:

$$d = L_0/\gamma + \gamma\beta^2 L_0, \tag{C.2a}$$

$$= \gamma L_0. \tag{C.2b}$$

There are other ways to prove this effect [Zaj92], but none of them quite relieve the unease at the heart of every physicist who hears the words "Lorentz" and "extension" in one sentence.

After the second E859 experimental run, we only had enough kaon pairs to perform the one-dimensional HBT analysis. The original results from this analysis showed the kaon source to be much smaller than the pion source, see figure C-1. This was very exciting since it was exactly what we had been looking for. Bill Zajc knew about the non-intuitive Lorentz properties of HBT source parameters described in section 6.2.2 and was therefore properly suspicious about the initial results. Figure C-2 shows that:

$$\langle\gamma_{\pi\pi}\rangle \approx 2\langle\gamma_{KK}\rangle \tag{C.3}$$

Thus, we expect nearly a factor of two difference between $R_Q(\mathrm{K^+K^+})$ and $R_Q(\pi^+\pi^+)$ from mundane kinematics. To obtain values for the true source sizes, we performed a Monte Carlo calculation [A+93, Zaj92]. E802 correlation results showed that the pion source in the nucleon-nucleon center-of-mass frame was well described by the q_0q parameterization with $R = \tau = 2\,\mathrm{fm}$ [A+92a]. For the calculation, it was assumed that the kaon source could be similarly described. Pions and kaons were then generated according to:

$$\frac{dn}{dp_\perp} \sim \exp\left(-\frac{\sqrt{m^2+p_\perp^2}}{E_0}\right), \tag{C.4}$$

where E_0 values were obtained from fits to the data, see table C.1. Pion and kaon pairs were weighted according to the correlation function given by the assumed parameterization. An acceptance filter was applied to the generated pairs, and those remaining were fit with the Q correlation function. This procedure allowed us to obtain Lorentz corrected radii, R_{conv}, see table C.1.

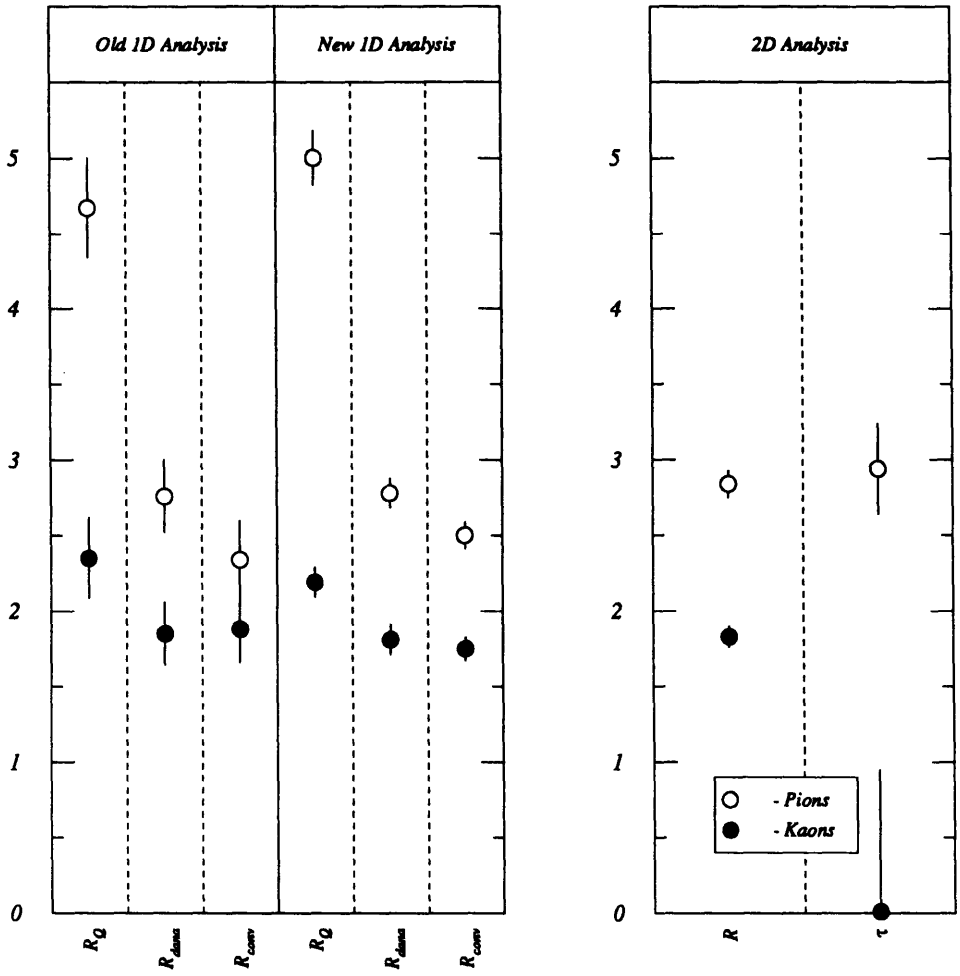

Figure C-1: Calibration of the Lorentz transformation properties of R_Q in the E859 acceptance. See text for details.

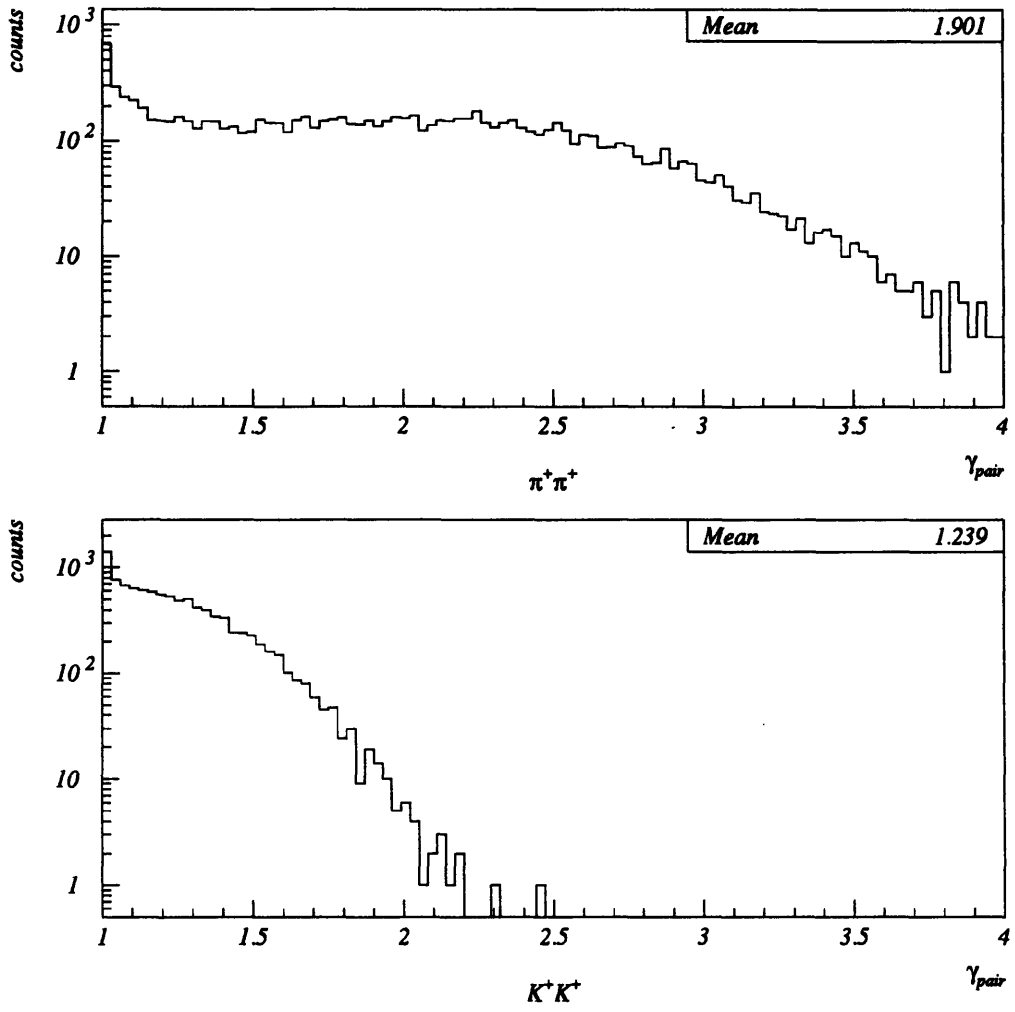

Figure C-2: Distributions of γ_{pair} for pions and kaons in the E859 acceptance.

	$\pi^+\pi^+$	K^+K^+
E_0	160 MeV	200 MeV
R	2 fm	2 fm
τ	2 fm	2 fm
R_{conv}/R_Q	0.49	0.79

Table C.1: Summary of input and output parameters for the Lorentz conversion Monte Carlo calculation. From [Zaj92].

Figure C-1 summarizes the results of this study. The first panel shows the original results for the fit values of R_Q and the extrapolated values of R_{conv}. Also shown are the fits to R_{dana} assuming $R = \tau$. The error bars shown are statistical only, we estimated systematic errors of 0.30 fm. On the basis of these results, it was decided that we could not see a statistically significant difference between the pion and kaon sources [A+93]. The second panel shows the values for these same parameters in the final analysis using the same Lorentz conversion factors.[2] Note that the values are nearly the same in the two different analyses, but the final error bars are much smaller. The final panel shows the values obtained in the two-dimensional q_0q analysis of both systems. This illustrates how well the Monte Carlo calculation did in predicting the Lorentz conversion factors (comfortably within the 0.30 fm systematic errors). It also illustrates the extent to which our assumption of $R = \tau$ was valid (very good for pions, not so clear for kaons).

[2]The major difference between the old and new analyses are a tripling of the K^+K^+ statistics. Improved reconstruction and PID algorithms also helped, resulting in better momentum determination, better PID, and a 35% increase in the $\pi^+\pi^+$ statistics.

APPENDIX C. LORENTZ EXTENSIONS IN E859

Appendix D

Data Structures

There are two primary data structures used in our analysis, "stream NTUPLES" and "QTUPLES." Stream NTUPLES [Cia94] were developed by Brian Cole and Chuck Parsons in order to add flexibility to the CERN NTUPLES [Cia94].[1] The two primary features of the stream NTUPLES are:

1. The ability to compress data. This greatly reduces their size, making them easier to manipulate. It can also be dangerous if one underestimates the amount of storage needed.

2. The ability to coordinate asynchronous data types (e.g., *event* data and *track* data). Each data type is represented by a number, known as a "key."

There are identical stream NTUPLES for both *Actual* and *Background* data. These data structures have four keys corresponding to *run*, *event*, *pair* and *track* information. The stream NTUPLES are used in the preliminary part of our analysis, at a stage where we want to keep as much information as possible. See tables D.1 - D.4 for a complete list of the information stored.

QTUPLES are standard CERN NTUPLES with entries detailed in table D.5. These are used in the final stages of analysis when all event and track definition cuts have been made. Only that information required to calculate the relative momentum has been retained making these data structures much faster to process than the stream NTUPLES.

[1] Many of their improvements were adopted by CERN in the development of the CWN data structure.

NTUPLE Tag	Array Id	Units	Min.	Res.	Bits (238)	Description
RUN_NUM	IDNRUN	—	1	1	14	Run #
BEAMSPEC	IDBMMT	—	0	1	32	Beam species
TARGSPEC	IDTGMT	—	0	1	32	Target species
TRGTTHIK	IDTTHK	mg/cm^2	270	10	10	Target thickness
SANG	IDSANG	rads	5	1	6	Spectrometer angle
PARTYPE1	IDPTP1	—	0	1	32	1st single particle
PARTYPE2	IDPTP2	—	0	1	32	2nd single particle
ACBKFLAG	IDACBK	—	0	1	32	Stream type indicator
TREDMETH	IDMETH	—	0	1	16	Reconstruction code
TIMESTMP	IDTIME	—	0	1	32	Stream creation time

Table D.1: HBT—Stream RUNKEY variables.

NTUPLE Tag	Array Id	Units	Min.	Res.	Bits (275)	Description
NEVNT	IDEVNT	—	1	1	17	Event #
N255	IDN255	—	2	1	5	# of 255 tracks
NPRS	IDNPRS	—	1	1	8	# of pairs of interest
TWD1	IDTWD1	—	0	1	16	Trigger word 1
TWD2	IDTWD2	—	0	1	16	Trigger word 2
TWD3	IDTWD3	—	0	1	16	Trigger word 3
GATEBEAM	IDGTBM	—	0	1	22	# BEAM between events
BCADCTOF	IDBTOF	Z	0	0.01	15	Charge on BTOF
BCADCTOT	IDBTOT	Z	0	0.01	15	Charge on BTOT
BCADCBE	IDBLZI	Z	0	0.01	15	Charge on BE
TMA_MTRU	IDMTRU	—	0	1	10	TMA counts
PBGLETOT	IDPBET	GeV	0	10	15	PBGL E_{tot}
PBGLEPRP	IDPBEP	GeV	0	10	14	PBGL E_T
ZCUP	IDZCLU	GeV	-500	0.01	18	ZCAL E_{UP}
ZCDOWN	IDZCLD	GeV	-500	0.01	18	ZCAL E_{DOWN}
ZCEAST	IDZCLE	GeV	-500	0.01	18	ZCAL E_{EAST}
ZCWEST	IDZCLW	GeV	-500	0.01	18	ZCAL E_{WEST}
EZCAL	IDEZCL	GeV	-500	0.01	19	ZCAL energy

Table D.2: HBT—Stream EVTKEY variables.

NTUPLE Tag	Array Id	Units	Min.	Res.	Bits (86)	Description
SP_PTR1	IDPTR1	—	1	1	9	First single pointer
SP_PTR2	IDPTR2	—	2	1	9	Second single pointer
QINV	IDQINV	GeV/c	0	0.00004	18	$\lvert\mathbf{p}_1 - \mathbf{p}_2\rvert$
MINV	IDMINV	GeV/c	0	0.00004	18	$\lvert\mathbf{p}_1 - \mathbf{p}_2\rvert$
WEIGHT	IDWGHT	—	0	1	32	Pratt weight

Table D.3: HBT—Stream PARKEY variables.

NTUPLE Tag	Array Id	Units	Min.	Res.	Bits (412)	Description
TARG-X	IDTRGX	cm	-2.5	0.0001	16	Target x-pos.
TARG-Y	IDTRGY	cm	-2.5	0.0001	16	Target y-pos.
TARG-Z	IDTRGZ	cm	-2.5	0.0001	16	Target z-pos.
MOMENTUM	IDMOM	GeV/c	0	0.00004	18	$\|\vec{p}\|$
THETA	IDTHET	rads	0	0.0001	14	Polar angle
PHI	IDPHI	rads	-1.3	0.0001	15	Azimuthal angle
T3T4XSLP	IDT34A	—	-0.82	0.0001	14	T3T4 $\frac{\Delta x}{\Delta z}$
T3T4YSLP	IDT34B	—	-0.21	0.0001	12	T3T4 $\frac{\Delta y}{\Delta z}$
T3T4XPOS	IDT34X	cm	-52	0.0001	20	T3T4 x-origin
T3T4YPOS	IDT34Y	cm	-26	0.0001	19	T3T4 y-origin
T3T4ZPOS	IDT34Z	cm	305	0.0001	21	T3T4 z-origin
PATHLEN	IDPLEN	cm	640.0	0.0001	19	Pathlength
MASS	IDMASS	GeV/c^2	-5.24	0.00004	18	PID mass
CHARGE	IDCHRG	Z	-1	1	2	PID charge
SLAT	IDSLAT	—	1	1	8	TOF slat hit
TSLW	IDTSLW	nsec	20	0.001	17	Corrected TOF
TOFELOSS	IDELOS	Yasuos	0	1	11	ΔE — I_{min} = 100
OVERLAP	IDTFOV	—	0	1	4	# tracks on slat
TFCLUSTR	IDTFCL	—	0	1	3	# neighbor slats hit
T1T2QUAL	IDT12Q	—	0	0.07	12	T1T2 Fit χ^2
T3T4QUAL	IDT34Q	—	0	0.02	13	T3T4 Fit χ^2
MATQUAL	IDMATQ	—	0	0.04	12	Connection quality
DELXSLOP	IDDMX	—	-0.0256	0.0001	9	Δx-slope
DELYSLOP	IDDMY	—	-0.0256	0.0001	9	Δy-slope
DELXT2PS	IDDXT2	cm	-3	0.003	11	T2 Δx-pos.
DELYT2PS	IDDYT2	cm	-3	0.006	10	T2 Δy-pos.
DELXTFPS	IDDXTF	cm	-8	0.008	11	TOFW Δx-pos.
DELYTFPS	IDDYTF	cm	-7.2	0.014	10	TOFW Δy-pos.
GEANTPID	IDGPID	—	0	1	7	TOF PID code
PICDPID	IDPICD	—	0	1	7	PICD PID code
STATPID	IDSPID	—	0	1	21	PICD status
TR1WIRE	IDTR1W	—	0	1	8	TR1 wire used
TR2WIRE	IDTR2W	—	0	1	9	TR2 wire used

Table D.4: HBT—Stream SGLKEY variables.

Entry Number	Tag	Description
1	EVTCTR	Event #, stored for mixing
2	WEIGHT	Pratt Weight, one for real data
3	E1	Energy of 1^{st} particle
4	PX1	x-momentum of 1^{st} particle
5	PY1	y-momentum of 1^{st} particle
6	PZ1	z-momentum of 1^{st} particle
7	SLAT1	TOF slat number of 1^{st} particle
8	E2	Energy of 2^{nd} particle
9	PX2	x-momentum of 2^{nd} particle
10	PY2	y-momentum of 2^{nd} particle
11	PZ2	z-momentum of 2^{nd} particle
12	SLAT2	TOF slat number of 2^{nd} particle

Table D.5: QTUPLE variables.

APPENDIX D. DATA STRUCTURES

Appendix E

E859 Detectors Not Used in this Analysis

E.1 Zero-Degree Calorimeter (ZCAL)

This detector is an iron-scintillator sampling calorimeter modelled after the zero-degree calorimeter of CERN experiment WA80 [A+]. The purpose of the ZCAL is to measure the amount of an event's kinetic energy remaining in a 1.5° cone about the beam axis 11 m downstream from the target. This is a very good measure of the *number of projectile spectators* if the ZCAL response is linear and the resolution is good. If this is the case, the ZCAL is also a good measure of the centrality of a *symmetric* collision.

Calibration and performance of this device before the E859 running period is described in [B+89a]. As shown in figure E-1, the response was extremely linear in the number of nucleons deposited in the ZCAL volume. The resolution was $\Delta E_{kin}/E_{kin} = 73\%/\sqrt{E_{kin}\,(GeV)}$, about one nucleon for the ^{28}Si beam. Unfortunately, the very intense ^{28}Si beams used by E859 took their toll on the scintillator material of the ZCAL. Halfway through the E859 running period, the ZCAL energy resolution had degraded by a factor of 2.5 [Chu]. Another complication of the high beam intensity was a rate dependence in the measured beam energy. This occurred because of long tails on the input signals that would pile up to form a pedestal whose magnitude increased with the instantaneous beam rate. The magnitude of the effect can be seen in figure E-2. This needs to be corrected for in any analysis using the ZCAL.

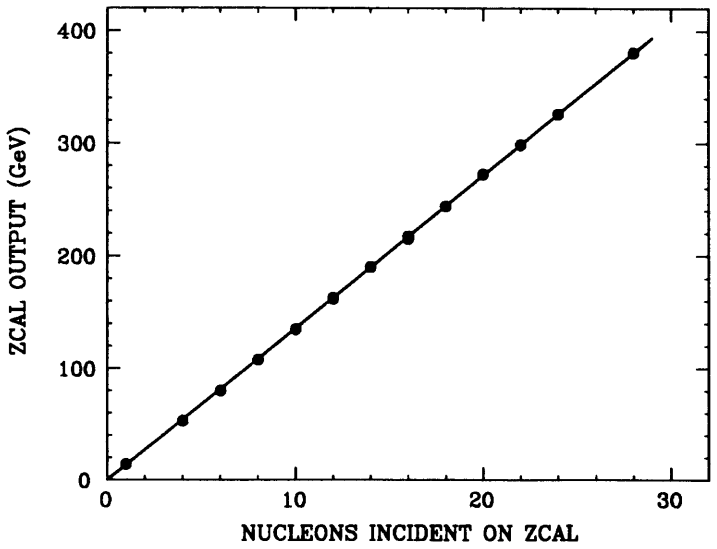

Figure E-1: ZCAL response as a function of nucleon number, A. From [B+89a].

Figure E-3 shows the expected anti-correlation between ZCAL and TMA for $^{28}Si + ^{197}Au$ collisions. Note the saturation of the ZCAL response at large TMA values. For asymmetric collisions the TMA provides a better measure of centrality. When the projectile is smaller than the target, there is a range of impact parameters in which the projectile nucleus is is completely occluded by the target, and there is no foward-going energy.

E.2 Lead Glass Array

A more complete description of the PBGL can be found in [A+90b]. The PBGL is an electromagnetic calorimeter consisting of 245 $14.5 \times 14.5 \times 40$ cm^3 SF5 type lead-glass blocks. The blocks are arranged in an approximate half-circle coaxial with the beam and cover a polar angle $8° \leq \theta \leq 32°$. The PBGL is designed to detect the neutral energy produced in the collision. γ-rays produced in π^0 decays are converted in a 1.9 cm thick steel plate. The resulting electromagnetic showers produce Čerenkov radiation in the lead-glass blocks that is proportional to the incident photon energy. The Čerenkov threshold for the lead-glass blocks is $\beta_\varepsilon \approx 0.8$ and it estimated that $\approx 50\%$ of the PBGL energy results from charged hadrons. Long term calibration is maintained by CsI/^{241}Am sources imbedded in each block, see figure E-4.

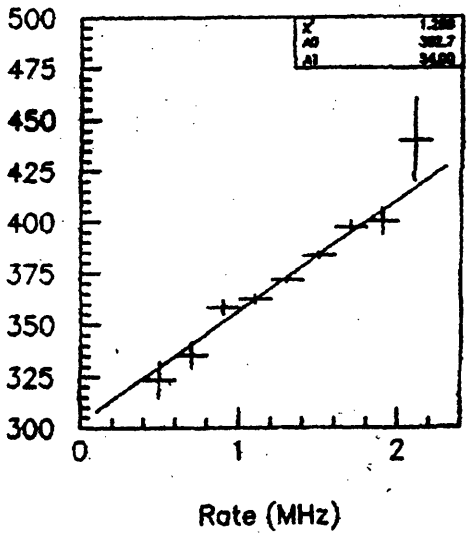

Figure E-2: E_{kin}^{beam}, measured by the ZCAL, as a function of the instantaneous beam rate [Chu]. The non-zero slope of this distribution indicates that there is a rate dependent pedestal. This pedestal is caused by the overlap of many long signal tails.

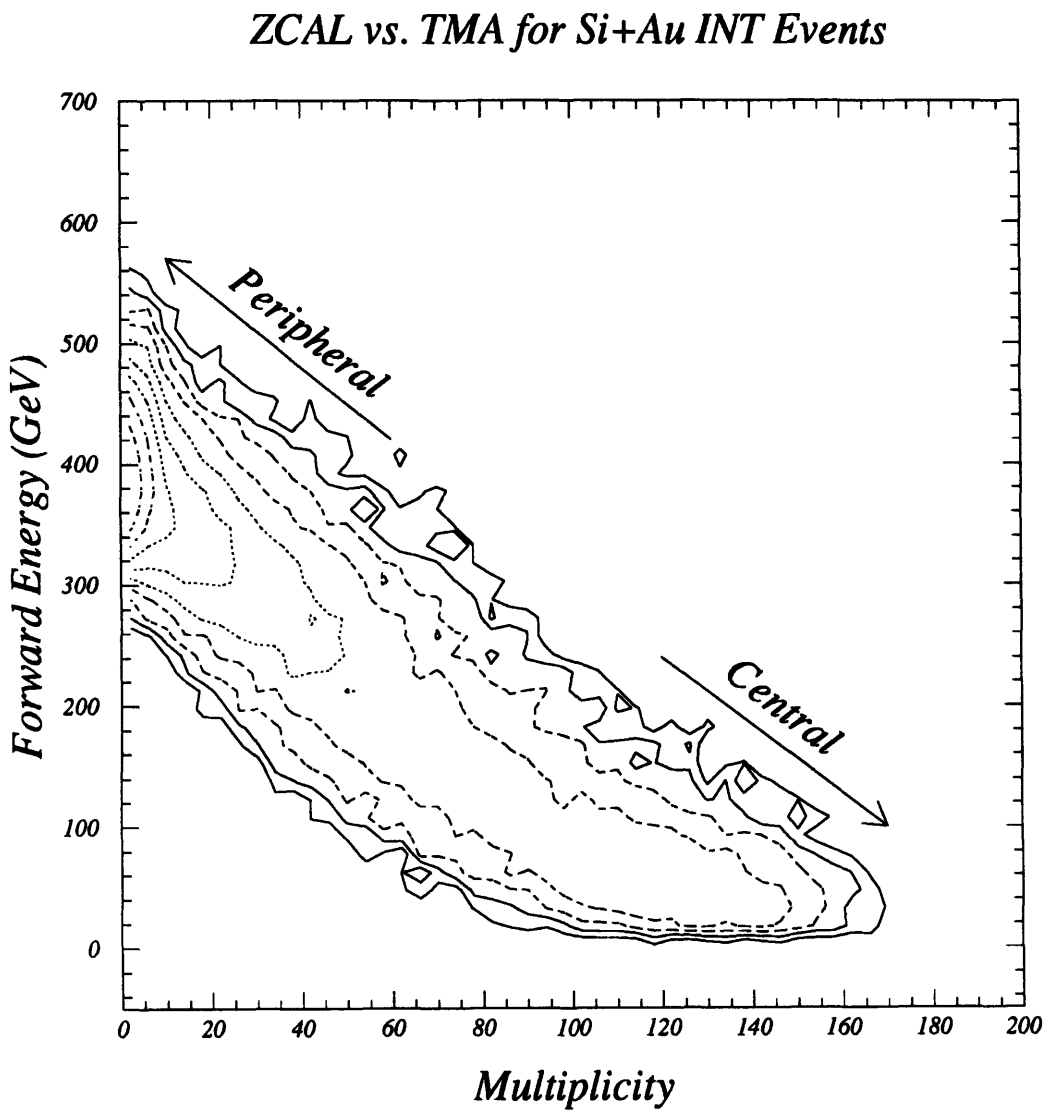

Figure E-3: Response of TMA vs ZCAL $^{28}Si + ^{197}Au$ collisions. The inset illustrates the reason for saturation of the ZCAL response for the most central collisions. For all impact parameters, $0 < b < R^{Au} - R^{Si}$, the silicon nucleus is completely occluded by the gold nucleus. No energy should be deposited in the ZCAL for any collisions in this impact parameter range.

E.3. PHOSWHICH ARRAY (PHOS)

The CsI scintillator fires when struck by the α particle emitted in the ^{241}Am decay [A$^+$87b].

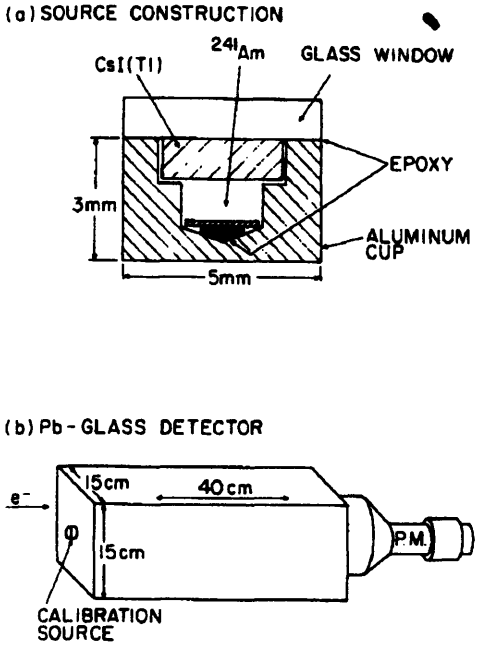

Figure E-4: Schematic of the PBGL CsI(Tl)/^{241}Am calibration modules [A$^+$87b].

E.3 Phoswhich Array (PHOS)

A more complete description of the PHOS can be found in [C$^+$93c]. The PHOS is an array of 42 $\Delta E - E$ plastic scintillator telescopes covering a range of $48° \leq \theta \leq 130°$ and $\Delta\phi \approx 24°$. The PHOS was installed as a part of the E859 upgrade in order to measure baryon distributions in the target rapidity region. The technique is very elegant - two optically coupled scintillators with significantly different decay times are read out by *a single phototube*. The decay times must simply be different enough that the signals can be separated by pulse-shape analysis.

E.4 Čerenkov Complex (ČC)

A more complete description of the CC can be found in [Col92, and references therein]. The ČC is a 1 msr single track spectrometer located downstream of the BACK counter. It is designed to provide very high momentum particle identification. Timing information, triggering capability and acceptance definition are provided by two "picket-fence" plastic scintillator

hodoscopes. A 4-element version is placed at the front of the complex and an 8-element version is placed at the back of the complex. Three drift chambers provide tracking capability. Three Čerenkov tanks form the heart of the complex. All are filled with Freon-12, two at a pressure of 0.8 atm and one at a pressure of 4.8 atm. This provides π/K separation up to 7.8 GeV/c and K/p separation up to 14.8 GeV/c.

Appendix F

A Brief History of Multiwire Chambers

Georges Charpak won the 1992 Nobel Prize in physics for the development of the multiwire proportional chamber (MWPC) [C+68]. Since his invention in 1968, MWPC's and their descendents, the drift chamber and the time projection chamber, have become ubiquitous in high energy and nuclear physics. MWPC's are part of an evolutionary chain leading from bubble chambers to spark chambers to "filmless" spark chambers. The discussion in this section largely follows that in [Sch93].

Bubble chamber data was in the form of photographs of bubbles created when charged particles passed through a superheated liquid causing it to boil. Milliseconds before the beam traversed the chamber, a giant piston would expand the liquid, causing it to become superheated. After the event was photographed, the piston would compress the liquid, raising its boiling point and erasing the bubbles. Sophisticated, electronic scanners did not exist in the heyday of the bubble chambers, so each event had to be analyzed by a human being. There was a daunting amount of data to analyze even though the number of pictures was severely limited by the piston's intolerably slow cycle speed of ≈ 1 Hz.

The basic unit of a spark chamber is a set of two electrodes sandwiched around a layer of gas. Charged particles ionize the gas. If a trigger counter indicated that an event should be recorded, a high voltage would be placed across the electrodes. This would cause a spark along the ionization trail which could be photographed. Although their spatial resolution was poorer than that of a bubble chamber, spark chambers were a big advance because of their $\approx$1000 Hz cycle speed. Even though a spark chamber could be triggered, the increased cycle speed resulted

in a much larger number of photographs that needed to be analyzed. This embarrassment of riches motivated the development of "filmless" spark chambers which allowed the information to be analyzed by a computer.

The first filmless spark chamber was the acoustic spark chamber. This detector made spatially separated recordings of the sound created by the spark. The differences between the arrival times of these sounds could be used to locate a particle. The cycle time of this detector was limited to 1000 Hz because the potential difference had to be recharged after every event.

The second filmless spark chamber was the multiwire spark chamber. The basic unit of all multiwire chambers is known as a drift cell. A drift cell is made up of several special purpose wires in volume filled with ionizable gas. A schematic of a typical drift cell is shown in figure F-1. Cathode wires shape the field, directing all ionization in a drift cell toward that cell's

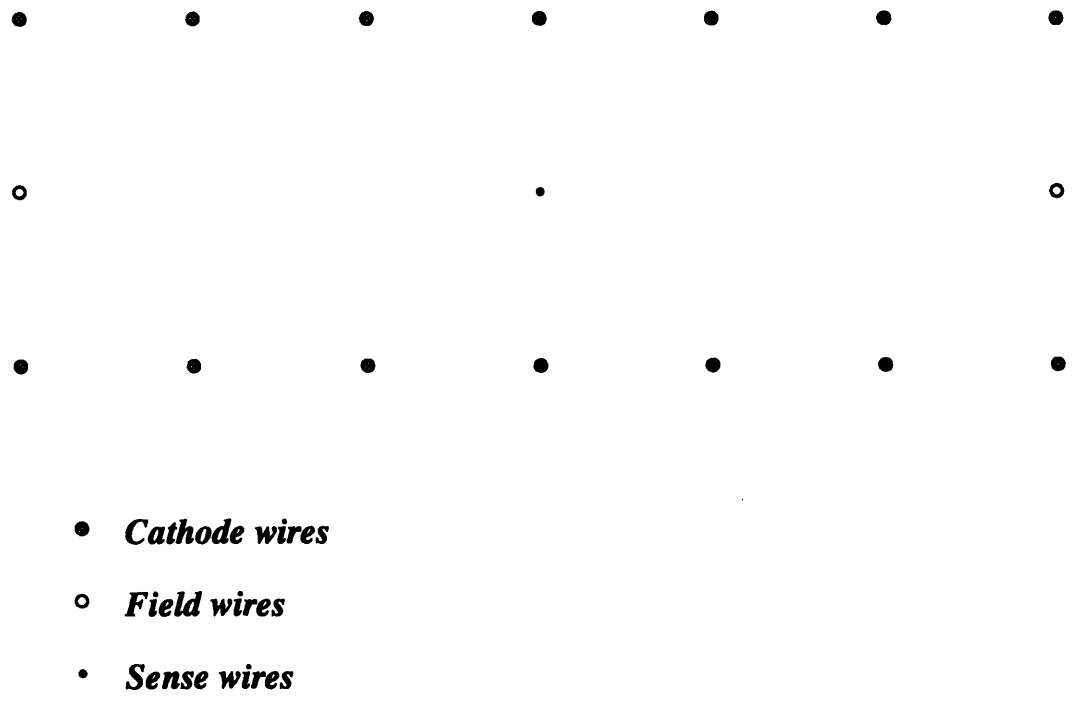

Figure F-1: Schematic of a typical drift cell. The field and cathode wires are roughly to scale. The sense wire is expanded by a factor of 2.5

sense (electrons) and field (ions) wires. Cathode wires also shield a drift cell's sense and field wires from ionization in neighboring drift cells. Field wires are maintained at high, negative voltage in order to attract the positive ions liberated by charged particles passing through the chamber's gaseous volume. Sense wires are maintained at high, positive voltage in order to attract the electrons liberated in the ionization events. It is the information from the sense

wires that is recorded by the experiment.

An ionizing detector can operate in three qualitatively different regions depending on the value of the applied voltage. At the lowest voltages, the electrons liberated by the ionizing particle are accelerated towards the sense wire without any amplification. This is known as the ionization region. At higher voltages, the electric fields can become large enough that between individual collisions with the gas molecules, electrons can gain enough energy to ionize the gas. This liberates more electrons which are then further accelerated and the whole thing begins to sound like a bad shampoo commercial. This runaway behavior is known as an avalanche. Until the voltage becomes too large the amplification gives a signal that is proportional to the original charge. Multiwire proportional chambers (MWPC) use operating voltages in this region. At high enough voltages, gas amplification saturates at a very large value and any ionization will result in a spark. This region, known as the Geiger region, is the one in which the multiwire spark chamber operated.

Just like the acoustic spark chamber described above, the potential difference of the multiwire spark chamber had to be recharged after every event. This similarly limited the multiwire spark chamber to a cycle speed of 1000 Hz. This author does not want to think about how badly the wires would be damaged in even a short running period. Because MWPC's operate in the proportional region, very small amounts of current are deposited on the wires and the high voltage is not discharged. This gives MWPC's rate capabilities in excess of 10^6 Hz.

MWPC's paved the way for the development of drift chambers like those that are the key to our momentum determination. A drift chamber is basically an MWPC in which the arrival time of the ionization pulse is recorded. In order to get excellent position resolution, the drift cell must be carefully designed and the chamber gas carefully chosen. Ideally, the electrons drift towards the sense wire with a nearly constant velocity. If the drift-time/drift-distance relationship is calibrated, the position resolution can be many times better than the wire spacing. Our drift chambers achieved a resolution of $\approx$150-200μm.

APPENDIX F. A BRIEF HISTORY OF MULTIWIRE CHAMBERS

Bibliography

[A+] T.C. AWES *et al.* WA80 projectile calorimeter. *Nuclear Instruments and Methods*, **A279** 503.

[A+77] C. ANGELINI *et al.* Observation of interference correlations between like pions in the reaction $p\bar{p} \rightarrow 2\pi^+2\pi^-\pi^0$ at low energy. *Lettere al Nuovo Cimento*, **19** (1977) 279–281.

[Å+85] T. AKESSON *et al.* Bose-Einstein correlations between kaons. *Physics Letters*, **B155** (1985) 128–132.

[A+87a] T. ABBOTT *et al.* Measurement of energy emission from O+A and p+A collisions at 14.5 GeV/c per nucleon with a lead-glass array. *Physics Letters*, **B197** (1987) 285–290.

[A+87b] D.E. ALBURGER *et al.* CsI(Tl)-^{241}Am calibration source for Pb-glass detectors. *Nuclear Instruments and Methods*, **A254** (1987) 88–90.

[A+90a] T. ABBOTT *et al.* Kaon and pion production in central Si+Au collisions at 14.6 A·GeV/c. *Physical Review Letters*, **64** (1990) 847–850.

[A+90b] T. ABBOTT *et al.* A single arm spectrometer detector system for high energy heavy ion experiments. *Nuclear Instruments and Methods*, **A290** (1990).

[A+91a] T. ABBOTT *et al.* Antiproton production in 14.6 A · GeV/c Si+A collisions. *Physics Letters*, **B271** (1991) 447–452.

[A+91b] T. ABBOTT *et al.* Comparison of p+A and Si+Au collisions at 14.6 GeV/c. *Physical Review Letters*, **66** (1991) 1567–1570.

[A+91c] T. ABBOTT *et al.* Forward and transverse energies in relativistic heavy ion collisions at 14.6 GeV/c per nucleon. *Physical Review*, **C44** (1991) 1611–1619.

[A+92a] T. ABBOTT *et al.* Bose-Einstein correlations in Si+Al and Si+Au collisions at 14.6 A · GeV/c. *Physical Review Letters*, **69** (1992) 1030–1033.

[A+92b] T. ABBOTT *et al.* Centrality dependence of K^+ and π^+ multiplicities from Si+A collisions at 14.6 A·GeV/c. *Physics Letters*, **B291** (1992) 341–346.

[A+92c] L. AHRENS *et al.* The operational status of the booster injector for the AGS accelerator complex and BNL. Technical Report 47119, BNL, 1992.

[A+93] Y. AKIBA *et al.* Bose-Einstein correlations in kaons in Si+Au collisions at 14.6 A · GeV/c. *Physical Review Letters*, **70** (1993) 1057–1060.

[Abb90] T. ABBOTT. *Search for Intermittency in Central Collisions of ^{16}O+Cu at 14.6 GeV/c.* PhD thesis, University of California, Riverside, 1990.

[B+74] V. BLOBEL *et al.* Multiplicities, Topological Cross Sections, and Single Particle Inclusive Distributions from pp Interactions at 12 and 24 GeV/c. *Nuclear Physics*, **B69** (1974) 454.

[B+89a] D. BEAVIS *et al.* A calorimeter for relativistic heavy-ion experiments. *Nuclear Instruments and Methods*, **A281** (1989) 367–372.

[B+89b] R. BRUN *et al.* PAW-Physics Analysis Workstation, the complete reference. Technical report, CERN, 1989. Version 1.07.

[B+93a] H. BØGGLID *et al.* Identified pion interferometry in heavy-ion collisions at CERN. *Physics Letters*, **B302** (1993) 510–516.

[B+93b] J. BOLZ *et al.* Interferometry of pions and kaons in high energy collisions. *Physics Letters*, **B300** (1993) 404–409.

[Bea] D. BEAVIS. Private communication.

[Ber89] G. BERTSCH. Pion interferometry as a probe of the plasma. *Nuclear Physics*, **A498** (1989) 173c–180c.

[BGJ90] D.H. BOAL *et al.* Intensity interferometry in subatomic physics. *Rev. Mod. Phys.*, **62** (1990) 553–602.

[Bow88] M.G. BOWLER. Extended sources, final state interactions and Bose-Einstein correlations. *Zeitschrift fur Physik*, **C39** (1988) 81–88.

BIBLIOGRAPHY

[Bow92] M.G. BOWLER. On surprises from Bose-Einstein correlations. *Physics Letters*, **B276** (1992) 237–241.

[C+68] G. CHARPAK *et al.* The use of multiwire proportional counters to select and localize charged particles. *Nuclear Instruments and Methods*, **62** (1968) 262–268.

[C+78] A.M. COOPER *et al.* A study of $K\bar{K}$ correlations in $\bar{p}p$ annihilations at 0.76 GeV/c. *Nuclear Physics*, **B139** (1978) 45–60.

[C+93a] R.Y. CHIAO *et al.* Faster than light? *Scientific American*, (1993) 52–60.

[C+93b] B.A. COLE *et al.* NEVIS wire chambers. Technical report, Brookhaven National Laboratory, 1993. Internal Memo to the E866 Collaboration, to be published.

[C+93c] J.B. COSTALES *et al.* A phoswich array for relativistic heavy ion collisions. *Nuclear Instruments and Methods*, **A330** (1993) 183–194.

[Chu] Y.Y. CHU. Private communication.

[Cia94] V. CIANCIOLO. Stream NTUPLES. Not yet released for public consumption, 1994.

[CL91] V. CIANCIOLO and R.J. LEDOUX. The joys of triggering or...how I learned to stop worrying and love PCOS. Technical report, Brookhaven National Laboratory, 1991. Internal Memo #1 to the E859 Collaboration.

[Coc74] G. COCCONI. Second-order interference as a tool for the determination of hadron fireball dimensions. *Physics Letters*, **B49** (1974) 459–461.

[Col92] B.A. COLE. *Particle Production at High Transverse Momentum in Nucleus-Nucleus Collisions at the AGS*. PhD thesis, Massachusetts Institute of Technology, 1992.

[COM92] *COMIS COmpilation and Interpretation System, Reference Manual*, 1992. Version 2.0.

[CSed] V. CIANCIOLO and R.A. SOLTZ. Vince and Ron's excellent HBT Memo. Technical report, Brookhaven National Laboratory, To be completed. Internal Memo to the E859 Collaboration.

[D+82] M. DEUTSCHMANN *et al.* A study of second-order interference for pions produced in various hadronic interactions. *Nuclear Physics*, **B204** (1982) 333–345.

[EK80] A. ETKIN and M.A. KRAMER. The Brookhaven National Laboratory's Multiparticle Spectrometer drift chamber system. *IEEE Transactions on Nuclear Science*, **NS-27** (1980) 139–144.

[Etk79] A. ETKIN. A drift chamber system for use in a high rate environment. *IEEE Transactions on Nuclear Science*, **NS-26** (1979) 54–58.

[F+79] A.G. FRODESEN *et al.* *Probability and Statistics in Particle Physics*. Universitetsforlaget, Bergen, Norway, 1979.

[F+86] B.L. FRIMAN *et al.* Converting mixed phase into hadrons. *Nuclear Physics*, **B266** (1986) 468–486.

[Fes85] H.C. FESEFELDT III. Simulation of hadron showers. Technical Report 85-02, Physikalishes Institute def RWTH Aachen Physikzentrum (PITHA), 1985.

[G+60] G. GOLDHABER *et al.* Influence of Bose-Einstein statistics on the antiproton-proton annihilation process. *Physical Review*, **120** (1960) 300–312.

[G+87] C. GREINER *et al.* Separation of strangeness from antistrangeness in the phase transition from quark to hadron matter: Possible formation of strange quark matter in heavy-ion collisions. *Physical Review Letters*, **58** (1987) 1825–1828.

[G+93] D.M. GREENBERGER *et al.* Multiparticle interferometry and the superposition principle. *Physics Today*, (1993) 22–29.

[G+94] C. GREINER *et al.* Strange matter — a new domain of nuclear physics. *Nuclear Physics*, **A566** (1994) 157c–166c.

[GEA92] *GEANT User's Guide*, 1992. Version 3.15.

[GKW79] M. GYULASSY *et al.* Pion interferometry of nuclear collisions I. Theory. *Physical Review*, **C20** (1979) 2267–2292.

[GM89] C. GREINER and B. MÜLLER. Pair correlations of neutral strange particles emitted in relativistic heavy ion collisions. *Physics Letters*, **B219** (1989) 199–204.

[GP90] M. GYULASSY and S. PADULA. Kaon vs. pion inteferometry signatures of quark-gluon plasma formation. *Physical Review*, **C41** (1990) R21–23.

[Gro90] PARTICLE DATA GROUP. Particle properties booklet. *Physics Letters*, **B239** (1990).

BIBLIOGRAPHY

[Gus94] G. GUSTAFSON. String models. *Nuclear Physics*, **A566** (1994) 233c–244c.

[Gyu92] M. GYULASSY. K_s pictures of strangeness distillation. *Physics Letters*, **B286** (1992) 211–215.

[Gyu93] M. GYULASSY. 2D χ^2 analysis of pion interferometry data from the AGS. In G.S.F. STEPHANS *et al.*, editors, *Proceedings of Heavy Ion Physics at the AGS*, pp. 350–361, 1993.

[H+93] S. HAYASHI *et al.* PID859 user's manual. Technical report, Brookhaven National Laboratory, 1993. Internal Memo # 11 to the E859 Collaboration.

[HB74] R. HANBURY-BROWN. *The Intensity Interferometer*. Taylor and Francis Ltd., London, 1974.

[Hig75] V. HIGHLAND. Some practical remarks on multiple scattering. *Nuclear Instruments and Methods*, **129** (1975) 497–499.

[HN85] O. HANSEN and S. NAGAMIYA. Studies of particle production at extreme baryon densities in nuclear collisions at the AGS. Technical report, Brookhaven National Laboratory, 1985. Proposal submitted to the AGS Program Committee.

[Hua88] H.Z. HUANG. Transfer matrix for Henry Higgins magnet. Technical report, Brookhaven National Laboratory, 1988. Internal Memo #22 to the E802 Collaboration.

[Hua90] H.Z. HUANG. *Semi-inclusive and Inclusive Spectra of Charged Pions, Kaons and Protons from Proton-Nucleus and Silicon-Nucleus Collisions at AGS Energy*. PhD thesis, Massachusetts Institute of Technology, 1990.

[Hum88] T.J. HUMANIC. Pion interferometry with ultrarelativistic heavy-ion collisions from the NA35 experiment. *Zeitschrift fur Physik*, **C38** (1988) 79–84.

[Hum94] T.J. HUMANIC. Identified partilce interferometry in heavy-ion collisions: results from the CERN NA44 experiment. *Nuclear Physics*, **A566** (1994) 115c–122c.

[Jac89] M. JACOB. Quark matter — facts and hopes. *Nuclear Physics*, **A498** (1989) 1c–32c.

[Jaf] R. JAFFE. Private communication.

[Jam80] F. JAMES. Monte Carlo theory and practice. *Rep. Prog. Phys.*, **43** (1980) 1145–1189.

[JR80] F. JAMES and M. ROOS. Errors on ratios of small numbers of events. *Nuclear Physics*, **B172** (1980) 475–480.

[JR92] F. JAMES and M. ROOS. MINUIT—function minimization and error analysis. Technical Report D506, CERN, 1992.

[K+93] S. KAHANA *et al.* Physics at the AGS with a relativistic cascade. In G.S.F. STEPHANS *et al.*, editors, *Proceedings of Heavy Ion Physics at the AGS*, pp. 263–282, 1993.

[Keh] W.L. KEHOE. Private communication.

[Koo77] S. KOONIN. Proton pictures of high-energy nuclear collisions. *Physics Letters*, **B70** (1977) 43–47.

[KP74] G.I. KOPYLOV and M.I. PODGORETSKIĬ. Mutual coherence functions of elementary particles and mutiple production. *Yad. Fiz.*, **19** (1974) 434–446.

[KUI91] *KUIP — Kit for a User Interface Package*, 1991.

[Kur92] K. KURITA. *Particle Production Study in Proton-Nucleus and Central Oxygen-Nucleus Collisions at 14.5 A·GeV/c*. PhD thesis, Columbia University, 1992.

[L+87] M.J. LEVINE *et al.* Distributed data acquisition for BNL802 I: The Front End. In *Proceedings of the 5th Conference on Real-Time Computer Applications in Nuclear, Particle and Plasma Physics*, pp. 830–834, San Francisco, CA, USA, 1987. IEEE Transactions of Nuclear Science.

[LeC87] FERA/FERET — Fast Encoding and Readout ADC/TDC Systems. Technical Report Application Note # AN-4004A, LeCroy, 1987.

[Lor89] B. LORSTAD. Boson interferometry: A review of high energy data and its interpretation. *Int. J. Mod. Phys.*, **A4** (1989) 2861–2896.

[M+92] I.N. MISHUSTIN *et al.* Pion production and Bose-enhancement effects in relativistic heavy-ion collisions. *Physics Letters*, **B276** (1992) 403–408.

[Mora] D.P. MORRISON. Private communication.

[Morb] R.J. MORSE. Private communication.

[Mor90] R.J. MORSE. *Bose-Einstein Correlation Measurements in 14.6* A · GeV/c *Nulceus-Nucleus Collisions*. PhD thesis, Massachusetts Institute of Technology, 1990.

BIBLIOGRAPHY

[Mor91] D.P. MORRISON. The LVL2 database and INTER. Technical report, Brookhaven National Laboratory, 1991. Internal Memo #2 to the E859 Collaboration.

[Mor94] D.P. MORRISON. *Rapidity Dependence of Kaon Production In Si+Au and Si+Al at 14.6 A GeV/c*. PhD thesis, Massachusetts Institute of Technology, 1994.

[Mül85] B. MÜLLER. *The Physics of the Quark-Gluon Plasma*. Springer Verlag, Heidelberg, Germany, 1985.

[P+90a] S.S. PADULA *et al.* Pion interferometric tests of transport models. *Nuclear Physics*, **B329** (1990) 357–375.

[P+90b] S. PRATT *et al.* Detailed predictions for two-pion correlations in ultrarelativistic heavy-ion collisions. *Physical Review*, **B42** (1990) 2646–2652.

[Par92] C. PARSONS. *Strange Particle Production in 14.6 GeV/A Nucleus-Nucleus Collisions*. PhD thesis, Massachusetts Institute of Technology, 1992.

[Praa] S. PRATT. Private communication.

[Prab] S. PRATT. Looking for quark droplets in ultrarelativistic collisions. To be published in *Nuclear Physics B*.

[Pra84] S. PRATT. Pion interferometry for exploding sources. *Physical Review Letters*, **53** (1984) 1219–1221.

[Pra86] S. PRATT. Pion interferometry of quark-gluon plasma. *Physical Review*, **D33** (1986) 1314–1327.

[Pra92] S. PRATT. Kaon pictures of QCD plasma droplets. *Physical Review Letters*, **68** (1992) 1109–1111.

[Pra94] S. PRATT. Testing transport theories with correlation measurements. *Nuclear Physics*, **A566** (1994) 103c–114c.

[Qua89] D.R. QUARRIE. YBOS programmer's reference manual. Technical Report 156, CDF, 1989. Version 3.3.

[Raf84] J. RAFELSKI. Strangeness production in the quark gluon plasma. *Nuclear Physics*, **A418** (1984) 215c–235c.

[Rat94] KEVIN RATHBUN. Electron production in heavy ion collisions. Master's thesis, Massachusetts Institute of Technology, 1994.

[RDB87] *RDB Reference Manual*, 1987.

[Rem] L.P. REMSBERG. Private communication.

[RLZ88] L.P. REMSBERG *et al.* Studies of high-density baryon matter from extended measurements of particle momentum distributions and from high-precision two-particle correlations. Technical report, Brookhaven National Laboratory, 1988. Proposal submitted to the AGS Program Committee.

[RM82] J. RAFELSKI and B. MÜLLER. Strangeness production in the quark-gluon plasma. *Physical Review Letters*, **48** (1982) 1066–1069.

[Rol] G. ROLAND. Private communication.

[Rot94] P. ROTHSCHILD. *Rapidity Dependence of Anti-Proton Production in Relativistic Heavy Ion Collisions at 14.6 A GeV/c.* PhD thesis, Massachusetts Institute of Technology, 1994.

[S+86] T. SUGITATE *et al.* 100 cm long time-of-flight scintillation counters with rms resolution of 50 ps. *Nuclear Instruments and Methods*, (1986).

[S+93a] T.C. SANGSTER *et al.* Target rapidity baryon distributions in ^{28}Si + ^{197}Au and ^{197}Au + ^{197}Au collisions at 14.6 and 11.7 A · GeV/c. In G.S.F. STEPHANS *et al.*, editors, *Proceedings of Heavy Ion Physics at the AGS*, pp. 61–71, 1993.

[S+93b] J.P. SULLIVAN *et al.* Bose-Einstein correlations of pion pairs and kaon pairs from Relativistic Quantum Molecular Dynamics. *Physical Review Letters*, **70** (1993) 3000–3003.

[S+94a] H. SORGE *et al.* Baryon pair production in ultrarelativistic nucleus-nucleus collisions. *Nuclear Physics*, **A566** (1994) 633c–640c.

[S+94b] J.P. SULLIVAN *et al.* Calculations of Bose-Einstein correlations from relativistic quantum molecular dynamics. *Nuclear Physics*, **A566** (1994) 531c–534c.

[Sak92] H. SAKURAI. *Study of Antiproton Production in ^{28}Si+A Collisions at 14.6 A GeV/c.* PhD thesis, University of Tokyo, 1992.

[Sar89] M. SARABURA. *Cluster Production in Relativistic Heavy-ion Collisions.* PhD thesis, Massachusetts Institute of Technology, 1989.

[Sau77] F. SAULI. Principles of operation of multiwire proportional and drift chambers. Technical Report 77-09, CERN, 1977.

[Sch93] B. SCHWARZSCHILD. Nobel physics prize to Charpak for inventing particle detectors. *Physics Today*, 46(1) (1993) 17–20.

[SL87a] R.A. SCHEETZ and M.J. LEVINE. An intelligent VME-based CAMAC crate controller. In *Proceedings of the 5th Conference on Real-Time Computer Applications in Nuclear, Particle and Plasma Physics*, pp. 1033–1035, San Francisco, CA, USA, 1987. IEEE Transactions of Nuclear Science.

[SL87b] R.A. SCHEETZ and M.J. LEVINE. A VME-VMX interface to FASTBUS via the LeCroy 1821 segment manager. In *Proceedings of the 5th Conference on Real-Time Computer Applications in Nuclear, Particle and Plasma Physics*, pp. 1006–1008, San Francisco, CA, USA, 1987. IEEE Transactions of Nuclear Science.

[Sol91] R.A. SOLTZ. Exercising the track-finding trigger. Technical report, Brookhaven National Laboratory, 1991. Internal Memo #4 to the E859 Collaboration.

[Sol93] R.A. SOLTZ. Pass3 timing calibration: Strategic design and implementation. Technical report, Brookhaven National Laboratory, 1993. Internal Memo to the E859 Collaboration.

[Sol94] R.A. SOLTZ. *Two Pion Correlation Measurement for Si+X at 14.6 A-GeV/c and Au+Au at 11.6 A-GeV/c*. PhD thesis, Massachusetts Institute of Technology, 1994.

[Sor93] H. SORGE. Energy dependence of strangeness production in ultrarelativistic pA and AA collisions. In G.S.F. STEPHANS *et al.*, editors, *Proceedings of Heavy Ion Physics at the AGS*, pp. 283–303, 1993.

[SQ87] M. SHAPIRO and D.R. QUARRIE. A beginner's guide to analysis_control and build_job. Technical Report 384, CDF, 1987. Version 1.01.

[Ste] G.S.F. STEPHANS. Private communication.

[Ste90] G.S.F. STEPHANS. Tracking chamber geometry arrays and data. Technical report, Brookhaven National Laboratory, 1990. Internal Memo #54 to the E802 Collaboration.

[Ste91] G.S.F. STEPHANS. Creating and checking geometry files. How to run the programs, 1991.

[Ste94] G.S.F. STEPHANS. Recent results from E859 using Si beams at 14.6 A · GeV/c. *Nuclear Physics*, **A566** (1994) 269c–276c.

[Str94] D. STROTTMAN. Status of fluid dynamic models for relativistic heavy ion reactions. *Nuclear Physics*, **A566** (1994) 245c–256c.

[Sun94] T. SUNG. *P_t dependence of kaon production in Si+Al and Si+Au collisions at 14.6 A·GeV/c*. PhD thesis, Massachusetts Institute of Technology, 1994.

[T+88] P. THIEBERGER *et al.* BNL setup. *Nuclear Instruments and Methods*, **A268** (1988) 513.

[V+91] A.P. VISCHER *et al.* Reactions of QCD plasma droplets in hot mixed-phase matter. *Zeitschrift fur Physik*, **A340** (1991) 315–324.

[Vos] O. VOSSNACK. Private communication.

[Vos94] O. VOSSNACK. *2K Correlations*. PhD thesis, Columbia University, 1994.

[Vut88] V. VUTSADAKIS. Description of the magnetic field of Henry Higgins. Technical report, Brookhaven National Laboratory, 1988. Internal Memo #19 to the E802 Collaboration.

[Vut92] V. VUTSADAKIS. *Small Relative Momentum Proton Correlations in Relativistic Heavy Ion Collisions*. PhD thesis, Massachusetts Institute of Technology, 1992.

[W+87] B. WADSWORTH *et al.* The trigger supervisor: Managing triggering conditions in a high energy physics environment. In *Proceedings of the 5th Conference on Real-Time Computer Applications in Nuclear, Particle and Plasma Physics*, pp. 980–983, San Francisco, CA, USA, 1987. IEEE Transactions of Nuclear Science.

[Wan] Y. WANG. Private communication.

[Wan94] Y. WANG. *Phi Production in Heavy Ion Collisions*. PhD thesis, Columbia University, 1994.

[WIL87] W.A. WATSON III and M.J. LEVINE. Distributed data acquisition for BNL802 II: Software. In *Proceedings of the 5th Conference on Real-Time Computer Applications in Nuclear, Particle and Plasma Physics*, pp. 900–903, San Francisco, CA, USA, 1987. IEEE Transactions of Nuclear Science.

[X+94] NU XU *et al.* Pion interferometery in ^{28}Si+ pb central collisions. *Nuclear Physics*, **A566** (1994) 585c–588c.

[YK78] F. YANO and S. KOONIN. Determining pion source parameters in relativistic heavy ino collisions. *Physics Letters*, **B78** (1978) 556–559.

[Z+84] W.A. ZAJC *et al.* Two-pion correlations in heavy ion collisions. *Physical Review*, **C29** (1984) 2173–2187.

[Zac94] D. ZACHARY. *Scaling of Energy and Baryon Densities in Relavistic Heavy Ion Collisions*. PhD thesis, Massachusetts Institute of Technology, 1994.

[Zaja] W.A. ZAJC. Private communication.

[Zajb] W.A. ZAJC. Overview of the E859 Level II Trigger. To be published in *Nuclear Instruments and Methods*.

[Zaj82] W.A. ZAJC. *Two-Pion Correlations in Heavy Ion Collisions*. PhD thesis, University of California, Berkeley, 1982.

[Zaj87] W.A. ZAJC. Monte Carlo methods for the generation of events with Bose-Einstein correlations. *Physical Review*, **35** (1987) 3396–3408.

[Zaj90] W.A. ZAJC. Extracting physics from two-particle correlations. In M. PLÜMER *et al.*, editors, *Proceedings from the International Workshop on Correlations and Multiparticle Production (CAMP) (LESIP IV)*, pp. 439–453, Marburg, West Germany, 1990. World Scientific.

[Zaj92] W.A. ZAJC. Recent results from E802 and E859. *Nuclear Physics*, **A544** (1992) 237c–254c.

[Zaj93] W.A. ZAJC. A pedestrian's guide to interferometry. In H.H. GUTBROD and J. RAFELSKI, editors, *Particle Production in Highly Excited Matter*, pp. 435–459. Plenum Press, 1993. Proceeding of the NATO Advanced Study Institute on Particle Production in Highly Excited Matter, July 12–24, 1993, Il Ciocco, Tuscany, Italy.

[ZEB92] *ZEBRA RZ — Random Access Package Reference Manual*, 1992.

E-802 Collaboration List

E-802 Collaboration, Brookhaven National Laboratory, Upton, NY 11973 USA
ANL-BNL-UCBerkeley-UCRiverside-Columbia-INS(Tokyo)-Kyoto-Kyushu-
LLNL-MIT-NYU-Tokyo-Tsukuba

Y. AKIBA[6], D. BEAVIS[2], P. BEERY[4], H.C. BRITT[9], B. BUDICK[11], C. CHASMAN[2], Z. CHEN[2], C.Y. CHI[5], Y.Y. CHU[2], V. CIANCIOLO[10], B.A. COLE[10], J.B. COSTALES[9], H.J. CRAWFORD[3], J.B. CUMMING[2], R. DEBBE[2], J. ENGELAGE[3], S.Y. FUNG[4], M. GONIN[2], S. GUSHUE[2], H. HAMAGAKI[6], O. HANSEN[2], R.S. HAYANO[12], S. HAYASHI[2], S. HOMMA[6], H. KANEKO[7], J. KANG[4], S. KAUFMAN[1], W.L. KEHOE[10], K. KURITA[13], R.J. LEDOUX[10], M.J. LEVINE[2], Y. MIAKE[13], D.P. MORRISON[10], R.J. MORSE[10], B. MOSKOWITZ[2], S. NAGAMIYA[5], M.N. NAMBOODIRI[9], T.K. NAYAK[5], C.A. OGILVIE[10], J. OLNESS[2], C.G. PARSONS[10], L.P. REMSBERG[2], D. ROEHRICH[2], P. ROTHSCHILD[10], H. SAKURAI[12], T.C. SANGSTER[9], R. SETO[4], R. SOLTZ[10], P. STANKUS[5], S.G. STEADMAN[10], G.S.F. STEPHANS[10], T. SUNG[10], Y. TANAKA[8], M.J. TANNENBAUM[2], J. THOMAS[9], S. TONSE[9], J.H. VAN DIJK[2], F. VIDEBAEK[2], O. VOSSNACK[5], V. VUTSADAKIS[10], F.Q. WANG[5], Y. WANG[5], H.E. WEGNER[2], D.S. WOODRUFF[10], Y.D. WU[5], X. YANG[5], D. ZACHARY[10] AND W.A. ZAJC[5]

[1] Argonne National Laboratory, Argonne, IL 60439-4843

[2] Brookhaven National Laboratory, Upton, NY 11973

[3] University of California, Space Sciences Laboratory, Berkeley, CA 94720

[4] University of California, Riverside, CA 92507

[5] Columbia University, New York, NY 10027 and Nevis Laboratories, Irvington, NY 10533

[6] Institute for Nuclear Study, University of Tokyo, Tokyo 188, Japan

[7] Kyoto University, Sakyo-Ku, Kyoto 606, Japan

[8] Kyushu University, Fukuoka 812, Japan

[9] Lawrence Livermore National Laboratory, Livermore, CA 94550

[10] Massachusetts Institute of Technology, Cambridge, MA 02139

[11] New York University, New York, NY

[12] Department of Physics, University of Tokyo, Tokyo 113, Japan

[13] University of Tsukuba, Tsukuba, Ibaraki 305, Japan

Acknowledgments

Contrary to popular opinion, the acknowledgments section of a thesis may be the single most important section. After all, this is the only place where a set of "thank-yous," accumulated over a period of more than six years, will be recorded. This section also appeals to a much larger audience *and* and it is certainly the most fun to write. I don't feel restricted to the analytical, left side of my brain, and I will probably be more effusive than eloquent.

The best part of becoming a scientist is the wonderful people I have met and have had the privelege of calling my friends. I would like to thank every heavy ion group member, past and present, for creating such a fun and challenging environment in which to work.

Bob Ledoux was with the group not nearly as long as we would have liked. Still, his contagious enthusiasm (and singing ability) seduced many of us into the group. His influence remains prominently stamped on all of us. Richard Morse and Vasilios Vutsadakis were both excellent HBT mentors. Richard's work ethic will haunt me to my grave. Chuck Parsons gave the group working drift chamber electronics, sharable PAW, and a fiercely independent streak. I will always regret missing his bravura performance when he single-handedly fixed the flooded T3 discriminator boards. Brian Cole may be the person most singularly responsible for making sure that E859 took data. It may not be a coincidence that "Brian" and "brain" are acronyms! Brian has had an enormous impact on my development as a physicist, always demanding that I keep searching for the *right* answer. I may never forgive Brian for introducing me to the E859 Monte Carlo program, although he did much to expiate this sin when he inspired me to brew beer. Walter Kehoe's thorough knowledge of the Long Island restaurant scene made our home away from home a much more civilized experience than it would have otherwise been. Walter also taught me that style is important, since without it, substance may get overlooked.

Steve Steadman has been instrumental in providing an excellent work environment. He has been an excellent group leader and he will be sorely missed next year. Craig Ogilvie has brought a new vision and atmosphere to the group. Marge Neal has been a second mother to all of us, and it is largely due to her that our drift chambers exist and work so well. I will try to forget her mnemonic for the resistor coloring scheme. Dave Woodruff has kept our computers in excellent shape. Very importantly, he has not been protective about the system password. Barbara Corbsier is the latest in a long line of heavy ion group secretaries. She has made our bureaucratic lives much simpler. Dan Zachary, Ted Sung and Peter Rothschild defected into our group just as were desperate for manpower. Ted's energy and Dan's wrestling prowess are

boundless. Thanks to Pete, we have an understandable reconstruction code. Mark Baker has earned my endless thanks for an inhumanly careful proofreading of this document. Larry Ahle has brought a touch of athleticism to this otherwise sedentary group (we'll see if he continues to run, swim, play squash, tennis, golf, baseball and basketball while he tries to write his thesis). Larry has also provided a measure of algebraic competence that was badly needed at several points in this analysis.

Dave Morrison was one of the first people I met at MIT and he has been one of my best friends for these last six years. Thank goodness he has forgiven me for abandoning him to get married during the summer of 1989. Dave is probably the funniest person I know, and he has kept us entertained during boring lectures and midnight shifts at Brookhaven. Dave has made all of our lives a lot simpler by virtue of being the group Internet connection - keep on futzing Dave!

Ron Soltz has been my officemate and another one of my best friends for many years now. He has taught me the meaning of the words "dedicated" and "meticulous." He has also introduced me to the all-you-can-eat diet, good cheesecake, and the pleasures of jazz. I am glad he is finally with his sweetie in San Francisco, but this office seems a lot emptier without him.

Ole Vossnack, Bill Zajc and Lou Remsberg are honorary heavy ion group members and so I shall thank them here. Ole brought a sense of sophistication to the locker room atmosphere known as the counting house. Ole is also responsible for making sure we had the best TOF calibrations possible, and got thanked with a bruised rib and a stolen wallet. Bill Zajc is very high on my list of physics heroes. I fervently hope that someday I will know as much about Bose-Einstein correlations as he has forgotten. I am honored that Bill agreed to be a member of my dissertation committee, taking the time to carefully read this thesis, and come to Boston for the defense. Lou had more intuition for the E859 trigger system than anyone. I will always regret not getting in that bike ride from the ferry to the lab.

George Stephans has been a better advisor I could have wished for. He always had the key insight that helped me progress, or kept me from making a fool out of myself. He always gave me the freedom to make my own mistakes. His support and motivation have been especially strong these last four months. One day we'll get to go cross-country skiing together.

I owe a debt of gratitude to all of my E859 collaborators and the staff of the AGS and Tandem accelerators. It takes a lot of people to make a large experiment work, and every one of these people did more than their part. Several people not on the collaboration list need a special note of thanks - Bob Scheetz, Kenny Asselta and Henry Diaz were always around when you needed them.

An experiment is largely defined by its spokesmen, and E859 has been a great success in large part due to Bob Ledoux, Lou Remsberg and Bill Zajc. These men provided motivation and vision, and made working on E859 a lot of fun. They trusted the graduate students, and acted on their suggestions and requests. Maybe it was part of a sink-or-swim philosophy on education, and educate us they did. It probably won't take me long to realize that I have been spoiled, and that one's bosses are *not* always looking out for one's best interest.

I want to thank Heinz Sorge for writing the RQMD code that was used in this analysis. He made the source code, and his advice, freely available. I want to thank Scott Pratt for writing the correlation code used in this analysis. He also made the source code, and his advice, freely available. Scott has explained many of the more subtler aspects of HBT (are there any other aspects?) to me.

I would like to thank my thesis committee, Wit Busza, Richard Milner and Bill Zajc, for reading this thesis carefully and giving valuable input.

I want to thank my in-laws for being much more than a family-in-law, a family-in-truth. Your concern, support and love has been very important to me.

I want to thank my brothers and sister for not laughing at me when I would gush at the dinner table about some neat physics tidbit I just learned. OK, so they did laugh.

It is not enough to thank my parents, but that is all I can do. Someday I hope to be as good of a parent to my own children. They provided a safe haven and refrained from ending my life despite the many times I pushed them to the brink; the dismembered bicycle was probably the closest I ever came. They taught me the value of hard work and the importance of doing somthing I enjoyed. They showed me, by example, how to be a good friend and team player. Most importantly, they gave me a self-confidence and a love of life and knowledge that can never be taken away. Thanks Mom and Dad!

Finally, and most importantly, I want to thank my lovely wife, Maureen, who has been my constant companion and strength throughout these years. For not yelling at me when I was late for dinner, for picking me up at Brookhaven on my birthday, for insisting that we go camping on a lovely weekend. For showing me all of the cool things about clouds, for listening to me babble on about computer problems I was having, for teaching me how to backpack. For my beer-brewing kit, for our lovely quilts and for maintaining family communications while I was holed away trying to finish up. For more things than I could fit in a book the size of this entire thesis — Te Amo.

Biographical Note

The author was born and raised outside of Detroit, the automobile capital of the world. Thus was born his passion for fast cars, bad baseball teams, and Motown music. He was raised in an Italian Catholic home and thinks that, given this, he is very patient, softspoken and even-tempered. Math, chemistry and biology captured his early curiosity — any physics aptitude that he may posess was very late blooming. He graduated from the University of Michigan, decided he didn't like optics after all, and found that MIT was the only school he had applied to with a strong nuclear physics program. As it turned out he was very lucky.

He is currently happily married and living in Cambridge, MA.